Block copolymer self-assembly and application for polymer electrodes

Sirikorn Chasvised

THÈSE

UNIVERSITE DE PAU ET DES PAYS DE L'ADOUR

École doctorale des sciences exactes et leurs applications (ED211)

Présentée et soutenue le 17 May 2021

par **Sirikorn CHASVISED**

pour obtenir le grade de docteur
de l'Université de Pau et des Pays de l'Adour
Spécialité : Chimie et Physico-chimie des Polymères

Block copolymer self-assembly and application for polymer electrodes

MEMBRES DU JURY

RAPPORTEURS

• Éric CLOUTET	Directeur de Recherche/ Université de Boudeaux
• Amorn CHAIYASAT	Professeur Associé/ Rajamangala University of technology Thanyaburi

EXAMINATEURS

• Stéphanie REYNAUD	Directrice de Recherche/ Université de Pau et des Pays de l'Adour
• Murielle CHAVAROT-KERLIDOU	Chargée de Recherche/ CEA Grenoble/ Université Grenoble Alpes

DIRECTEURS

• Laurent BILLON	Professeur/ Université de Pau et des Pays de l'Adour
• Antoine BOUSQUET	Maître de conferences/ Université de Pau et des pays de l'Adour

ACKNOWLEDGEMENTS

All the work presented in this thesis was carried out within the IPREM institute (mixed research unit UMR 5254 CNRS, Université de Pau et des Pays de L'Adour). This thesis is in a partial fulfilment of the requirement for obtaining the Ph.D. degree in Polymer Chemistry. The Ph.D. study was carried out from January 2017 to May 2021.

My kind acknowledgement goes to the Royal Thai Government scholarship for financial support to study abroad, this funding gave me the great opportunity to learn and succeed in my academic study in polymer chemistry field. My acknowledgement also goes to the Rambhai Barni Rajabhat University, Thailand for promoting the time spent supporting and financial support during my Ph.D. study. I also grateful for the funding from the Innovacion for a Severo Ochoa Excellence Accreditation grant 2020-2023 (CEX2019-000925-S, MIC/AEI), EU-funded ITN eSCEALED (Grant agreement ID: 765376), all analysis of SEC, NMR and AFM were supported by a public grant overseen by the French National Research Agency ANR-10-EQPX-16 XYLOFOREST and Kuraray Co., Ltd, is acknowledged for providing MBM20. Thanks to the groups of Pr A. Llobet (ICIQ) and Dr V. Artero (CEA) for providing nice catalyst to incorporate in the electrode I was developing.

I am highly grateful to my supervisors, Professor Laurent BILLON for his dedication and great help throughout the whole project. Over his supervision, his kindness and to give me an opportunity to study in France. I was impressed since the first day when I arrived in France, with his attention and give great advices to me. I would like also take this chance to greatly acknowledge my co-supervisor Associate Professor Antoine BOUSQUET who has had great impact on the scientific works for his dedicated supervision. His advice helps me to successfully fulfill my Ph.D. study. Through the frequent free discussion, I earned a lot of valuable inspirations for conducting my work.

I would like warmly thank Laurent AUTHIER and Cyril CUGNET for their great supervision in electrochemistry knowledge. Their guidance helped me to perform this work in electrochemistry part of my research. My gratitude also goes to Laurence PESSONI for her assistance during my experiments and taking care of me during my study. I also thanks for Pierre MARCASUZAA, Nicolas BENOOT and Coste MAWELE LOUDY for their great help.

Thanks also go to all of the present and former colleagues of IPREM and eSCALED project group, for providing a functioning social, friendship and a great working environment.

A special thank goes to my family, for their supporting and encourage me all the time. I highly appreciated their patience to await me to finish my Ph.D.

List of abbreviation

χ: Flory-Huggins interaction parameter

λ: the persistence length of the rod segments

β: the relative length of the rod segment to the coil segment

Γ: surface overage

μN: Maier-Saupe interaction strength

AFM: atomic force microscopy

Ag NWs: silver nanowires

ATRP: atomic transfer radical polymerization method

BCPs: block copolymers

bda: 2,2'-bipyridine-6,6'-dicarboxylate

BF: breath figure

bpy: 4,4'-bipyridine

BuA: butyl acrylate

C_{60}: fullerene

CA: chronoamperometry

CE: counter electrode

$CHCl_3$: chloroform

CNTs: carbon nonotubes

CP: chronopotentiometry

CPE: controlled potential electrolysis

CPS: Closed-packed spheres

CuAAC: copper catalyzed azide-alkyne cycloaddition

CV: cyclic voltammetry

d: density

D: linear dodecyl

d: periodic length-scale

DCC: *N,N'*-dicyclohexylcarbodiimide

DCM: dichloromethane

DEH-PPV: poly[2,5-de(2'-ethyl)hexyloxy)-1,4-phenylenevinylene]

DIS: disordered

DMF: *N,N'*-dimethylformanide

DMPU: N,N’-dimethylpropyleneeurea

DMSO: dimethyl sulfoxide

DOSY: diffusion order spectroscopy

DP: degree of perimerization

DPV: differential pulse voltammetry

DSC: differential scanning calorimetry

EC: ethylene cellulose

EH: ethylhexyl

EHD: electro-hydrodynamic

f: volume fraction

FTIR: Fourier transformed infrared spectroscopy

H: cylinder with hexagonal packed

H: linear hexyl

HC: honeycomb structure

HFC: hydrogen fuel cells

HIPS: high impact polymetric styrene

hv-WS: light-induced water splitting

KCTP: Kumada catalyst-transfer polycondensation

L: lamellae structure

LIBs: lithium-ion batteries

LiTFSI: lithium bis(trifluoromethane)sulfonamide

MALDI-TOF MS: matrix assisted lasewr desorption ionization time-of-flight mass spectroscopy

MDMO-PPV: poly(2-methoxy-5-(3,7-dimethyloctyloxy)-1,4-phenylene vinylene)

MeOH: methanol

MMA: methyl methacrylate

M_{ni}: molecular weight

MoS_2: molybdenum disulfide

MPEs: molecular screen-printed electrodes

MW: microwave

MWCNTs: multi walled carbon nanotubes

N: degree of polymerization

Ni(dppp)Cl_2: [1,3-bis(diphenylphosphino)propane]dichloronikel(II)

NMR: nuclear magnetic resonance spectroscopy

NTf_2^-: bis(trifluoromethane) sulfonimide anion

ODT: order disorder transition temperature

P(MMA-r-HEMA): poly(methyl methacrylate-r-hydroxyethyl methacrylate)

P2VP: poly(2-vinylpyridine)

P3AT: poly(3-alkyl thiophene)

P3HT: poly(3-hexylthiophene)

P4PV: poly(4-vinylpyridine)

PANI: polyaniline

PCBM: [6,6]-phenyl C61-butyric acid methyl ester

PDMS: polydimethylsiloxane

PE: printed electronics

PEC: photoelectrochemical cells

PEDOT: poly(3,4-ethylenedioxythiophene)

PEO: poly(ethylene oxide)

PET: polyethylene terephthalate

PF: polyfluorene

PHEAA: poly(N-hydroxylethylacrylamide)

PI: polyisoprene

PLA: polylactic acid

PLLA: poly(L-lactide)

PMMA: poly(methyl methacrylate)

PnBuA: poly(n-butyl acrylate)

PNIPAAm: poly[2,7-(9,9-dihexylfluorene)]

PPO: poly(propylene oxide)

PPV: poly(diethylhexyloxy-p-phenylenevinylene)

PPy: polypyrrole

PS: polystyrene

PSS: poly(styrenesulfonate)

PVA: poly(vinylacetate)

PVB: poly(vinylbutyral)

PVDF: poly(vinylidene difluoride)

PVs: photovoltaic devices

pyp: 4-(pyrene-1-yl)pyridine

Q229: body-centered spheres

Q230: double-gyroid phase

RE: reference electrode

SEC: size exclusion chromatography

SP: screen printing

SPAAC: strain promoted alkyne azide cycloaddition

SPCEs: screen-printed carbon-based electrodes

T_a: annealing temperature

t_a: processing time

T_c: crystallization temperature

tda: [2,2':6', 2''-terpyridine]-6,6''-dicarboxylate

TEG: thermoelectric power generator

TEG: triethylene glycol monomethyl ether

TFH: transparent film heaters

Tg: glass transition temperature

THF: tetrahydrofuran

V: volume of polymer

v_i: volume of the monomer

WAXS: wide-angle X-ray scattering

WE: working electrode

WOCs: water oxidation catalysts

ZnO: zinc oxide

Block copolymer self-assembly and application for polymer electrodes

Table of contents

General Introduction.....1

CHAPTER 1. State of the Art and position of the Project.....3

1. Context: Block copolymers and Electrodes.....5

2. Bulk Self-Assembly of Coil-Coil BCPs 7

2.1 Basics of coil-coil BCP self-assembly…….7

2.2 From thermal to microwave annealing, a processing time divided by 100!.....9

3. Bulk Self-Assembly of Rod-Coil BCPs.....13

3.1 Introduction to rod-coil self-assembly……...13

3.2 Influence of copolymer chain structure over film morphology……17

3.2.1 Impact of volume fraction.....17

3.2.2. Influence of the rod lateral chains.....20

3.2.3 Introducing a centered charge 22

4. The synthesis of conjugated rod-coil BCPs.....26

4.1 The Atom Transfer Radical Polymerization method (ATRP)……27

4.2 Kumada catalyst-transfer polycondensation (KCTP)……30

4.3 Click chemistry process and Huisgen azide-alkyne cycloaddition……34

4.3.1 Copper catalyzed azide-alkyne cycloaddition 34

4.3.2 Metal-free azide-alkyne cycloaddition 37

5. Polymer electrode in printed electronics 39

5.1 Introduction……...39
5.2 Among printing technologies: screen printing……..39
5.3 Conductive inks and polymer binder…….42
5.4 Applications for polymer electrode made via screen-printing……..43
5.4.1 Sensors 43
5.4.2 Batteries.....43
5.4.3 Solar Cells 45
5.4.4 Film Heaters 47
5.4.5 Catalysis 48
6. Conclusion 50
References: 53
CHAPTER 2. Hierarchically organized block copolymer films through “breath figure” templating and microwave induce self-assembly.....71
1. Introduction 75
2. Results & discussion 77
2.1. Hierarchical polymer film…….77
2.2. Microwave induced self-assembly of triblock copolymers continuous film……..80
2.3. Microwave induced self-assembly of Hierarchical polymer film……82
3. Conclusions 84
4. Experimental Section 85
4.1. Thin films preparation……..85
4.2. Honeycomb film preparation……85
4.3. Microwave annealing……85
4.4. Ellipsometry……..85

4.5. Surface analysis……86
4.6. Differential Scanning Calorimetry……86
4.7. Size Exclusion Chromatography……..86
References 87
Supporting Information.....89
CHAPTER 3. Robust and Efficient Screen-Printed Molecular Anodes with Anchored Water Oxidation Catalysts 99
_1. Introduction.....102
_2. Results and Discussion 103
2.1. Screen-printed electrodes……103
2.2. Anchoring of Ru WOCs on PE and redox properties……105
2.3. Long term performance of MPE……108
_3. Conclusions.....111
_References.....113
_Supplementary information 117
Method……..118
^{1}H-NMR Spectroscopy……127
Electrochemical Characterization……129
DPV before and after activation……130
TOF_{max} Calculation by FOWA……..131
CPE of 1-tda-pyp@CNT@PE and 15-tda-bpy@CNT@PE.....134
CVs for CP 25 – 225 µA……135
CV for CP at 100 µA over 20 hours……..138
CVs for CA at 1.45 V over 20 hours……141
CHAPTER 4. Fibrils or not fibriles: How to control P3HT-based copolymer thin film morphology? 145

1. Introduction 149

2. Experimental section 152

2.1. Materials 152

2.2. Instrumentation 152

2.3. Synthesis of alkyne-terminated P3HT (HC≡C-P3HT) by GRIM 153

2.4. Synthesis of Azide-terminated PMMA (PMMA-N_3) by ATRP 153

2.5. Synthesis of $P3HT_{5K}$-*b*-$PMMA_{10K}$ by click reaction 154

2.6. Quaternization of $P3HT_{5K}$-b^+-$PMMA_{10K}.I^-$ 154

3. Results and discussion 155

3.1. Synthesis and characterization of $P3HT_{16K}$-b-$PMMA_{10K}$ copolymer 155

3.2. Synthesis and characterization of $P3HT_{16K}$-b^+-$PMMA_{10K}.I^-$ copolymer 156

3.3. Morphology of block copolymer thin films 159

3.3.1 Solvent/solute interactions 159

3.3.1.1. Solution temperature 159

3.3.1.2. Effect of concentration 160

3.3.1.3. Influence of the copolymer composition: Introducing a charge and varying P3HT block length 161

3.3.1.4. Influence of the solvent 163

3.3.2. Physical treatment after the film formation 165

3.3.2.1. Thermal annealing treatment 165

3.3.2.2. Microwave annealing 166

4. Conclusion 171

Reference 172

Supplementary information 179

CHARPTER 5. Artificial metallo-enzyme based on a diimine-dioxime cobalt complex end-capped conductive poly(3-hexylthiophene**)** 189

_1. Introduction 193

_2. Experimental 195

Materials……195

Instrumentation……..195

Synthesis of cobalt complex-functionalized P3HT (P3HT-Co)……196

_3. Results and discussion 198

3.1. Synthesis and characterization of the artificial-metallo-enzyme P3HT-Cobalt (P3HT-Co)……198

3.2. Electrochemical characterization of P3HT-NH_2 and P3HT-Co complex catalyst……...202

_4. Conclusion 204

_Reference.....205

_Supplementary information 211

General Conclusion …….……219

General Introduction

Introduction: Climate change resulting from accumulation of anthropogenic carbon dioxide in the atmosphere and the uncertainty in the amount of recoverable fossil fuel reserves are driving forces for the development of renewable, carbon-neutral energy technologies. Hydrogen photosynthesis appears to be an appealing approach for a sustainable energy generation because it produces a "solar fuel" in a stable and storable chemical form, from solar energy and H_2O. A cost-effective and reliable process would have a tremendous societal impact since this achievement could transform European and worldwide Energy production, distribution and policies in the near future. Fuels as energy storage are far superior to batteries in terms of volume and transport costs, and it would constitute a renewable carbon-neutral process with no deleterious impact on the environment. Furthermore, many industries depend on fuels, where an adaptation from fossil to solar would be much preferred. H_2 is produced from photocatalytic water splitting through the reaction $H_2O \rightarrow H_2 + \frac{1}{2}O_2$ with an energy barrier of 1.23 eV. This barrier can be overcome by the energy brought by the photons, absorbed by a semiconductor. The semiconductors can be part of an external solar panel which is powering an electrochemical cell in which H2 is produced at one electrode by proton reduction and O2 is produce at the other electrode by water oxidation, like in Figure 0.

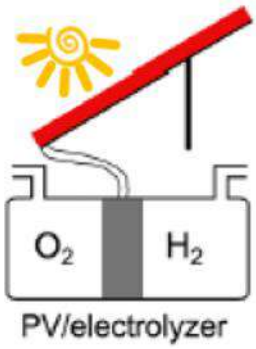

Figure 0. Schematic view of an electrochemical cell powered by a photovoltaic panel.

In this device many materials are used, and **during my PhD we have only focused our attention on the ones used in the electrochemical cell, and more precisely we developed polymers to be used in the electrode for proton reduction and water oxidation. First, we studied different diblock copolymers as binder material to make cheap and conductive electrode by screen-printing. Secondly, we worked on the electrocatalytic matters with**

both a polymer/catalyst complex blend for water splitting and an artificial metallo-enzyme for proton reduction.

My PhD thesis was as a side project, part of the eSCALED project, which is a contribution to structure early-stage research training at the European level and strengthen European innovation capacity to elaborate an artificial leaf. This project has received funding from the European Union's Horizon 2020 research and innovation program under the Marie Sklodowska-Curie grant agreement No 765376. Many partners are working together with different field of expertise. I had the chance to work around this network and profit from the materials developed and knowledge of the researchers involved. Especially, I worked in close collaboration with Pr Antoni Llobet group (ICIQ, Spain) for the project around water oxidation and with Dr Vincent Artero group (CEA, France) for the hydrogen evolution project.

In this PhD, we have developed polymeric electrodes from various BCPs. The use of such materials affords flexible and lightweight properties, the possibility to scale up the fabrication by cheap processes such as screen-printing and finally the possibility to use the polymers as a binder for both conductive charges and molecular catalysts.
Two kind of BCPs have been used during this PhD thesis:

- The first one is based on methyl methacrylate (MMA) and butyl acrylate (BuA). MMA is used for its capacity to bind the fluorinated NAFION electrode substrate, and thus preventing from delamination typically occurring during electrolysis at high potential. BuA has been selected for its low glass transition temperature (*Tg*) providing nice film-forming property and flexibility. The self-assembly behavior of this copolymer has been first studied **(chapter 2)** and then electrodes have been developed for water oxidation reaction **(chapter 3)**.
- The second copolymer is based on MMA for the reason discussed above and 3-hexyl thiophene for both the semi-conducting behavior of the polymer and its affinity with carbon charge *via* π-interaction. Again, the self-assembly of this copolymer has been first studied **(chapter 4)** and then an electrode for hydrogen evolution was produced from P3HT **(chapter 5)**.

First of all, this PhD manuscript is started in chapter 1 by a block copolymer State of the Art, their synthesis and self-assembly. The use of polymers as binder will be also presented for the elaboration of electrode by printing technologies

CHAPTER 1

State of the Art and Positioning of the Project

Table of contents

1. Context: Block copolymers and Electrodes 5

2. Bulk Self-Assembly of Coil-Coil BCPs 7

2.1 Basics of coil-coil BCP self-assembly……7

2.2 From thermal to microwave annealing, a processing time divided by 100!.....9

3. Bulk Self-Assembly of Rod-Coil BCPs 13

3.1 Introduction to rod-coil self-assembly……...13

3.2 Influence of copolymer chain structure over film morphology……17

3.2.1 Impact of volume fraction.....17

3.2.2. Influence of the rod lateral chains.....20

3.2.3 Introducing a centered charge.....22

4. The synthesis of conjugated rod-coil BCPs 26

4.1 The Atom Transfer Radical Polymerization method (ATRP)……27

4.2 Kumada catalyst-transfer polycondensation (KCTP)……30

4.3 Click chemistry process and Huisgen azide-alkyne cycloaddition……34

4.3.1 Copper catalyzed azide-alkyne cycloaddition 34

4.3.2 Metal-free azide-alkyne cycloaddition 37

5. Polymer electrode in printed electronics 39

5.1 Introduction……...39

5.2 Among printing technologies: screen printing……..39

5.3 Conductive inks and polymer binder……42
5.4 Applications for polymer electrode made via screen-printing……43
5.4.1 Sensors 43
5.4.2 Batteries.....43
5.4.3 Solar Cells 45
5.4.4 Film Heaters 47
5.4.5 Catalysis 48
6. Conclusion..... 50
REFERENCES: 53

1. Context: Block copolymers and Electrodes

Block copolymers (BCPs) are macromolecules composed of two or more kind of monomer units in which there is a linear arrangement of blocks; a block being defined as a portion of a polymer molecule in which the monomeric units have at least one constitutional or configurational feature absent from the adjacent portions. BCPs that contain two polymer blocks (PA) and (PB) attached on one end is called diblock copolymer PA-*b*-PB **(Figure 1a)**.[1] Depending of the microstructure of the polymer, coil-coil polymer can be produced in which both blocks are amorphous or if one or two block presents crystallinity the rod-coil or rod-rod terms are respectively employed. A large range of application is now attributed to BCPs such as information storage, nanoporous membranes, organic optoelectronics or anti-reflection coatings.[1-2] Indeed they present several advantages compared to competitor materials:

- A precise control of their film structuration at the nanometer scale, can be achieved. The different component in BCPs usually mix endothermically, and while short blocks may mix at high temperatures, long blocks are incompatible (i.e. thermodynamically immiscible). Consequently, the material (bulk) morphology of many BCPs is dominated by their tendency to spontaneously separate into microphases, for example lamellae **(Figure 1b)**, when the temperature is lowered.[2] This behavior is called "self-assembly" of BCPs, and will be further developed in this chapter.

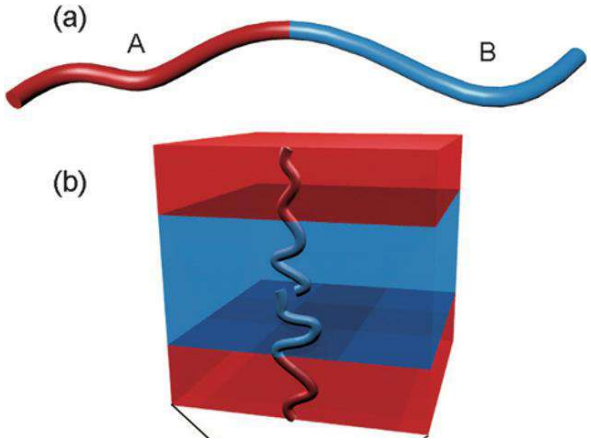

Figure 1. (a) schematic representation of diblock copolymer, (b) the rearrangement of A and B blocks in lamellar morphology.[2]

- In terms of physical and mechanical properties, BCPs surpass the corresponding random copolymers. The important properties of transition temperatures, tensile strength, modulus, and elastic properties depend upon the structural arrangement of the

molecular units comprised within the polymer structure. Most of available data in the literature suggest overwhelmingly that properties of BCPs are superior to those of random copolymers.[3] A BCPs can have properties characteristic of each of the homopolymers blocks.

- There is a large choice of monomers that can be polymerized and therefore, this bring an almost infinite combination of functionalities and properties in the final BCPs material.

In this PhD, we have developed polymeric electrodes from various BCPs. The use of such materials affords flexible and lightweight properties, the possibility to scale up the fabrication by cheap processes such as screen-printing and finally the possibility to use the polymers as a binder for both conductive charges and molecular catalysts.

Two kind of BCPs have been used during this PhD thesis:

- The first one is based on methyl methacrylate (MMA) and butyl acrylate (BuA). MMA is used for its capacity to bind the NAFION electrode substrate, and thus preventing from delamination typically occurring during electrolysis at high potential. BuA has been selected for its low glass transition temperature (*Tg*) providing nice film-forming property and flexibility. The self-assembly behavior of this copolymer has been first studied **(chapter 2)** and then electrodes have been developed for water oxidation reaction **(chapter 3)**. In this bibliographic part, we will present the basics of BCP self-assembly, the recent advances in this field with a focus on the use of microwave annealing and eventually describe the use of polymer binders for electrodes.
- The second copolymer is based on MMA for the reason discussed above and 3-hexyl thiophene for both the semi-conducting behavior of the polymer and its affinity with carbon charge *via* π-interaction. Again, the self-assembly of this copolymer has been first studied **(chapter 4)** and then an electrode for hydrogen evolution was produced from it **(chapter 5)**. Therefore, in this bibliography, the special features of rod-coil BCP self-assembly are explained (P3HT, as a conjugated aromatic polymer is rigid) and the synthetic ways to produce such polymers are presented.

2. Bulk Self-Assembly of Coil-Coil BCPs

2.1 Basics of coil-coil BCP self-assembly

As a definition, coil-coil BCPs are a full combination of flexible homopolymer chains, presenting amorphous domains characterized by a glass transition and no crystalline phase. When two homopolymers of different nature are mixed, a macro-segregation occurs most of the time, due to an immiscibility of the monomer units. On the contrary, when these two polymers are covalently linked in a BCP, the segregation can only be done at the length-scale of the chain, and the strength of repulsive interaction between blocks drives the morphologies of films in micro-domains (typically 10 to 100 nm).[4-5] This behavior is called "self-assembly" of BCPs. Various microdomain structures can be obtained, lamellar, cylinder, sphere,… and are related to the volume ratio between blocks and chain architectures.[6] This segregation can be achieved when the product of the Flory-Huggins interaction parameter (χ) and the total degree of polymerization (N) is usually higher than 10.5.[7] Below this value the two blocks are miscible and no segregation is observed. When $\chi N >> 10.5$, the segregation goes up to a strong regime and nanodomains can clearly be identified. Control over the chain length, and thus molar mass, directly governs the periodic length-scale (d) of the resulting assembly with an approximate relationship of $d = N^{2/3}.\chi^{1/6}$ for the strong-segregation regime. [8] As an example, coil-coil PS-*b*-PMMA is one of the most studied BCPs for lithography application due to the possibility to produce ordered morphologies such as lamellae or cylinders on a large area and presenting a perpendicular orientation of the domains towards the substrate. [9]

Another parameter is of great importance, the volume ratio of the blocks, which will dictates the morphology of the BCP film. The area minimization at the interface of two blocks takes place to lower the interfacial energy and induces microphase structuration in order to reach the lowest free energy. A typical coil-coil phase diagram is shown in **Figure 2a**.[2, 6-7] In this figure the volume fraction is represented by

$$f \text{ or } f_A = V_A/(V_A+V_B) \qquad \text{Equation 1}$$

where V_A *and* V_B are the volume of block A and B respectively. Or:

$$f_A = \frac{N_A v_A}{N_A v_A + N_{AB} v_B} \qquad \text{Equation 2}$$

Where N_i is the *DP* of block i et v_i is the volume of the monomer i calculated as such:

$$v_i = \frac{M_{ni}}{dN_i} \qquad \text{Equation 3}$$

M_{ni} and d are the molecular weight and the density of the monomer respectively.

By varying the f_A value a range of morphology can be obtained as depicted in **Figure 2b**.

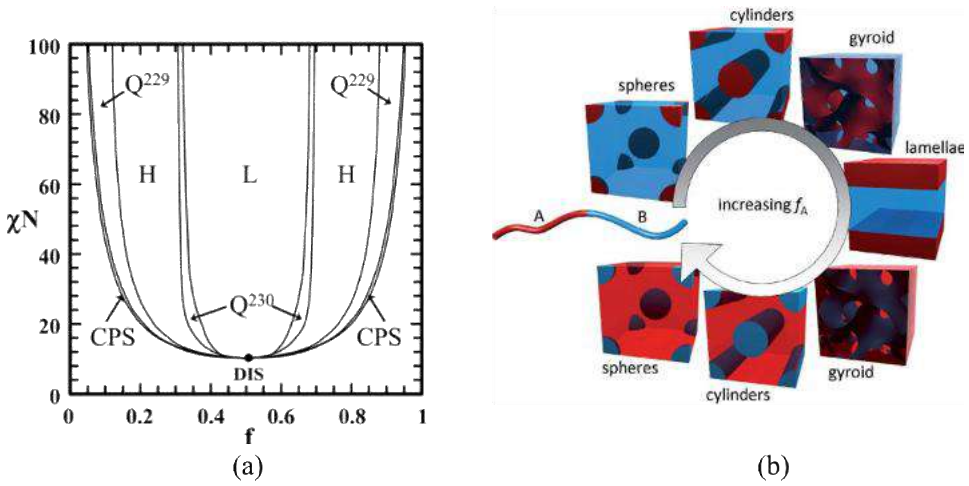

Figure 2. (a) The typical phase diagram of a coil-coil BCPs with the relationship between χN and f, L: lamellae, H: cylinder with hexagonal packed, Q230: double-gyroid phase, Q229: body-centered spheres, CPS: closed-packed spheres, DIS: disordered. (b) The different morphologies of BCPs resulted by increasing f_A.[4]

Thus, for a symmetrical BCP, f_A = 0.5, the interface between blocks is planar and lamellae are produced. For a non-symmetrical system, a curvature is produced to minimize interfaces and leads to different morphologies such as gyroid, cylindrical or spherical as depicted in Figure 2b.[10] The variety of the morphology reachable and the size of the domain, that can go in the smallest cases below 10 nm, have opened the door for the use of BCPs in emerging application where lithography is needed such as chip manufacturing.

Despite the apparent advantages of the BCPs method to produce nanodomains, a number of important challenges remain and have been the subject of much research. These include:

- achieving patterns with long-range order [11]
- controlling orientation (towards the substrate) [11]
- decreasing the size of the pattern. [12-13]
- tuning the functionality of the domains. [14-15]

A less addressed challenge is the need to process pattern development in relatively short times comparable with what is used in the semiconductor industry.[11] Indeed, microphase separation in BCP thin films is normally achieved using thermal or solvent annealing that can

be time-consuming (from several hours to days). In the following part, is discussed the evolution of the annealing step and the rise of microwave induced thermal treatment.

2.2 From thermal to microwave annealing, a processing time divided by 100!

The self-assembly of BCP thin films is then a versatile method for producing periodic nanoscale patterns with a variety of shapes. The key to reach a desired pattern or structure is the annealing step undertaken to facilitate the reorganization of nanoscale phase-segregated domains of the BCPs. Annealing is the physical method that increases the mobility of segments in BCPs, allowing the film of polymers to reach more rapidly its thermodynamic equilibrium and final structure. Typically annealing procedures are accomplished by either thermal or a solvent vapor treatment.[5] In order to increase the mobility of polymer chains, the sample can be heated and held at temperature above the glass transition temperature (T_g) but below the decomposition temperature.[8-9] For solvent vapor annealing, the sample is held under selected compatible solvent vapor atmosphere with controlled system, the absorption of solvent vapor induces a rise of the chains mobility within the film, allowing the material to reach its thermodynamic equilibrium faster.[5]

Concerning the thermal annealing technique, both annealing temperature (T_a) and processing time (t_a) affect to the dynamics of domain coarsening and the orientation of nanostructure in self-assembled BCPs.[16-18] Above *Tg*, at 130°C for the classical PS-*b*-PMMA system a structural long-range order is achieved in the time scale of half a day. At 190 °C, a perfect morphology was achieved after an annealing for 50 minutes **(Figure 3)**.[18] The typical equipment for the annealing is a hot plate or thermal oven and much energy is lost during the process.[19]

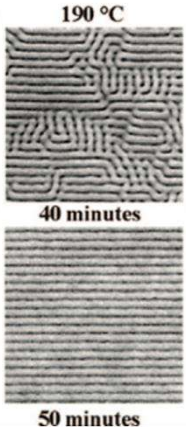

Figure 3. SEM micrographs of the directed assembly of PS-*b*-PMMA at 190°C.[18]

Since 2011 the International Technology Roadmap for Semiconductors specifically stated that the BCPs annealing process needed to be complete in "a few minutes to represents a realistic time scale for potential processing applications". [20] Therefore there have been strong efforts to reduce the annealing time and microwave induced annealing has been successful in this way.

Microwave annealing is an inexpensive method at laboratory scale, normal domestic microwave oven could be used to anneal the BCP films. Some high ordered nanostructures were created and observed rapidly under 90 seconds with using an apparatus obtained for less than $100 USD.[21] This pioneered work in the field was followed up by Morris and co-workers who demonstrated the use of microwave annealing of BCP films to fabricate rapidly high ordered cylinder and perforated lamellar pattern structures. A high order was achieved in the order of minutes.[22-24]

The mechanism of microwave heating was revealed through several important papers, and is attributed to the interaction of microwaves with substrates.[19,25-26] When polar materials are exposed to microwave radiation, the molecules try to rearrange themselves to follow the alternating electromagnetic field. The resulting swaying molecules are resisted by other molecular forces and these resistive forces induce heat.[27] The heated substrates then act as a pan for the deposited BCP films and induce well-organized microphase separation. In 2014, Buriak and co-workers investigated the impact of the substrate resistivity, using different silicon wafers (*n*- or *p*-type) for the self-assembly of PS-*b*-P2VP and PS-*b*-PMMA.[24]

With an *in-situ* temperature monitoring, thanks to a fiber optic temperature probe in direct contact with the sample, they have demonstrated that the silicon substrate is the dominant source of heating if the doping of the silicon wafer is sufficiently low. Surface temperatures as high as 240 °C are reached in under 1 min for high resistivity silicon wafers. The *in situ* temperature monitoring also showed that the polymers do not heat to any significant extent on their own (on an inert substrate like glass for example). Interestingly, it was also proven that BCP annealing can be carried out in 60 s onto non-microwave-responsive substrates, if a piece of high resistivity silicon wafer is in contact with the sample at the opposite side (represented in **Figure 4** by the orange element, the microwave absorber). Annealing and self-assembly of polystyrene-*block*-poly(2-vinylpyridine) (PS-*b*-P2VP) and PS-*b*-PMMA where successfully achieved by this way into horizontal cylinder structures in less than 1 min, in a household microwave oven.

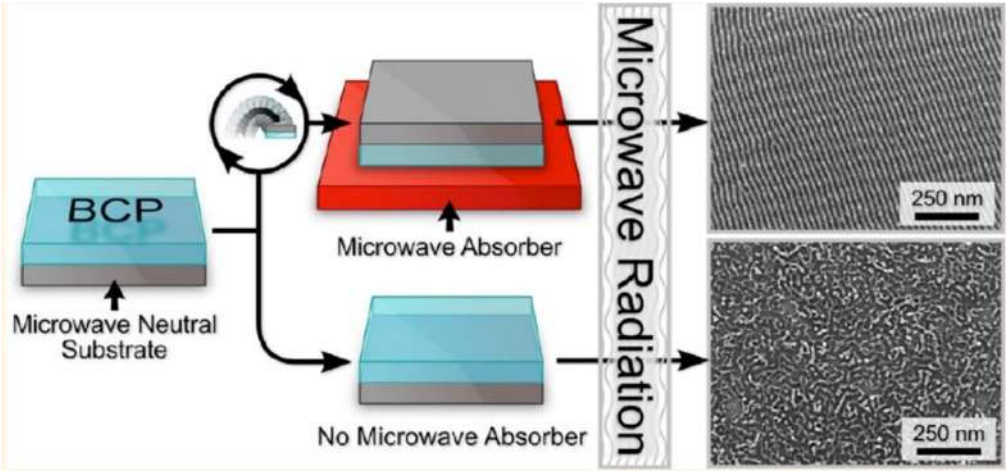

Figure 4. The microwave annealing of PS-*b*-P2VP and PS-*b*-PMMA.[24]

Microwave annealing was used in combination with solvent annealing in a smart set-up by Buriak and co-worker in 2010 **(Figure 5)**.[27] In order to increase the reorganization rate, a solvent was placed in the reactor vessel during microwave annealing process. In this study, tetrahydrofuran (THF) and toluene were compared as solvent for PS-*b*-P2VP self-assembly. The annealing was set at different temperatures from 80 to 160 ºC and the chosen temperature was held for 60s.

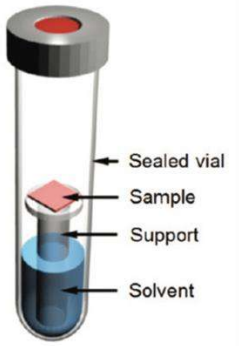

Figure 5. Schematic representation of microwave reactor.[27]

SEM images of the BCP films are shown in **Figure 6**, from which three main information can be extracted:

- the use of a solvent increases drastically the rate of the segregation by creation of vapor that swell the BCP film.
- the nature of the solvent plays its role, nearly parallel lines persist across the entire 1.5 µm . 1.5 µm image at 140 °C with THF, when 160 °C is required with toluene to achieve

a roughly comparable pattern. Two reasons can be advanced, THF vapors are produced at lower temperature and THF is a better solvent for the diblock.

- In the best case the long-range order is achieved in just 60s at 140°C.

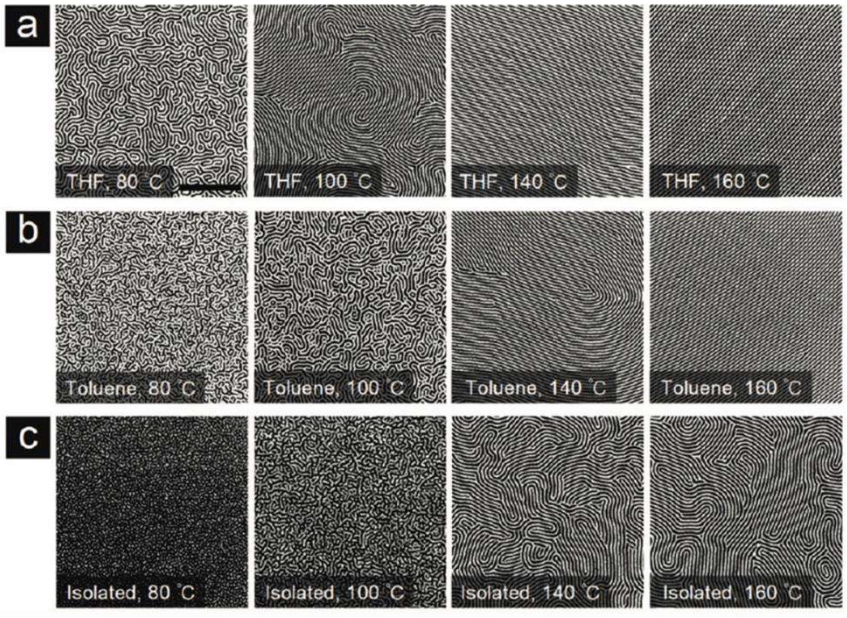

Figure 6. AFM images of PS-*b*-P2VP thin films annealed at various powers/temperatures under microwave during 60 seconds, (a) in the presence of THF, (b) toluene, (c) without solvent. Adapted from ref27.

Different block polymers have been ordered in nice morphologies by microwave induced thermal or solvothermal annealing such as polystyrene-*block*-polydimethylsiloxane (PS-*b*-PDMS)[28] or polystyrene-*block*-polylactic acid (PS-*b*-PLA).[29] In this last example, Morris and co-workers studied the kinetics and mechanism of rapid self-assembly during solvo-microwave annealing of PS-*b*-PLA thin films. They studied the formation of PS-*b*-PLA lamellae by using controlled power microwave irradiation in the presence of THF. The ordered lamellar structure was observed in 60 sec after an annealing at 30W or 55 °C on Si substrate. On the contrary, no microphase segregation was revealed in the absence of solvent. Since THF is a polar solvent, it can absorb microwave energy and heat up very fast swelling the polymer film and increasing chain mobility.[29]

Since microwave-mediated techniques has the potential to help reaching the thermodynamic equilibrium in 60 seconds in average for the different polymers studied, we decided to investigate its effect on our polymer binder, based on PMMA and PBuA. Moreover,

we have shown that in specific condition, a hierarchical micro/nano organization could be achieved by using this process combined with the breath figure methodology **(see Chapter 2)**.[30]

3. Bulk Self-Assembly of Rod-Coil BCPs

3.1 Introduction to rod-coil self-assembly

Self-assembly of rod-coil BCPs have been reported since they are widely used in organic electronic devices, optoelectronics applications, biotechnology, environmental technology, etc.[31-36] Several classes of rod segments such as fluorene, phenylene, thiophene or quinoline have been used for π-conjugated rod-coil BCPs. For the example, the BCPs based on polyfluorene (PF) such as the luminescent rod-coil BCPs of poly(2,7-fluorene)-*b*-poly(ethylene oxide) (PF-*b*-PEO) and thermos-responsive conjugated rod-coil-coil triblock copolymer of poly[2,7-(9,9-dihexylfluorene)]-*b*-poly(*N*-isopropylacrylamide)-*b*-poly(*N*-hydroxylethylacrylamide) (PF-*b*-PNIPAAm-*b*-PHEAA) have been synthesized because PF and derivative are highly luminescent for light-emitting diodes (LEDs).[37-39] Phenylene based rod-coil BCPs are also widely used in photovoltaic devices. Donor-acceptor BCPs based on poly[(2,5-di(2'-ethyl)hexyloxy)-1,4-phenylenevinylene] (DEH-PPV) were synthesized on which C60 and fullerene were grafted to be used as active layer in photovoltaic devices.[40-41] Thiophene based rod-segment is a good candidate for rod-coil BCPs because of a high chemical stability, high absorption coefficient at 500 nm, but also easy synthesis and functionalization, thus highly ordered rod-coil BCPs based on P3HT have been studied and reported.[31-34,42] For example, a well-defined electron donor-acceptor type of diblock based on poly(3-hexyl thiophene) (P3HT) (electron donor) and fullerene (electron acceptor) was synthesized. P3HT was linked with poly(methyl methacrylate-*r*-hydroxyethyl methacrylate) (P(MMA-*r*-HEMA)) and fullerene derivative were coupled with the HEMA units.[43] **Figure 7** presents a quick overview of the rod and coil sequences used to produce diblock copolymer based on conjugated segment.[45]

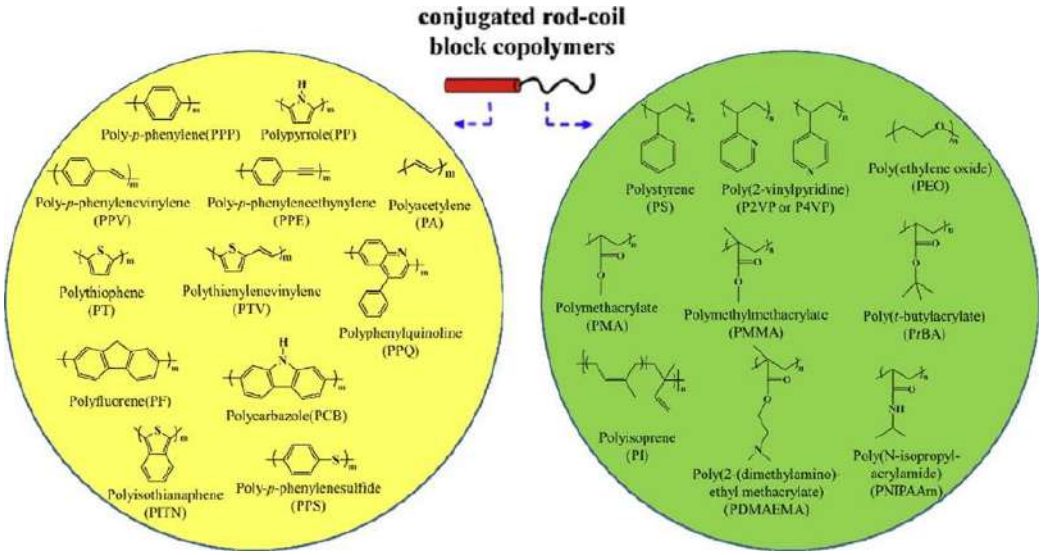

Figure 7. General polymers of conjugate rod-coil BCPs reported from [45].

As mentioned before, the microphase segregation of coil-coil BCPs is generally dominated by the effect of volume fractions (*f*) of the blocks and the degree of incompatibility between each block.[45] Thus the value of χN and f are the important parameters for self-assembly property of coil-coil BCPs. If one of the blocks has a more rod-like or semiflexible character, additional degrees of freedom should be taken into consideration to determine the morphology and average molecular orientation of the chain segments, due to the rigidity of the conjugated block and the development of π-π interaction between rod-rod sequences. These degrees of freedom include the persistence length of the rod segments (λ), the relative length of the rod segment to the coil segment (β), and Maier–Saupe interaction parameter (μ) for dipole-dipole interactions between neighboring semi flexible segments.[45,47] **Figure 8** from DeLongchamp and co-worker nicely illustrates these parameters.[53]

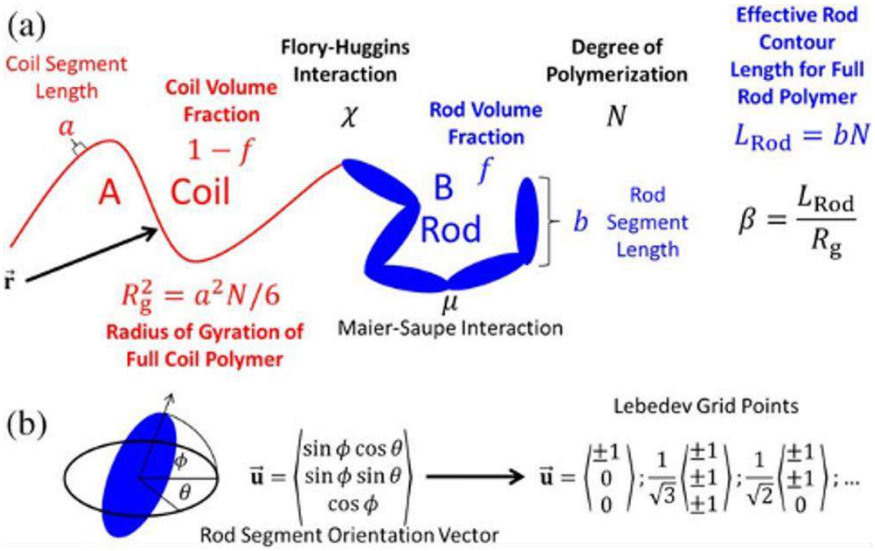

Figure 8. (a) Schematic diagram of rod-coil BCPs system and their relevant physical parameters.[53]

The ratio of μ/χ is often calculated and theoretical diagrams are depicted from it. In short, for a $\mu/\chi = 0$, the phase diagram of a coil-coil copolymer is obtained. For a $\mu/\chi = 1$ the diagram in **Figure 9** was calculated with a centered part of the diagram covered by the lamellar phase. The right part (when the rod volume fraction is high) is dominated by liquid-crystalline smetic and nematic phases. Finally, for rod fraction between 0.2 and 0.3 spheres or cylinders can be produced. By increasing the μ/χ ratio, the smectic and nematic phase takes a wider space in the diagram, until for a $\mu/\chi=8$ all morphologies other than these could not be reached anymore.[53]

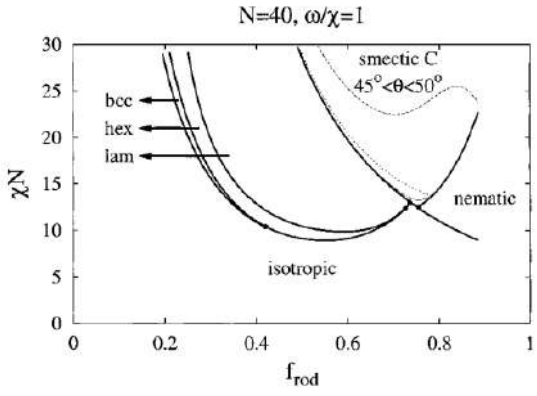

Figure 9. Phase diagram with N = 40, and $\mu/\chi = 1$.[52]

The field of rod-coil diblock copolymer self-assembly has been widely studied for more than 45 years.[46] Some rod-coil BCPs were used to form nanostructured materials for advanced

application such as electronics, optoelectronic, photovoltaics (PVs) devices, etc. [45] Indeed, an optimal photovoltaic device requires the ordered orientation of donor and acceptor phases of around 20 nm and orientated perpendicularly to the electrode **(Figure 10)**.[36,45]

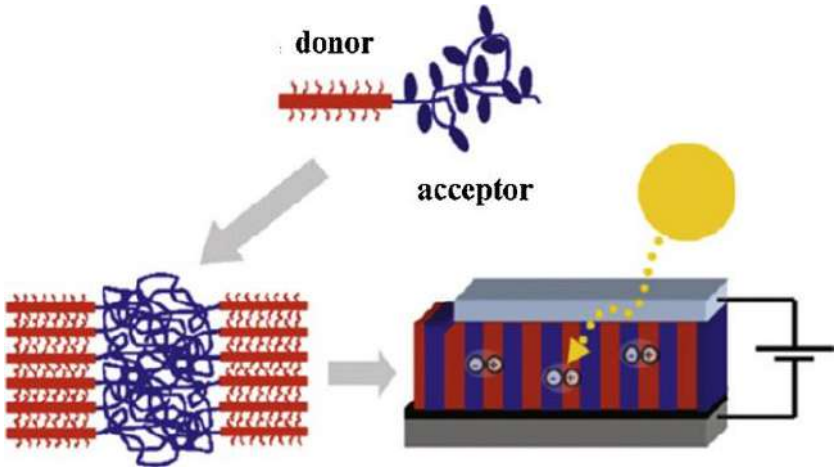

Figure 10. An ideal morphology of self-assembly BCPs in photovoltaic deviced.[36]

P3HT-*b*-Poly(L-lactide) (P3HT-*b*-PLLA) was synthesized and used as at structure-directing agent to pattern active material for PV cells.[47,50] The self-assembly of this polymer in thin film led to a lamellar morphology of P3HT-*b*-PLLA with perpendicular orientation. After the hydrolysis and removal of the PLLA phase the porous films was filled with the fullerene electron acceptor **(Figure 11)**. Hence a donor-acceptor material consisting of ordered nanostructured domains was formed and is expected to improve the effectiveness of internal processes such as charge generation at the donor/accepter interface and charges transportation.

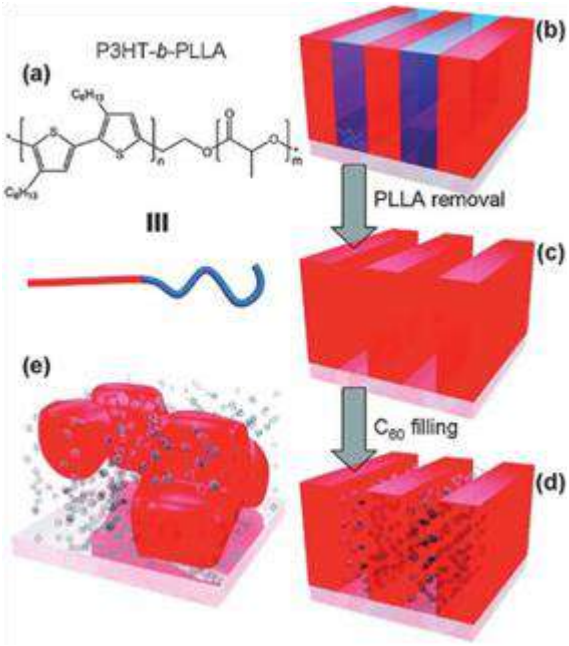

Figure 11. (a) The schematic representation and chemical structure of P3HT-b-PLLA. (b) The lamellae oriented perpendicular to the substrate morphology of P3HT-b-PLLA. (c) Ordered P3HT lamellae domains after removal PLLA block. (d) The self-assembled P3HT donor domains that were separated by C_{60} acceptor. (e) Both P3HT donor and C_{60} acceptor in less ordered morphology that obtain in simply blending method. (d and e) Comparison of ordered and disordered P3HT consist C_{60}.[50]

3.2 Influence of copolymer chain structure over film morphology

3.2.1 Impact of volume fraction

Hadziioannou and co-workers, in an attempt to use diblock copolymer in solar cell, synthesized poly(4-vinylpyridine)-*block*-poly(diethylhexyloxy-*p*-phenylenevinylene) (P4VP)-*b*-(PPV). Indeed, this system was relevant because of the possibility of forming poly(4-vinylpyridine)/fullerene (P4VP:C60) complexes, thus enabling the use of P4VP as a chaperone matrix for hosting electron acceptor C_{60} molecules. Therefore, the design of PPV-*b*-P4VP: C60 with large electron donor/electron acceptor interfaces, is believed to help for the dissociation of the excitons forming upon light exposure. However, in order to fully exploit this system, continuous percolating mesophases such as lamellar, cylindrical, or gyroidal must be designed to allow electron transfer to the electrode. Hadziioannou and co-workers found that the morphologies in P4VP-*b*-PPV varied from lamellar, to hexagonal, and spherical when the volume fraction of the rod was progressively reduced respectively for 0.45, 0.19 and 0.12.[46] The transitions from smectic to lamellar as well as the hexagonal and spherical morphologies

reported in their paper were nicely predicted by Reenders and Brinke with their use of Landau expansion theory.[52] This remarkable consistency between experiments and theoretical predictions is reported in **Figure 12**.

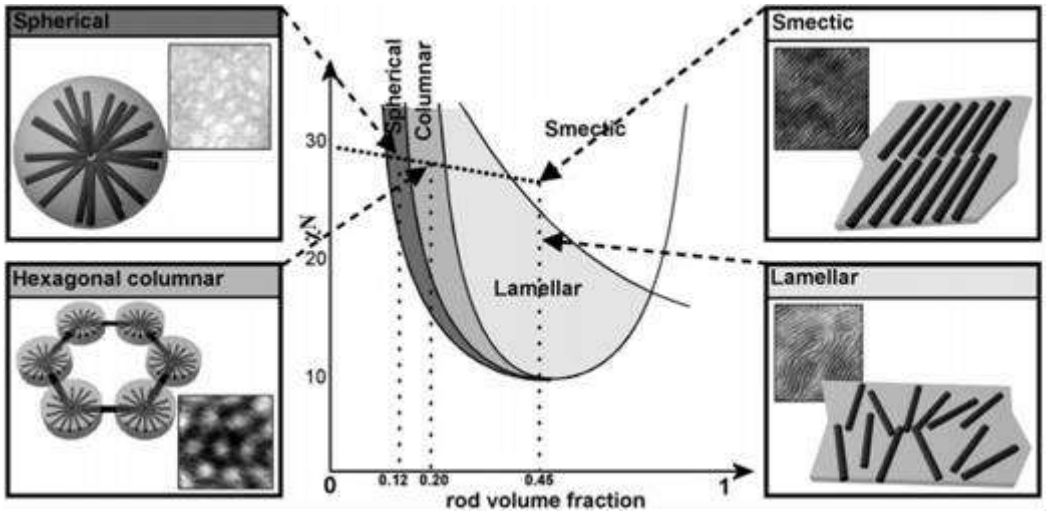

Figure 12. The phase diagram for rod-coil BCPs of PPV-*b*-P4VP, compared on the experimental results and the theoretical prediction of microphase separated morphologies.[46]

Olsen and Selgalman studied the self-assembly of a series of rod-coil BCPs in the weak segregation limit.[48] The copolymer was composed of polyisoprene (PI) coil blocks and poly(alkoxyphenylene vinylene) (PPV) rod blocks solubilized with alkoxy side groups. Because of thermodynamic compatibility of the blocks, these polymers are in the weak segregation limit, and order - disorder and nematic - isotropic transitions have been accessed. Above the ODT, it is possible for the rod-coil BCPs to be in multiple disordered states: a nematic (oriented) or an isotropic (un-oriented) phase. Besides X-ray scattering, optical microscopy is a powerful tool to investigate crystal-liquid behavior since the nematic and lamellar phases exhibit birefringence whereas the isotropic phase does not. The authors showed that at low coil fractions and around 230°C, the polymers exhibit an isotropic phase, with transitions to a broad nematic region followed by lamellar (smectic-like) phases at 120°C. At high coil fraction an isotropic phase is only found.

For intermediately segregated BCPs, such as in the system of poly(diethylhexyloxy)-p-phenylenevinylene)-*block*-poly(methyl methacrylate) (DEH-PPV-*b*-PMMA), at the low volume fraction of PMMA coil (<54%), the DEH-PPV rod segment formed lamellar

structures.[54] By further increasing the PMMA volume fraction, the self-assembly switched to smectic-hexagonal structures due to the packing of PPV block into hexagonal lattice. TEM images of BCP films are presented in **Figure 13** in which clear region refer to PMMA-rich phases and dark is for DEH-PPV. Lamellae are continuous with lengths of several hundreds of nanometers or even up to a micrometer. The authors attributed this remarkable persistence length to a very high bending modulus of DEH-PPV rod. At high coil volume the DEH-PPV rods pack into strip like aggregates assembled, and 6-fold symmetry of hexagonal structure with high degree of orientation appeared **(Figure 13 d,e,f)**.

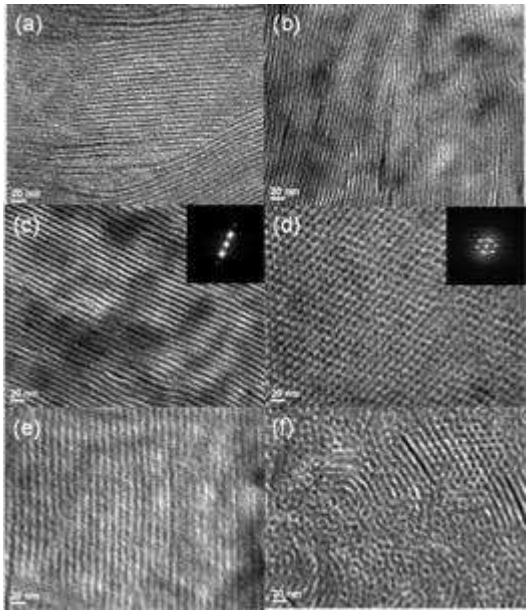

Figure 13. TEM images of PPV-*b*-PMMA BCPs. Stained by RuO_4, dark display to PPV nanodomains and light reveals to PMMA nanodomains for all images. (a) PPV_{10}-*b*-$PMMA_{13}$, (b) PPV_{10}-*b*-$PMMA_{36}$, (c) PPV_{10}-*b*-$PMMA_{49}$, (d,e) PPV_{10}-*b*-$PMMA_{84}$, (f) PPV_{10}-*b*-$PMMA_{126}$.[54]

In addition, with increasing temperature, the packing order of in the rod phase evolved from a smectic phase to an isotropically disordered phase both in lamellar or cylindrical morphology, as sketched in **Figure 14**. Then at around 200°C the disordered phase is found with an intimate mixture of rod and coil.

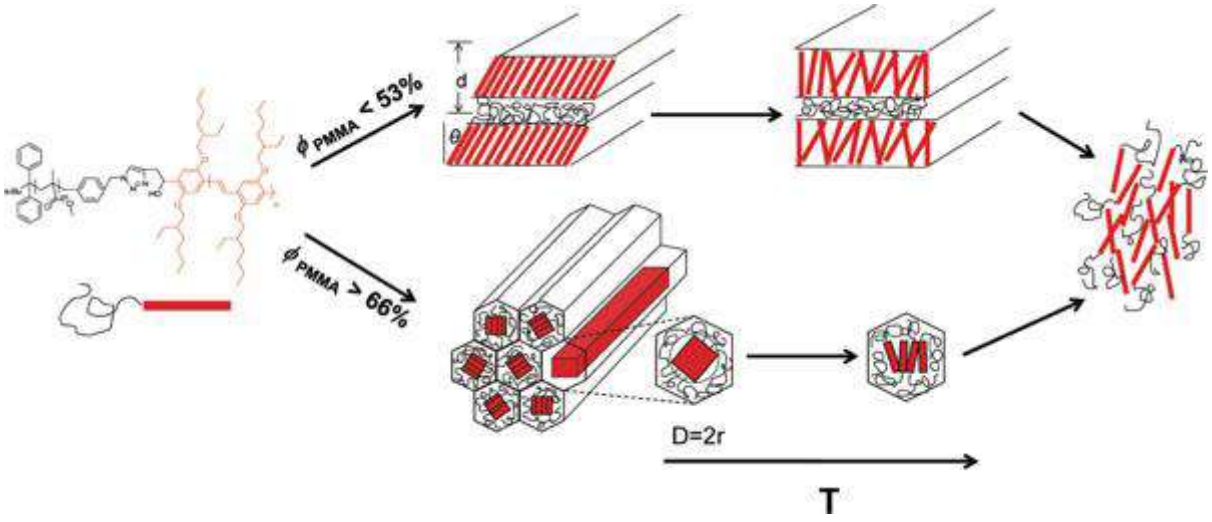

Figure 14. Schematic illustrations of possible rod segment packing in PPV-*b*-PMMA rod-coil BCPs. Lamellar structure and hexagonal structure are presented from above to below, the rods aggregate to tilt lamellae when the coil fraction is lower than 53% while rods packed into hexagonal structure in higher coil fraction.[54]

3.2.2. Influence of the rod lateral chains

The density, length and volume of rod lateral chains play important roles in the planarity and intermolecular stacking of macromolecules. The side-chain motion occurs before backbone motion and they could drive the conformational change of the chain.[49] Longer and/or branched alkyl side-chains and higher alkyl side-chain density could cause an increase of the inter-ring torsion and lead to a relatively more coil-like and flexible conformation, which decreases aggregation and electronic transport.[56]

Su and co-workers presented an extensive study on the effect of rod-segment side chains variation on the morphology of BCPs, they chose to vary the side chain of poly(3-alkylthiophene)-*block*-poly(methyl methacrylate) (P3AT-*b*-PMMA).[58] By altering the alkyl side chain of polythiophene from linear hexyl (H) to longer dodecyl (D) and to branch 2-ethylhexyl (EH), both rod-coil and rod-rod interaction were decreased with increasing spatial occupation of alkyl side chain. With tunable conformational asymmetry, the presence of different morphologies was observed for BCPs all presenting a rod volume fraction of 0.5 **(Figure 15)**. For hexyl side chain the authors observed a lamellar morphology and an order to disorder transition (ODT) at 210°C. For longer dodecyl side chain a cylindrical structuration was observed followed by first transition at 185°C to a gyroid phase and an ODT at 215°C.

Finally, for the branched side chain, the same morphologies were observed but the transition temperatures were lower with a cylinder to gyroid transition at 165°C and an ODT at 180°C. The authors calculated the *G* parameter which is the μ/χ ratio. The P3EHT-*b*-PMMA has the lowest *G* value among these three BCPs (0.337), indicating that the π-π interaction between P3EHT rods were smaller than the rod-coil interaction between P3EHT and PMMA segments. They authors suggested that the morphology of P3EHT-*b*-PMMA was dominated by microphase separation. In contrast, P3HT-*b*-PMMA presented the largest *G* parameter (1.282), resulting from stronger π-π interaction of P3HT compared to P3HT/PMMA interaction resulting in lamellar/fibril morphology. Indeed, differential scanning calorimetry showed that only in the case of P3HT BCPs, the crystallization of the rod happened before vitrification of the PMMA driving the morphology towards lamellar/fibril phase.

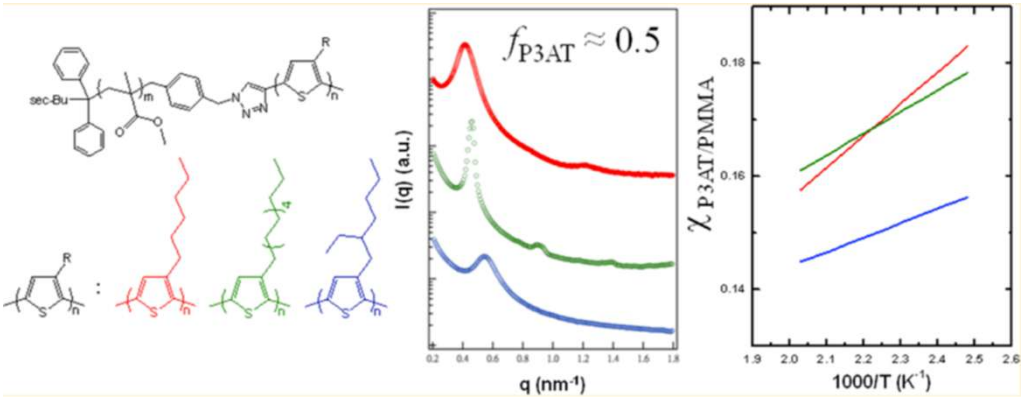

Figure 15. Synchrotron-SAXS profiles and temperature dependence of the Flory-Huggins interaction parameter between P3AT and PMMA; poly(3-hexylthiophene) (red), poly(dodecylthiophene) (green) and poly(3-(2-ethylhexyl)thiophene) (blue).[58]

Other studies showed the effect of the varying the rod side chains such as Segalman with a poly(3-ethylhexylthiophene)-*block*-poly(methyl acrylate).[51]

Raising the coil fraction or increasing the volume of the rod side chains are therefore effective ways to increase the influence of χ over μ to produce diblock copolymer self-assembly of diverse morphologies. However, the increase of the size of the coil will lead to an increase of the phase size, this effect is not desirable in some application such as microprocessors where a patterning under 10 nm is expected to increase data storage. At the same time, changing the side chain affects the electron conduction and this is detrimental for

photovoltaic application. Therefore, other strategies to reduce μ or/and increase χ were still developed such as the introduction of ionic functional groups into polymer chain.

3.2.3 Introducing a centered charge

Introducing a charge in the polymer is a direct way to drive the self-assembly and produce high ordered phase separation in BCPs. Lodge and co-workers have presented the addition of lithium salt of lithium bis(trifluoromethane)sulfonamide (LiTFSI) into a polymer blend of PEO, PS and PS-*b*-PEO BCPs. The addition of LiTFSI results to dramatically increase the segregation strength of the polymer blend, and well-ordered segregated domains were observed.[62] Moreover, much attention has been given to a certain group of ion-containing polymers called ionomers. Basically, they are synthetic organic polymers that have an ion content of up to 15 mol % and are generally insoluble in water. On the contrary, polyelectrolytes have much higher ion contents and are insoluble in organic solvents. The reason for the great interest in ionomers lies in the often-profound changes in properties caused by the introduction of ions into nonionic polymers such as melt viscosities, glass-transition temperatures, and rubbery moduli of ionomers. For instance, incorporation of 9 mol % sodium methacrylate into polystyrene raises the *Tg* from 100° C to 130°C.[55]Altered phase separation of BCPs was also reported in the literature as a consequence of the electrostatic interaction of ionic units.[58-61] The ion pairs in ionomers induce the aggregation of polymers and even resulted in chains crosslinking, and unusual geometries such as rods or sheets were observed for these systems.[63-64]

Schädler and Wiesner reported that the stabilization or destabilization of microphase separation of PS-*b*-PI could be controlled by introducing ionic groups at one or both chain-ends of copolymers.[65] Differences in lamellar spacing were the result from changing the chain conformation due to aggregation of ionic chain ends. By introducing quaternized ammonium and/or sulfonate groups at the chain ends of lamellar PS-*b*-PI diblock copolymers, the authors were able to prove by X-ray scattering a change in the dimension of the phase **(Figure 16)**.

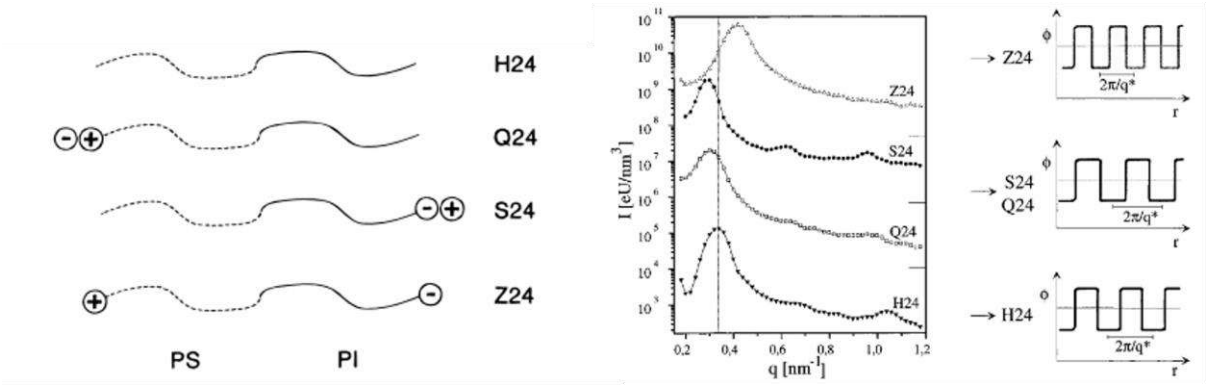

Figure 16. A series of end-capped symmetric PS-*b*-PI diblock copolymers (left hand side) and SAXS patterns for the different end-capped BCPs; the unity intensity points of each BCPs (middle) that indicated for H24, Q24, S24, and Z24 (right hand side).[65]

Beside the variation of the periodicity, the same authors showed two years later a salt-induced changes in the phase morphology of such functionalized BCPs. The same copolymer PS-*b*-PI was functionalized with one ionic group at the block junction point (quaternary amine) and another one with opposite charge at one chain-end (sulphonate group). These opposite charges induced a loop conformation of the chains. Moreover, addition of low molecular weight salt (LiCl) induces a change of the bulk microphase morphology by screening the charges and releasing the loop **(see Figure 17).**[66]

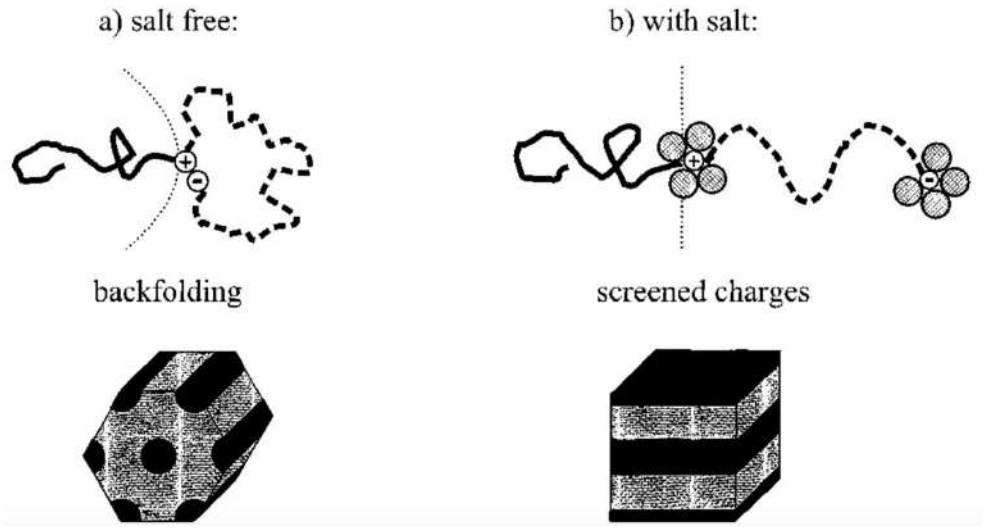

Figure 17. Schematic drawing of the chain conformation of BCPs, (a) the conformation without salt and (b) the conformation with salt.[66]

Furthermore, Luo and co-workers have reported the concept of improving thin-film assembly of BCPs through the establishment of an ionic unit at the junction of two blocks on polydimethylsiloxane-*block*-poly(ethylene oxide) (PDMS-*b*-PEO).[67] The BCPs was assembled by Huisgen cycloaddition which produces at the center of the resulting macromolecules a triazole cycle **(Figure 18)**. In a last synthetic step, one of the nitrogens of this triazole group was quaternized to give raise to a new centered ionomer. The additional electrostatic interactions between counterions between adjacent domain junctions leaded to enhanced segregation strength and phase separation. As a consequence, this drastically increased the ODT temperature from 135°C (for the neutral parent polymer) to 185°C. These results demonstrate that a large increase in segregation strength can be implemented through subtle addition of ionic functionality.

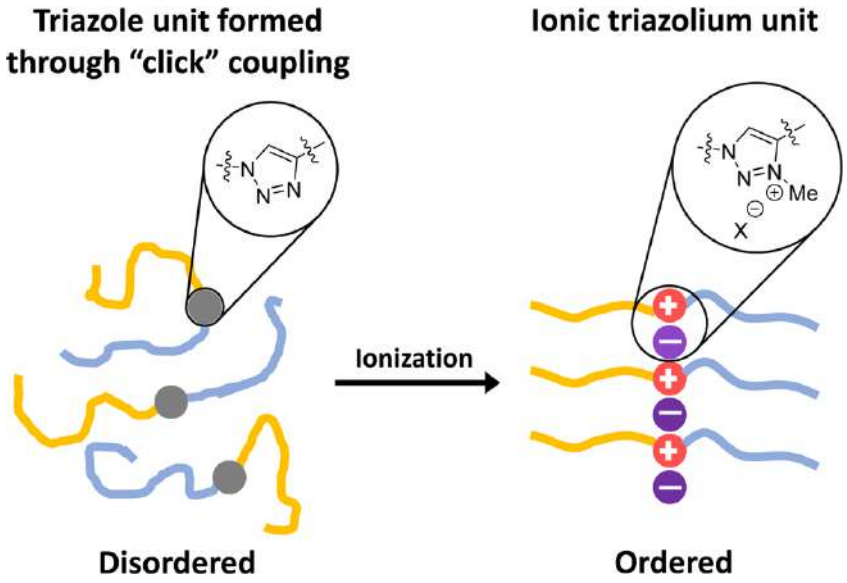

Figure 18. The graphical representation of phase segregation behavior for BCPs through introduction of ionic at 1,2,3-triazolium units block junctions.[67]

In a recent work, our group used the ionomer strategy to reduce μ influence over χ in order to improve the organization of diblock copolymers containing a semicrystalline block. They introduced an ionic group to the linking unit between the two blocks of P3HT-*b*-PMMA. Two 1,2,3-triazolium-linked BCPs were prepared *via* quaternization of the 1,2,3-triazole unit with methyl iodide and iodide ion was replaced by the more stable bis(trifluoromethane) sulfonimide anion (NTf_2^-) *via* subsequent anion exchange method. The randomly oriented fibrillar structure observed in P3HT-homopolymer, as shown in **Figure 19a**, is typical morphology of P3HT due to its crystallization. Similarly, the neutral P3HT-*b*-PMMA

presented densely packed and disoriented nanofibrils **(Figure 19b)** as a consequence of the crystallization of P3HT happening before segregation of the blocks. When the 1,2,3-triazolium-based BCP with iodide as the counterion was imaged, it displayed highly organized fibrils, meaning that the diblock phase segregation χ becomes predominant over the Maier-Saupe ($\pi-\pi$) interaction μ of rod segments, and lamellae of P3HT-b-PMMA were formed before the crystallization of the P3HT segment. Finally, after the iodide ion was replaced by NTf_2^-, the P3HT phase was disrupted and no crystallization was observed by WAXS or DSC).[57]

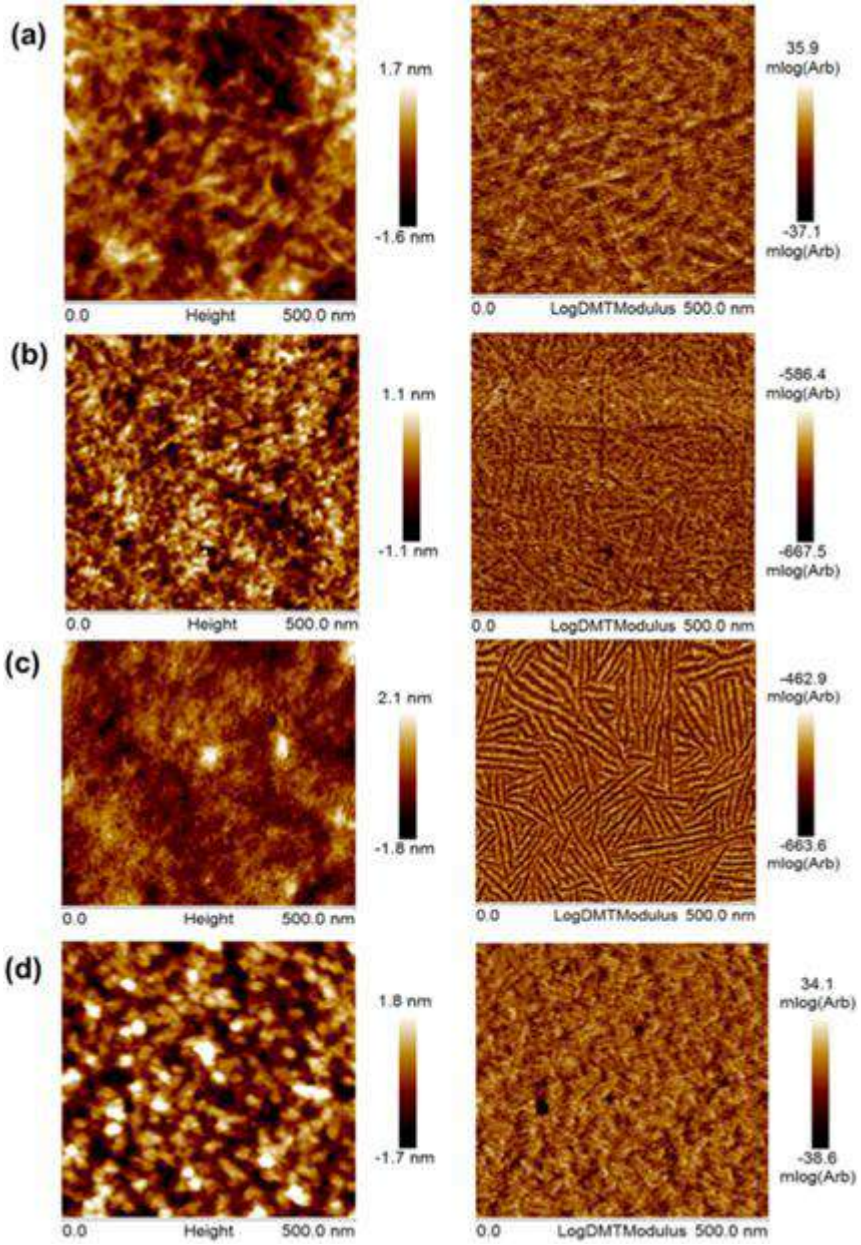

Figure 19. PeakForce QNM-mode AFM images of (a) ethynyl-homoP3HT, (b) neutral P3HT-*b*-PMMA, (c) ionized P3HT-b^+-PMMA.I^-, (d) P3HT-b^+-PMMA.NTf_2^-.[57]

Therefore rod-coil self-assembly is a very exciting field of research in which many parameters and strategies can be tune and follow to vary the morphology and properties of materials.

4. The synthesis of conjugated rod-coil BCPs

Conjugated rod-coil BCPs are generally synthesized by the combination of two different polymerization techniques. [45] Two general strategies have been developed for the synthesis of conjugated rod-coil BCPs, the "grafting-from" methodology in which a macroinitiator or macro-end-capper is introduced in the polymerization of the second monomer; and the "grafting onto" where the two blocks are polymerized separately and coupled in a last reaction.[38] The synthetic routes of the grafting-from and grafting-onto methods presented in **Figure 20**.

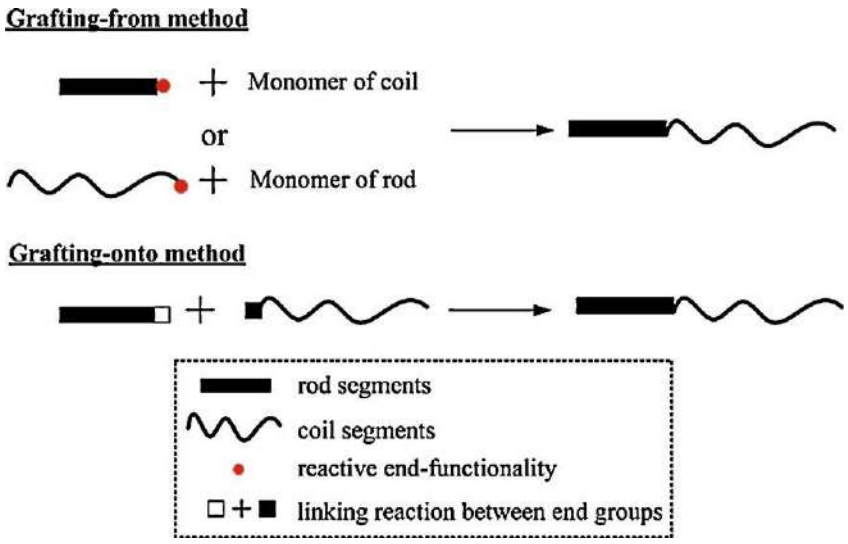

Figure 20. Synthesis methodology model of rod-coil BCPs.45

The grafting-from method consist of two major steps. First, the preparation a functional rod or coil homopolymer with an end-group able to initiate the polymerization of the second monomer or act as a macro-end-capper in the polycondensation of conjugated monomers (as an example). Second is the polymerization of the second block. Since a lot of different polymerization techniques were used to produce rod-coil copolymer in the literature we chose to focus this bibliography on the ones used during this PhD, *i.e.* atom transfer radical polymerization method and Kumada catalyst transfer polymerization.

The grafting-onto method for synthesis BCPs undergoes the independent polymerization of the two blocks and then their coupling. The two blocks must also be functionalized with complementary functions that will allow the coupling of the macromolecules. One of the widely used coupling reaction is the Huisgen cycloaddition, a "click reaction" that involved acetylenes and azide functions. This process has gained numerous applications because of its high efficiency, high monomer tolerance and tolerance of both homogeneous and heterogeneous conditions etc.[68] This chemistry will be presented in this chapter.

4.1 The Atom Transfer Radical Polymerization method (ATRP)

A successful method to control radical polymerization, named "atom transfer radical polymerization" was reported independently by the two different groups of Matyjaszewski and Sawamoto in 1995.[69-70] ATRP is now ubiquitous in the field of polymer science and it has had a tremendous impact on the synthesis of macromolecules with well-defined composition, architectures and functionalities.[71-73] Indeed, control of molecular architecture in a conventional radical polymerization was considered impossible at a level similar to other living ionic systems because two radicals always terminate (dismutation or recombination) at a very fast, diffusion-controlled rate. Then the concept of dynamic equilibrium was introduced and decreased the proportion of terminated chains (typically between 1 and 10 mol %) by lowering drastically the concentration of propagating radical species. The formation of the required dynamic equilibria in ATRP is accomplished by employing a reversible deactivation of propagating radicals to form dormant species that can be intermittently reactivated in a catalytic manner by metal complexes.[74] ATRP mechanism is shown in **Scheme 1**.

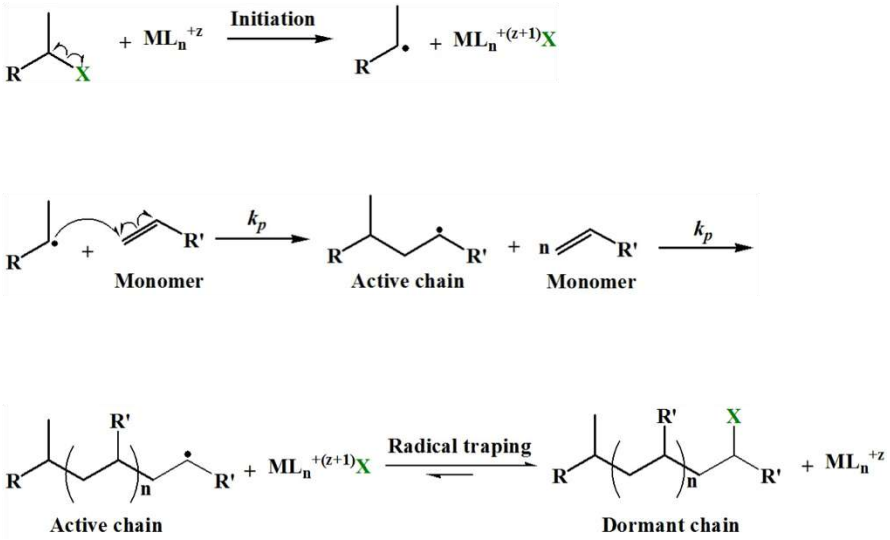

Scheme 1. Metal catalyzed atom transfer radical polymerization.

A general mechanism for ATRP is usually initiated by the activation (homolytic cleavage) of the carbon-halogen bond of an initiator through a reversible redox process catalyzed by a transition metal complex (activator, ML_n^{+Z}) which undergoes a one-electron oxidation with concomitant abstraction of a (pseudo)halogen atom (X) to form the propagating species or initiating radicals species ($R^{\bullet}$) and higher oxidation state of metal center ($ML_n^{+(z+1)}X$). Then the initiating radicals react with monomer and generate the intermediate radical species or an active chain, polymer chains grow by the addition of the active chain to monomers in a manner similar to a conventional radical polymerization, with the rate constant of propagation (k_p).[85,88-89] ATRP is controlled by the reversible deactivation of propagating radicals by the metal II complex, via an equilibrium between active chains and dormant species formed by alkyl halide (R-X).[77] Several transition metals have been used and successfully mediated for ATRP, such as Ti, Ru, Os, Co, Ni or Cu.[84-86] The idea of this equilibrium relies on extending life of propagating chains from about 1 second in conventional radical polymerization to more than 1 day, by inserting dormant periods of ~1 minute after each ~1 ms activity. As mentioned before, if one can avoid irreversible chain termination, then one can synthesize BCPs by sequencing the introduction of monomer in the medium. Furthermore, if the initiating step is sufficiently fast, the dispersity of the chains sample will be low (around 1.1) and in the case of BCPs nice morphologies can be reached by mass self-assembly.

Therefore, ATRP method is a method of choice to synthesize rod-coil conjugated BCP.[80] Most of the time the strategy consists in generating a conjugated polymer bearing at

the end of the chain an ATRP radical initiator. In a second step the ATRP of the alkene monomer is performed (Scheme 1a). [75] Some examples of synthetic strategies to elaborate rod-coil BCPs with the use of ATRP are presented below.

Well-defined poly(diethylhexyl-p-phenylenevinylene-*b*-styrene) (PPV-*b*-PS) was prepared through ATRP. First, a PPV-based ATRP macroinitiators (3 or 4 in **Scheme 2**) was synthesized from a monoaldehyde end-functionalized PPV. The aldehyde end-group was reduced in alcohol and further involved in an esterification to introduce the alkyl-halide ATRP initiator. Finally, the PPV macroinitiator was reacted with styrene *via* ATRP to produce PPV-*b*-PS (5).[81]

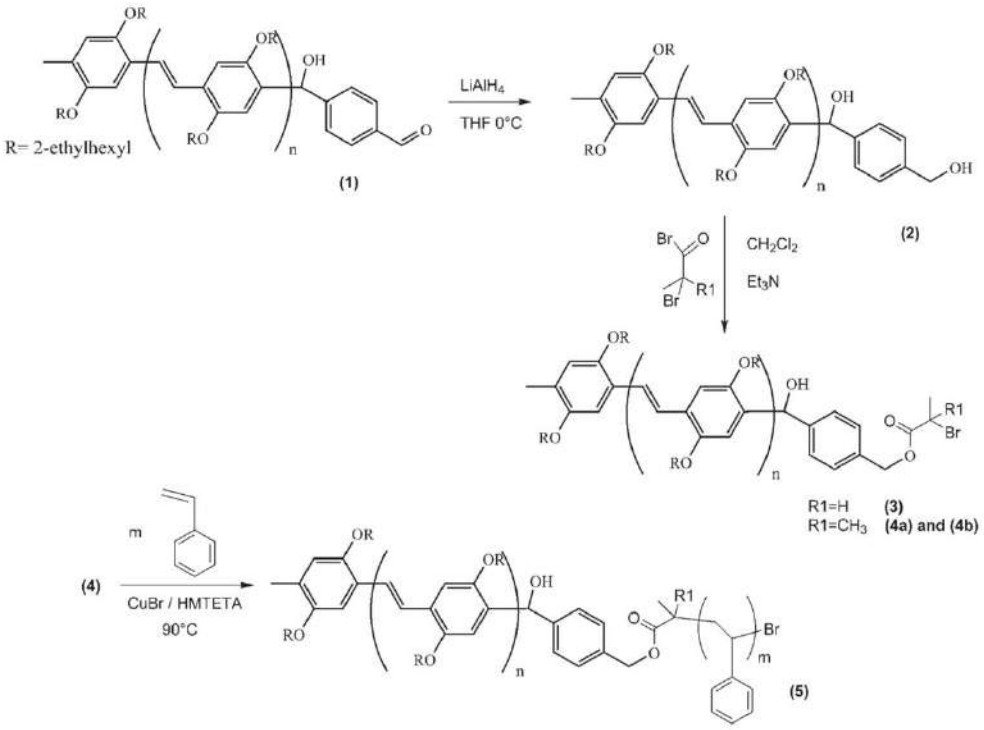

Scheme 2. Synthesis pathway of PPV-based ATRP macroinitiators for the polymerization of PPV-*b*-PS BCP.[81]

The luminescent rod-coil diblock of oligo(*p*-phenyleneethynylene)-*b*-polystyrene (OPPE-*b*-PS), was synthesized *via* ATRP method. The OPPE rod segments were functionalized by attaching with 2-bromopropionyl chloride. The functionalized OPPE were used as a macroinitiators for ATRP of styrene monomers.[82] Rod-coil BCP based on Polyfluorene (PF) can also be prepared *via* ATRP. Poly[2,7-(9,9-dihyxylfluorene)]-*b*-poly(acrylic acid) (PF-*b*-PAA) amphiphilic copolymers were prepared by ATRP from a bromide-end chain of PF (PF-Br) used as a macroinitiator. The radical polymerization of tert-

butyl acrylate (tBA) and hydrolysis of the ester on this monomer unit led to the obtention of PF-*b*-PAA.[83] The synthesis of rod-coil BCPs by the ATRP method from PF-based macroinitiators were used in polymerization reaction of other coil segments including poly(methyl methacrylate)[84], poly(2-(dimethylamino)ethyl methacrylate)[85], and poly[3-(trimethoxysilyl)propyl methacrylate].[86]

4.2 Kumada catalyst-transfer polycondensation (KCTP)

Polythiophenes (P3HT) have been widely used as conjugated polymers for the production of electronic devices because it is a thermally stable materials and its synthesis allows control over the molar mass, dispersity and end-chain fonctionalisation.[87] P3HT is typically prepared by catalyst cross-coupling method, and a famous polymerization method for P3HT is Kumada catalyst-transfer polycondensation (KCTP).

KCTP is widely used and allows the development of advanced architectures such as BCPs (BCPs) and CP brushes from inorganic or metals substrates **(Figure 21)**.[88-92] KCTP is also referred as Grignard metathesis polymerization and involves a selective intramolecular transfer of the nickel catalyst which allows the propagation of the chain by a chain-growth mechanism rather than the typical step-growth mechanism observed for other conjugated monomer polymerization.[88-92, 93-95],

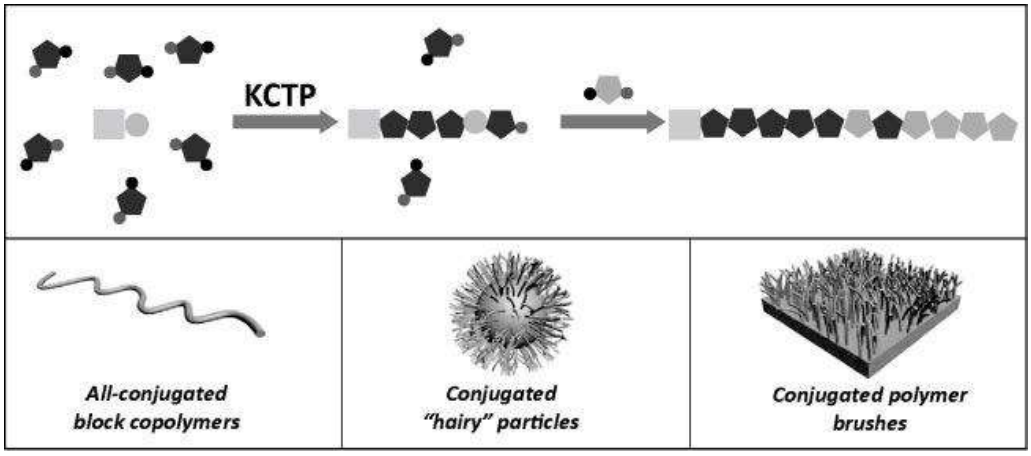

Figure 21. The reaction model of KCTP and the example of advance architecture of BCPs.[88]

KCTP was developed from the selective cross-coupling reaction, reported by Kumada and co-workers in 1972, of an aryl halide with a Grignard reagent and catalyzed by a nickel-phosphine complex **(Scheme 3)**.[89]

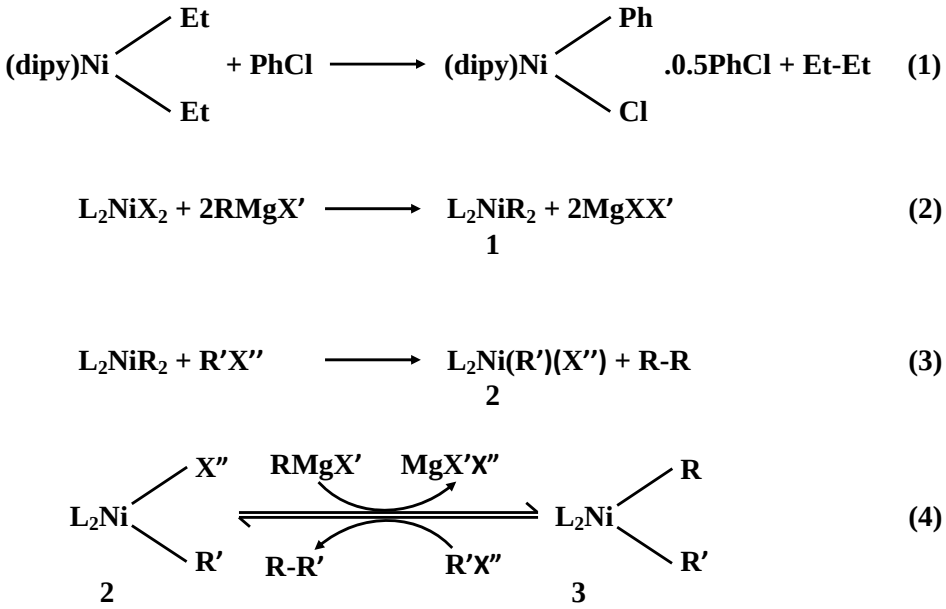

Scheme 3. The proposed reaction partway of the selective cross-coupling reaction catalyzed by Ni-complex catalyst.[89]

The mechanism of the Kumada cross-coupling involves three basic steps in the catalytic cycle, which are oxidative addition, trans-metalation and reductive elimination as shown in **Scheme 4**.[93] The trans-metalation step is the rate-limiting step.

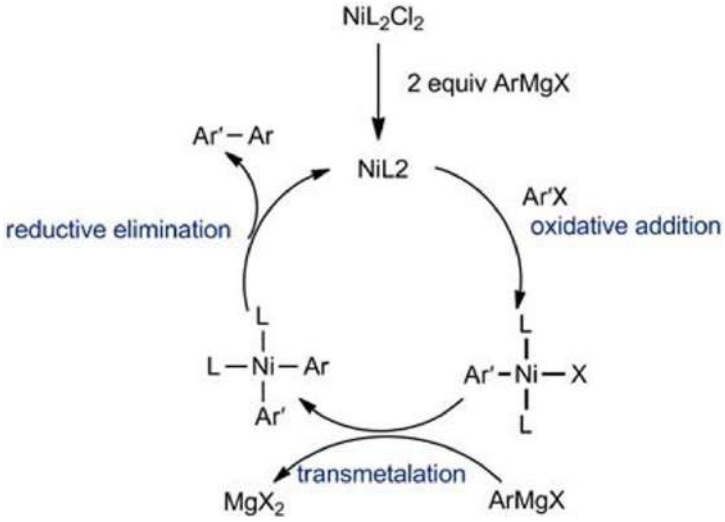

Scheme 4. The catalytic cycle of Kumada cross-coupling mechanism.[93]

From the catalytic cycle in Scheme 4, the polymerization for conjugated monomer (bearing two functional groups) should proceed *via* a step-growth mechanism.

The Kumada cross-coupling was first utilized by McCullough and co-workers in the early 1990s of the last century, for the polymerization of regio regular P3AT by cross-coupling of 2-bromo-5-magnesiobromothiophene, prepared by insertion of magnesium metal into 2,5-dibromothiophene monomers **(Scheme 5)**.[96-99]

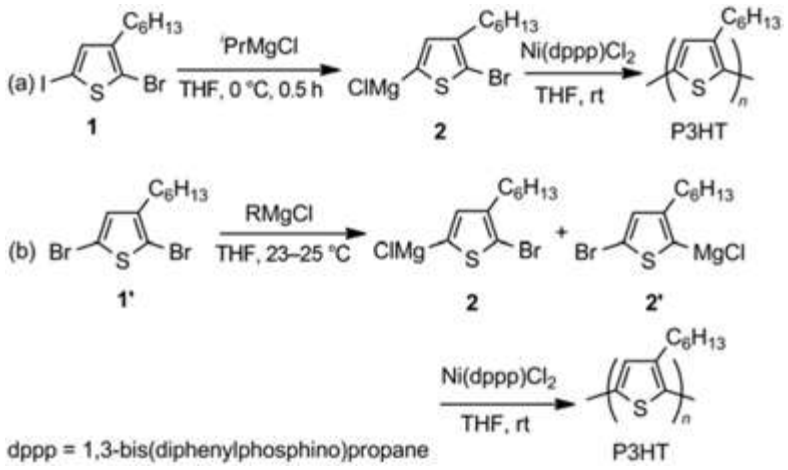

Scheme 5. The synthesis routes for regioregular P3HT. (a) The route of Yokozawa (b) The route of McCullough.[93]

In 2005, Yokozawa and co-workers observed that, the reaction of Ni(dppp)Cl_2 with Grignard reagent solution in THF at room temperature provided regio regular P3HT with M_n increasing linearly with monomer conversion and dispersity was ≤ 1.4. All these informations indicated that, the nickel-catalyzed cross-coupling polymerization undergoes a chain-growth mechanism and also a living polymerization behavior.[94-95, 100-101] The experiments were studied by McCullough and co-workers, they also confirmed the control of the polymerization *via* a chain-growth mechanism.

The mechanism proposed by both Yokozawa and McCullough is shown in **Scheme 6**. In the first step, the reaction is initiated by the trans-metallation of 2 equivalent of **2** with Ni(dppp)Cl_2 affording the organonickel compound **3.** Then reductive elimination immediately happens to result in an associated pair of 2,2'-dibromo-3,3'-dialkyl-5,5'-bithiophene **4** and the active Ni(0)-complex **5**, which immediately undergoes oxidative addition into one C-Br bond of bithiophene molecule.[93, 102-103] Yokozawa suggested an intramolecular transfer of the Ni(II)-complex to the terminal C-Br bond .[95] Propagation then occurs *via* trans-metallation of another **2** provided **7**, followed by reductive elimination to give an associated pair of tert-thiophene **8**

and Ni(0)-complex **9**. Chain growth proceeded by an insertion of one new monomer (**2**) for each cycle as shown in the reaction cycle (**10**-**11**-[**12**,**9**]-**10**), in which the catalytic Ni(0) species are able to walk or transfer along the chain. [78, 93, 102, 104] The termination can be triggered by the addition in the medium of MeOH/HCl that provide a proton and produce H-end-chains.

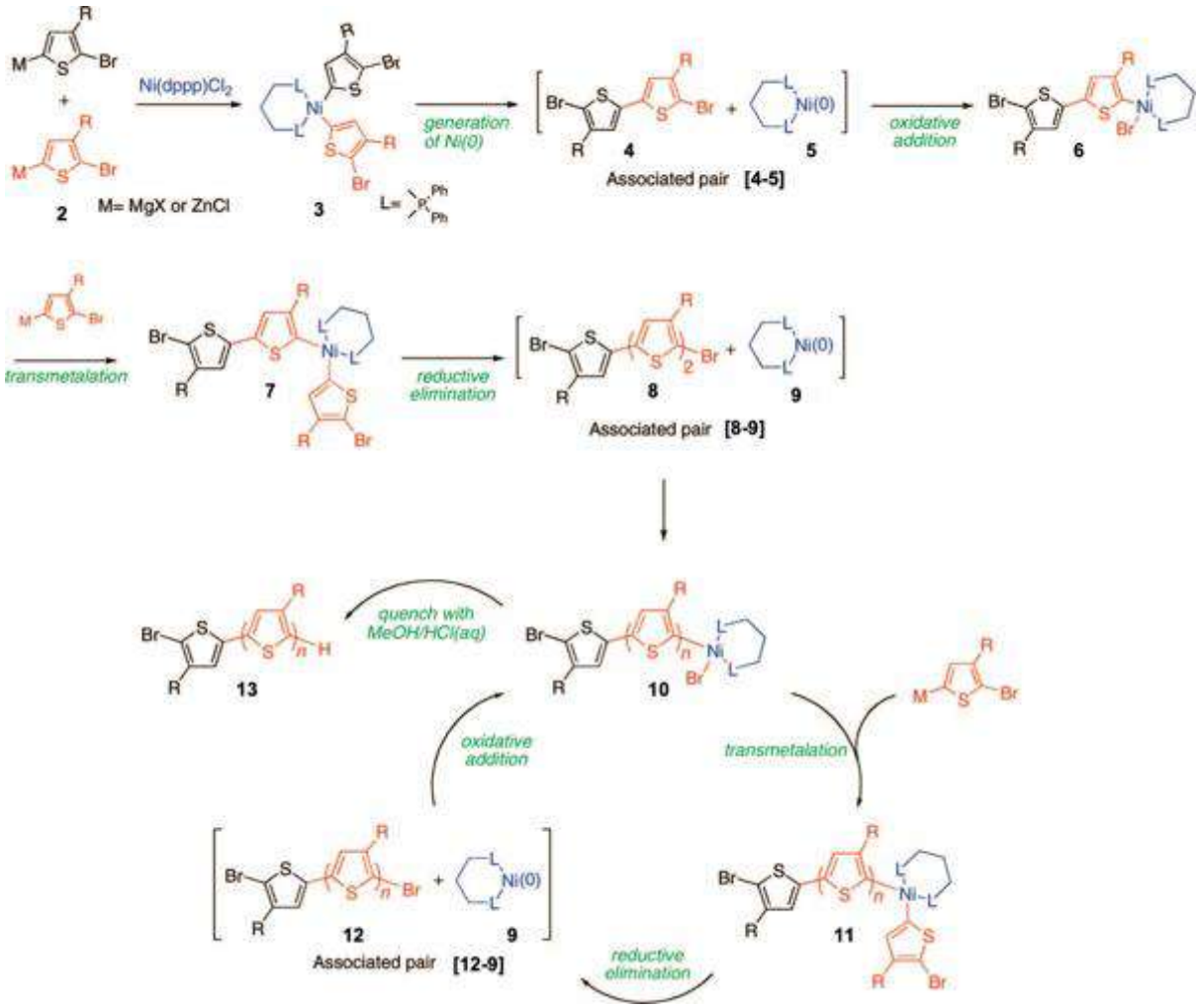

Scheme 6. The proposed mechanism of nickel-catalyzed polymerization for P3HT synthesis.[102]

Instead of H end group, various Grignard compound can used to functionalize and endcap the chains.[88, 95, 105] This *in situ* functionalization has become a famous route toward the preparation of P3HT macroinitiators for the synthesis of rod-coil BCPs.

4.3 Click chemistry process and Huisgen azide-alkyne cycloaddition

4.3.1 Copper catalyzed azide-alkyne cycloaddition

The term “click chemistry” first described by Kolb *et al.*, described the goal to develop a class of efficient, versatile, selective, and modular chemical reaction between two entities (here focused on polymer blocks).[106-107] The copper-catalyzed azide-alkyne cycloaddition (CuAAC) is one of these famous click reactions, based on the reaction of an azide with an alkyne to form a 5-membered heteroatom ring, named triazole **(Scheme 7)**. The efficiency and robustness of CuAAC reaction have led to form complex molecular architectures and to its use for many applications.[108-109]

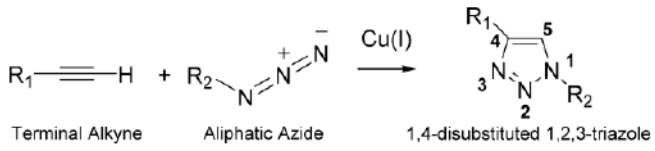

Scheme 7. CuAAC click reaction.

Huisgen’s work in the 1960’s, pioneered the development of this cycloaddition.[110-111] The last generally accepted mechanism of the CuAAC reaction is shown in **Scheme 8**. The reaction begins with the alkyne undergoing a hydrogen abstraction by the base and the creation of a σ-bound copper-acetylide bearing also a second copper complex by π-bonding (I scheme 8). Following by reaction with azide, reversibly coordinates an organic zide and complex II is formed. Then an intermediate of six-membered copper complex (III) is formed by nucleophilic attack at N-3 of azide. After the ligand exchange of this intermedia and followed by the formation of C-N bound result the ring closure and form the triazole-copper derivative. In the last step, the 1,4-substitured 1,2,3-triazoles reaction product is observed by protonolysis and close the full catalytic cycle.[112-115] Huisgen 1,3-dipolar cycloaddition has been optimized by Sharpless and co-worker.[113-116]

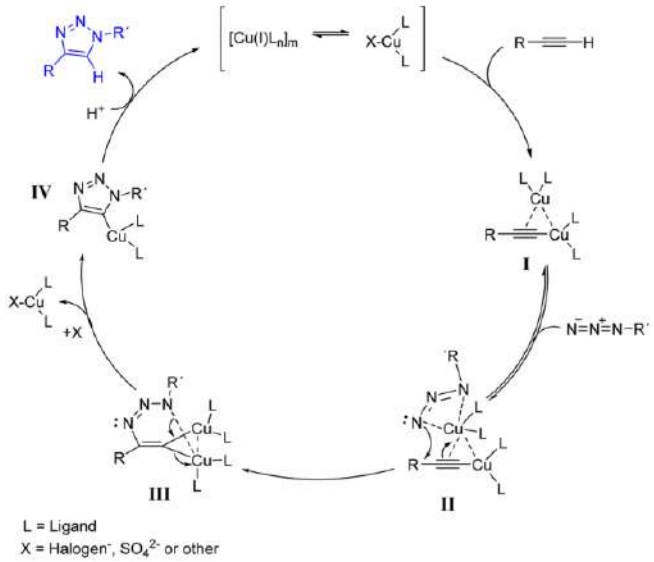

Scheme 8. Proposed catalytic cycle for the Cu(I)-catalyzed to form triazole ring.[113]

Because of its easy of procedure and high efficiency, the Cu-catalyzed azide-alkyne cycloaddition has had enormous impact in polymer field for the preparation of various "hybrid" BCPs in which the monomers cannot be polymerized by the same polymerization technique. This procedure can be performed in both aqueous or organic media with little or no side reactions in a wide temperature range.[3,117-118] For the example, a click reaction in aqueous media has been presented by Wang and co-workers, they reported the synthesis of multiblock copolymer of α,ω-azido-terminated and *α,ω*-alkynyl-terminated poly(ethylene oxide)-*block*-poly(propylene oxide)-*block*-poly(ethylene oxide) triblock copolymer by using a combination of self-assembly and click reaction in water. Indeed PEO block is water soluble and PPO is not, then the tri-blocks form polymeric core-shell micelles. The schematic of synthesis pathway shown in **Scheme 9**.[117]

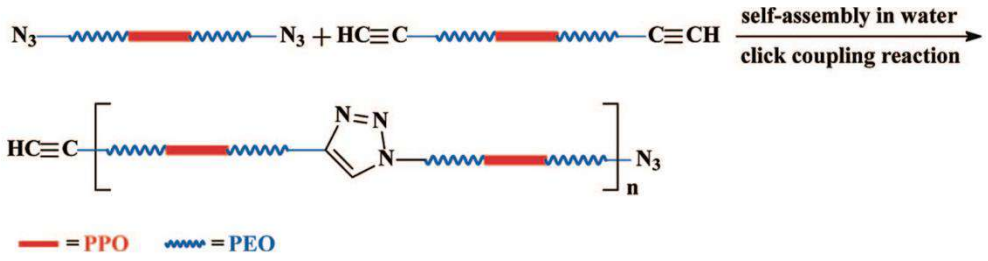

Scheme 9. Synthesis of (PEO-*b*-PPO-*b*-PEO-)$_n$ multiblock copolymer by multiple coupling procedure using a combination of self-assembly and click chemistry in water.[117]

The facile synthetic route for well-defined A_2B miktoarm star copolymer consisting of regio-regular poly(3-hexylthiophene) and poly(methyl methacrylate) $(P3HT)_2$-*b*-PMMA) by using the Huisgen 1,3-dipolar cycloaddition click reaction in THF was reported by Park and co-workers.[118] The α,α'-diazido-terminated PMMA (PMMA-$(N_3)_2$) block and the ethynyl-capped P3HT were synthesized by anionic polymerization and KCTP, respectively. Finally, the click coupling reaction of parent blocks was performed and led to the miktoarm star copolymer with a narrow dispersity; the synthesis route shown in **Scheme 10**.[118]

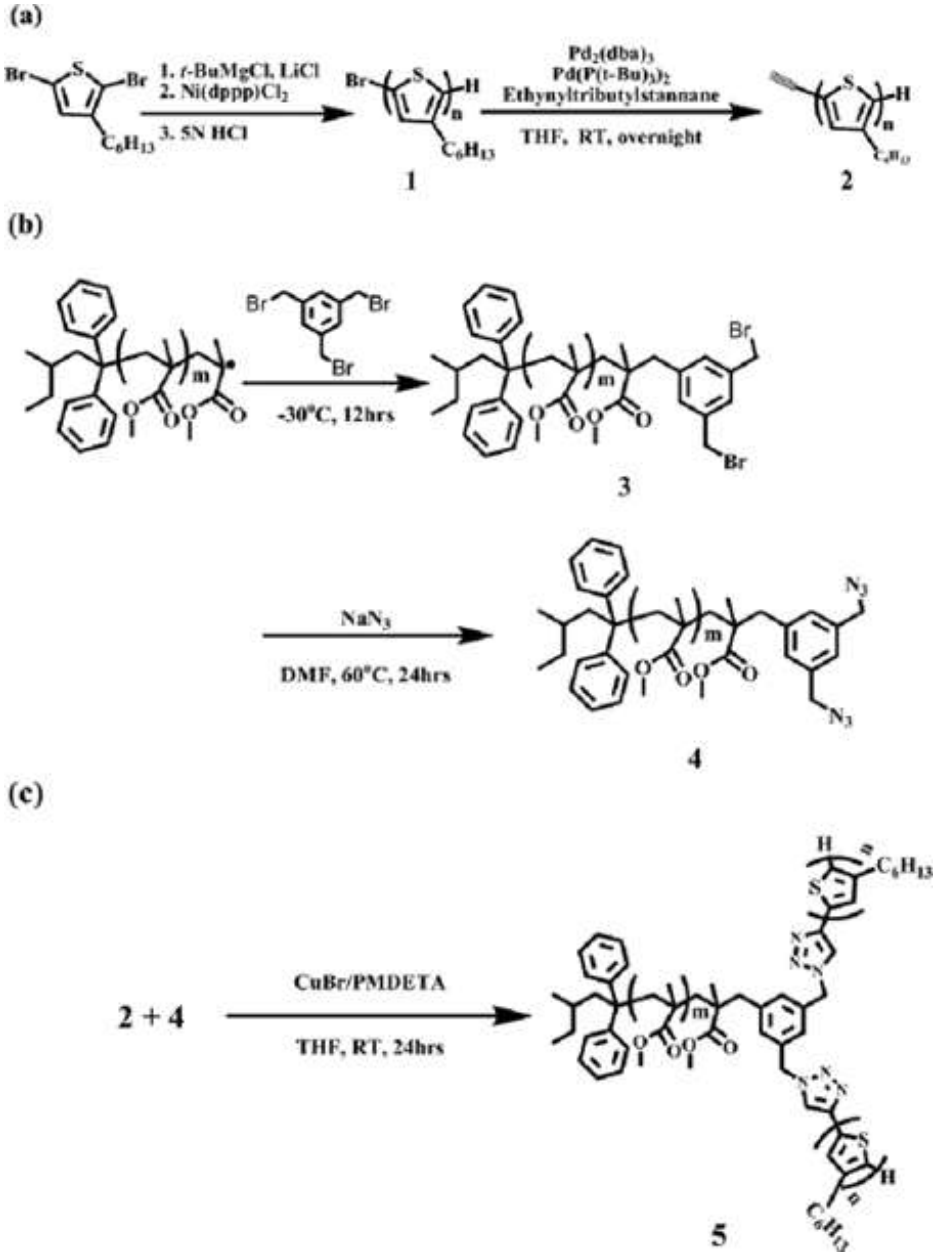

Scheme 10. Synthesis of BCPs of triblock $(P3HT)_2$-*b*-PMMA *via* Huisgen 1,3-dipolar cycloaddition click reaction.[118]

Some interesting rod-coil copolymer were prepared from P3HT with coil-like chains such as PEO, poly(2-vinylpyridine) (P2VP), PS and PMMA to improve solubility and to produce nanostructures either in bulk or in water. [120-122] In each of these cases "click chemistry" between azido end group and alkynyl end group was used to synthesize the conjugated BCPs. Furthermore, PMMA can be easily removed by UV irradiation and a high-density array of nanoscopic pore (then filled with electron acceptor materials) was generated in the P3AT matrix of a P3AT-*b*-PMMA BCPs .[123-125]

4.3.2 Metal-free azide-alkyne cycloaddition

The click reaction of azide-alkyne cycloadditon can be activated by copper catalysts, however the metal catalysts involve severe cytotoxic effect for long-term side effect for live cells or organisms.[126-127] As a solution, a metal-free Huisgen cycloaddition was developed for coupling two molecules.[128] With the use of cyclooctyne, the smallest stable cycloalkyne, a stain-promoted cycloaddition with phenyl azide was reported by Wittig and Krebs and "proceeded like an explosion" to give a triazole product. The activated alkyne increased the reactivity by introducing ring strain and allowed the reaction with azides without metal-catalysts **(Scheme 11)**. This reaction was named "strain promoted alkyne azide cycloaddition (SPAAC)".[129-133] In Scheme 11, the alkyne is also electronically activated by the two fluorine atoms.

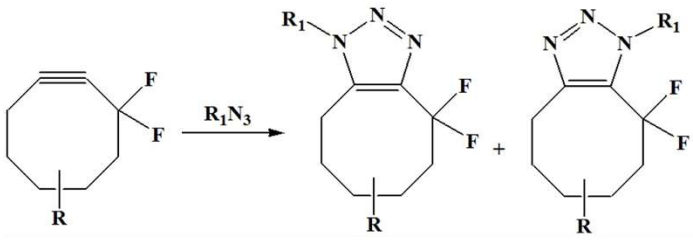

Scheme 11. Reagents and reaction pathway of metal-free cycloaddition.[129-132]

Metal-free alkyne-azide cycloadditon was used in applications such as in labeling glycans in protein or tissue.[127,134] Moreover, it has been employed for functionalizing carbon nanotubes with Cobalt catalyst for H_2-evolution reaction.[135] Azido-functionalized cobalt complex was reacted with cycloalkyne-funtionalized multiwalled CNTs electrode **(Scheme 12)**.

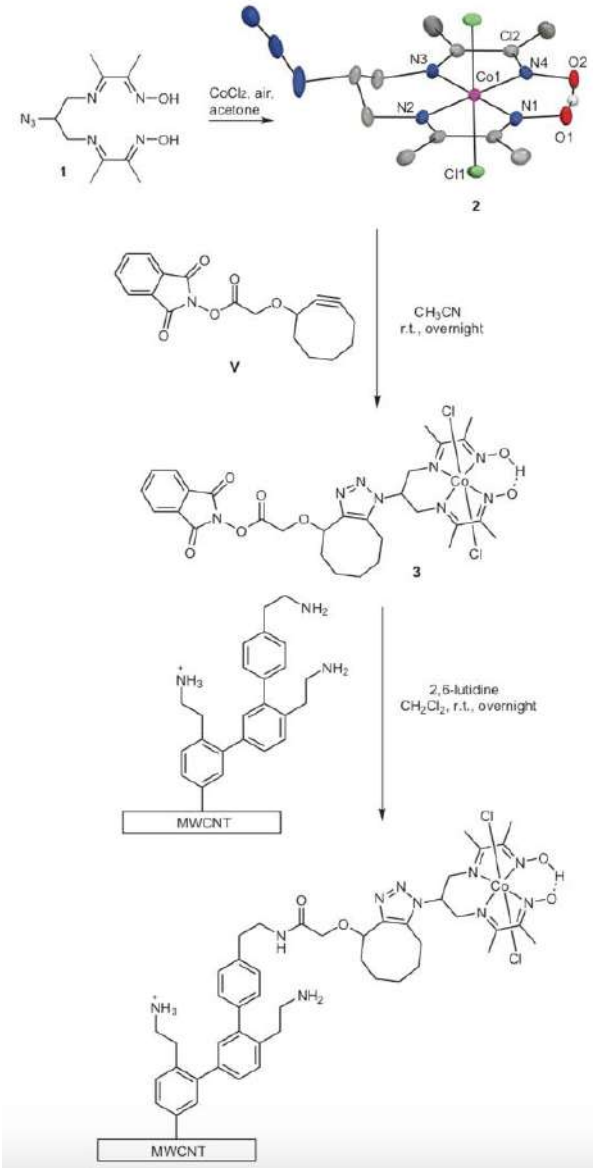

Scheme 12. Synthetic methodology for preparation of multiwalled CNTs functionalized with cobalt complex by using copper-free click reaction.[135]

Since the metal-free alkyne-azide cycloaddition can be used for selective modification of biomolecules or living cells without apparent physical harm[132], this reaction expanded rapidly.

5. Polymer electrode in printed electronics

5.1 Introduction

Recently, thin polymer films have been used in electronic displays due high flexibility, lightweight (the weight of polymer films in display is only 1/6 of a glass substrate) and durability.[136-137] Printed flexible electrodes with conductive inks have attracted much attention in wearable flexible electronic displays[138], touch screen displays[139], polymer solar cell,[140] electronic paper,[141] ultramicroelectrode,[142] ... The term "conductive inks" is used to design a solution of conductive material developed for printed electrode. These inks enable electrical circuits to be printed on paper, tissue or other flexible surfaces. The inks are often based on dispersed metal nanoparticle such as silver, gold and copper, due to their high electrical conductivity, mixed with a polymer binder and of course a solvent.[143-144] However, the price of metal-based inks is high and some metal such as copper nanoparticles-based inks are easily oxidized, thus an objective in the electrode community is to lower material cost and develop inexpensive printing processes.[143,145-146] Other materials such as conductive polymer-based inks and carbon nanotube (CNT) inks have been developed.[143,147-149]

Printed electronics (PE) refers to a type of electronics that are created by conventional printing technologies. The key advantages of PE include low-cost manufacturing with high throughput, compatibility with flexible systems (e.g., large-area electronics and hybrid system fabrication on flexible or stretchable substrates using the materials described above), and relative ease of integration. By contrast, silicon-based microfabrication technologies, such as photolithography and vacuum-based techniques (e.g., evaporation, sputtering, and chemical vapor deposition), typically require complicated manufacturing processes and relatively high production cost. The global PE market should reach $26.6 billion by 2022 from $14.0 billion in 2017 at a compound annual growth rate of 13.6%.[150]

In this last part of the bibliographic chapter I, will present the materials that are commonly used in conductive inks, with a special emphasis on the polymer binder. Then the printing techniques developed for low cost production will be discussed with a focus to the one developed in this PhD, *i.e.* screen-printing. Finally, the application of printed polymer electrodes will show and review work done for electrocatalysis deposition.

5.2 Among printing technologies: screen printing.

PE devices are manufactured by a variety of printing techniques that can be divided into two categories: non-contact patterning (or nozzle-based patterning) and contact-based

patterning. The non-contact techniques include inkjet printing, electro-hydrodynamic (EHD) printing, aerosol jet printing, and slot die coating. On the contrary screen printing, gravure printing, and flexographic printing are examples of contact techniques. These techniques present advantages and drawbacks, but they all rely on the principle of transferring inks onto a substrate.

Inkjet printing technology is very promising in this field due to its easy, rapid, low-cost printing, non-contact with the substrate and can be controlled by computer to access different and complex shapes.[173-176] Some fascinating conductive circuit composted of CNTs can be prepared by inkjet printing technique by printed the solution of CNTs onto the surface of substrate. The general process of inkjet printing involves to heat the ink solution in the ink chamber to forms vapor bubbles in a few microseconds, then the bubbles expand rapidly and are finally ejected through the nozzle and print onto the substrate.[174] Therefore, the ink must be a low viscosity solution.

3D printing is one of the rapidly growing technique in manufacturing technology, it is an attractive technique due to the extreme design freedom allowing the production of advanced materials in various fields such as actuators, sensor, electronic devices.[177-179] The concentration of ink is a very important parameter in 3D printing technique, for example in graphene oxide (GO) ink, a low GO concentration exhibited liquid-like behavior and was found unfit for 3D printing whereas GO inks presenting gel-like behavior (high GO concentration) with a high elastic modulus, can print nice filaments or complex 3D architectures.[177] In this example, 3D printing was used to prepare GO-based electrode in lithium-ion batteries. Ink filaments were extruded directly from a nozzle and deposited layer-by-layer to pattern the electrodes **(Figure 22)**.[177]

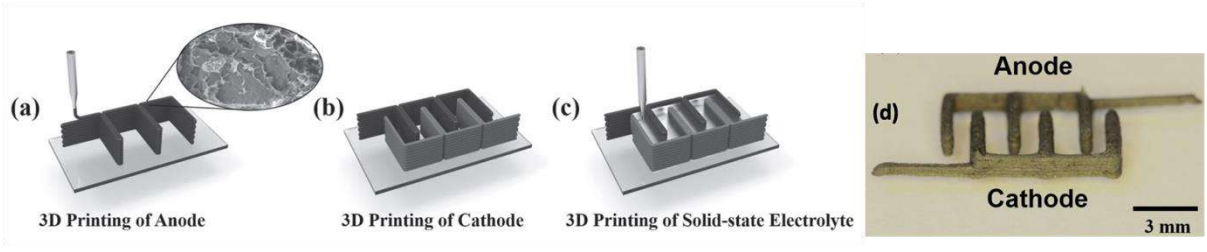

Figure 22. Schematic of 3D-printing of GO electrode, (a) 3D-printed of LTO/GO ink for anode preparation, (b) 3D-printed of LFP/GO ink for cathode, (c) the composite ink injected in the channel between cathode and anode electrodes, (d) digital image of electrode including cathode and anode.[177]

Among the various printing technique available, screen printing is widely used because it's simple, versatile, fast and cheap. Screen printing (SP) is a mass printing method performed by pressing an ink through a patterned stencil with a squeegee. The squeegee moves against the screen and presses the ink through it **(Figure 23)**.[152-153] One of the most distinct feature of screen printing compared with other printing methods is the high aspect ratio of printed patterns. The typical wet layer thicknesses are in the range of 10–500 µm, which can be useful for PE where high conductivity is needed. Viscosity of the ink, wetting of the substrate, and other parameters determine the applicability of this method.[155-157] From rheological perspectives, it has been well-known that polymer materials and conductive charges particulates, like silver, copper or carbon, possess distinct viscoelastic features and, therefore, may be utilized to complement each other in view of controlling the processing and products properties.[151] Indeed, SP is compatible with a wide variety of substrates and functional inks such as graphene and carbon nanotubes (CNT).[180-183] The resolution of screen printed object is highly dependent on the quality of the screen mask, which is usually produced by photo-crosslinked patterned polymers on a screen mesh.

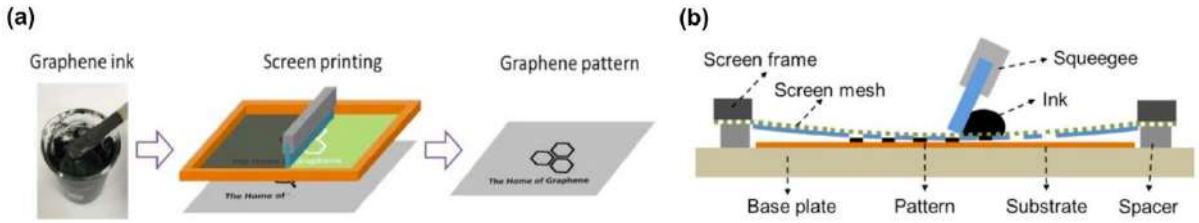

Figure 23. (a) The screen-printing process model used for the printing of graphene ink, (b) cross-section schematic of the screen-printing procedure, showing the ink was brush by the squeegee and pass through a screen mesh then coated on the substrate.[143]

Huang and coworkers first demonstrated a screen-printed graphene-based ink by dispersing graphene sheets in terpineol with ethylene cellulose as binder, which can be used as counter electrodes for dye-sensitized solar cells.[154] However, harsh thermal sintering at 400 °C was used to burn off the binder to obtain desirable conductivity, which inevitably affected the adhesive properties of the printed patterns. Therefore, there is a real need to develop materials and formulation suitable for screen-printing in view of electronics applications.

5.3 Conductive inks and polymer binder

Todays, conductive inks are available on the market for a wide range of applications and from a large number of producers. Despite this fact, for research purposes it is highly beneficial to have the possibility of in-house inks preparation. This ensures the control over the material composition and subsequently over the physical parameters of printed layers. As mentioned before a conductive ink is generally composed of a conductive charge, a solvent to make it processable, and a polymer binder to increase mechanical and adhesion properties to the final film. An additional surfactant can be found in some case to improve the dispersion of the conductive particles.

Among the conductive nanomaterials, metals represent the main system of choice. Ag nanoparticles are the most extensively studied material because it has the highest room-temperature electrical conductivity ($\sigma = 6.3x10^7$ S.m^{-1}). Since Cu possesses also a very high conductivity ($\sigma = 5.9x10^7$ S.m^{-1}) and is much cheaper, Cu have also drawn much attention. In addition to metal nanomaterials, carbon nanomaterials (σ around $1x10^4$ S.m^{-1} for graphitic carbon), including carbon black, graphite, graphene and carbon nanotubes (single or multiwalled), are also promising in printable flexible and stretchable electronics due to their high intrinsic current mobility. Due to the low dispersibility of carbon materials in a variety of solvents, it is a real challenge to fabricate printable carbon inks with high loading and avoiding aggregation.[162] Several conductive polymers have been intensively investigated, considering their low cost and that no sintering process is required; in particular, polyaniline (PANI), polypyrrole (PPy), poly(3,4-ethylenedioxythiophene) poly(styrenesulfonate) (PEDOT:PSS), etc.[163-166]

Polymer binder is an indispensable component for SPE because it improves the conductive particle network strength and helps conductive particles to stick to the substrate. Polymer binders for printable ink should be stable, electrochemically inactive and make the conductive particle spread and cover on the surface of electrode.[143,167-168] Many types of binders have been used in the ink formulation including ethylene cellulose (EC) [169], poly(vinylbutyral) (PVB) [170], poly(vinylacetate) (PVA) [171], and poly(vinylpyrrolidone).[172] Poly(methyl methacrylate) (PMMA) is also widely used due to it is a transparent material, stable and electronic inertness.[173-175] Moreover, PMMA is nontoxic material for human tissue[176-177] and has good adhesion properties with NAFION[178] which is commonly used as proton permeable membrane.[179] Because of these advantages, we have chosen PMMA as the binder for our electrode. Since PMMA is known as glassy polymer with a glass transition temperature of

100°C, films lack of flexibility and often know cracks which is decreasing mechanical properties of the material. In order to solve this problem, Yuca and co-worker reported the incorporation of triethylene glycol monomethyl ether (TEG) as a soft moiety part in polymethacrylic acid (PMAA) to serve as flexible interfaces for Lithium ion batteries.[180] The hard-soft-hard triblock copolymer of poly(methyl methacrylate)-*b*-poly(*n*-butylacrylate)-*b*-poly(methylmethacrylate) (PMMA-*b*-PnBa-*b*-PMMA) (also industrially called MBM) is also a flexible derivative of PMMA, highly stable and showing high adhesion to polar plastic substances.[181]

Binder content has a huge impact on the inks rheology and this lead to important consequences for the screen-printing technique. A too high binder content will result in increased ink tackiness which in turn affects the printability and quality of the resultant films. On the contrary, a too low binder content will cause film cracking/degradation during/after the drying of the final films as a result of reduced particle network strength.[182]

5.4 Applications for polymer electrode made via screen-printing

5.4.1 Sensors

Screen-printed carbon-based electrodes (SPCEs) have been studied in several field such as analytical chemistry and a fine review is available from Martinez *et al.*[152] As an example, *pH* sensor electrode based on graphite screen-printed electrodes (SPCEs) was produced by Galdino and co-workers. The SPCE *pH* sensor was shown as an excellent electrode to monitor *pH* in range of 1-13 in sample solution. The sensing mechanism underwent forming oxygenated species on the electrode surface and this was analyzed by voltammetric technique.[158] Another SPEs based-on graphite ink printed on a flexible polyester film have been used as an immunoassay or immunosensors for determination of alkaline phosphatase.[193-195]

5.4.2 Batteries

As recently reviewed by Sun *et al.*, carbon electrodes made *via* screen-printing have also been used and studied for energy storage technology, due to their highly attractive thermal, electrical conductivity and chemical stability.[196] Lithium-ion batteries (LIBs) are the most widely used portable energy storage devices and are constituted of a graphite negative electrode and a lithium metal oxide positive electrode separated by a polymer separator immersed in an organic liquid electrolyte. During the charge, lithium ions are extracted from the cathode,

migrate across the electrolyte, and intercalate between graphite layers in the anode, forming LiC_6. During discharge, the reverse electrochemical reaction occurs – lithium ions are removed from the graphite and reinsert into the cathode. These processes produce and consume electrons *via* oxidation and reduction reactions, respectively. In 2007, Kim *et al.*[197] were the first to develop an ink formulation comprised of mesocarbon microbeads, carbon black, and poly(vinylidene difluoride) PVDF binder dispersed in dibasic ester and print it onto a glass slide. Although it was by a laser printing technique, it showed the feasibility and opened the way to a new range of application. Their technique was used to create patternable thick carbon films. The high porosity of the mesocarbon microbeads led to increased ionic conduction through the electrodes, resulting in higher capacities compared to other thin-film micro-batteries. As another example, the screen-printable lithium-ion batteries using "green solvent" *N,N*'-dimethylpropyleneurea (DMPU) and poly(vinylidene difluoride) (PVDF) as a binder was reported by Gören and co-worker. The inks were based on lithium iron phosphate (C-$LiFePO_4$) and graphite for cathode and anode respectively and were developed to produce and innovative electrode for printed batteries. Electrode films presented a continuous and smoot surface morphology and made an electrical network structure produced by the homogenous conductive particles distribution. The schematic illustration procedure for screen-printing process and surface morphologies of cathode and anode films is presented in **Figure 24**.[198]

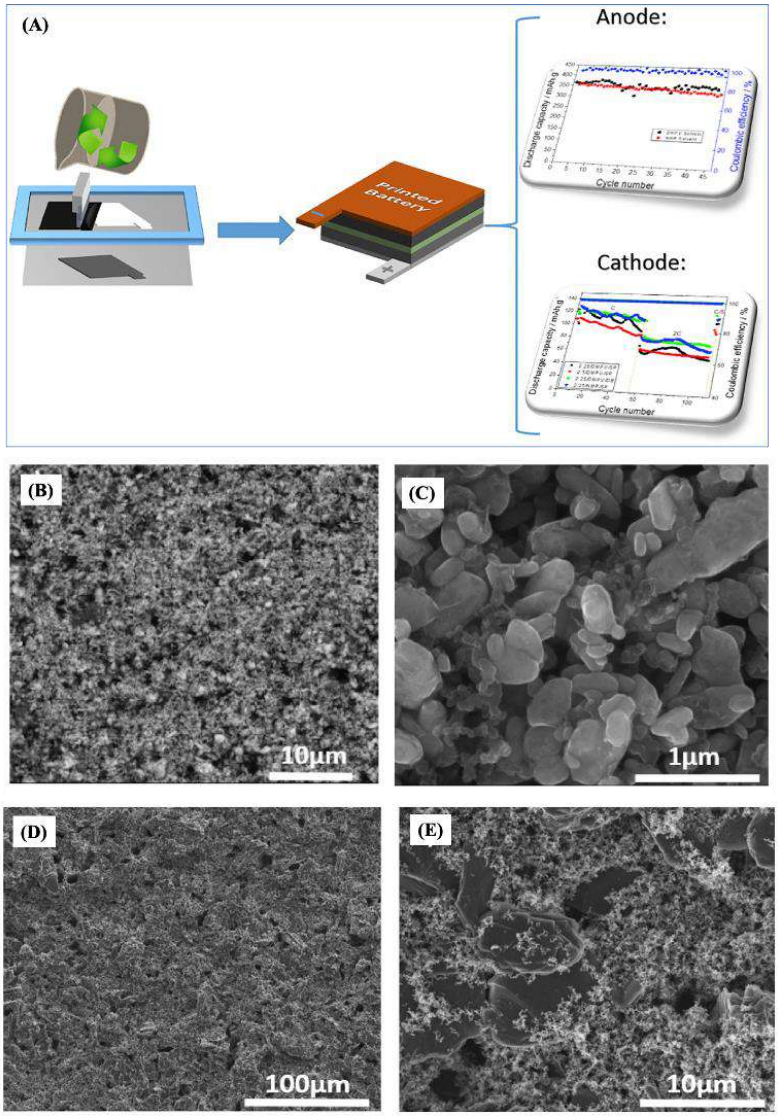

Figure 24. (A) a screen-printing model for the preparation of cathode and anode in Li-ion battery. (B), (C) back-scattered electron and secondary electron SEM images of films surface of cathode respectively. (D), (E) SEM images of the film surface of the anode with low and high magnifications.[198]

5.4.3 Solar Cells

Solar cells absorb photons and convert their energy into electrical energy. When a photon is absorbed, an electron-hole pair is created in the semiconducting material of the cell via the photoelectric effect. Electron and hole are then collected at the opposite electrodes to produce the current. To replace Indium-Tin oxide electrode, printing techniques were used either from Aluminum nanoparticles/graphene composite using screen-printing or using graphene oxide and stamping technology.[199-200] Also, Shaheen and co-workers reported the fabrication of an

ultra-smooth organic-based solar cell, with an active layer consists of a blend of conjugated polymer [poly(2-methoxy-5-(3,7-dimethyloctyloxy)-1,4-phenylene vinylene)] (MDMO-PPV) and the [6,6]-phenyl C61-butyric acid methyl ester (PCBM). This active layer was screen-printed onto the PEDOT:PSS layer with an average thickness of 40 nm. [201] They achieved an impressive power conversion efficiency of 4.3%. A description of the screen-printing process and the structure of the bulk-heterojunction solar cell is shown in **Figure 25**.

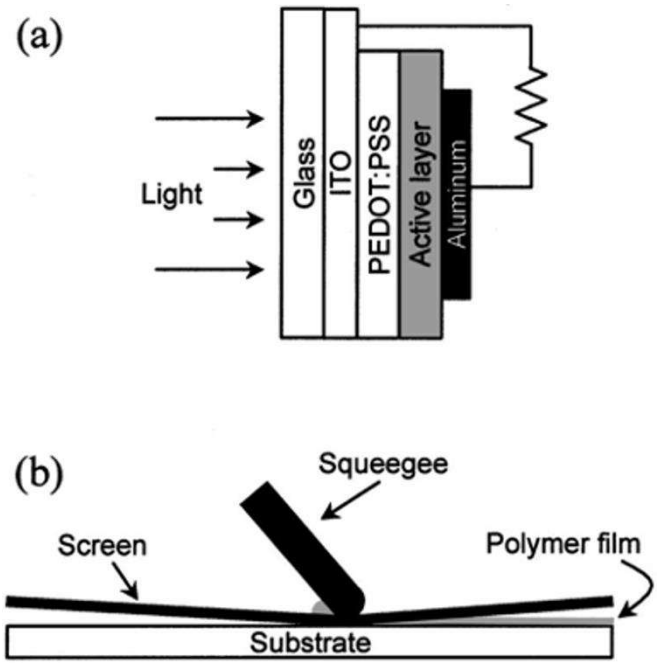

Figure 25. Schematic diagrams of (a) the bulk heterojunction solar cell and (b) the screen-printing equipment and working process of this technique.[201]

Finally, in 2009 Krebs and co-workers.[202] produced more than 2000 modules of low-cost polymer solar cell, from the blend of poly-(3-(2-methylhexan-2-yl)-oxy-carbonyldithiophene) (P3MHOCT)/PCBM/ZnO (zinc oxide nanoparticles). All inks were printed and squeeze through several size mesh screen. The solar cell was located on the top of a hat and a radio and ear plugs was integrated in the hat, called “Solar hat” and presented in **Figure 26**. Moreover, 32 solar cell modules were assembled in the upper surface of a large parasol that was made by the connection in series or parallel of each segment.[202]

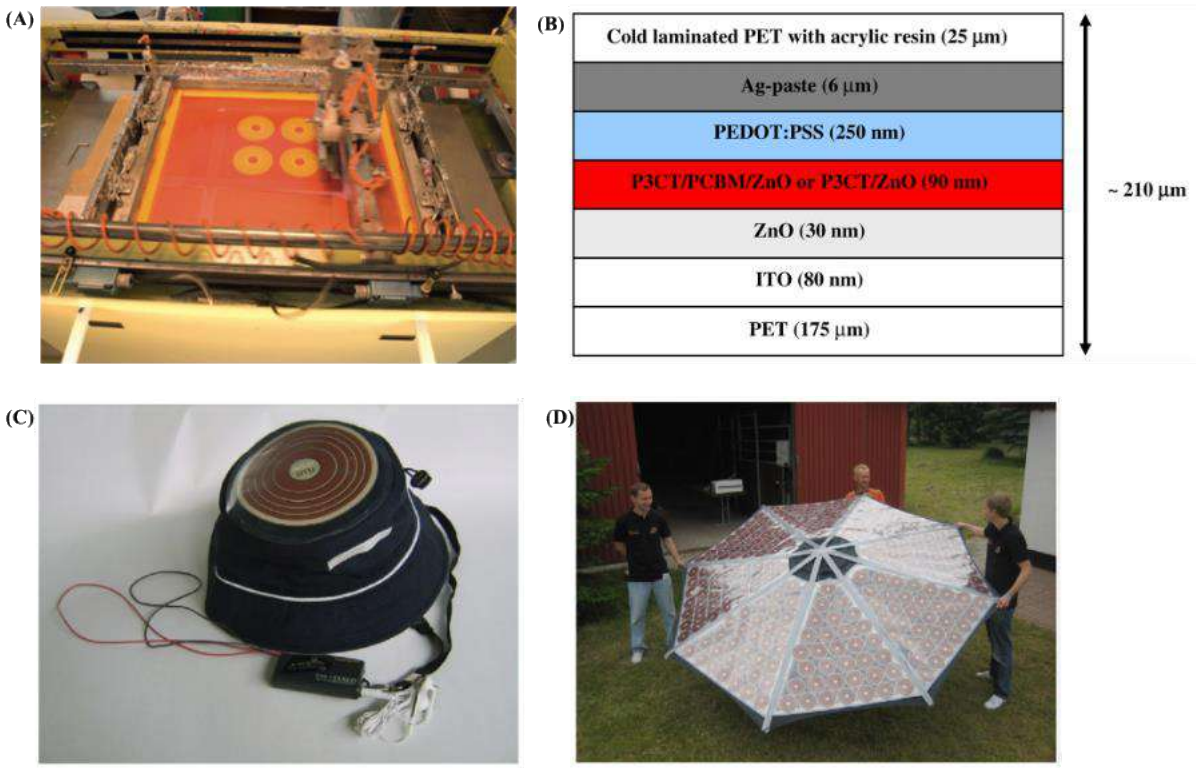

Figure 26. (A) the printing of the films on the solar cell, (B) the structure of the solar cell devices, (C) the "Solar hat" consists the polymer solar cell and (D) large parasols comprised eigth segments of 30-32 polymer solar cells.[202]

5.4.4 Film Heaters

Film heaters are device that can convert electric energy into heat. Recently, great attention has been devoted to transparent film heaters (TFH) due to the emergence of applications in defrosting or defogging vehicle windows and outdoor panel displays.[206-207] He and co-workers demonstrated the preparation of a transparent and flexible film heater based on a hybrid material made of poly(3,4-ethylenedioxythiophene) poly(styrenesulfonate) (PEDOT:PSS) and silver nanowires (Ag NWs).[205] The composite films were fabricated by using screen-printing on polyethylene terephthalate (PET) substrates. By a 40 V potential through the films, the devices temperature raised from 49 °C to 99 °C within 50 s. We and co-workers reported the production of flexible high-performance thermoelectric power generator (TEG) modules, based on a hybrid composite of Bi_2Te_3 (*n*-type) and Sb_2Te_3 (*p*-type) blended with the organic conducting polymers PEDOT:PSS. The films were screen-printed and the displays showed a high flexibility without degradation of the output property of the module.

The TEG modules were successfully used to harvest body heat, generating an output electricity of 12.1 mV as presented in **Figure 27**.[206]

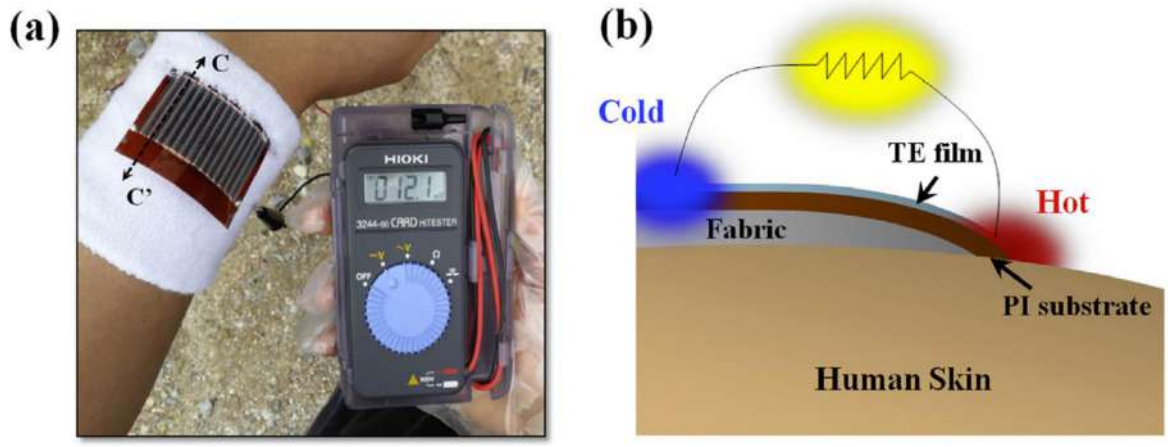

Figure 27. (a) Performance demonstration of the harvesting body heat of flexible TEG module and generate heat to electrical energy, (b) the cross section of the electrical generation by using body heat through the film heater.[206]

5.4.5 Catalysis

Catalysis is the process of increasing the rate of a reaction by the use of a catalyst. Hydrogen fuel cells (HFC) are capable of producing current from hydrogen oxidation occurring at the anode and oxygen reduction reactions occurring at the cathode. To increase the efficiency of HFC, the researchers have focused on reducing the onset potential (reducing the overpotential) of the above-mentioned reaction by incorporating catalyst to both electrodes. In 2017, Rowkey-Neale and co-workers developed a screen-printed electrode by incorporating molybdenum disulfide (MoS_2) into a graphitic ink **(Figure 28)**.[208] These electrodes were shown to be electrocatalytic toward oxygen reduction and can be produced in large volumes.

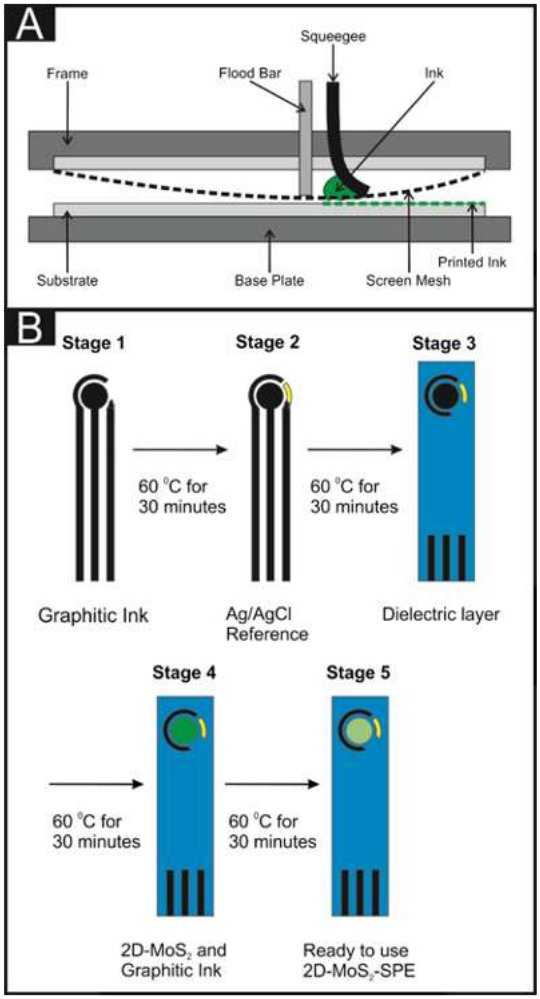

Figure 28. An overviews procedure of (A) screen-printing process model and (B) the individual steps for preparing the modified 2D-MoS_2-SPEs electrode.[208]

As another example, Chikae and co-workers studied the electrodeposition of gold and platinum nanoparticles on the screen-printed carbon electrodes.[209] The catalytic activity over proton reduction of the metal nanoparticle-modified SPCE were demonstrated by electrochemical measurements. The combination of electrodeposition and screen-printing process is a nice way to produce electrodes for hydrogen evolution.

6. Conclusion

This chapter showed the importance of polymers for producing flexible and lightweight electrodes and how BCPs could make a difference, by the variety of their composition that can bring multi-functionalities, multi-properties but also nanopatterned morphologies. Therefore, synthesis and self-assembly of these BCPs are crucial domains to master.

Concerning the self-assembly, BCPs are often composed of immiscible segments covalently linked which produce a segregation at the nanoscale. This segregation can produce different morphologies and dimensions that are linked by the volume fraction and length of the blocks. This technology is now widely used in application in which 10 nm patterns are desired but lack from the duration of the processed needed to reach thermodynamic equilibrium. The conventional heating or solvent annealings are the classic ways to provide mobility to the chains and a morphology showing long scale order with an absent of defect can be acceded a treatment of around half a day.

In this bibliography, it was reviewed that recently, some research teams showed the potential for microwave irradiation to promote high ordering of BCPs morphology in the time scale of the minute. This behavior is explained by the irradiation absorption by the substrate which then reacts as a pan to heat the polymer film above lying. From this SoA, we decided to study the effect of microwave on the copolymers we had selected as binders of our electrodes. The first copolymer, commercial, is based on methyl methacrylate (MMA) and butyl acrylate (BuA). MMA was selected for its capacity to be miscible the NAFION membrane, and BuA for its low glass transition temperature (*Tg*) providing nice film forming property and flexibility.

In Chapter 2, the reader will find the study of the self-assembly of this copolymer under the use of microwave annealing. Additionally, a second structuration, at the micrometer scale will be provided by the use of the "breath figure methodology" that will be presented in the introduction of Chapter 2.

In Chapter 3, the use of this PMMA-*b*-PBuA-*b*-PMMA triBCPs, also called MBM, is reported as a binder to produce electrode by screen-printing. This bibliography shows the development of polymer electrode as flexible, lightweight and cheap material to be inserted in electrochemical devices such as batteries, fuels cells or photovoltaics. MBM blends with conductive graphite particles to make an electrode were used on which ruthenium catalysts provided by Pr Antoni Llobet's group were deposited. Printing parameters were studied to

produce stable and conductive electrode and the catalytic activity upon water oxidation was investigated.

Concerning the synthesis, since the polymerization mechanisms and coupling strategies are numerous, only the techniques used during this PhD work were discussed in the present first chapter. On the one hand, the controlled behavior obtained by atomic transfer radical polymerization (ATRP) is a simple, inexpensive and convenient way to prepare functional polymers for various functional monomers such as (meth)acrylates, styrenics and other vinyl monomers. The major advantages of ATRP is the possibility to obtain polymer product with high molar mass and low dispersities and various copolymers composition and topology. On the other hand, conjugated polymers cannot be produced by radical polymerization, but few of them can still be following a chain-growth mechanism and present low dispersity and control over molar mas and end-chain functionality. The nickel-catalyzed Kumada catalyst-transfer polycondensation (KCTP) has been widely used to synthesis well-defined P3HT, a rod polymer presenting light absorption from 400 to 600 nm and semi-conducting properties. Using these two polymerization techniques we will show in **Chapter 4** the synthesis of a BCPs P3HT-*b*-PMMA and the study of its self-assembly in mass. Indeed, the mass self-assembly of this kind of rod-coil copolymer is very interesting and rich since not only the Flory-Huggins parameter and copolymer length influence the morphology of the material, but also the strong π interactions between the aromatic backbones of the semiconducting segments. Thus, a huge challenge in this kind of BCPs is controlling the microstructure. As shown in this bibliography, raising the volume fraction of coil segment or increasing the volume of the rod side chains are effective ways to decrease the influence of μ over χ. In this PhD, another strategy was followed to reduce μ, by introducing of an ionic unit at the junction of the P3HT and PMMA blocks and by playing on physical parameter such as the solvent of the initial solution or the use of an annealing induced by microwave.

The last part of this thesis relied on the use of the second BCPs P3HT-*b*-PMMA as a binder for electrode, but also on the synthesis of a new macromolecular catalyst, as artificial metallo-enzyme, to be integrated in the electrode for hydrogen evolution (proton reduction). The catalyst was synthesized by metal-free alkyne-azide cycloaddition of a P3HT functionalized with a strained cyclooctyne to react with an azido derivative of Cobalt complex. Indeed, this bibliography showed that “click chemistry” have been used to generate substances by joining two or more units together with covalent links. Huisgen cycloaddition was widely used to link two of different homopolymers or small molecules functionalized with azide and

ethynyl moieties. In addition, progress in chemistry lead to the development of metal free click reaction *via* the use of the strain-promoted azide-alkyne cycloaddition. In **Chapter 5**, the electrocatalytic properties of modified electrodes and the electrochemical analysis of P3HT-Co catalyst were studied.

REFERENCES:

(1) S. B. Darling. Block copolymers for photovoltaics. *Energy Environ. Sci*. **2009**, 2, 1266-1273.

(2) E. L. Schwartz.; C. K. Ober. *Phase-selective chemistry in block copolymer system. in advanced nanomaterial*, Ed by K. E. Geckeler.; H. Nishide, **2009**, Wiley-VCH, Weinheim.

(3) J. F. Kenney. Properties of block versus random copolymers. *Polymer engineering and science*. **1968**, 8, 216-226.

(4) Y.-C. Tseng.; S. B. Darling. Block copolymer nanostructures for technology. *Polymers*. **2010**, 2, 470-489.

(5) H.-C. Kim.; S.-M. Park.; W. D. Hinsberg. Block copolymer based nanostructures: materials, processes, and applications to electronics. *Chem. Rev*. **2010**, 110, 146-177.

(6) C. Park.; J. Yoon.; E. L. Thomas. Enabling nanotechnology with self assembled block copolymer patterns. *Polymer*. **2003**, 44, 6725-6760.

(7) H. Feng.; X. Lu.; W. Wang.; N.-G. Kang.; J. W. Mays. Block copolymers: synthesis, self-assembly, and applications. *Polymers*. **2017**, 9, 494.

(8) M. Stefik.; S. Guldin.; S. Vignolini.; U. Wiesner.; U. steiner. Block copolymer self-assembly for nanophotonics. *Chem. Soc. Rev*. **2015**, 44, 5076-5091.

(9) A. P. Lane.; X. Yang.; M. J. Maher.; G. Blachut.; Y. Asano.; Y. Someya.; A. Mallavarapu.; S. M. Sirard.; C. J. Ellison.; C. G. Willson. Directed self-assembly and pattern transfer of five nanometer block copolymer lamellae. *ACS. Nano*. **2017**, 11, 7656-7665.

(10) D. J. Meier. Theory of block copolymers. I. Domain formation in A-B block copolymers. *J. Polymer sci.: Part C*. **1969**, 26, 81-98.

(11) D. Borah.; M. T. Shaw.; J. D. Holmes.; M. A. Morris. Sub-10 nm feature size PS-b-PDMS block copolymer structures fabricated by a microwave-assisted solvothermal process. *ACS Appl. Mater. Interfaces*. **2013**, 5, 2004-2012.

(12) S. Gottlieb.; B. Rösner.; L. Evangelio.; M. Fernández-Regúlez.; A. Nogales.; M. C. García-Gutiérrez.; T. F. Keller.; J. Fraxedas.; T. A. Ezquerra.; C. David.; F. Perez-Murano. Self-assembly morphology of block copolymers in sub-10 nm topographical guiding patterns. *Mol. Syst. Des. Eng*. **2019**, 4, 175-185.

(13) R. A. Lawson.; A. J. Peters.; P. J. Ludovice.; C. L. Henderson. Tuning domain size of block copolymers for directed self assembly using polymer blending: molecular dynamics simulation studies. *Proceeding of SPIE-The international society for optical engineering*. **2013**, 8680, 86801Z-1-86801Z-10.

(14) V. Schädler.; V. Kniese.; T. Thurn-Albrecht.; U. Wiesner.; H. W. Spiess. Self-assembly of ionically end-capped diblock copolymers. *Macromolecules*. **1998**, 4828-4837.
(15) H. Y. Jung.; S. Y. Kim.; O. Kim.; M. J. Park. Effect of the protogenic group on the phase behavior and ion transport properties of acid-bearing block copolymers. *Macromolecules*. **2015**, 48, 6142-6152.
(16) F. F. Lupi.; T. J. Giammaria.; F. G. Volpe.; F. Lotto.; G. Seguini.; B. Pivac.; M. Lus.; M. Perego. High aspect ratio PS-b-PMMA block copolymer masks for lithographic applications. *ACS Appl. Mater. Interfaces*. **2014**, 6, 21389-21396.
(17) M. Ceresoli.; F. F. Lupi.; G. Seguini.; K. Sparnacci.; V. Gionotti.; D. Antonioli.; M. Laus.; L. Boarino.; M. Perego. Evolution of lateral ordering in symmetric block copolymer thin films upon rapid thermal processing. *Nanotechnology*. **2014**, 25, 275601.
(18) A. M. Welander.; M. Kang.; K. O. Stuen.; H. H. Solak.; M. Müller.; J. J. de Pablo.; P. F. Nealey. Rapid directed assembly of block copolymer films at elevated temperatures. *Macromolecules*. **2008**, 41, 2759-2761.
(19) C.-J. Ko.; Y.-K. Lin.; F.-C. Chen. Microwave annealing of polymer photovoltaic devices. *Adv. Mater*. **2007**, 19, 3520-3523.
(20) *Assembly and packing*. International technology roadmap for semiconductor, 2011 ed.; Semiconductor industry association: San Jose, CA, 2011.
(21) X. Zhang.; J. N. Murphy.; N. L. Y. Wu.; K. D. Harris.; J. M. Buriak. Rapid assembly of nanolines with precisely controlled spacing from binary blends of block copolymers. Macromolecules. 2011, 44, 9752-9757.
(22) D. Borah.; M. T Shaw.; J. D Holmes.; M. A Morris. Sub-10 nm feature size PS-b-PDMS block copolymer structures fabricated by a microwave-assisted solvothermal process. ACS Appl. Mater. Interfaces. 2003, 5, 2004-2012.
(23) D. Borah.; R. Senthamaraikannan.; S. Rasappa.; B. Kosmala.; J. D Holmes.; M. A Morris. Swift nanopattern formation of PS-b-PMMA and PS-b-PDMS block copolymer films using a microwave assisted technique. ACS Nano. 2003, 7, 6583-6596.
(24) C. Jin.; J. N. Murphy.; K. D. Harris.; J. M. Buriak. Deconvoluting the mechanism of microwave annealing of block copolymer thin films. *ACS Nano*. **2014**, 8, 3979-3991.
(25) D. Adam. Out of kitchen. *Nature*. **2003**, 42, 571-572.
(26) Z. Qiang.; C. Ye.; K. Lin.; M. L. Becker.; K. A. Cavicchi.; B. D. Vogt. Evolution in surface morphology during rapid microwave annealing of PS-b-PMMA thin films. *Journal of polymer science, part B: polymer physics*. **2016**, 54, 1499-1506.

(27) X. Zhang.; K. D. Harris.; N. L. Y. Wu.; J. N. Murphy.; J. M. Buriak. Fast assembly of ordered block copolymer nano structures through microwave annealing. *ACS Nano*. **2010**, 4, 7021-7029.

(28) D. Borah.; R. Senthamaraikannan.; S. Rasappa.; B. Kosmala.; J. D. Holmes.; M. A. Morris. Swift nanopattern formation of PS-b-PMMA and PS-b-PDMS block copolymer films using a microwave assisted technique. *ACS Nano*. **2013**, 7, 6583-6596.

(29) P. Mokarian-Tabari.; C. Cummins.; S. Rasappa.; C. Simao.; C. M. S. Torres.; J. D. Holmes.; M. A. Morris. Study of the kinetics and mechanism of rapid self-assembly in block copolymer thin films during solvo-microwave annealing. *Langmuir*. **2014**, 30, 10728-10739.

(30) E. Ji.; V. Pellerin.; F. Ehrenfeld.; A. Laffore.; A. Bousquet.; L. Billon. Hierarchically honeycomb-structured films by directed self-assembly in "breath figure" templating of ionizable "clicked" P3HT-*b*-PMMA diblock copolymers: ionic group/counter-ion effect on porous polymer film morphology. *Chem. Commun*. **2016**, 00, 1-3.

(31) V. Ho.; B. W. Boudouris.; B. L. McCulloch.; C. G. Shuttle.; M. Burkhardt.; M. L. Chabinyc.; R. A. Segalman. Poly(3-alkylthiophene) Diblock copolymers with Ordered Microstructures and Continuous Semiconducting Pathways. *J. Am. Chem. Soc*. **2011**, 133, 9270-9273.

(32) S. Y. Choi.; J. U. Lee.; J. W. Lee.; S. Lee.; Y. J. Song.; W. H. Jo.; S. H. Kim. Highly Ordered Poly(3-hexylthiophene) Rod Polymers via Block Copolymer Self-Assembly. *Macromolecules*. **2011**, 44, 1771-1774.

(33) H. C. Moon.; A. Anthonysamy.; J. K. Kim. Facile Synthetic Route for Well-Defined Poly(3-hexylthiophene)-block-poly(methyl methacrylate) copolymer by Anionic Coupling Reaction. *Macromolecules*. **2011**, 44, 1894-1899.

(34) Y-H. Lee.; Y-L. Yang.; W-C. Yen.; W-F. Su.; C-A. Dai. Solution self-assembly and phase transformations of form II crystals in nanoconfined poly(3-hexylthiophene) based rod-coil block copolymers. *Nanoscale*. **2014**, 6, 2194-2200.

(35) B. D. Olsen.; R. A. Segalman. Nonlamellar Phases in Asymmetric Rod-Coil Block Copolymers at Increased Segregation Strengths. *Macromolucules*. **2007**, 40, 6922-6929.

(36) R. A. Segalman.; B. McCulloch.; S. Kirmayer.; J. J. Urban. Block copolymers for organic optoelectronics. *Macromolecules*. **2009**, 42, 9205-9216.

(37) Q. Pei.; Y. Yang. Efficient Photoluminescence and Electroluminescence from a Soluble Polyfluorene. *J. Am. Chem. Soc*. **1996**, 118, 7416-7417.

(38) D. Marsitzky.; M. Klapper.; K. MÜllen. End-Functionalization of poly(2,7-fluorene): A Key Step toward Novel Luminescent Rod-Coil Block Copolymer. *Macromolecules.* **1999**, 32, 8685-8688.

(39) S-T. Lin.; K. Fuchise.; Y. Chen.; R. Sakai.; T. Satoh.; T. Kakuchi.; W-C. Chen. Synthesis, thermomorphic characteristics, and fluorescent properties of poly[2,7-(9,9-dihexylfluorene)]-*block*-poly(N-isopropylacrylamide)-*block*-poly(N-hydroxyethylacrylamide) rod-coil-coil triblock copolymers. *Soft Matter*. **2009**, 5, 3761-3770.

(40) MH. van der Veen.; B. de Boer.; U. Stalmach.; KI. van de Wetering.; G. Hadziioannou. Donor-Acceptor diblock copolymers based on PPV and C60: synthesis, thermal properties, and morphology. *Macromolecules*. **2004**, 37, 3673-3684.

(41) S. Barrau.; T. Heiser.; F. Richard.; C. Brochon.; C. Ngov.; K. van de Wetering.; G. Hadiioannou.; D. V. Anokhin.; D. A. Ivanov. Self-assembling of novel fullerene-grafted donor-acceptor rod-coil block copolymers. *Macromolecules*. **2008**, 41, 2701-2710.

(42) C-N. Dai.; W-C. Yen.; Y-H. Lee.; C-C. Ho.; W-F. Su. Facile synthesis of well-defined block copolymers containing regioregular poly(3-hexyl thiophene) via anionic macroinitiation method and their self-assembly behavior. *J. Am. Chem. Soc*. **2007**, 129, 11036-11038.

(43) J. U. Lee.; A. Cirpan.; T. Emrick.; T. P. Russell.; W. H. Jo. Synthesis and photophysical property of well-defined donor-acceptor diblock copolymer based on regioregular poly(3-hexylthiophene) and fullerene. *J. Mater. Chem*. **2009**, 19, 1483-1489.

(44) B. Li.; G. Sauve.; M. C. Lovu.; M. Jeffries-EL.; R. Zhang.; Jessica. Cooper.; S. Santhanam.; L. Schultz.; J. C. Revelli.; A. G. Kusne.; T. Kowalewski.; J. L. Snyder.; L. E. Weiss.; G. K. Fedder.; R. D. McCullough.; D. N. Lambeth. Volatile organic compound detection using nanostructured copolymers. *Nano Lett*. **2006**, 6, 1598-1602.

(45) C.-L. Liu.; C.-H. Lin.; C.-C. Kuo.; S.-T. Lin.; W.-C. Chen. Conjugated rod-coil block copolymers: synthesis, morphology, photophysical properties, and stimuli-responsive applications. *Progress in Polymer Science*. **2011**,36, 603-637.

(46) N. Sary.; L. Rubatat.; C. Brochon.; G. Hadziioannou.; J. Roukolainen.; F. Mezzenga. Self-assembly of poly(diethylhexyloxy-*p*-phenylenevinylene)-*b*-poly(4-vinylpyridine) rod-coil block copolymer system. *Macromolecules*. **2007**, 40, 6990-6997.

(47) M. He.; F. Qiu.; Z. Lin. Conjugated rod-coil and rod-rod block copolymers for photovoltaic applications. *J. Mater. Chem*. **2001**, 21, 17039-17048

(48) B. D. Olsen.; R. A. Segalman. Structure and thermodynamics of weakly segregated rod-coil block copolymers. *Macromolecules*. **2005**, 38, 10127-10137.

(49) K. Yazawa.; Y. Inoue.; T. Shimizu.; M. Tansho.; N. Askawa. Molecular dynamics of regioregular poly(3-hexylthiophene) investigated by NMR relaxation and interpretation of temperature dependent optical absorption. *J. Phys. Chem. B*. **2010**, 114, 1241-1248.

(50) I. Botiz.; S. B. Darling. Self-assembly of poly(3-hexylthiophene)-*block*-polylactide block copolymer and subsequent incorporation of electron acceptor material. *Macromolucules.* **2009**, 42, 8211-8217.

(51) E. C. Davidson.; R. A. Segalman. Thermal control of confined crystallization within P3HT block copolymer microdomains. *Macromolecules*. **2017**, 50, 8097-8105.

(52) M. Reenders.; G. T. Brinke. Compositional and orientational ordering in rod-coil diblock copolymer melts. *Macromolecules*. **2002**, 35, 3266-3280.

(53) A. F. Hannon.; R. J. Kline.; D. DeLongchamp. Advancing the computational methodology of rigid rod and semiflexible polymer system: a new solution to the wormlike chain model with rod-coil copolymer calculations. *Journal of polymer science, part B: polymer physic*. **2009**, 57, 29-39.

(54) C.-C. Ho.; Y.-H. Lee.; C.-A. Dai.; R. A. Segalman.; W.-F. Su. Synthesis and self-assembly of poly-(diethylhexyloxy-*p*-phenylenevinylene)-*b*-poly(methyl methacrylate) rod-coil block copolymers. *Macromolucules*. **2009**, 42, 4208-4219.

(55) M. Navratil.; A. Eisenberg. Ion clustering and viscoelastic relaxation in styrene-based ionomers. III. Effect of counterions, carboxylic groups, and plasticizers. Macromolecules. 1974, 7, 84-89.

(56) E. Mena-Osteritz.; A. Meyer.; B. M. W. Langeveld-Voss.; R. A. J. Janssen.; E. W. Meijer.; P. Bäuerle. Two-dimensional crystals of poly(3-alkylthiophene)s: direct visualization of polymer folds in submolecular resolution. *Angew. Chem. Int. Ed*. **2000**, 39, 2679-2684.

(57) E. Ji.; V. Pellerin.; L. Rubatat.; E. Grelet.; A. Bousquet.; L. Billon. Self-assembly of ionizable “clicked” P3HT-*b*-PMMA copolymers: ionic bonding group/counterion effects on morphology. *Macromolecules.* **2017**, 50, 235-243.

(58) S.-H. Lin.; S.-J. Wu.; C.-C. Ho.; W.-F. Su. Rational design of versatile self-assembly morphology of rod-coil block copolymer. *Macromolucules*. **2013**, 46, 2725-2732.

(59) C. G. Bazuin; A. Eisenberg. Ion-containin polymers:ionomers. *Journal of chemical education*. **1981**, 58, 938-943.

(60) X. Lu.; W. P. Steckle.; Jr.; R.A. Weiss. Morphological studies of a triblock copolymer ionomer by small angle X-ray scattering. *Macromolecues.* **1993**, 26, 6526-6530.

(61) W. Lu.; W. P. Steckle.; R. A. Weiss. Ionic Aggregation in block copolymer ionomer. *Macromolecules*. **1993**, 26, 5876-5884.

(62) M. T. Irwin.; R. J. Hickey.; S. Xie.; F. S. Bates.; T. P. Lodge. Lithium salt-induced microstructure and ordering in diblock copolymer/homopolymer blends. *Macromolecules*. **2016**, 49, 4839-4849.

(63) C. B. Bazuin.; A. Eisengerg. Modification of polymer properties through ion incorporation. *Ind. Eng. Chem. Prod. Res. Dev*. **1981**, 20, 271-286.

(64) I. Capek. Nature and properties of ionomer assemblies. II. *Advances in colloid and interface science*. **2005**, 118, 73-112.

(65) V. Schädler.; U. Wiesner. Salt-controlled lamellar spacing in ionically end-capped symmetric diblock copolymers. *Macromolecules*. **1997**, 30, 6698-6701.

(66) M. Schöps.; H. Leist.; A. DuChesne.; U. Wiesner. Salt-introduced switching of microdomain morphology of ionically functionalized diblock copolymers. *Macromolecules*. **1999**, 32, 2806-2809.

(67) Y. Lou.; D. Montarnal.; N. J. Treat.; P. D. Hustad.; M. D. Christianson.; E. J. Kramer.; G. H. Fredrickson.; C. J. Hawker. Enhanced block copolymer phase separation using click chemistry and ionic junctions. *ACS Macro Lett*. **2015**, 4, 1332-1336.

(68) W. H. Binder.; R. Sachsenhofer. 'Click' chemistry in polymer and material science: an update. *Macromol. Rapid Commun*. **2008**, 29, 952-981.

(69) M. Kato.; M. Kamigaito.; M. Sawamoto.; T. Higashimura. Polymerization of methyl methacrylate with the carbon tetrachloride/dichlorotris-(triphenylphosphine) ruthenium(II)/ methylaluminum Bis(2,6-di-tert-butylphenoxide) initiating system: possibility of living radical polymerization. *Macromolecules*. **1995**, 28, 1721-1723.

(70) J-S. Wang.; K. Matyjaszewski. Controlled/"living" radical polymerization. Atom transfer radical polymerization in the presence of transition-metal complexes. *J. Am. Chem. Soc*. **1995**, 117, 5614-5615.

(71) V. Coessens.; T. Pintauer.; K. Matyjaszewski. Functional polymers by atom transfer radical polymerization. *Prog. Polym. Sci*. **2001**, 26, 337-377.

(72) T. Pintauer.; K. Matyjaszewski. Atom transfer radical addition and polymerization reaction catalyzed by ppm amounts of copper complexes. *Chem. Soc. Rev.* **2008**, 37, 1087-1097.

(73) H. Sun.; L. Yang.; M. P. Thompson.; S. Schara.; W. Cao.; W. Choi.; Z. Hu.; N. Zang.; W. Tan.; W. Tan.; N. C. Gianneschi. Recent advances in amphiphilic polymer-oligonucleotide nanomaterials via living/controlled polymerization technologies. *Bioconjugate Chem*. **2019**, 30, 1889-1904.

(74) T. Patten.; K. Matyjaszewski. Copper(I)-catalyzed atom transfer radical polymerization. *Acc. Chem. Res.* **1999**, 32, 895-903.

(75) K. Matyjaszewski.; T.P. Davis. *Handbook of radical polymerization*. WILEY, Hoboken, 2002.

(76) T. Pintauer.; K. Matyjaszewski. Structural aspects of copper catalyzed atom transfer radical polymerization. *Coordination chemistry reviews*. **2005**, 249, 1155-1184.

(77) K. Matyjaszewski. Atom transfer radical polymerization (ATRP): current status and future perspectives. *Macromolecules*. **2012**, 45, 4015-4039.

(78) K. Matyjaszewski.; J. Xia. Atom transfer radical polymerization. *Chem. Rev*. **2001**, 101, 2921-2990.

(79) M. Kamigaito.; T. Ando.; M. Sawamoto. Metal-catalyzed living radical polymerization. *Chem Rev*. **2001** 101, 3689-3745.

(80) C-L. Liu.; C-H. Lin.; C-C. Kuo.; S-T. Lin.; W-C. Chen. Conjugate rod-coil block copolymers: Synthesis, morphology, photopysical properties, and stimulti-responsive applications. *Prog. Polym. Sci.* **2011**, 36, 603-637.

(81) C. Brochon.; N. Sary.; R. Mezzenga.; C. Ngov.; F. Richard.; M. May.; G. Hadziioannou. Synthesis of poly(paraphenylene vinylene)-polystyrene-based rod-coil block copolymer by Atom transfer radical polymerization: toward a self-organized lamellar semiconducting material. *J Appl Polym Sci*. **2008**, 110, 3664-3670.

(82) P. K. Tsolakis.; J. K. Kallitsis. Synthesis of Luminescent rod-coil block copolymers using atom transfer radical polymerization. *Macromolecule*s. **2002**, 35, 5758-5762.

(83) Y-C. Tung.; W-C. Wu.; W-C. Chem. Morphological transformation and photophysical properties of rod-coil poly[2,7(9,9-dihexylfluorene)]-block-poly(acrylic acid) in solution. *Macromol. Rapid. Commun*. **2006**, 27, 1838-1844.

(84) C-C. Kuo.; Y-C. Tung.; C-H. Lin.; W-C. Chen. Novel luminescent electrospun fibers prepared from conjugated rod-coil block copolymer of poly[2,7-(9,9-dihexylfluorene)]-block-poly(methyl methacrylate). *Macromol. Rapid Commun*. **2008**, 29, 1711-1715.

(85) S-T. Lin.; Y-C. Tung.; W-C. Chen. Synthesis structures and multifunctional sensory properties of poly[2,7-(9,9-dihexylfluorene)]-block-poly[2-dimethylamino)ethylmethacrylate] rod-coil diblock copolymers. *J. Mater. Chem*. **2008**, 18, 3985-3992.

(86) Y-C. Tung.; W-C. Chen. Poly[2,7-(9,9-dihexylfluorene)]-*block*-poly[3-(trimethoxysilyl) propylmethacrylate] (PF-*b*-PTMSPMA) rod-coil block copolymers: synthesis, morphology and photopysical properties in mixed solvents. *Reactive & Functional Polymers*. **2009**, 69, 507-518.

(87) RD. McCullough. The chemistry of conducting polythiophene. *Adv. Mater*. **1998**, 10, 93-116.

(88) A. Kiriy.; V. Senkovskyy.; M. Sommer. Kumada catalyst-transfer polycondensation: mechanism, opportunities, and challenges. *Macromol. Rapid Commun*. **201**1, 32, 1503-1517.

(89) K. Tamao.; K. Suimtani.; M. Kumada. Selective carbon-carbon bond formation by cross-coupling of Grignard reagent with organic halide. Catalysis by nickel-phosphine complexes. *J. Am. Chem. Soc*. **1972**, 94, 4374-4376.

(90) N. Marshall.; S. K. Sontag.; J. Locklin. Surface-initiated polymerization of conjugated polymers. *Chem. Commun*. **2011**, 47, 5681-5689.

(91) J. Liu.; E. Sheina.; T. Kowalewski.; R. D. McCullough. Tuning the electrical conductivity and self-assembly of regioregular polythiophene by block copolymerization: nanowire morphologies in new di- and triblock copolymers. *Angew. Chem. Int. Ed*. **2002**, 41, 329-332.

(92) B. W. Boudouris.; F. Molins.; D. A. Blank.; C. D. Frisbie.; M. A. Hilmyer. Synthesis, optical properties, and microstructure of a fullerene-terminated poly(3-hexylthiophene). *Macromolecules*. **2009**, 42, 4118-4126.

(93) G. YanHou.; H. Li.; W. ShuPeng.; W. FoSong. Kumada chain-growth polycondensation as a universal method for synthesis of well-defined conjugated polymers. *Sci China Chem*. **2010**, 53, 1620-1633.

(94) A. Yokoyama.; R. Miyakoshi.; T. Yokozawa. Chain-growth polymerization for poly(3-hexylthiophene) with a defined molecular weight and a low polydispersity. *Macromolecules*. **2004**, 37, 1169-1171.

(95) R. Miyakoshi.; K. Shimono.; A. Yokoyama.; T. Yokozawa. Catalyst-transfer polycondensation for the synthesis of poly(p-phenylene) with controlled molecular weight and low dispersity. *J. Am. Chem. Soc*. **2006**, 128, 16012-16013.

(96) R. S. Loewe.; S. M. Khersonsky.; R. D. McCullough. A simple method to prepare head-to-tail coupled, regioregular poly(3-alkylthiophenes) using Grignard metathesis. *Adv. Mater*. **1999**, 11, 250-253

(97) R. D. McCullough.; R. D. Lowe.; M. Jayaraman.; D. L. Anderson. Design, synthesis, and conducting polymer architectures: structurally homogeneous poly(3-alkylthiophenes). *J. Org. Chem*. **1993**, 58, 904-912.

(98) T. Yamamoto.; K. Sanechika.; A. Yamamoto. Preparation of thermostable and electric-conducting poly(2,5-thienylene). *Journal of polymer science: polymer letters edition*. **1980**, 18, 9-12

(99) J. W-P. Lin.; L. P. Dudek. Synthesis and properties of poly(2,5-thienylene). *Journal of polymer science: polymer chemistry edition*. **1980**, 18, 2869-2873.

(100) M. C. Iovu.; E. E. Sheina.; R. R. Gil.; R. D. McCullough. Experimental evidence for the Quasi-"living" nature of the Grignard metathesis method for synthesis of regioregular poly(3-alkylthiophenes). *Macromolecules*. **2005**, 38, 8649-8656.

(101) E. E. Sheina.; J. Liu.; M. C. Iovu.; D. W. Laird.; R. D. McCullough. Chain growth mechanism for regioregular nickel-initiated cross-coupling polymerization. *Macromolecules*. **2004**, 37, 3526-3528.

(102) I. Osaka.; R. D. McCullough. Advances in molecular design and synthesis of regioregular polythiophenes. *Accounts of Chemical Research*. **2008**, 41, 1202-1214.

(103) M. C. Iovu.; E. E. Sheina.; R. R. Gil.; R. D. McCullough. *Macromolecules*. **2005**, 38, 8649-8656.

(104) R. Tkachov.; V. Senkovskyy.; H. Komber.; J.-U. Sommer.; A. Kiriy. Random catalyst walking along polymerized poly(3-hexylthiophene) chains in Kumada catalyst-transfer polycondensation. *J. Am. Chem. Soc*. **2010**, 132, 7803-7810.

(105) M. Jeffries-El.; G. Sauvé.; R. D. McCoullough. In-situ end-group functionalization of regioregular poly(3-alkylthiophene) using the Grignard metathesis polymerization method. *Adv. Mater*. **2004**, 16, 1017-1019.

(106) K. Nwe.; M. W. Brechbiel. Growing applications of "click chemistry" for bioconjugation in contemporary biomedical research. *Cancer biotherapy & radiopharmaceuticals*. **2009**, 24, 288-302

(107) H. C. Kolb.; M. G. Finn.; B. Sharpless. Click chemistry: diverse chemical function from a few good reaction. *Angew. Chem. Int. Ed*. **2001**, 40, 2004-2021.

(108) M. Meldal.; C. W. TornØe. Cu-catalyzed azide-alkyne cycloaddition. *Chem. Rev*. **2008**, 108, 2952-3015.

(109) C. W. TornØe.; C. Christensen.; M. Meldal. Peptidotroazoles on solid phase: [1,2,3]-triazoles by regiospecific copper(I)-catalyzed 1,3-dipolar cycloadditions of terminal alkynes to azides. *J. Org. Chem*. **2002**, 67, 3057-3064.

(110) R. Huisgen.; G. Szeimies.; L. Möbius. Kinetik der additionen organischer azide an CC-mehrfach-bindungen. *Chem. Ber*. **1967**, 100, 2494.

(111) R. Huisgen. Kinetics and reaction mechanisms: selected examples from the experience of forty years. *Pure & Appl. Chem*. **1989**, 61, 613-628.

(112) F. Amblard.; J. H. Cho.; R. F. Schinazi. Cu(I)-catalyzed Huisgen azide-alkyne 1,3-dipolar cycloaddition reaction in nucleoside, nucleotide, and oligonucleotide chemistry. *Chem. Rev*. **2009**, 109, 4207-4220.

(113) B. T. Worrell.; J. A. Malik.; V. V. Fokin. Direct evidence of a dinuclear copper intermediate in Cu(I)-catalyzed azide-alkyne cycloadditions. Science. 2013, 340, 457-460.

(114) V. V. Rostovtsev.; L. G. Green.; V. V. Fokin.; K. B. Sharpless. A stepwise Huisgen cycloaddition process: copper(I)-catalyzed regioselective "ligation" of azide and terminal alkynes. *Angew. Chem. Int. Ed*. **2002**, 41, 2596-2599.

(115) D. Spiteri.; J. E. Moses. Copper-catalyzed azide-alkyne cycloaddition: regioselective synthesis of 1,4,5-trisubstituted 1,2,3-triazoles. *Angew. Chem. Int. Ed*. **2010**, 49, 31-33.

(116) J. E. Hein.; J. C. Tripp.; L. B. Krasnova.; K. B. Sharpless.; V. V. Fokin. Copper(I)-catalyzed cycloaddition of organic azides and 1-iodoalkynes. *Angew. Chem. Int. Ed*. **2009**, 48, 8018-8021.

(117) W. Wang.; T. Li.; T. Yu.; F. Zhu. Synthesis of multiblock copolymers by coupling reaction based on self-assembly and click chemistry. *Macromolecules*. **2008**, 41, 9750-9754.

(118) J. Park.; H. C. Moon.; J. K. Kim. Facile synthesis for well-defined A2B mitoarm star copolymer of poly(3-hexylthiophene) and poly(methyl methacrylate) by the combination of Anionic polymerization and click reaction. *Journal of polymer science, part A: polymer chemistry*. **2013**, 41, 2225-2232.

(119) R. D. McCullough. The chemistry of conducting polythiophenes. Adv. Mater. 1998, 10, 93-116.

(120) M. G. Mohamed.; C.-C. Cheng.; Y.-C. Lin.; C.-W. Huang.; F.-H. Lu.; F.-C. Chang.; S.-W. Kuo. Synthesis and self-assembly of water-soluble polythiophene-graft-poly(ethylene oxide) copolymers. *RSC Adv*. **2014**, 4, 21830-21839.

(121) M. Urien.; H. Erothu.; E. Cloutet.; R. C. Hiorns.; L. Vignau.; H. Cramail. Poly(3-hexylthiophene) based block copolymers prepared by "click" chemistry. *Macromolecules*. **2008**, 41, 7033-7040.

(122) J.-S. Kim.; Y. Kim.; H.-J. Kim.; H. J. Kim.; H. Yang.; Y. S. Jung.; G. E. Stein.; B. J. Kim. Regioregularity-driven morphological transition of poly(3-hexylthiophene)-based block copolymers. *Macromolecules*. **2017**, 50, 1902-1908.

(123) S.-H. Lin.; S.-J. Wu.; C.-C. Ho.; W.-F. Su.; Rational design of versatile self-assembly morphology of rod-coil block copolymer. *Macromolecules*, **2013**, 46, 2725-2732.

(124) J. Park.; K. S. Lee.; C. Choi.; J. Kwak.; H. C. Moon.; J. K. Kim. Effect of molecular weight on competitive self-assembly of poly(3-dodecylthiophene)-*block*-poly(methyl methacrylate) copolymers. *Macromolecules*. **2016**, 49, 3647-3653.

(125) J. Park.; H. C. Moon.; C. Choi.; J. K. Kim. Synthesis and characterization of [poly(3-dodecylthiophene)]$_2$ poly(methyl methacrylate) miktoarm star copolymer. *Macromolecules*. **2015**, 48, 3523-3530.

(126) E. M. Sletten.; C. R. Bertozzi. From mechanism to mouse: a tale of two biorthogonal reactions. *Accounts of chemical research*. **2011**, 44, 666-676.

(127) J. C. Jewett.; C. R. Bertozzi. Cu-free click cycloaddition reactions in chemical biology. *Chem. Soc. Rev*. **2010**, 39, 1272-1279.

(128) S. Yoshida. Sequential conjugation methods based on triazole formation and related reactions using azides. *Org. Biomol. Chem*. **2020**, 18, 1550-1562.

(129) G. Wittig.; A. Krebs. Zur Existenz niedergliedriger cycloalkane, I1). *Chem. Ber*. **1961**, 94, 3260-3275.

(130) P.-H. Elchinger.; P.-A. Faugeras.; B. Boëns.; F. Brouillette.; D. Montplaisir.; R. Zerrouki.; R. Lucas. Polysaccharides: the “click” chemistry impact. *Polymers*. **2011**, 3, 1607-1651.

(131) J. A. Codelli.; J. M. Baskin.; N. J. Agard.; C. R. Bertozzi. *J. Am. Chem. Soc*. **2008**, 130, 11486-11493.

(132) N. J. Agard.; J. A. Prescher.; C. R. Bertozzi. A strain-promoted [3+2] azide-alkyne cycloaddition for covalent modification of biomolecules in living system. *J. Am. Chem. Soc*. **2004**, 126, 15046-15047.

(133) N. E. Mbua.; J. Gou.; M. A. Wolfert.; R. Steet.; G.-J. Boon. Strain-promoted alkyne-azide cycloadditions (SPAAC) reveal new features of glycoconjugated biosynthesis. *ChemBiochem*. **2011**, 12, 1912-1921.

(134) E. Lallana.; E. Fernandez-Megia.; R. Riguera. Surpassing the use of copper in the click functionalization of polymeric nanostructures: astrain-promoted approach. *J. Am. Chem. Soc*. **2009,** 131, 5748-5750.

(135) E. S. Andreiadis.; P.-A. Jacques.; P. D. Tran.; A. Leyris.; M. Chavarot-Kerlidou.; B. Jousselme.; M. Matheron.; J. Pécaut.; S. Palacin.; M. Fontecave.; V. Artero. Molecular engineering of a cobalt-based electrocatalytic nanomaterial for H_2 evolution under fully aqueous conditions. *Nature chemistry*. **2003**, 5, 48-53.

(136) J.-Y. Kim.; S. Sohn.; E.-R. Kim. Polymer-based multi-layer conductive electrode film for plastic LCD applications. *Appl. Phys*. A. **2001**, 72, 660-704.

(137) J.-Y. Kim.; M.-H. Kwon.; J.-T. Kim.; J.-H. Lee.; T.-W. Kim.; S. Kwon. P1-163: polymer electrode and micro-patterning using PEDOT and its organic display applications. In SID Symposium Digest of Technical Papers (Vol. 38, No1, pp. 810-812). Oxford, UK: Blackwell Publishing Ltd.

(138) X. Wang.; W. Guo.; Y. Zhu.; X. Liang.; F. Wang.; P. Peng. Electrical and mechanical properties of ink printed composite electrodes on plastic substrates. *Appl. Sci*. **2008**, 8, 2101.

(139) S. Li.; B. N. Peele.; C. M. Larson.; H. Zhao.; R. F. Shepherd. A strechable multicolor display and touch interface using photopatterning and transfer printing. *Adv. Mater*. **2016**, 28, 9770-9775.

(140) C. Zhang.; Q. Luo.; M. Wu.; H. Li.; J. Lai.; G. Ji.; L. Yan.; X. Wang.; D. Zhang.; J. Lin.; L. Chen.; J. Yang.; C. Ma. Roll-to-roll micro-gravure printed large-area zinc oxide thin film as the electron transport layer for solution-processed polymer solar cells. *Organic Electronics*. **2017**, 45, 190-197.

(141) B. Comiskey.; J. D. Albert.; H. Yoshizawa.; J. Jacobson. An electrophoretic ink for all-printed reflective electronic displays. *Nature*. **1998**, 394, 253-255.

(142) E. Daviddi.; Z. Chen.; B. B. Massani.; J. Lee.; C. L. Bentley.; P. R. Unwin.; E. L. Ratcliff. Nanoscale visualization and multiscale electrochemical analysis of conductive polymer electrodes. *ACS Nano*. **2019**, 13, 13271-13284.

(143) He, P.; Cao, J.; Ding, H.; Liu, C.; Neilson, J.; Li, Z.; Kinloch, I. A.; Derby, B., Screen-Printing of a Highly Conductive Graphene ink for Flexible Printed Electronics. *Acs Appl. Mater. Interfaces*, **2019**, 11, 32225-32234.

(144) A. Kamyshny.; A. Magdassi. Conductive nanomaterials for printed electronics. Small. 2014, 10, 3515-3535.

(145) A. Louwen.; W. van Shark.; R. Schropp.; A. Faaij. A cost roadmap for silicon heterojunction solar cells. Solar Energy Materials & Solar Cells. 2016, 147, 295-314.

(146) S.-P. Chen.; H.-L. Chiu.; P.-H. Wang.; Y.-C. Liao. Inkjet printed conductive tracks for printed electronics. ECS J. Solid State Sci. Technol. 2015, 4, P3026-P3033.

(147) C.-K. Cho.; W.-J. Hwang.; K. Eun.; S.-H. Choa.; S.-I. Na.; H.-K. Kim. Mechanical flexiblility of transparent PEDOT:PSS electrodes prepared by gravure printing for flexible organic solar cells. Solar Energy Materials & Solar Cells. 2011, 95, 3269-3275.

(148) K. Kordás.; T. Mustonen.; G. Tóth.; H. Jantunen.; M. Lajunen.; C. Soldano.; S. Talapatra.; S. Kar.; R. Vajtai.; P. M. Ajayan. Inket printing of electrically conductive patterns of carbon nanotubes. Small. 2006, 2, 1021-1025.

(149) L. Xu.; Y. Liu.; M. P. Garrett.; B. Chen.; B. Hu. Enhancing Seebeck effects by using exited states in organic semiconducting polymer MEH-PPV based on multilayer electrode/polymer/electrode thin-film structure. J. Phys. Chem. C. 2013, 117, 10264-10269.
(150) M. Sullivan.; Printed electronics: global markets to 2022. BCC research LLC, Massachusetts, USA, 2018.
(151) C. P. Hsu.; R. H. Guo.; C. C. Hua.; C.-L. Shih.; W.-T. Chen.; T.-I. Chang. Effect of polymer binders in screen printing technique of silver pastes. J Polym. Res. 2013, 20, 277.
(152) O. D. Renedo.; M. A. Alonso-Lomillo.; M.J. A. Martínez. Recent developments in the field of screen-printed electrodes and their related applications. Talanta. 2007, 73, 202-219.
(153) J. Wang. Decentralized electrochemical monitoring of trace metals: from disposable strips to remote electrodes. Analyst. 1994, 199, 763-766.
(154) D. W. Zhang.; X. D. Li.; H. B. Li.; S. Chen.; Z. Sun.; X. J. Yin.; S. M. Huang. Graphene-based counter electrode for dye-sensitized solar cells. Carbon. 2011, 49, 5328-5388.
(155) M. Alvarez-Icaza.; U. Bilitewski. Mass Production of Biosensors. *Analytical chemistry*. **1993**, 65(11), 525A-533A.
(156) P. L. Helditch.; M. J. Green. Disposable electrochemical biosensors. *ANALYST*. **1991**, 116, 1217-1220.
(157) J. P. Hart.; S. A.Wring. Screen-printed voltammetric and amperometric electrochemical sensors for decentralized testing. *Electroanalysis*, **1994**, 6(8), 617-624.
(158) F. E. Galdino.; J. P. Smith.; S. I. Kwamou.; D. K. Kampouris.; J. Iniesta.; G. C. Smith.; J. A. Bonacin.; C. E. Banks. Graphite Screen-Printed Electrodes Applied for the Accurate and Reagentless Sensin of pH. *Anal. Chem*. **2015**, 87, 11666-11672.
(159) C. Parat.; S. Betelu.; L. Authier.; M. Potin-Gautier. Determination of labile trace metals with screen-printed electrode modified by a crown-ether based membrane. *Analytica Chimica Acta*, **2006**, 530-574, 14-19.
(160) S. J. Rowley-Neale.; G. C. Smith.; G. E. Banks. Mass-producible 2D-MoS_2-Impregnated Screen-Printed Electrodes that Demonstrate Efficient Electrocatalysis toward the Oxygen Redudtion Reaction. *Acs Appl. Mater. Interfaces*, **2017**, 9, 22539-22548.
(161) M. I. Prodromidis.; P. G. Veltsistas.; M. I. Karayanis. Electrochemical Study of Chemically Modified and Screen-Printed Graphite Electrodes with $[Sb^{V}O(CHL)_2]$Hex. Applecation for the Selective Determination of Sulfide. *Anal. Chem*. **2000**, 72, 3995-4002.
(162) D. Li.; W. Y. Lai.; Y. Z. Zhang.; W. Huang. *Adv. Mater*. **2018**, 30, 1704738.

(163) E. N. Zare.; P. Makvandi.; B. Ashtari.; F. Rossi.; A. Motahari.; G. Perale. Progress in conductive polyaniline-based nanocomposites for biomedical applications: a review. *J. Med. Chem*. **2020**, 63, 1-22.
(164) D. Gan.; L. Han.; M. Wang.; W. Xing.; T. Xu.; H. Zhang.; K. Wang.; L. Fang.; X. Lu. Conductive and tough hydrogels based on biopolymer molecular templates for controlling in situ formation of polypyrrole nanorods. *ACS Appl. Mater. Interfaces*. **2018**, 10, 36218-36228.
(165) L. Lindell.; A. Burequel.; F. L. E. Jakobsson.; V. Lemaur.; M. Berggren.; R. Lazzaroni.; J. Cornil.; W. R. Salaneck.; X. Crispin. Transparent, plastic, low-work-function poly(3,4-ethylenedioxytiophene) electrodes. *Chem. Mater*. **2006**, 18, 4246-4252.
(166) Y. Koizumi.; M. Ohira.; T. Wantanabe.; H. Nishiyama.; I. Tomita.; S. Inagi. Synthesis of poly(3,4-ethylenedioxythiophene)-platinum and poly(3,4-ethylenedioxythiophene)-poly(styrenesulfonate) hybrid fibers by alternating current bipolar electropolymerization. *Langmuir*. **2018**, 34, 7598-7603.
(167) Y. Fu.; C. Chen.; C. Qiu.; X. Ma. Vinyl ethylene carbonate as an additive to ionic liquid electrolyte for lithium ion batteries. *J. Appl. Electrochem*, **2009**, 39, 2597-2603.
(168) R. Gonçalves.; J. Oliveira.; M. P. Silva.; P. Costa.; L. Hilliou.; M. M. Silva.; C. M. Costa.; S. Lanceros-Méndez. Poly(styrene-butene/ethylene-styrene): A New Polymer Bindr for High-Performance Printable Lithium-Ion Battery Electrodes. *Acs Appl. Energy Mater*. **2018**, 1, 3331-3341.
(169) M. Hatala.; P. Gemeiner.; M. Hvojnik.; M. Mikula. The effect of the ink composition on the performance of carbon-based conductive screen printing inks. *Journal of materials science: Materials in electronics*. **2019**, 30, 1034-1044.
(170) L. A. Salam.; R. D. Matthews.; H. Robertson. Pyrolysis of polyvinyl butyral (PVB) binder in thermoelectric green tapes. *Journal of the european ceramic society*. **2000**, 20, 1375-1383.
(171) D. Marani.; C. Gadea.; J. Hjelm.; P. Hjalmarsson.; M. Wande.; R. Kiebach. Influence of hydroxyl content of binders on rheological properties of cerium-gadolimium oxide (CGO) screen printing inks. *Jounal of the european ceramic society*. **2015**, 35, 1495-1504.
(172) M. Yang.; S. Xie.; Q. Li.; Y. Wang.; X. Chang.; L. Shan.; L. Sun.; X. Huang.; C. Gao. Effects of polyvinylpyrrolidone both as a binder and pore-former on the release of sparingly water-soluble topiramate from ethylcellulose coated pellets. *International journal of pharmaceutics.* **2014**, 465, 187-196.
(173) M. Chen.; P. Mao.; Y. Qin.; J. Wang.; b. Xie.; X. Wang.; D. Han.; G-H. Wang.; F. Song.; M. Han.; J-M. Liu.; G. Wang. Response Characteristics of Hydrogen Sensors Based on

PMMA-Mambrane-Coated Palladium Nanoparticle films. *Acs Appl. Mater. Interfaces*. **2017**, 9, 27193-27201.

(174) K-R. Wee.; M. K. Brennaman.; L. Alibabaei.; B. H. Farnum.; B. Sherman.; A. M. Lapides.; T. J.Meyer. Stabilization of Ruthenium(II) Polypyridyl Chromophores on nanoparticle Metal-Oxide Electrodes in Water by Hydrophobic PMMA Overlayers. *J. Am. Chem. Soc.* **2014**, 136, 13514-13517.

(175) B. Zhang.; G. Xia.; d. Sun.; F. Fang.; X. Yu. Magnesium Hydride Nanoparticles Self-Assembled on Graphena as anode Material High-Perfarmance Lithium-Ion Batteries. *ACS Nano*. **2018**, 12, 3816-3824.

(176) S. Aghyarian.; E. Bentley.; T.N. Hoang.; I. M. Gindri.; V. Kosmopoulos.; H. K. W. Kim.; D. C. Rodrigues. In Vitro and in Vivo Characterization of Premixed PMMA-CaP Composite Bone Cements. *ACS Biomater. Sci. Eng*. **2017**, 3, 2267-2277.

(177) A. K. Riau.; D. Mondal.; G. H. F. Yam.; M. Setiawan.; B. Liedberg.; S. S. Venkatraman.; J. S. Mehta. Surface Modification of PMMA to Improve Adhesion to Corneal Substitutes in a Synthetic Core-Skirt Keratoprosthesis. *Acs Appl. Mater. Interfaces.* **2015**, 7, 21690-21702.

(178) K. Liu.; H. Sun.; S. dong.; C. Lu.; Y. Li.; J. Cheng.; J. Zhang.; X. Wang.; X. Chen.; G. Cui. A rational desing of high-performance sandwich-structured quasisolid state Li-O2 battery with redox mediator. *Adv. Mater. Interfaces*. **2017**, 4, 1700693.

(179) K. J. Chae.; M. Choi.; F. F. Ajayi.; W. Park.; I. S. Chang.; I. S. Kim. Mass transport through a proton exchange membrane (Nafion) in microbial fuel cells. *Energy & Fuels*. **2008**, 22, 169-176.

(180) N. Yuca.; H. Zhao.; X. Song.; M. F. Dogdu.; W. Yuan.; Y. Fu.; V. S. Battaglia.; X. Xiao.; G. Liu. A Systematic Investigation of Polymer Binder Flexibility on The Electrode Performance of Lithium-Ion Batteries. *ACS Appl. Mater. Interfaces*. **2014**, 6, 17111-17118.

(181) J. Oertel.; S. Kishii.; D. Kilian.; K. Hamada.; Y. Morishita.; T. Kurihara.; T. Ito. Acrylic TPE approaching automotive. *TPE Magazine*, **2020**, 2, 30-35.

(182) J. W. Phair. Rheological analysis of concentrated zirconia pastes with ethyl cellulose for screen printing SOFC electrolyte films. *J. Am. Ceram. Soc.* **2008**, 91, 2130-2137.

(183) A. Al-Halhouli.; H. Qitouqa.; A. Alashqur.; J. Abu-Khalaf. Inkjet printing for the fabrication of flexible/stretchable wearable electronic devices and sensors. *Sensor Review*. **2018**, 38, 438-452.

(184) G. C. Jensen.; C. E. Krause.; G. A. Sotzing.; J. F. Rusling. Inkjet-printed gold nanoparticle electrochemical arrays on plastic. Application to immudodetection of a cancer biomarker protien. *Phys. Chem. Chem. Phys*. **2011**, 13, 4888-4894.

(185) S. K. Eshkalak.; A. Chinnappan.; W.A.D.M. Jayathilaka.; M. Khatibzadeh.; E. Kowsari.; S. Ramakrishna. A review on inkjet printing of CNT composites for smart applications. *Applied materials today*. **2017**, 9, 372-386.

(186) K. Fu.; Y. Wang.; C. Yan.; Y. Yao.; Y. Chen.; J. Dai.; S. Lacey.; Y. Wang.; J Wan.; T. Li.; Z. Wang.; Y. Xu.; L. Hu. Graphene oxide-based electrode inks for 3D-printed lithium-ion batteries. *Adv. Mater*. **2016**, 28, 2587-2594.

(187) X. Su.; X. Li.; C. Y. A. Ong.; T. S. Herng.; Y. Wang.; E. Peng.; J. Ding. Metallization of 3D printed polymers and their application as a fully functional water-splitting system. *Adv. Sci*. **2019**, 6, 1801670.

(188) M. Falahati.; P. Ahmadvand.; S. Safaee.; Y.-C. Chang.; Z. Lyu.; R. Chen.; L. Li.; Y. Lin. Smart polymers and nanocomposites for 3D and 4D printing. *Materials today*. **2020**, nd, nd.

(189) A. M. Joseph.; B. Nagendra.; E. B. Gowd.; K. P. Surendran. Screen-printable electronic ink ou ultrathin boron nitride nanosheets. *ACS Omega*. **2016**, 1, 1220-1228.

(190) D. A. Pardo.; G. E. Jabbour.; N. Peyghambarian. Application of screen printing in the fabrication of organic light-emetting devices. *Adv. Mater*. **2000**, 12, 1249-1252.

(191) M. Magliulo.; M. Y. Mulla.; M. Singh.; E. Macchia.; A. Tiwari.; L. Torsi.; K. Manoli. Printable and flexible electronics: from TFTs to bioelectronic devices. *J. Mater. Chem. C*. **2015**, 3, 12347-12363.

(192) H. Menon.; R. Aiswarya.; K. P. Surendran. Screen printable MWCNT inks for printed electronics. *RSC Adv*. **2017**, 7 44076-44081.

(193) O. Bagel.; B. Limoges.; B. Schöllhorn.; C. Degrand. Subfemtomolar determination of alkaline phosphatase at a disposable screen-printed electrode modified with a perfluorosulfonated ionomer films. *Anal. Chem*. **1997**, 69, 4688-4694.

(194) L. Authier.; B. Schöllhorn.; B. Limoges. Detection of cationic phenolic derivatives at a surfactant-doped screen-printed electrode for the sensitive indirect determination of alkaline phosphatase. *Electroanalysis*. **1998**, 10, 1255-1259.

(195) L. Authier.; B. Schöllhorn.; J. Moiroux.; B. Limoges. Ion-exchange voltammetry at a surfactant-doped electrode: model of mass transfer kinetics to an anionic surface-charged electrode and its application for the sensitive determination of alkaline phosphatase. *Journal of Electroanalytical Chemistry*. **2000**, 488, 48-58.

(196) S. Lawes.; A. Riese.; Q. Sun.; N. Cheng.; X. Sun. Printing nanostructured carbon for energy storage and conversion applications. *Carbon*. **2015**, 92, 150-176.

(197) H. Kim.; R. C.Y. Auyeung.; A. Piqué. Leser-printed thick-film electrodes for solid-state rechargeable Li-ion microbatteries. *Journal of power sorces*. **2007**, 165, 413-419.

(198) A. Gören.; J. Mendes.; H.M. Rodrigues.; R.E. Sousa.; J. Oliveira.; L. Hilliou.; C.M. Costa.; M.M. Silva.; S. Lanceros-Méndez. High performance screen-printed electrodes prepared by a green solvent approach for lithium-ion batteries. *Journal of power sources*. **2016**, 334, 65-77.

(199) X. chen.; B. Jia.; Y. Zhang.; M. Gu. Exeeding the limit of plasmonic light trapping in textured screen-printed solar cells using Al nanoparticles and wrinkle-like graphene sheets. *Light: science & applications.* **2013**, 2, e92.

(200) D. H. Wang.; J. K. Kim.; J. H. Seo.; I. Park.; B. H. Hong.; J. H. Park.; a. J. Heeger. Transferable graphene oxide by stamping nanotechnology: electron-transport layer for efficient Bulk-heterojunction solar cells. *Angew Chem Int Ed*. **2013**, 52, 2874-2880.

(201) S. E. Shaheen.; R. Radspinner.; N. Peyghambarian.; G. E. Jabbour. Fabrication of bulk heterojunction plastic solar celles by screen printing. *Applied physics letters*. **2001**, 79, 2996-2998.

(202) F. C. Kerbs.; M. Jørgensen.; K. Norrman.; O. Hagemann.; J. Alstrup.; T. D. Nielsen.; J. Fyenbo.; K. Larsen.; J. Kristensen. A complete process for production of flexible large area polymer solar cells entirely using screen printing—first public demonstration. *Solar energy material & solar celles*. **2009**, 93, 422-441.

(203) T. Kim.; Y. W. Kim.; H. S. Lee.; H. Kim.; W. S. Yang.; K. S. Suh. Uniformly interconnected silver-nanowire networks for transparent film heaters. *Adv. Funct. Mater*. **2013**, 23, 1250-1255.

(204) Q. H.; W. Shen.; X. Fang.; G. Chen.; J. Guo.; W. Xu.; R. Tan.; W. Song. Highly flexible and transparent film heaters based on polyimide films embedded with silver nanowires. *RSC. Adv.* **2015**, 5, 45836-45842.

(205) X. He.; R. He.; Q. Lan.; W. Wu.; F. Duan.; J. Xiao.; M. Zhang.; Q. Zeng.; J. Wu.; J. Liu. Screen-printed fabrication of PEDOT:PSS/silver nanowire composite films for transparent heaters. *Materials*. **2017**, 10, 220.

(206) J, H. We.; S. J. Kim.; B. J. Cho. Hybrid composite of screen-printed inorganic thermoelectric film and organic conducting polymer for flexible thermoelectric power generator. *Energy*. **2014**, 73, 506-512.

(207) P.-S. Chang.; C.-N. Liao. Screen-printed flexible thermoelectric generator with directional heat collection design. *Journal of alloys and compounds*. **2020**, 836, 155471.

(208) S. J. Rowley-Neale.; G. C. Smith.; C. E. Banks. Mass-producible 2D-MoS_2-impregnated screen-printed electrodes that demonstrate efficient electrocatalysis toward the oxygen reduction reaction. *ACS Appl. Mater. Interfaces*. **2017**, 9, 22539-22548.

(209) M. Chikae.; K. Idegami.; K. Kerman.; N. Nagatani.; M. Ishikawa.; Y. Takamura.; E. Tamiya. Direct fabrication of catalytic metal nanoparticles onto surface of a screen-printed carbon electrode. *Electrochemistry communications*. **2006**, 8, 1375-1380.

CHAPTER 2

Hierarchically organized block copolymer films through "breath figure" templating and microwave induced self-assembly.

Context:

With the aim to use the commercial triblock copolymer poly(methyl methacrylate)-*block*-poly(*n*-butylacrylate)-*block*-poly(methyl methacrylate) (PMMA-*b*-P*n*BuA-*b*-PMMA) as binder for the production of screen-printed electrodes (see chapter 3), we first study its self-assembly behaviour in thin ans thick films. The self-assembly of block copolymers (BCPs) has been widely studied due to their unique properties and large range of application such as information storage, nanoporous membranes or organic optoelectronics. Moreover, hierarchically organized polymer films can produced with different level of structuration. The breath figure (BF) is an alternative way to prepare highly ordered microporous honeycomb films due to it is an efficient, inexpensive, and versatile method.[1-2]

Hierarchically organized polymer films are produced in this chapter with a high level of order from the combination of block copolymer nanophase segregation, "breath figure" methodology and microwave irradiation. A block copolymer based on poly(methyl methacrylate) and poly(*n*-butylacrylate) featuring cylindrical nanopatterns is involved in the "breath figure" process to create a microporous honeycomb structure. These films are submitted to microwave annealing to enhance the degree of ordering of the nano-segregation without the destruction of the honeycomb microstructure, which is not possible by classical thermal or solvent annealing. Ellipsometry, optical and atomic force microscopy are used to study three key parameters; the substrate nature, the film thickness and the microwave irradiation power. Silicon wafer is the substrate of choice to efficiently act as the heating transfer element and 60 seconds at 10 watts are enough to nicely order 1 μm thick copolymer films. These conditions are eventually applied on hierarchically organized polymer film to obtain a hexagonal array of 100 nm deep holes within a matrix of perpendicularly aligned nano-cylinder.

This work has been performed with the collaboration of other researchers, thanks to Nicolas Benoot, Pierre Marcasuzaa, Laurence Pessoni and Stéphanie Reynaud and published in *Soft Matter* journal in 2018.

Reference:

(1) Z. Li.; X. Ma.; Q. Kong.; D. Zang.; X. Guan.; X. Ren. Static and dynamic hydrophobic properties of honeycomb structured films via breath figure method. *J. Phys. Chem. C*. **2016**, 120, 18659-18664.

(2) A. Zhang.; C. Du.; H. Bai.; Y. Wang.; J. Wang.; L. Li. Formation of breath figure arrays in methanol vapor assisted by surface active agents. *ACS Appl. Mater. Interfaces*. **2014**, 6, 8921-8927.

Table of contents

1. Introduction 75

2. Results & discussion 77

2.1. Hierarchical polymer film 77

2.2. Microwave induced self-assembly of triblock copolymers continuous film 80

2.3. Microwave induced self-assembly of Hierarchical polymer film 82

3. Conclusions 84

4. Experimental Section 85

4.1.Thin films preparation 85

4.2. Honeycomb film preparation 85

4.3. Microwave annealing 85

4.4. Ellipsometry 85

4.5. Surface analysis 86

4.6.Differential Scanning Calorimetry 86

4.7. Size Exclusion Chromatography 86

References 87

Supporting Information 99

This chapter was the object of a publication DOI:10.1039/c8sm00137e

Hierarchically organized block copolymer films through "breath figure" templating and microwave induced self-assembly.

1. Introduction

Hierarchical assembly of materials is one of the most promising yet challenging aspects of nanoscience.[1, 2] Nature has provided many elegant examples of hierarchical designs and has shown the extraordinary properties resulting from this multi-scale structures.[3, 4] Researchers are developing new methods and strategies to obtain materials with outstanding properties for various applications such as Li-ion batteries[5], membranes or high-performance liquid chromatography[6]. Polymers are promising candidates as they can exhibit structural hierarchy from the nano to the micrometer scale.[6, 7]

At the micrometer scale, the "breath figure" (BF) method, reported by François and co-workers, has been widely used to prepare porous polymer films with hexagonal patterns.[8] Compared to other techniques, the BF method is a fast (less than one minute), simple (one-step) and template-free technique.[9-12] This bottom-up method relies on the fast drying of a polymer solution under a humid atmosphere. The evaporation induces a surface cooling that triggers the condensation of water droplets into close-packed hexagonal arrays due to the Benard-Marangoni convections. Upon complete evaporation of the solvent/water mixture, a porous honeycomb (HC) structure is obtained that is reminiscent of the water droplets template. Different approaches have been developed to prepare sub-micrometer porous films[13] where the pore size of the honeycomb films can be controlled by the casting conditions, *i.e.* humidity and air flow, and also by the chemical structure, the molar mass and the concentration of the polymer.[9, 12] At the nanometer scale, patterning of block-copolymers (BCP) through phase separation process is now a key process in the development of new technologies from nanolithography to the achievement of functional surfaces for photovoltaic devices for example.[14, 15] The International Technology Roadmap for Semiconductors describes BCP-based patterning technology as "a viable and competitive patterning option".[16] The phase separation phenomenon is led by the product χN where χ is the Flory-Huggins interaction parameter and N is the total degree of polymerization. This phase separation allows the

copolymer to self-assemble in different organized nanopatterns, in order to reduce the energy of the system.[17] Appropriate BCPs may be responsive to temperature and solvent conditions[18], to shear, electric, and magnetic fields, and finally to substrate topography and surface energy.[19] To achieve long range order in the self-assembly of BCPs thin films, several hours or days of thermal annealing, solvent annealing or combination of both are usually needed.[20]

Hierarchically-structured polymer films have already been described by Rodriguez-Hernandez and co-workers.[21] They used a blend of a polymer matrix and a triblock copolymer additive. The interplay of the breath figure formation and self-assembly of the triblock copolymer, during the spin-coating, allowed the preparation of polymer surfaces having micrometer-sized cavities decorated with block copolymers nano-organisation. Our team have also previously exploited strong χN polymer systems to generate nanopatterns in between the pores of the honeycombs.[22-26] However, the issue of these hierarchical structures lies in the low order of the nanophase segregation. Indeed, there is a competition between the fast "breath figure" process (less than one minute at room temperature) and the time needed to reach the thermodynamic equilibrium of block copolymer films. A thermal or solvent vapour annealing could be further applied to the polymer but this process would irreversibly damage the HC structure. Indeed, Ghannam *et al.* demonstrated the impact of the polymer glass transition temperature *Tg* on the HC film formation. [27] For a ''soft'' polymer, like poly(*n*-butylacrylate) (*Tg* ≈ -55°C), the « Breath figure » mechanism appeared initially with formation of microsized water droplets at the surface of the film, but at the end of the evaporation process, the water-droplet template disappeared and a homogenous and continuous film without pores was obtained. The authors claimed the creep of the elastomer polymer inside the pores. This result enhanced the influence of thermal properties of the polymer, which must be formed by a block with a *Tg* above room temperature, at least. Therefore, the development and the optimization of other strategies are needed to improve the order in these hierarchical materials, but keeping the temperature always lower than the *Tg* value of the polymer or using short time of annealing to minimize the polymer flow inside pores.

Microwave annealing has recently emerged as an efficient way to obtain long range ordered nanostructures patterns. Block copolymer such as polystyrene-*block*-poly(methylmethacrylate), polystyrene-*block*-poly(dimethylsiloxane) or polystyrene-*block*-poly(-2-vinylpyridine) have been self-assembled under microwave irradiation within minutes or even seconds.[28, 29] The mechanism of the microwave annealing process remains under discussion. Some works have reported well-ordered patterns at temperatures below the polymer glass transition temperature; the assembly was then attributed to the electromagnetic field

effect on polar polymer chains.[30] Other studies have shown that the organisation of BCPs is improved by microwave-induced thermal annealing. The microwaves cause a strong heating of the substrate which in turn provokes the melting/reorganization of the polymer film.[31]

In this article, we report the preparation of hierarchical polymer films and our investigations to increase the nanostructure order, *via* microwave annealing, while keeping the microstructure intact. For this purpose a triblock copolymer poly(methyl methacrylate)-*block*-poly(*n*-butylacrylate)-*block*-poly(methyl methacrylate) (PMMA-*b*-P*n*BuA-*b*-PMMA) featuring well-defined cylindrical nanopatterns, given its high molar mass, low dispersity and the difference between blocks in term of glass transition temperature, adhesion and toughness, was involved in the BF templating process and the films were then submitted to microwave irradiation.

2. Results & discussion

2.1. Hierarchical polymer film

PMMA-*b*-P*n*BuA-*b*-PMMA (with $f_{v(PMMA)}$ = 20 %, M_n = 114 kg/mol and $Đ$ = 1,07), named MBM20 in this report, was casted onto glass substrates from dichloromethane solution in the "breath figure" conditions. The water droplet condensation/evaporation led to a hexagonal arrangement of 3 µm pores in the copolymer matrix (see supporting information, **Figure S1**). Within this microporous framework, the BCP generated nanopatterns, leading to the desired hierarchically structured material. Before any annealing procedures were performed, atomic force microscopy was used to identify the nanostructures **(Figure 1)**. On the thickest part of the matrix (the "pillar zone" in **Figure 1**), the nano-organisation appeared to be a mixture of *in plane* and *out of plane* cylinders whereas on the thinnest part of the matrix (close to the pore, the "side zone" in **Figure 1**), cylinders appeared ordered and perpendicular to the surface. In **Figure 1b** the border between the pillar and the side zones is marked with a white dashed line to guide the eyes (see supporting information for detailed images of the pillar and side zones, **Figure S2**).

The mechanism of HC formation through the breath figure methodology is a non-equilibrium process. During the solvent evaporation, the surface nano-organization is influenced by the air/polymer and water/polymer interface tensions, but also by the confinement forces associated to the porous honeycomb architecture.

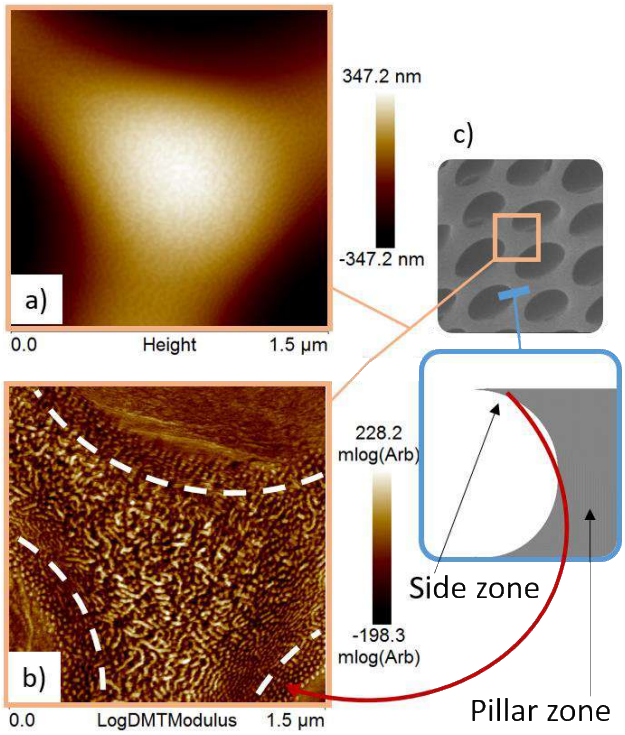

Figure 1. a) and b) AFM images in peak force mode c) scheme of a honeycomb organization d) scheme of the cross-section of the honeycomb illustrating the difference in thickness through the pores (see ref 24 for TEM cross section of Honeycomb films).

In order to confirm the role of the confinement forces in the organisation process, continuous BCPs films of different thickness, 26 and 220 nm, were produced by spin-coating to mimic respectively the side and pillar zones of the HC films. AFM images of the 26 nm continuous polymer films (without annealing) showed the start of a long range organisation with cylinders standing perpendicular to the substrate **(Figure 2a)**. On the contrary thicker continuous films of 220 nm **(Figure 2b)** led, without annealing, to nanopatterns similar to those observed on honeycomb pillar (the thickest part). The long-range organisation was disturbed and a mixture of standing and lying cylinders (perpendicular and parallel to the substrate) was identified.

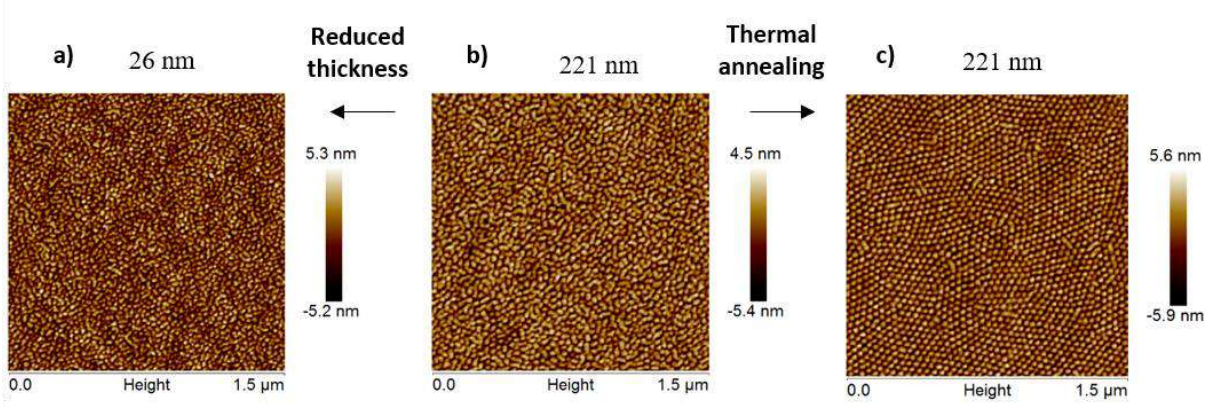

Figure 2. AFM images in peak force mode of a film made from a 0.35 wt% MBM20 solution in DCM for a) and 2 wt% for b) and c), spin-coated on silicon wafer at 3000 rpm. In c) the surface was thermally annealed at 160 °C for 1 hour. The film thickness is mentioned above the images.

This last film was submitted to a thermal annealing of 160°C for 1 hour to obtain well-organised *out of plane* nano-cylinders **(Figure 2c)**. Importantly, glass transition temperatures *Tg* of -43 °C and 91 °C were determined by Differential Scanning Calorimetry (DSC) for the P*n*BuA and PMMA blocks, respectively.

To go further and following the objective to increase the nano-phase segregation order without destroying microporosity, the same procedure (160°C for 1 hour) was applied to HC films. During the thermal annealing, PMMA is exposed above its *Tg* and as a consequence the whole film melted; the microstruture disappeared and was replaced by a continuous film, as already described by our group when *Tg* value is reached or below than working temperature **(Figure S3)**. [27]

In this context, short annealing time in a microwave oven appeared as an attractive strategy to achieve our goal: getting a long range ordered nanosegregation of BCP while keeping the microporosity induced by the BF templating. Indeed, it has been reported that the microwave treatment may have a beneficial effect on the structure within 2 minutes (min) or less. However, since the annealing conditions strongly depend on the copolymer nature, they have first been carefully studied on continuous films.

2.2. Microwave induced self-assembly of triblock copolymers continuous film

In a first approach, the impact of the microwave irradiation upon the cylinders organization was evaluated on continuous thin films spin-coated from a toluene solution. Polymer solutions were first spin-coated onto glass substrates in order to obtain 200 nm thick polymer layer. Several microwave irradiation powers were applied to the samples for one minute, in a fixed mode, meaning that the microwave irradiation power is kept as set during 1 min. The AFM images of the treated samples are presented in **Figure 3a**. An irradiation power of 20 W, didn't lead to any improvement of the cylinders organization. Cylinders both parallel and perpendicular to the substrate were simultaneously observed. Increasing the microwave irradiation power up to 50 W and 100 W, *in* and *out of plane* cylinders were still obtained. However, at 200 W, a reorganization started to appear with cylinders vertically aligned. Keeping a set power at 200 W, the irradiation time was increased up to 30 min and as a consequence, a long-range order of hexagonally arranged cylinders was obtained **(Figure S4)**. Since such a structure is also reached in one hour by thermal annealing (160°C), the time saved with microwave is not remarkable.

Buriak and co-workers have demonstrated that the substrate have a huge influence on the result of microwave treatment, with the use of *in-situ* temperature monitoring thanks to a fibre optic temperature probe in direct contact with the sample. [31] More specifically the microwave absorption of the substrate is related to its resistance which appears to be the key point for optimizing the annealing step. Following their findings, glass substrates were replaced in our study by high resistance silicon ones (1-30 Ohms, type *p*, Boron doped) onto which continuous polymer film were spin-coated from the polymer/toluene solution described above to obtain 200 nm thick films. Those films were annealed under microwave irradiations at several irradiation powers, during one minute **(Figure 3b)**. Organized patterns appeared under a microwave irradiation power of 10 W. At a lower irradiation power (1 W or 5 W), no regular patterns were obtained and the surface remained unchanged. For stronger powers, at 50 W, the surface aspect changed drastically, the polymer layers seemed to be deteriorated or even burnt. Ellipsometric measurements of the samples irradiated at 50 W, showed polymer films thickness of 24.2 ± 0.1 nm, *i.e.* 10 % only of their initial value (200 nm). The thermogravimetric analysis of the copolymer revealed that degradation of the polymer started at 250°C and at 400°C the sample was completely wiped out (see supporting information **Figure S5**). Hence the silicon

wafer heated *via* microwaves at 50 W during 60 seconds must have reached temperatures above 250°C to lead to the destruction of the polymer film.

Therefore there is a huge influence of the substrate on the performance of microwave irradiation. The improvement of the cylinders organization seems to be associated to the polymer motion induced by the heat emitted from the substrate. No intrinsic effect of the microwave field on the macromolecules was identified. In a very recent report Howse and coworkers reported that a polystyrene-*block*-polyethylene was a really poor microwave absorber in itself.[32] They observed variation in the diblock morphology, by *in-situ* small angle X-ray scattering, only when a small molecule microwave interactive was added in the polymer matrix.

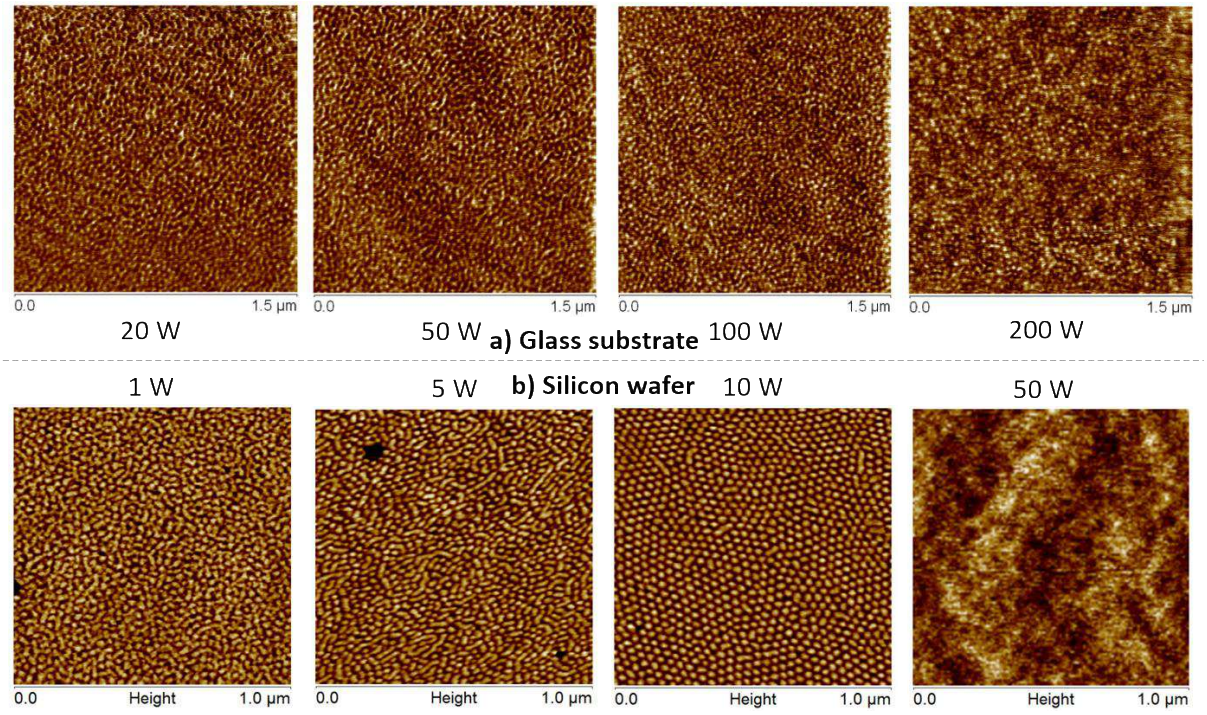

Figure 3. AFM images in peak force mode of MBM20 films of 200 nm, spin-coated at 2000 rpm from toluene solution on glass (a, above dashed line)) and silicon (b, below dashed line) substrate. Each samples have been annealed 60 seconds in a microwave oven at different powers indicated on the figure.

One of the drawback of the microwave process is the temperature measurement. Even though microwave oven are commonly equipped with an IR and/or an optic fiber probe(s), this parameter should always be carefully examined for understanding and optimization. The evolution of the measured temperature inside the vial throughout the microwave annealing process, at several power irradiation is presented in Supporting Information **(Figure S6)**. After

1 min at 200 W the temperature reached 50 °C and 110 °C respectively for glass and silicon substrates. These values were detected *via* an infrared probe that measures the temperature at the bottom of the glass vial in which the substrates were inserted. These temperature values obviously are not representatives of the ones that could be measured at the substrates surface, given in particular the non-contact between the substrate and the container, and the weak thermal conductivity of the glass container. Nevertheless, these values may be compared and illustrate the huge difference in the heat emitted by the substrates, as thoroughly studied in the work of Buriak and coworkers.[31] Without more information about the evolution of the real temperature of the system, only the irradiation power could be related with the nanopatterns evolution. As a conclusion of this substrate study, silicon wafers were selected as the substrate of choice for the following experiments.

The influence of the layers thickness was studied; 1500, 200, 150 and 50 nm polymer films have been casted onto silicon wafers. A microwave treatment of 1 min at 5 W was enough to reach a high order of standing cylinders from the 2 thinnest layers (150 and 50 nm, **Figure S7**). On the contrary for the 2 thickest films (1500 and 200 nm), an irradiation of 10W during 1 min was needed to reorganize the cylinders perpendicularly to the surface (see **Figure 3** for the film with thickness 200 nm and **Figure S8** and **S9** for the film with thickness 1500 nm). The influence of the thickness is again in agreement with the hypothesis that the substrate acts as the heating element. It has to be pointed out that the thickest films 1.5 μm were drop casted from DCM solution at the same concentration (5 g/L) that the one used in the "breath figure" methodology to prepare honeycomb films. These last experiments confirmed that a 10 W/ 1 min microwave protocol was enough to treat the amount of matter needed to elaborate honeycomb films.

2.3. Microwave induced self-assembly of Hierarchical polymer film

Honeycomb films were then produced onto silicon substrate in order to study the effect of microwave annealing on the nano-segregation and the micro-organisation of hierarchical polymer films. Drop-cast film without annealing were first analysed *via* AFM, and height images at 1 and 10 μm scale are reported in **Figure 4a**. The 10 μm images show a regular microporosity with pore diameter of 3 μm and depth of 830 nm; these structures have already been observed on glass substrates **(Figure 1)**. When an annealing of 5 W during 1 min was applied, neither the microporosity nor the nano-segregation were affected (image in supporting

information **Figure S10**). Furthermore, the surface nano-organisation seemed unaltered using a microwave irradiation power of 5 W for 10 min.

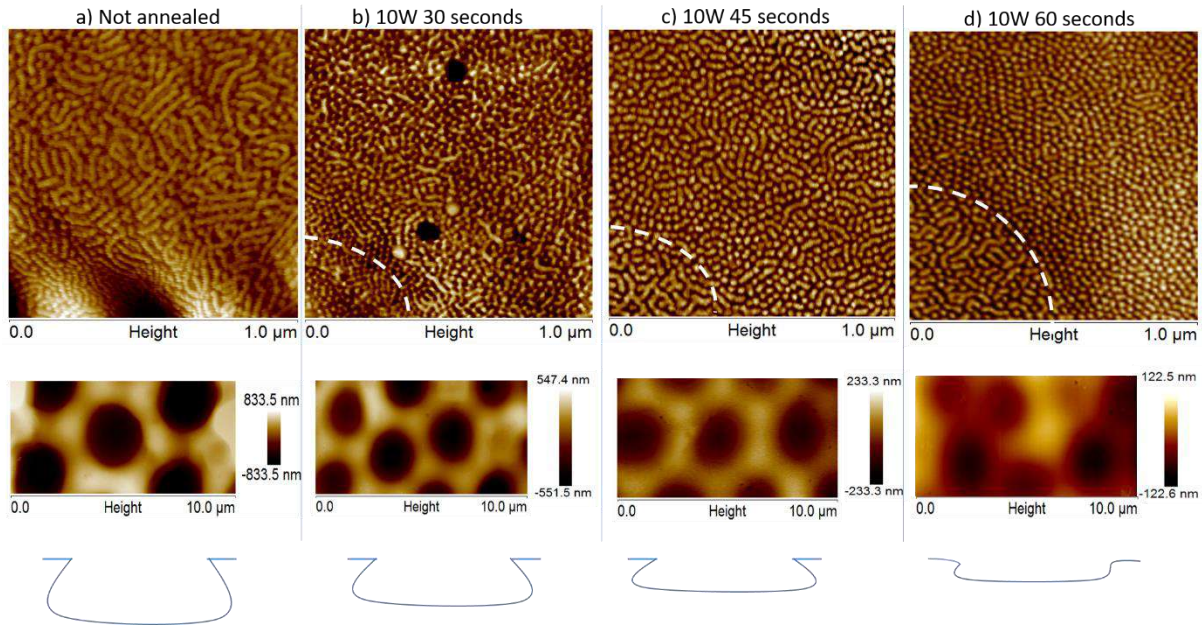

Figure 4. AFM images in peak force mode of honeycomb structures made in static method at 60% of relative humidity, from a 5 g/L solution of MBM20 in dichloromethane. These films have been annealed under microwave irradiation at 10W during different times. The blue curves below the images are schematics of the pores geometry after the microwave treatments.

Since the heating element is the silicon substrate due to a higher dielectric constant (ε = 11.7 @ 300K) than the MMA and BuA (ε = 2.6 and 2.4 @ 300K, respectively), [33] it was reasonable to assume that the microwave-transparent HC film were too thick to melt the whole volume and change the surface nano-organisation. This is in agreement with what has been reported above on continuous films with the influence of thickness. Therefore a 10 W treatment was applied to HC films during 1 min. **Figure 4d** shows height image of 1 µm where vertically aligned *out of plane* cylinders are clearly observed between the pores. On the 10 µm image the hexagonal porosity can still be observed but the depth of the pores was decreased to 120 nm. At this depth a nano-segregation could also be observed inside the pores with *in plane* cylinders. A longer microwave treatment up to 2 min at 10 W resulted in a continuous film without any pores and all nano-cylinders are oriented perpendicularly **(Figure S11)**. To further study the microwave-assisted annealing procedure, HC films were treated during different times: 30 **(Figure 4b)** and 45 seconds **(Figure 4c)** under 10 W. **Figure 4b** and c showed the

resulted AFM images at 1 and 10 μm. After 30 seconds, micropores with a depth of 550 nm are observed and the surface is composed of an equivalent mixture of standing and lying cylinders. After 45 seconds the percentage of *out of plane* structures clearly increased and the pore depth decreased to 230 nm. These variations over time illustrate the effect of the substrates annealing *via* the microwave treatment. The polymer films melt from the base in contact with the substrate and matrix cylinders straightened up. In parallel, some polymer chains are flowing inside the micro-pores and, at the end of the annealing, are frozen in a nano-structure clearly identified as *in plane* cylinders, inside the holes. Both temperature and time parameters affect the HC films. As reported before,[27] if the main parameter is indeed the temperature which has to be maintained below the *Tg* value of the polymer or one block of the BCP, nevertheless, for non-thermal conductive polymer, the temperature is directly correlated to the exposition time: longer time, higher temperature.

So here, the use of microwave permits to tune the annealing temperature, finely, by adjusting the power but also the time as an undirected trigger of the inner temperature of the polymer HC film. Indeed, as the instant heating is high and short, we can finely adjust the inner temperature of the film in order to avoid the total flow of the polymer inside pores.

3. Conclusions

Microwave annealing is an efficient technique to get ordered nanopatterns of BCP. It allows obtaining, within a min, nanostructures that are not available in the same time with conventional heating. In this study we report the elaboration of a hierarchically ordered polymer films *via* microwave irradiation. First the substrate was identified as the heating element involved in the microwave annealing process. Since the copolymer doesn't absorb itself the microwaves, silicon substrates were used as heating platforms. Key parameters such as the film thickness and the irradiation power were studied on continuous copolymer films and tuned to reach a high order of nano-cylinders standing perpendicular to the substrate. Finally microporous honeycomb films made *via* the "breath figure" templating methodology were submitted to microwave treatment. This annealing procedure successfully ordered the nano-cylinders while maintaining the micro-structure in 60 seconds. We believe that this treatment could be performed with many polymer systems to get hierarchical materials that are not easy to reach *via* classical solvent or thermal annealing but more importantly that could lead to novel properties and applications. For example it could be applied on trigger-sensitive amphiphilic BCP films to control surface wettability and (bio)adhesion.[34, 35, 36]

4. Experimental Section

4.1. Thin films preparation

Solutions of MBM20, PMMA-*b*-PnBuA-*b*-PMMA with $f^{v}_{(PMMA)} = 0.2$ provided from Kuraray Co., Ltd (LA2330), were prepared in toluene and dichloromethane (DCM). Acetone washed glass substrates (VWR microscope slides & Heathrow Scientific LLC – 25x75x1mm) and silicon wafers (TED PELLA – prod. n°16010) were spin-coated with BCPs solutions at different rotation speeds, following the desired thickness.[37] For DCM solution, dynamic dispenses were realized while the substrate was rotating in order to prevent solvent evaporation effects on the surface homogeneity. Toluene solutions of 3 w% in polymer were used to obtained thickness of 210.23 ± 0.07 nm.

4.2. Honeycomb film preparation

100 µL of MBM20 solutions in dichloromethane (DCM) were drop casted on a glass or silicon surface. It turned out that a concentration of 5 g/L led to the best organized structures. (Figure S1) This drop casting was performed following the static method described by Li *et al.* [38] to prepare honeycomb structures, at a controlled relative humidity of 60 % RH.

4.3. Microwave annealing

A CEM microwave was used on fixed mode at several set powers for a controlled time. The temperature was followed by the in-situ infrared probe of the microwave oven. Microwave heating films were cast on substrate with a surface of 0,7 x 0,7 cm². The set-up used to submit the wafers to the microwave irradiation is described in supporting information (Figure S12)

4.4. Ellipsometry

The thickness of the continuous films were calculated through ellipsometry. The ellipsometric values, Is and Ic were measured in a spectrum of 0,6 eV to 6 eV at an incidence angle of 70° in configuration II and configuration III, by an Uvisel© ellipsometer from Horiba. By using an

adapted model with the software DeltaPsi, a good estimation of the thickness was made, as described in Supporting Information (Figure S13).

4.5. Surface analysis

Microscopy pictures were taken from microscope *DMLM* (LEICA©) equipped with *DFC280* camera. Scanning Electron Microscopy (SEM) images were taken through a Hirox© SH-3000 device. The samples were observed through Atomic Force Microscopes (AFM) MultiMode8® from Brucker©, on peak force modes.

4.6. Differential Scanning Calorimetry

The glass transition temperatures were determined by Differential Scanning Calorimetry (DSC).The polymer was heated up to 200 °C for 5min, then cooled down to -90 °C for 5 min, before to be heated up again to 200 °C for 5 min with heating/cooling rate of 10 °C/min. Glass transition temperatures of -43 °C and 91 °C were found respectively for the PnBuA block, and the PMMA block (Figure S14).

4.7. Size Exclusion Chromatography

The number average molar mass (M_n) and the dispersity ($Đ$) were obtained by Size Exclusion Chromatography (SEC) in DMF. PMMA conventional calibration was used to determine M_n = 114 kg/mol and $Đ$ = 1,07.

Supporting Information

Complementary information such as ellipsometric data, temperature evolution in the microwave chamber or additional AFM images can be found in this file.

Acknowledgements

P.M. and L.P.’s positions were financially supported by a CDAPP and ISIFOR Carnot fellowships, respectively. L. B. thanks the CNRS for his “Délégation” fellowship. SEC, NMR and AFM analyses were supported by a public grant overseen by the French National Research Agency ANR-10-EQPX-16 XYLOFOREST. Kuraray Co., Ltd, is acknowledged for providing MBM20.

NB and PM contributed equally to this work.

References:

1. R. Lakes, *Nature*, 1993, **361**, 511-515.
2. P. S. Weiss, *ACS Nano*, 2008, **2**, 1085-1087.
3. J. Kastelic, A. Galeski and E. Baer, *Connective Tissue Research*, 1978, **6**, 11-23.
4. K. Autumn, M. Sitti, Y. A. Liang, A. M. Peattie, W. R. Hansen, S. Sponberg, T. W. Kenny, R. Fearing, J. N. Israelachvili and R. J. Full, *Proceedings of the National Academy of Sciences of the United States of America*, 2002, **99**, 12252-12256.
5. A. Magasinski, P. Dixon, B. Hertzberg, A. Kvit, J. Ayala and G. Yushin, *Nature Materials*, 2010, **9**, 353-358.
6. Z. Y. Yuan and B. L. Su, *Journal of Materials Chemistry*, 2006, **16**, 663-677.
7. L. Feng, Y. Zhang, J. Xi, Y. Zhu, N. Wang, F. Xia and L. Jiang, *Langmuir*, 2008, **24**, 4114-4119.
8. G. Widawski, M. Rawiso and B. François, *Nature*, 1994, **369**, 387-389.
9. P. Escalé, L. Rubatat, L. Billon and M. Save, *European Polymer Journal*, 2012, **48**, 1001-1025.
10. M. Hernandez-Guerrero and M. H. Stenzel, *Polymer Chemistry*, 2012, **3**, 563-577.
11. A. Muñoz-Bonilla, M. Fernández-García and J. Rodríguez-Hernández, *Progress in Polymer Science*, 2014, **39**, 510-554.
12. L. S. Wan, L. W. Zhu, Y. Ou and Z. K. Xu, *Chemical Communications*, 2014, **50**, 4024-4039.
13. H. Yabu, M. Tanaka, K. Ijiro and M. Shimomura, *Langmuir*, 2003, **19**, 6297-6300.
14. D. J. C. Herr, *Journal of Materials Research*, 2011, **26**, 122-139.
15. C. J. Ko, Y. K. Lin and F. C. Chen, *Advanced Materials*, 2007, **19**, 3520-3523.
16. S. I. Association, *International Technology Roadmap for Semiconductors*, 2011, **San Jose,CA**.
17. M. J. Fasolka and A. M. Mayes, *Annual Review of Materials Science*, 2001, **31**, 323-355.
18. W. I. Park, K. Kim, H. I. Jang, J. W. Jeong, J. M. Kim, J. Choi, J. H. Park and Y. S. Jung, *Small*, 2012, **8**, 3762-3768.
19. P. W. Majewski and K. G. Yager, *Journal of Physics Condensed Matter*, 2016, **28**.
20. J. N. L. Albert and T. H. Epps, *Materials Today*, 2010, **13**, 24-33.
21. A. Muñoz-Bonilla, E. Ibarboure, E. Papon and J. Rodriguez-Hernandez, *Langmuir*, 2009, **25**, 6493-6499.

22. P. Escalé, M. Save, A. Lapp, L. Rubatat and L. Billon, *Soft Matter*, 2010, **6**, 3202-3210.
23. P. Escalé, M. Save, L. Billon, J. Ruokolainen and L. Rubatat, *Soft Matter*, 2016, **12**, 790-797.
24. A. Bertrand, A. Bousquet, C. Lartigau-Dagron and L. Billon, *Chemical Communications*, 2016, **52**, 9562-9565.
25. A. Bertrand, F. Dumur, M. Mruczkiewicz, M. Perrin, C. Lartigau-Dagron, A. Bousquet, L. Vignau, L. Billon and S. Fasquel, *Organic Electronics: physics, materials, applications*, 2018, **52**, 222-229.
26. E. Ji, V. Pellerin, F. Ehrenfeld, A. Laffore, A. Bousquet and L. Billon, *Chemical Communications*, 2017, **53**, 1876-1879.
27. L. Ghannam, M. Manguian, J. François and L. Billon, *Soft Matter*, 2007, **3**, 1492-1499.
28. X. Zhang, K. D. Harris, N. L. Y. Wu, J. N. Murphy and J. M. Buriak, *ACS Nano*, 2010, **4**, 7021-7029.
29. P. Mokarian-Tabari, C. Cummins, S. Rasappa, C. Simao, C. M. S. Torres, J. D. Holmes and M. A. Morris, *Langmuir*, 2014, **30**, 10728-10739.
30. D. Borah, R. Senthamaraikannan, S. Rasappa, B. Kosmala, J. D. Holmes and M. A. Morris, *ACS Nano*, 2013, **7**, 6583-6596.
31. C. Jin, J. N. Murphy, K. D. Harris and J. M. Buriak, *ACS Nano*, 2014, **8**, 3979-3991.
32. D. T. W. Toolan, K. Adlington, A. Isakova, A. Kalamiotis, P. Mokarian-Tabari, G. Dimitrakis, C. Dodds, T. Arnold, N. J. Terrill, W. Bras, D. Hermida Merino, P. D. Topham, D. J. Irvine and J. R. Howse, *Physical Chemistry Chemical Physics*, 2017, **19**, 20412-20419.
33. David R. Lide, *CRC Handbook of Chemistry and Physics*, CRC Press Inc, 2009, 90^{e} ed.
34. P. Escalé, L. Rubatat, C. Derail, M. Save and L. Billon, *Macromolecular Rapid Communications*, 2011, **32**, 1072-1076.
35. P. Escalé, W. Van Camp, F. Du Prez, L. Rubatat, L. Billon and M. Save, *Polymer Chemistry*, 2013, **4**, 4710-4717.
36. H. Yin, A.L. Bulteau, Y. Feng, L. Billon *Advanced Material Interfaces*, 2016, **3**, 1500623
37. K. Norrman, A. Ghanbari-Siahkali and N. B. Larsen, *Annual Reports on the Progress of Chemistry - Section C*, 2005, **101**, 174-201.
38. X. Y. Li, Q. L. Zhao, T. T. Xu, J. Huang, L. H. Wei and Z. Ma, *European Polymer Journal*, 2014, **50**, 135-141.

Supporting Information

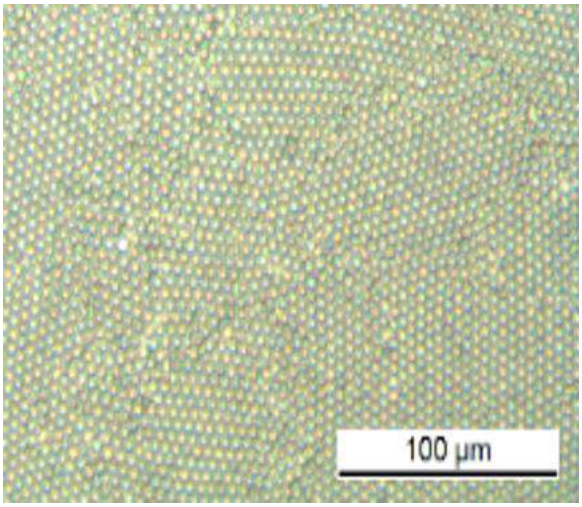

Figure S1. Optical microscopy of honeycomb structures made in static method at 60% of relative humidity. A solution of MBM20 in dichloromethane (5g/L) has been used for the drop casting.

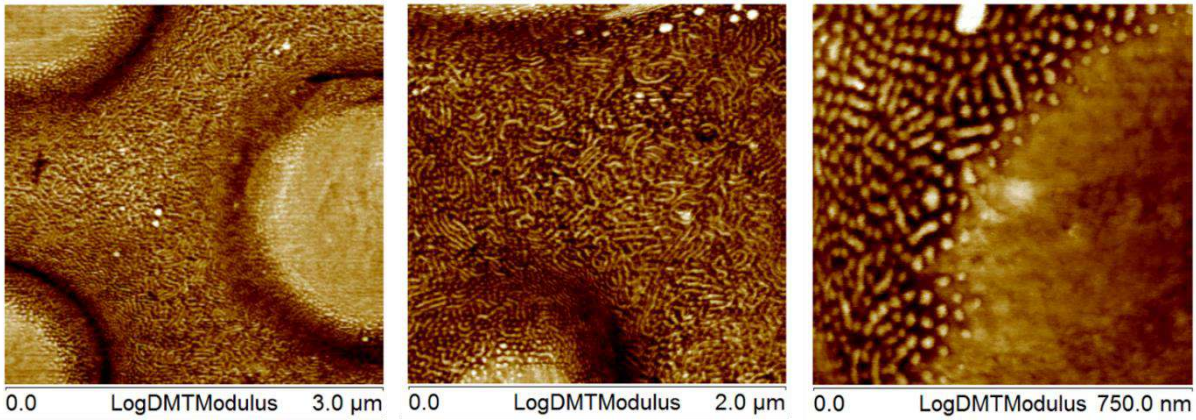

Figure S2. AFM images of honeycomb structures made in static method at 60% of relative humidity, with a solution of MBM20 in dichloromethane has been used for the drop casting. 5g/L. Zoom on the pillar zone (image in the middle) and on the side pore zone (image on the right).

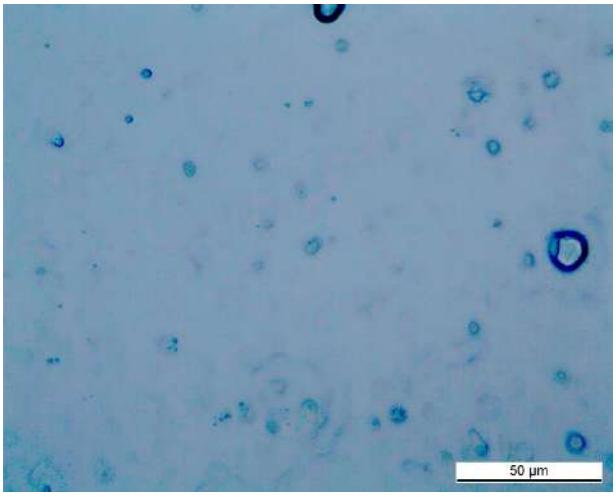

Figure S3. Optical microscopy of honeycomb structures after a thermal annealing at 160°C during 5 min. The film was made in static method at 60% of relative humidity, with a solution of MBM20 in dichloromethane has been used for the drop casting.

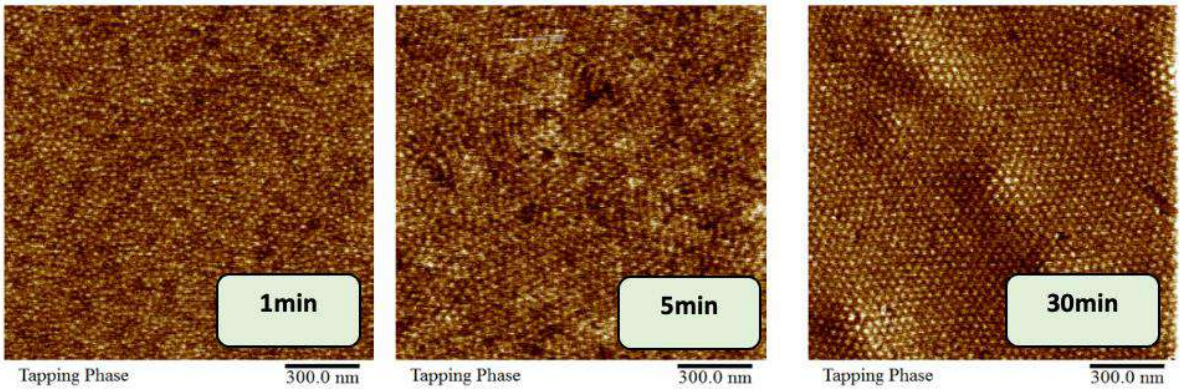

Figure S4. AFM pictures in tapping mode of MBM20 solutions at 1,5w% in DCM spin-coated at 3000rpm on a cut glass microscope slide, washed with acetone. The samples has been annealed in a CEM microwave at 200W annealed at 0,5cm from the bottom of the vial. The annealing time was 1 min, 5 min and 30 min.

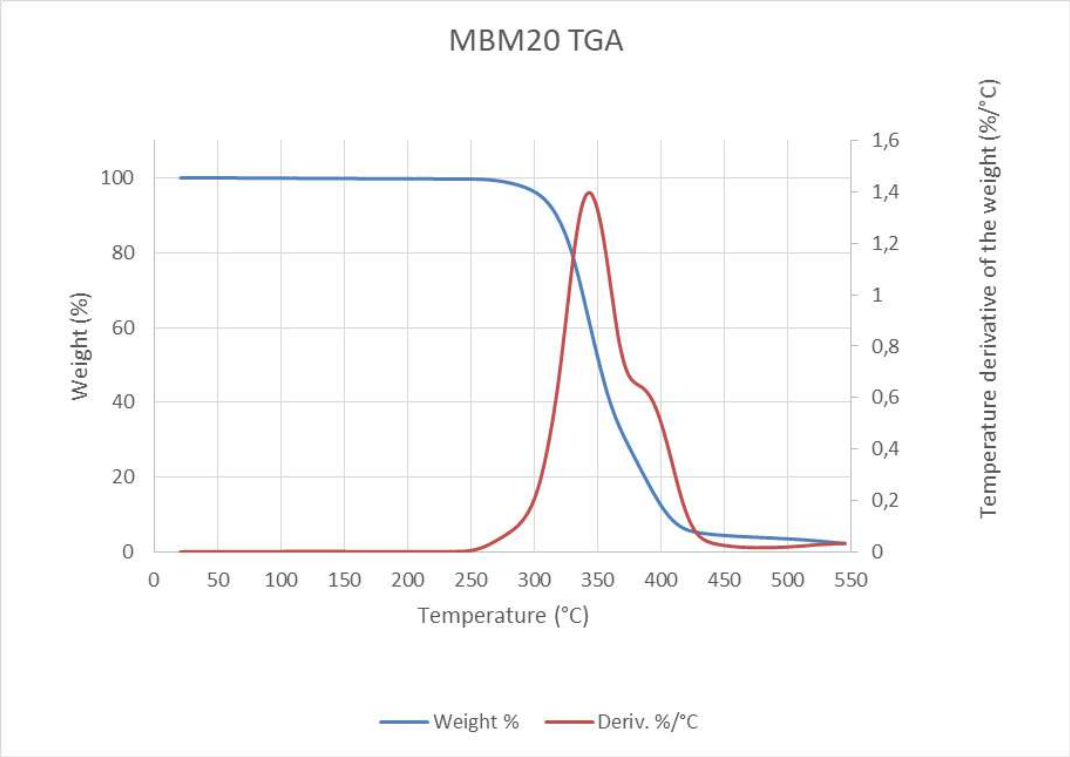

Figure S5. TGA curves of MBM20. The sample was heated from ambient temperature to 550 °C with a heating rate of 10°C/min under air. The graph shows the evolution of the weight (blue) and its temperature derivative (red), in function of the temperature.

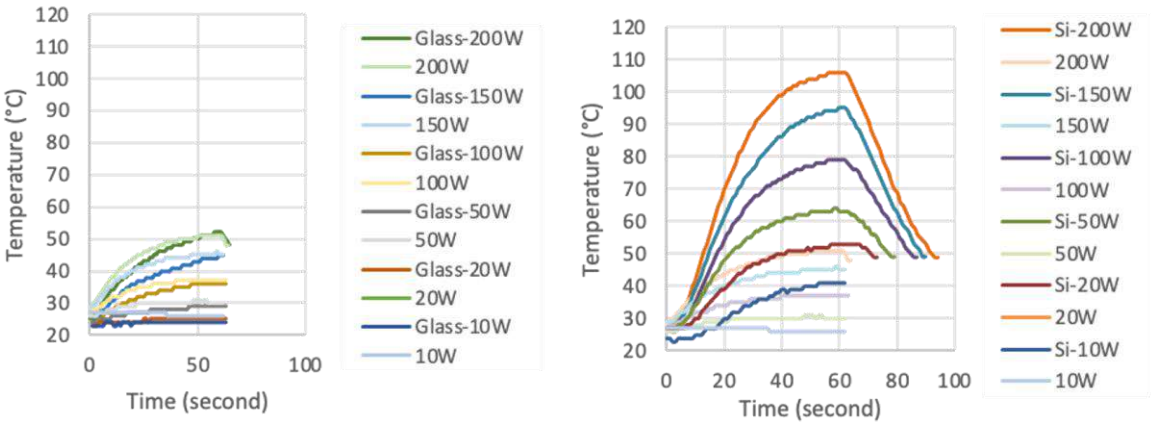

Figure S6. Evolution of measured temperatures at different powers in function of time with cooling of the vial during the microwave annealing. Results of vials with silicon shard (right) and with glass piece (left) are compared with empty vials (Em.) temperature measurements.

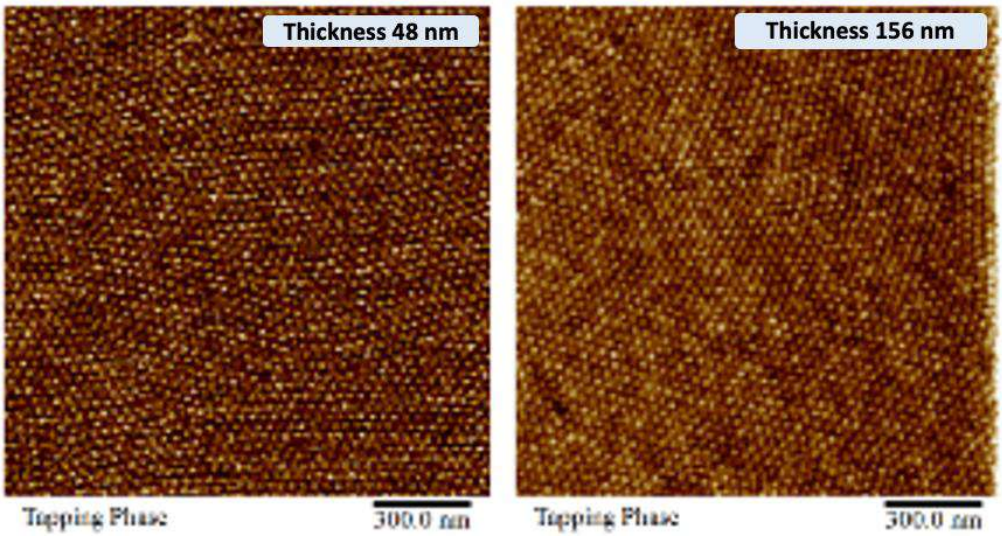

Figure S7. AFM pictures in tapping mode of MBM20 solutions at 8.7 g.L-1 (1 wt%) in toluene (left) and at 20,3 g.L-1 (1.5 wt%) in DCM spin-coated on a cleaned silicon wafer respectively at 2000 rpm and 3000 rpm. The samples has been annealed in a CEM microwave at 5 W for 1 minute at 0,5 cm from the bottom of the vial.

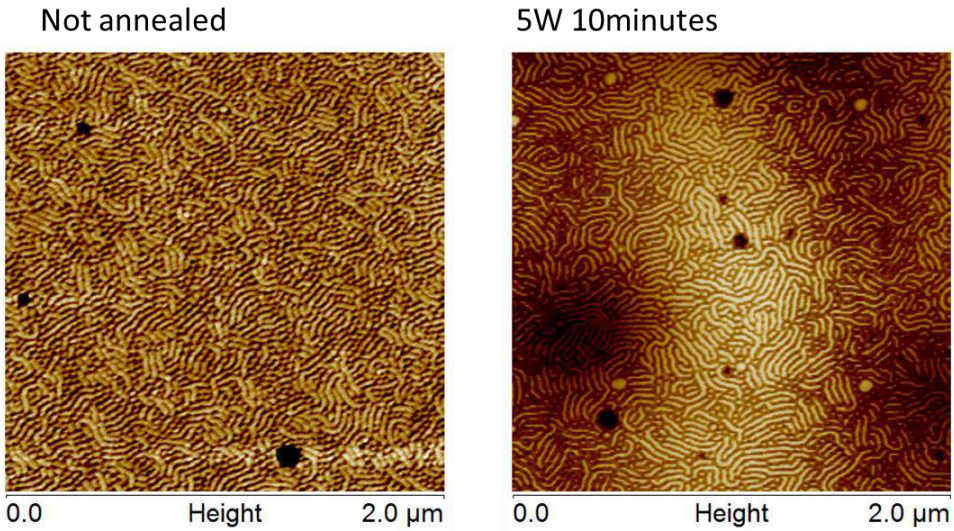

Figure S8. AFM images of MBM films made on silicon substrate from drop casted dichloromethane solution (5 g/L, **film thickness 1500 nm**). The left image shows the film without any annealing and the right one presents the film annealed at 5W during 10 minutes. We first tried an annealing for 1 minute at 5W but the structuration didn't change. Then we increased the irradiation time to 5 and even 10 minutes but we couldn't obtain perpendicular cylinders. These continuous films were produced to compare with porous honeycomb films.

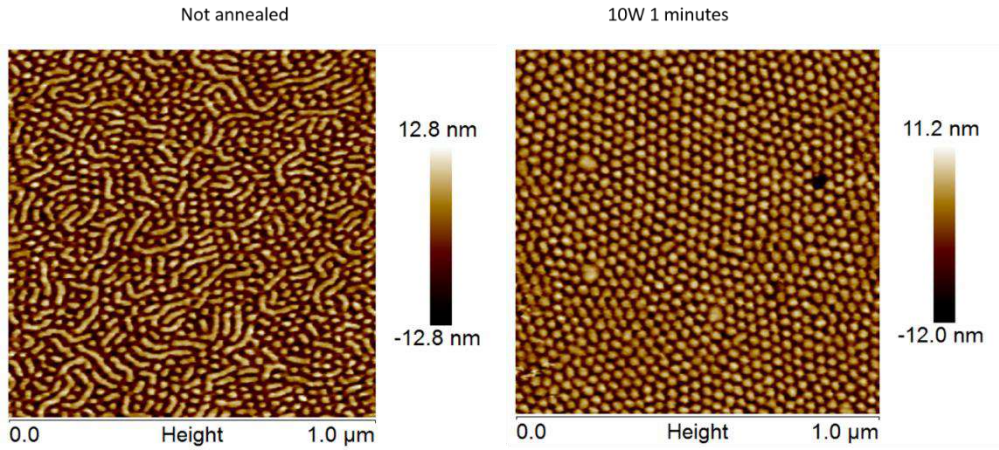

Figure S9. AFM images of continuous MBM films made on silicon substrate from drop casted dichloromethane solution (5 g/L, **film thickness 1500 nm**). These continuous films were produced to compare with porous honeycomb films.

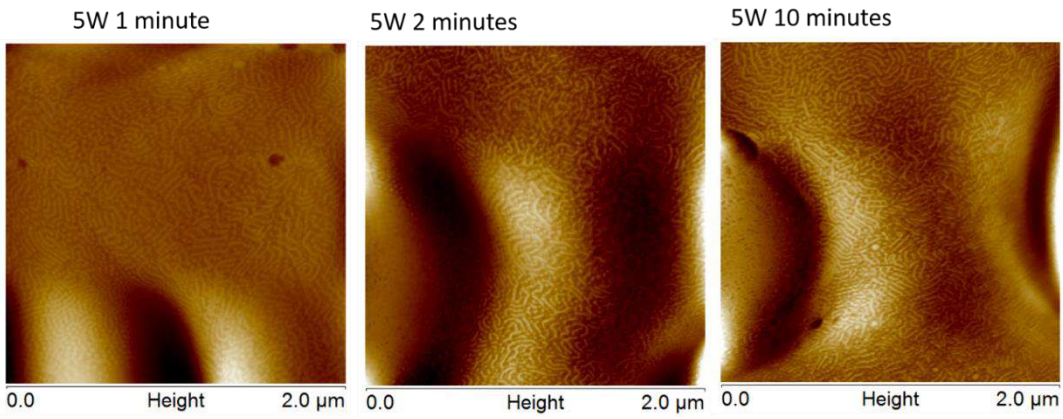

Figure S10. AFM images of honeycomb structures made in static method at 80% of relative humidity, with a solution of MBM20 in dichloromethane has been used for the drop casting. 5g/L. These films have been annealed with microwave irradiation at 5W during different times.

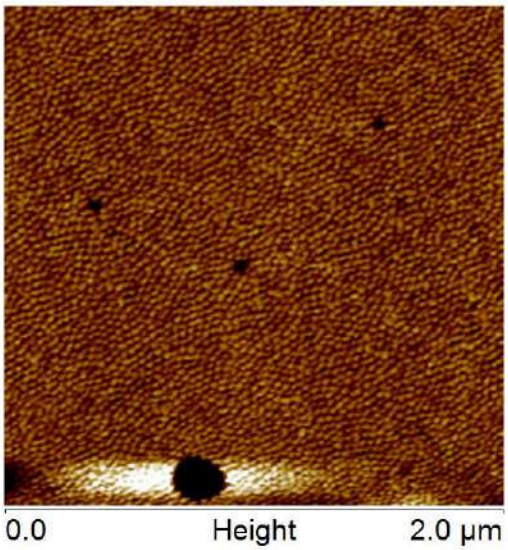

Figure S11. AFM image of honeycomb structures made in static method at 80% of relative humidity, a solution of MBM20 in dichloromethane has been used for the drop casting. 5g/L. This films has been annealed with microwave irradiation at 10W during 2 minutes

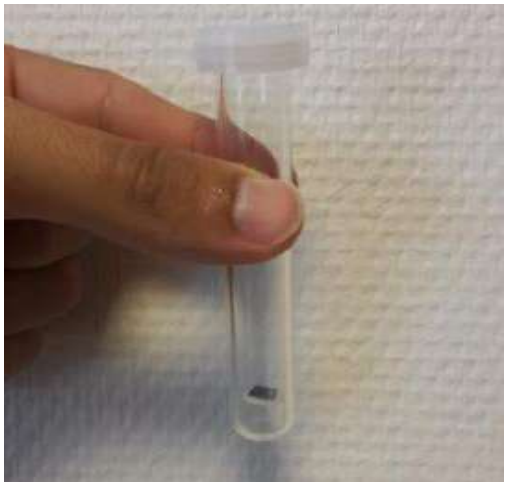

Figure S12. Picture of the set-up used to submit the wafers to the microwave irradiation.

S13 - Thickness measurement

The thickness of the continuous films were calculated through ellipsometry measurement. The ellipsometric values, Is and Ic were measured in a spectrum of 0.6 eV to 6 eV at an incidence angle of 70° in configuration II and configuration III, by an Uvisel® ellipsometer from Horiba©. According to the relations below, the

ellipsometric parameters Δ and ψ are determined respectively with acquisition data from *configuration II* and *configuration III*.

Configuration II: Is = sin2Ψ sinΔ Ic= sin2Ψ cosΔ

Configuration III: Is = sin2Ψ sinΔ Ic= cos2Ψ

The model used to fit the parameters is composed of a classical Si <100> material as substrate, and a layer upon it with a variable thickness. This thickness is guessed in a range between 1 nm and 300 nm. The composition of the layer in PMMA and PnBua is fixed as the volume fraction of each block has been previously determined by NMR. The optical behavior of the PMMA is described with the new amorphous model found in the software. However, for the PnBuA, thin layers of PnBuA homopolymer spin-coated at 1500 and 2000 rpm on silicon. Finally the BCP model was composed with each modelled material, following the volume fraction of each block.

The PnBuA optical parameters are determined by using an absolute fitting process, in which each parameter is guessed between limits that keep a physical meaning, as it's described in the Table S1. The term n_∞ is at least greater than one and equal to the value of the refractive index when the incident beam energy tend to the infinite. The parameter ω_g is correlated to the energy band gap. It's the energy from which the absorption starts to be non-zero. In the same way, ω_1 is approximately the energy at which the extinction coefficient is maximum (peak of absorption). The f_1 and Γ_1 parameters are related respectively to the strength (amplitude) and the broadening of the extinction peak.

Table S1. Limits used for the absolute fitting process to determine the new amorphous parameters of the PnBuA block

$1 < n_\infty < 2$
$1{,}5\ eV < \omega_g < 10\ eV$
$0\ eV < f_1 < 1\ eV$
$1{,}5\ eV < \omega_1 < 10\ eV$
$0{,}2\ eV < \Gamma_1 < 8\ eV$

The optical parameters of the new amorphous model has been taken from a 3w% solution of PnBuA in toluene. This solution has been spin coated at 1500 rpm and

2000 rpm on a piece of silicon wafer. The average value of each parameter is used for the MBM20 model.

Table S2. New amorphous model parameter fitted from spin-coated

Rotation speed [rpm]	*1500*			*2000*			***Average***		
n_∞	1,513	±	0,005	1,533	±	0,013	**1,523**	±	**0,009**
ω_g [eV]	4,182	±	0,047	4,367	±	0,099	**4,274**	±	**0,073**
f_1 [eV]	0,032	±	0,004	0,039	±	0,006	**0,035**	±	**0,005**
ω_1 [eV]	4,066	±	0,13	4,119	±	0,439	**4,092**	±	**0,284**
Γ_1 [eV]	0,758	±	0,118	1,434	±	0,259	**1,096**	±	**0,189**

Quantitatively, the polymer film thickness h follows the empiric formula, where k and β are material specific constants, η_0 is the initial polymer solution viscosity, Ω is the spin-coating angular velocity and α is a constant for the system with certain dispersity in function of the studied system with a value in general around -0,5 for most polymers.

$$h = k\eta_0^{\beta}\Omega^{\alpha}$$

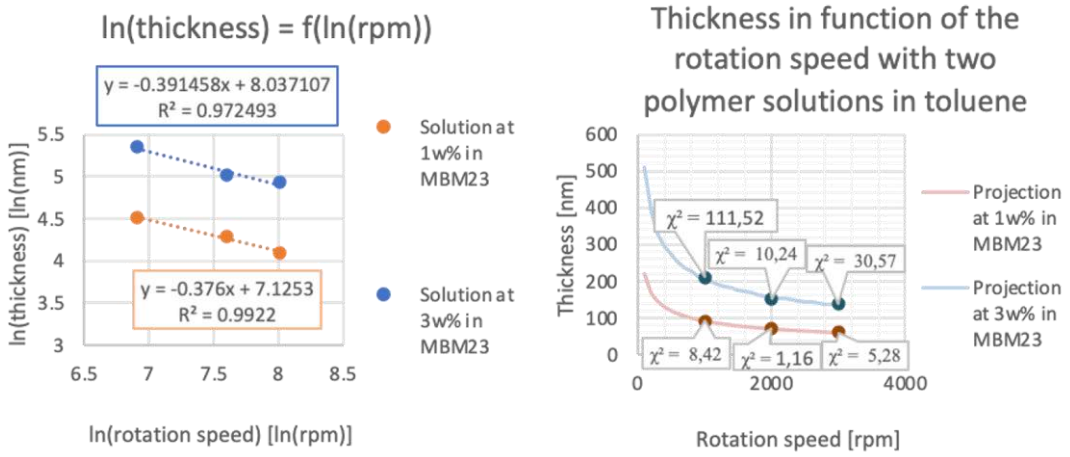

Figure S13 (A) Representation of the logarithm of the thickness taken in nanometers in function of the logarithm of the rotation speed taken in rpm. (B) Representation of the thickness in nanometer in function of the spin coating rotation speed in rpm. The red dots and blue dots line are respectively from a 8.7 g.L-1 (1 wt%) and a 26.8 g.L-1 (3 wt%) solution of MBM20 in Toluene. The projection is made with the value from the linear regressions above.

According to this relation, we can verify the relative validity of the thickness measurement by tracing: $\ln(h) = ln(k\eta_0{}^{\beta}) + \alpha \times \ln(\Omega)$. As show the *Figure SI2*-(A), the coefficient α obtained by a linear regression is coherent with the empiric relation presented above. The linear regression coefficient for the two solution is quit satisfying, with a R^2 close to 1. Here χ^2 is correlated with the difference between the acquisition graph and the graph calculated from the model. As show the *Figure SI2*-(B), the 1w% solution show good χ^2 parameter inferior to 10. However the 3w% solution show a χ^2 value higher. As show the following chapter, this system demonstrate a strong phase separation without any annealing process. This phenomena could lead to a depolarization of

S14– Differential Scanning Calorimetry

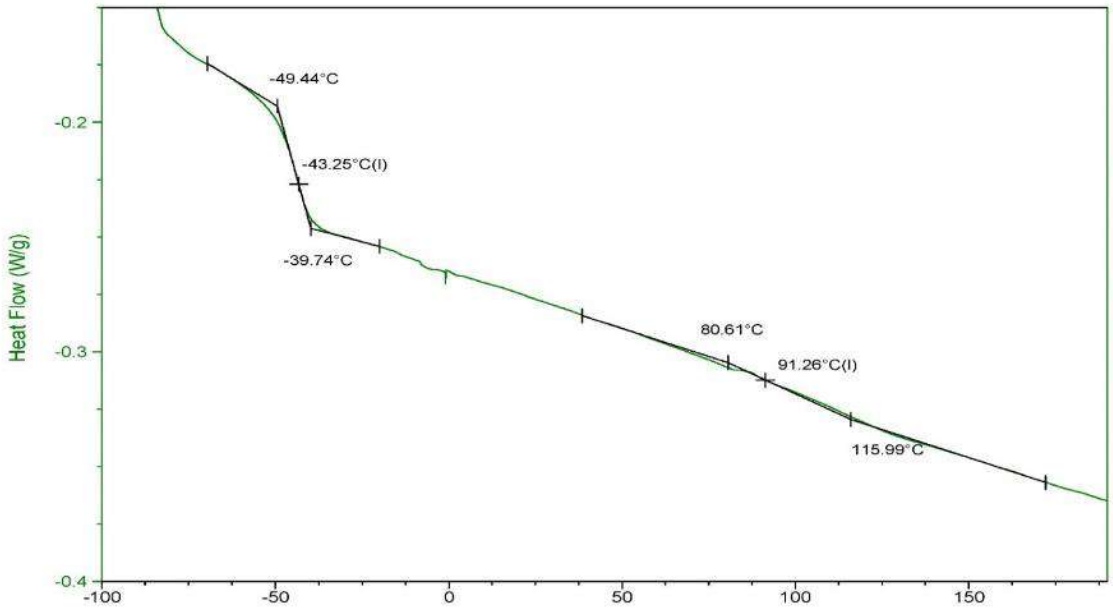

Figure S14. Differential Scanning calorimetry graph of MBM20. The PnBuA Tg and PMMA Tg are found respectively between -49°C and -40°C, at -43°C and between 80°C and 116°C, at 9

CHAPTER 3

Robust and Efficient Screen-Printed Molecular Anodes with Anchored Water Oxidation Catalysts

Context: The impact of fossil fuel usage in our modern societies have urged the development of alternative energy sources. The future energy scenario relies on the capacity to create alternative fuels that can store energy in chemical bonds.[1] Inspired by nature, an artificial photosynthesis with catalysts that efficiently reduce abundant substrates such as H_2O, N_2 or CO_2 to respectively produce hydrogen, ammonia or hydrocarbon that can generate clean and sustainable fuels with as an ideal the challenging $4e^-/4H^+$ oxidation of H_2O to O_2.[1-2] Ru complexes including the family of Ru-bda are an impressive and robust material for water oxidation catalysts (WOCs) that allow the catalysis with low overpotentials.[1-2] To incorporate these catalysts into technologically useful devices based on photoelectrochemical (PEC) cells, the anchoring WOCs on electrode surface is a very attractive system for generation of hybrid materials for heterogeneous water oxidation process.[3]

In this chapter, the preparation of highly stable and active screen-printed anodes for electrochemical water splitting in neutral media will be presented. By the combination of printed electrodes that I developed from the triblock PMMA-*b*-PnBuA-*b*-PMMA (studied in Chapter 2) and molecular water oxidation catalyst produced by the Pr Llobet group (ICIQ, see Figure 0), we successfully take advantage of a low-cost and up-scalable fabrication method of graphitic electrodes with the outstanding catalytic activity and stability of oligomeric ruthenium based molecular water oxidation catalysts, offering a promising electro-anode for water oxidation applications.

This work has been done in collaboration between IPREM (Pau, France) and ICIQ (Tarragona, Spain) members in the eSCALED framework, thanks to Robin Dürr, Andrew Howe, Van N'Guyen, Saeed Sadhegi, Stephanie Reynaud, Cyril Cugnet, Laurent Authier, Marcos Gil Sepulcre, Carolina Gimbert and Toni Llobet.

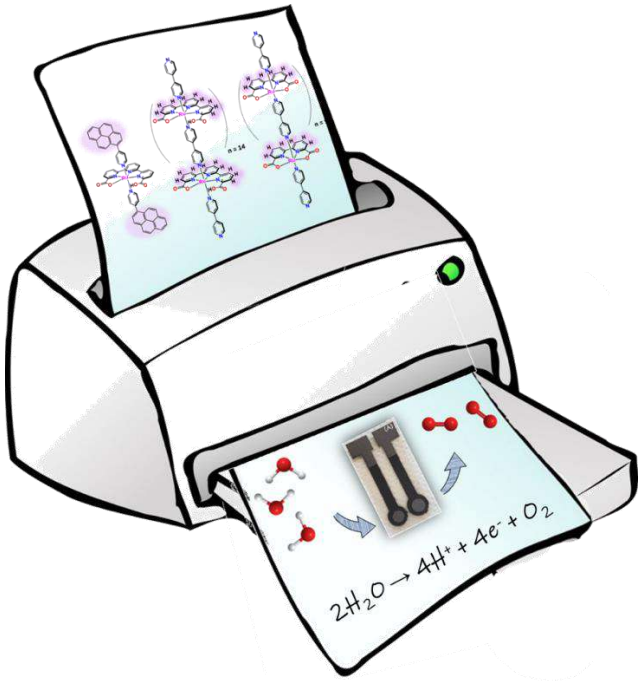

Figure 0. Graphic representing Robust and Efficient Screen-Printed Molecular Anodes with Anchored Water Oxidation Catalysts

Reference:

(1) R. Matheu.; M. Z. Ertem.; M. Pipelier.; J. Lebreton.; D. Dubreuil.; J. Benet-Buchholz.; X. Sala.; A. Tessier.; A. Llobet. The role of seven-coordination in Ru-catalyzed water oxidation. *ACS Catal*. **2018**, 8, 2039-2048.

(2) R. Matheu.; M. Z. Ertem.; J. Benet-Buchholz.; E. Coronado.; V. S. Batista.; X. Sala.; A. Llobet. Intramolecular proton transfer boots water oxidation catalyzed by a Ru complex. *J. Am. Chem. Soc*. **2015**, 137, 10786-10795.

(3) R. Matheu.; L. Francàs.; P. Chernev.; M. Z. Ertem.; V. Batista.; M. Haumann.; X. Sala.; A. Llobet. Behavior of the Ru-bda water oxidation catalyst covalently anchored on glassy carbon electrodes. *ACS Catal*. **2015**,5,3422-3429.

Table of contents

1. Introduction 102

2. Results and Discussion 103

2.1. Screen-printed electrodes……103

2.2. Anchoring of Ru WOCs on PE and redox properties……..105

2.3. Long term performance of MPE……108

3. Conclusions 111

References 113

Supplementary information 117

Method……..118

^{1}H-NMR Spectroscopy……..127

Electrochemical Characterization……..129

DPV before and after activation……130

TOF_{max} Calculation by FOWA……..131

CPE of 1-tda-pyp@CNT@PE and 15-tda-bpy@CNT@PE.....134

CVs for CP 25 – 225 µA……135

CV for CP at 100 µA over 20 hours……..138

CVs for CA at 1.45 V over 20 hours……141

This Chapter will be soon submitted and most of the figures can therefore be found in its supporting information.

Robust and Efficient Screen-Printed Molecular Anodes with Anchored Water Oxidation Catalysts

1. Introduction

The impact of fossil fuel usage in our modern societies have urged the scientific community to find alternative fuels that can sustain current energy demands using carbon-neutral, clean and sustainable sources.[1,2] Inspired by nature, artificial photosynthesis aims at capturing and storing the energy from solar photons into chemical bonds, generating clean and sustainable fuels, that obtained in this manner are termed solar fuels.[3,4] Light-induced water splitting (*hυ*-WS), where the energy from sunlight is stored into H-H and O-O bonds, can be considered a model case.[5,6] Nevertheless, many scientific challenges still need to be overcome to be able to implement *hυ*-WS as a widespread technology. One of the most critical challenges, includes the performance of low-cost catalysts in terms of efficiency and stability, as well as their capacity to harmoniously interact with the light absorber.[7]

One of the crucial issues that needs to be solved in *hυ*-WS, is the need to have access to efficient and robust Water Oxidation Catalyst (WOC) that can be easily incorporated into robust electrodes. The water oxidation reaction is particularly challenging because it involves the removal of four electrons and four protons from two water molecules and the formation of an O-O bond.[8,9] Furthermore, it is a thermodynamically unfavorable reaction with a formal redox potential of 1.23 V vs. NHE at pH 0.[10] From a molecular perspective, the best WOCs described up to now are based on Ru complexes coordinated with Flexible Adaptive Multidentate Equatorial (FAME) ligands, including the family of Ru-tda and Ru-bda coordination complexes. [11,12] To incorporate these catalysts into technologically useful devices based on photoelectrochemical PEC cells, they must be anchored on conductive and/or semi-conductive surfaces so that efficient molecular (photo)anodes can be developed. For this point of view, the choice of the anchoring strategy is essential because it simplifies the construction engineering as opposed to use the catalysts in homogeneous phase.[13] So far, several strategies have been developed for the anchoring of WOCs into surfaces that include covalent bonding,[14,15]

polymerization into insoluble but conductive polymers [13] and supramolecular interactions such as CH-π[16] and π-π.[17,18]

In addition, the possibility of using the screen-printing processing technologies [19] to generate electro-anodes and cathodes makes it highly attractive to advanced applications for PECs because it simplifies its construction and thus it also reduces its costs.

Here on, we describe the use of a screen-printing technique in order to easily prepare electrode-anodes containing molecular WOCs based on monomeric and oligomeric Ru complexes suitable to perform water oxidation catalysis.

2. Results and Discussion

2.1. Screen-printed electrodes

A commercial triblock copolymer Poly(Methyl MethAcrylate)-*b*-Poly(*n*-Butyl Acrylate)-*b*-Poly(Methyl MethAcrylate) (MBM) is used as a matrix to bind graphite powder to generate an ink containing Mesitylene or *o*-xylene as solvent, that can be used as a scaffold to immobilize carbon nanotubes supported ruthenium catalyst (WOC@CNT) and presenting a high affinity with the perfluorinated NAFION membrane. [20, 21] The preparation of screen-printed electrodes consisted on using a polymeric Nafion or high impact polymeric styrene (HIPS) substrate [22] as support where we could deposit our conductive ink. After solvent evaporation, a molecular water oxidation catalyst anchored on multi walled carbon nanotubes (MWCNTs or CNTs) is deposited, generating a molecular anode (**Figure 1a**). Further, an easily up-scalable screen-printing methodology was developed to provide flexible electrode coated on NAFION proton membrane.

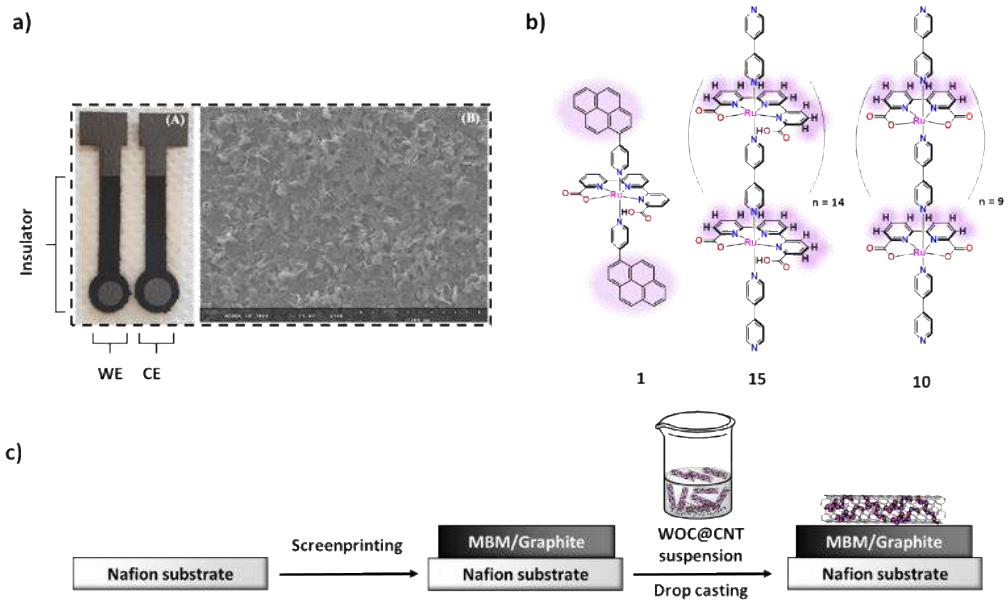

Figure 1. (**A)** picture of the screen-printed electrodes and its SEM image. **(B)** drawing of the molecularly discrete catalyst **1** and oligomers **10** and **15**. **(C)** sequential strategy used for the preparation of molecular printed electrodes MPEs.

To prepare the electrodes, several parameters were optimized such as MBM/graphite ratio, the solvent used during the ink preparation and the number of printed layers (Table 1). The characterization of these new electrodes included the measurement of their film thickness and porosity, their conductivity and their electrochemical response through evaluation of peak-to-peak separation for the ferrocene/ferrocenium (III/II) redox couple, used as internal standard. The main results obtained from these experiments are gathered in Table 1 and Figure SI-1. The best electrode in terms of conductivity and film thickness turn out to be prepared with MBM/Graphite (30:70), also labeled as "**PE**", and thus was the one used throughout this work unless explicitly mentioned (Table 1, entry 6).

Table 1. Selected synthetic details and properties of printed electrodes based on MBM/graphite combination prepared in this work

Entry	MBM/Graphite (w%)	Solvent	[MBM] ($g \cdot L^{-1}$)	Nº of printed layer	Conductivity (S/cm)	Thickness (μm)	ΔE_{ox}-E_{red} (V)
1	40% - 60%	mesitylene	100	1	0.79	4.0	1.32
2	40% - 60%	mesitylene	100	2	1.20	7.0	1.34
3	40% - 60%	o-xylene	200	1	2.88	4.5	1.34
4	40% - 60%	o-xylene	200	2	4.17	9.0	1.34
5	30% - 70%	o-xylene	200	1	4.90	7.0	1.32
6	30% - 70%	o-xylene	200	2	6.20	9.0	1.34

**The volume of mesitylene to dissolved 400 mg of MBM was 4.0 ml and need solubilizing time more than 6 h.*
**The volume of O-xylene to dissolved 400 mg of MBM was 2.0 ml and need solubilizing time less than 1.30 h.*

2.2. Anchoring of Ru WOCs on PE and redox properties.

In order to obtain powerful anodes for the water oxidation reaction, the next step involved the anchoring of molecular WOCs onto the PE described above. For this purpose, we used a family of monomeric and oligomeric Ru-based molecular of WOCs that were anchored *via* π-π stacking interactions or *via* CH-π interactions on graphitic surfaces. Therefore, we choose the WOC [Ru(tda)(pyp)$_2$], **1,** (tda^{2-} is [2,2':6',2''-terpyridine]-6,6''-dicarboxylate and *pyp* is 4-(pyrene-1-yl)pyridine) containing a pyrene functionality that strongly attaches to graphitic surface *via* π-π interactions. We further chose {[Ru(bda)(bpy)]$_{10}$(μ-bpy)}, **10,** (*bda* is 2,2'-bipyridine-6,6'-dicarboxylate; *bpy* is 4,4'-bipyridine) and {[Ru(tda)(bpy)]$_{15}$(μ-bpy)}, **15** , which are capable to form CH-π interactions with graphitic surfaces through hydrogens of the equatorial ligand backbone (see Figure 1B for a drawing of WOCs). All these complexes were prepared following the methods previously described in the literature and characterized by 1H NMR (Figures SI-2 to 4) . [16,17,23] The catalysts were then anchored on CNTs by mixing a solution of the corresponding WOC and a sonicated suspension of the CNT (See supporting information for details and Scheme SI-1) to generate the WOC@CNT. This hybrid material was sequentially dryed and mixed with methanol, and subsequently drop casted onto the PE, forming the WOC@CNT@PE molecular printed electrodes MPE, that will be used as water oxidation anodes, as outlined in Figure 1C. The prepared hybrid MPE are named **1@CNT@PE**, **10@CNT@PE** and **15@CNT@PE** depending of contained WOC. The Ru

loading (Γ) at the surface of the electrode ranges from 0.5 to 9 nmol/cm^2 (Table 2), depending on the catalyst and on the anchoring strategy. It is interesting to realize here that as shown in the Table 2, the anchoring through aromatic CH-π interaction can generate a mass deposition up to 18 times higher than the π–π staking interaction.

Table 2. Selected properties of the molecular printed electrodes used in this work.

Cat@CNT@PE	Anchoring strategy.	Support	Experiment	R[a]/Ω	Γ/nmol·cm^2 before	Γ/nmol·cm^2 after	TOF s^{-1}	TONs
GC-bda				3-30	12.2			
1-H_2O	π–π	HIPS	CP 25 µA – 225 µA	3.800	0.49	-	1182	92200
15-H_2O	CH-π	Nafion	CP 25 µA – 225 µA	3.000	9.07	5.13	396	7300
			CP 100 µA	3.800	6.13	2.25		15500
			CA 1.45 V	1.200	0.80	0.63		58100
10-(H_2O)$_2$	CH-π	Nafion	CP 25 µA – 225 µA	2.000	0.46	1.28	2642	144800
			CP 100 µA	1.200	3.72	3.48		39800
			CA 1.45 V	4.800	0.95	0.94		53800

** taken after 2 hours exposure.*

[a] uncompensated resistance as determined via the iR compensation routine of the CHI potentiostat.

The electrocatalytic performance of the molecular electrodes was tested in a three-electrode half-cell configuration with a 1.0 M phosphate buffer (pH 7). The electrochemical analysis is based on Cyclic Voltammetry (CV) (Figure SI-5), Differential Pulse Voltammetry (DPV) (Figure SI-6) and controlled potential-current techniques. The molecular printed electrodes (WOC@CNT@PE) were used as working electrode (WE), a platinum mesh was employed as counter electrode (CE) and a Hg_2SO_4 (K_2SO_4 sat.) electrode was used as reference (RE). All potentials were converted to NHE by adding 0.65 V to the measured potential. Before usage, the uncompensated resistance of the electrode was determined for all the MPEs prepared in this work, following the CHI potentiostat iR compensation routine. It is important to realize here that the combination of printed electrodes, CNTs and catalysts gives resistances that are two to three orders of magnitude larger than for instance typical glassy carbon disk electrodes with an immobilized hybrid molecular Ru-based catalyst, anchored to CNTs via CH-π interactions. This increase in resistance is mainly due to the low conductivity of the ink generated, which contains a combination of graphitic material (highly conductive) with the

MBM binder that is a non-electrically conductive polymer. The limited conductivity of the overall screen-printed molecular anode, will only affect to redox processes where large current densities are involved, particularly the electrocatalytic waves, as will be discussed in the next section. An additional consequence of these large electrode resistances is the decrease on the measured TOF_{max} (k_{obs}), by one to two orders of magnitude as compared to their counterparts in homogeneous phase or anchored on graphitic electrodes. [11,16,17,23] The TOF_{max} values for **1@CNT@PE**, **10@CNT@PE** and **15@CNT@PE** were measured by using Foot of the Wave Analysis (FOWA),[24] are in the range of 396 – 2642 s^{-1} as indicated in Table 2 (Figures SI-7 to 9).

The CV of **1@CNT@PE** showed the typical Ru^{III}/Ru^{II} and Ru^{IV}/Ru^{III} redox couples at $E_{1/2}$ = 0.61V (ΔE = 100 mV) and $E_{1/2}$ = 1.05 V (ΔE = 70 mV) respectively as can be observed in Figure 2A. In case of **15@CNT@PE** the Ru^{III}/Ru^{II} and Ru^{IV}/Ru^{III} redox couples are visible at $E_{1/2}$ = 0.67 V (ΔE = 230 mV) and $E_{1/2}$ = 1.13 V (ΔE = 260 mV), respectively (Figure 2B), which is in accordance with previously reported values. [11,16,17,23] For the **10@CNT@PE** the Ru^{III}/Ru^{II} redox couple is detected at $E_{1/2}$ = 0.66 V (ΔE = 200 mV) and the redox potential of Ru^{IV}/Ru^{III} is visible at $E_{1/2}$ = 0.83 V (ΔE = 170 mV) (Figure 2C).

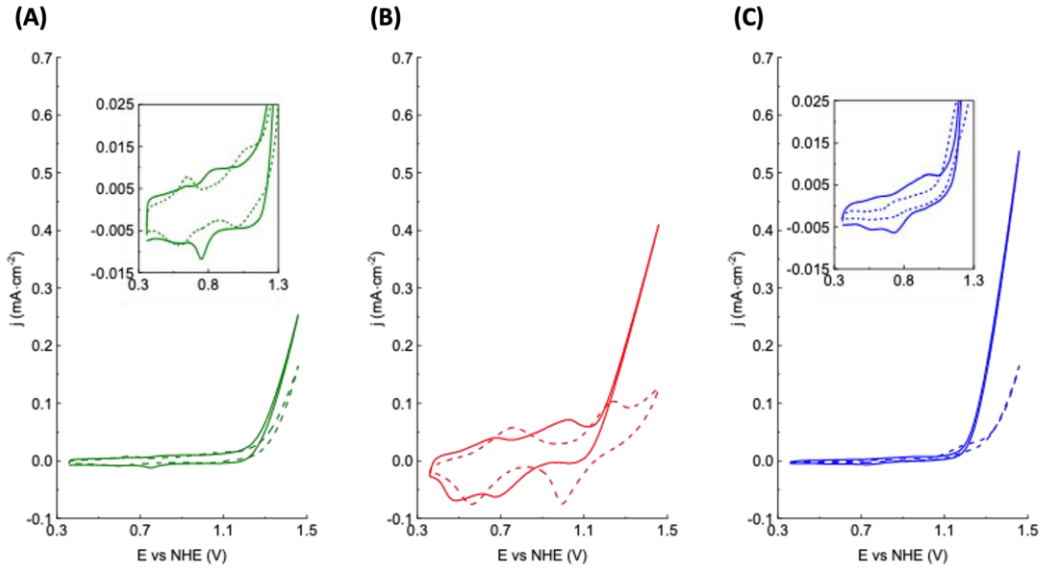

Figure 2. CV experiments of the MPEs recorded in a pH 7 (1.0 M phbf) aqueous solution at a ν = 10 $mV \cdot s^{-1}$ and 1000 Ω iR compensation. **(A) 1@CNT@PE** (green dashed line) and **1-H_2O@CNT@PE** (green solid line); **(B) 15@CNT@PE** (orange dashed line) and **15-H_2O@CNT@PE** (orange solid line); **(C) 10@CNT@PE** (blue dashed line) and **10-$(H_2O)_2$@CNT@PE** (blue solid line). The *inset* in **A** and **C** show the enlargement of the non-catalytic redox waves.

Additionally, a third oxidation (Ru^{V}/Ru^{IV}) that appears at 1.2 V is noted, which is related to water oxidation to dioxygen. Complexes **1** and **15** are not water oxidation catalyst but precursors to active catalysts and thus they need an activation step to generate the indispensable Ru-OH_2 group. On the other hand, complex **10** readily coordinates a water molecule in presence of aqueous solutions and therefore catalyzes water oxidation already in the first scan. It is important to point out here that once anchored on a graphitic surface and with repetitive CV scans in the potential range of the catalytic wave, **10** additionally coordinates a second water molecule, generating the more active Ru-$(OH_2)_2$ species.[23] The presence of this new species can be easily monitored by CV and DPV and shows three redox couples at 0.59 V (Ru^{III}/Ru^{II}), 0.74 V (Ru^{IV}/Ru^{III}) and 0.92 V (Ru^{V}/Ru^{IV}) together with a large electrocatalytic wave in the range of 1.2-1.3 V (Figure 2c and Figures SI-5 & 6). In case of **1@CNT@PE** and **15@CNT@PE**, the activation is carried out *via* Chronoamperometry (CA; also named as Controlled Potential Electrolysis, CPE, or Bulk Electrolysis, BE), at E_{app} = 1.32 V for 1000 s in a pH 11.6 phosphate buffer (phbf) (see Figure SI-10 for additional details). This generates new redox features that are due to the redox couples Ru^{III}/Ru^{II} at $E_{1/2}$ = 0.62 V (ΔE = 60 mV) and Ru^{IV}/Ru^{III} at $E_{1/2}$ = 0.8 V (ΔE = 100 mV) for **1-H_2O@CNT@PE** and $E_{1/2}$ = 0.59 V (ΔE =190 mV) and $E_{1/2}$ = 0.87 V (ΔE = 370 mV) for **15-H_2O@CNT@PE**.[11,16] In both cases, a new large electrocatalytic wave assigned to water oxidation appears in the range of 1.2-1.3 V.

2.3. Long term performance of MPE

To test the long term stability under different working conditions a series of Chronopotentiometries (CP) and Chronoamperometries (CA) were carried out for **1-H_2O@CNT@PE**, **15-H_2O@CNT@PE** and **10-$(H_2O)_2$@CNT@PE** and the results are reported in Figure 3 and Figures SI-11 to 16. The figure 3 shows the CP obtained setting a constant current of 25, 50, 100, 125, 175 and 225 μA (J = 0.13-1.15 mA·cm^2) for two hours each at pH 7 (1 M phbf). From 25 to 175 μA the three molecular electrodes are very stable over the 2 h period tested. However, the potentials needed to reach the corresponding current intensity are always lower for **10** and **15** than for **1**. In the case of i_{app} = 25 μA, the potentials needed are 1.25, 1.31 and 1.42 V for **15-H_2O@CNT@PE**, **10-$(H_2O)_2$@CNT@PE** and **1-H_2O@CNT@PE** respectively, while the blank that involves the use of CNT as a WOC appears at 1.75 V. For **1-H_2O@CNT@PE** and **15-H_2O@CNT@PE**, since the active site is similar as is the uncompensated resistance, the 150 mV difference can be associated with the much larger catalyst loading deposited at the surface of the electrode that is about 18 times

larger for **15-H_2O@CNT@PE** (9.1 nmols/cm^2) than for **1-H_2O@CNT@PE** (0.5 nmols/cm^2). Accordingly, this potential difference increases as the current set, is increased up to 175 μA where it reaches a difference value of 300 mV. It is interesting to see that upon increasing the set current densities, the electrodes need to increases the applied potential accordingly. However, the increase of required potential for **10-$(H_2O)_2$@CNT@PE** for increased current is smaller than for **15-H_2O@CNT@PE** and this generates a crossing potential at 100 μA. This smaller increase is mainly due to much lower resistivity of **10-$(H_2O)_2$@CNT@PE** with regard to **15-H_2O@CNT@PE**. It is also interesting to see that the CNT at low current densities can achieve relatively stable water oxidation catalysis but above 50 μA there is a clear deviation from linearity indicating electrode oxidation. In these experiments, assuming 100% Faradaic Efficiency (FE) according to reported values in the literature,[16,17,23] the number of TONs achieved are 7.300, 144.800 and 92.200 for **15-H_2O@CNT@PE**, **10-$(H_2O)_2$@CNT@PE** and **1-H_2O@CNT@PE** respectively, that clearly outlines the robustness of the present MPEs.

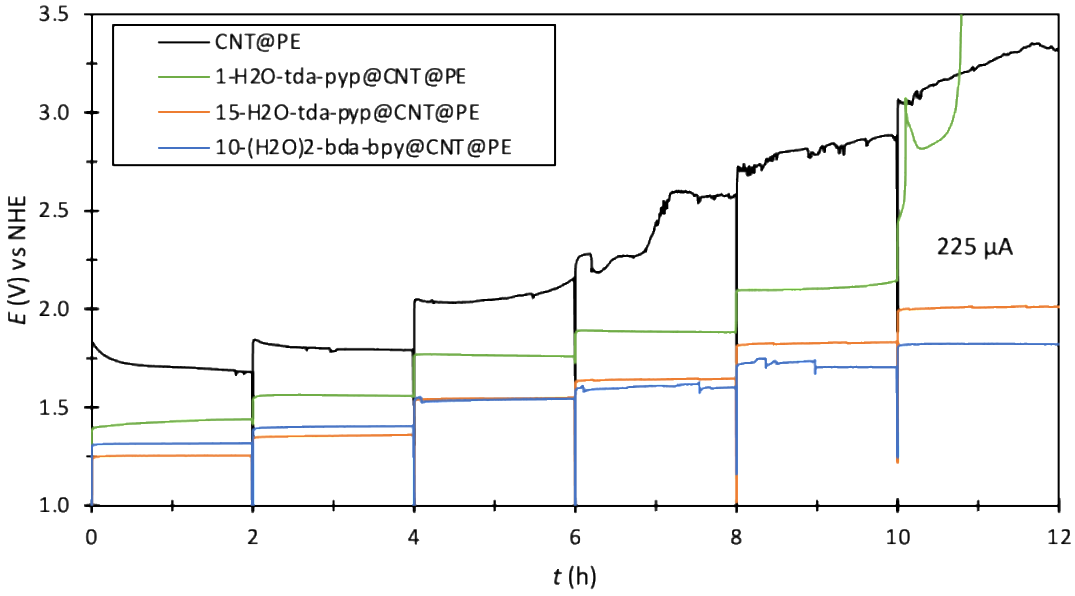

Figure 3. CP of **CNT@PE** (black line), **1-H_2O@CNT@PE** (green line), **10-$(H_2O)_2$@CNT@PE** (blue line) and **15-H_2O@CNT@PE** (red line).

To evaluate the integrity of the catalyst on the previously presented CP experiments, a CV was carried out every two hours and these results are exhibited in Figure 4. On the righthand side, a plot of the catalytic current density at 1.45 V as well as the loading of Ru, after each CP experiment is displayed for **15-H_2O-tda-bpy@CNT@PE**. It can be graphically observed that

as the catalyst loading progressively decrease, the catalytic current remains constant. The fact that the catalytic current is independent of catalyst loading indicates that the current density is limited by the overall conductivity of the electrode material. This is also clearly manifested with CV shape of the present electrode in comparison of the catalyst behaviour directly anchored on a highly conductive surface such as a glassy carbon electrode, as mentioned above.[16,23] The mass de-anchoring during CP experiments is associated with the de-anchoring of the CNT from the PE and/or the de-anchoring of the WOC from the CNTs. The fact that no new species appear during CVs used to monitor the whole process discards the presence of degrading pathways for the molecular catalyst.

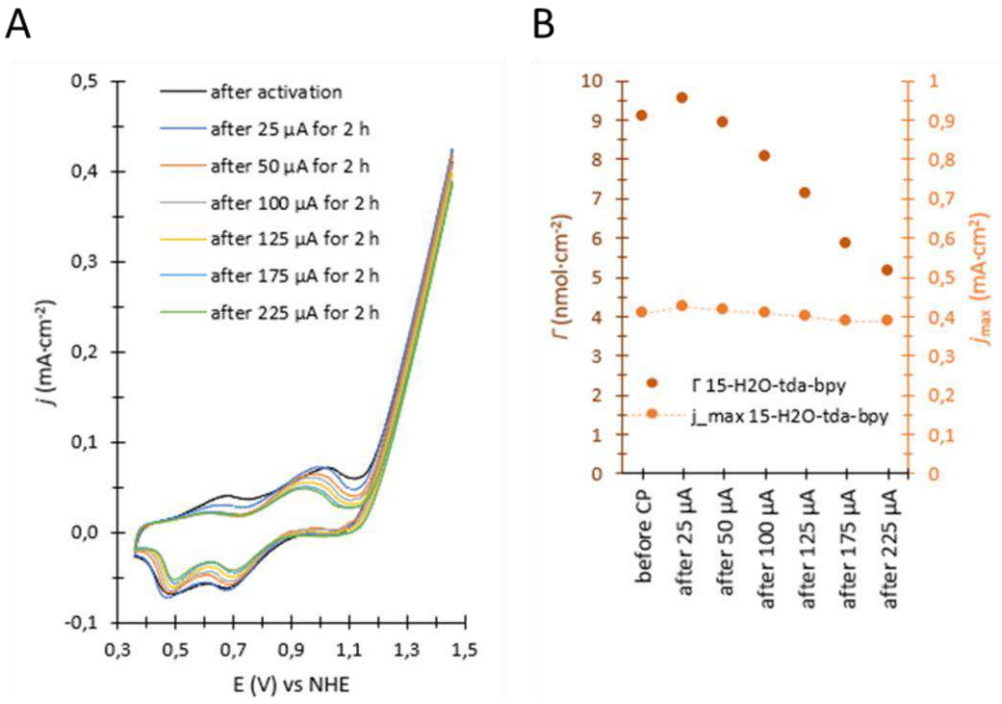

Figure 4. (A) CV evolution of **15-H_2O@CNT@PE** during CPE, taken after each step, in 1.0 M phosphate buffer pH 7 with 10 $mV \cdot s^{-1}$. **(B)** Γ (dark red marks) and j_{max} (orange marks with dashed line) of **15-H_2O@CNT@PE**, obtained from the corresponding CV.

A similar CV monitoring of the CP experiment was also carried out for **10-$(H_2O)_2$@CNT@PE** and the results are shown in Figure 5. As observed in the Γ vs i_{app} plot, there seems to be a process of oligomeric reorganization within the CNT, that increases the number of active sites accessibility to the electrode as the CP proceeds up to 125 µA where it then becomes constant. An additional long term CP experiment was carried out at 100 µA for 20 h for

10-(H_2O)$_2$@CNT@PE and **15-(H_2O)@CNT@PE**, that again showed a stable behavior over the whole experiment (Figure SI-17 and Table 2), with *E* values of 1.36 and 1.65 V and TONs of 15.500 and 39.800, respectively. Finally, a CA experiment was carried out for **15-(H_2O)@CNT@PE** at a constant E_{app} = 1.45 V for 20 h, again showing a high stability achieving more than 58.100 TONs (Table 2 and Figure SI-15).

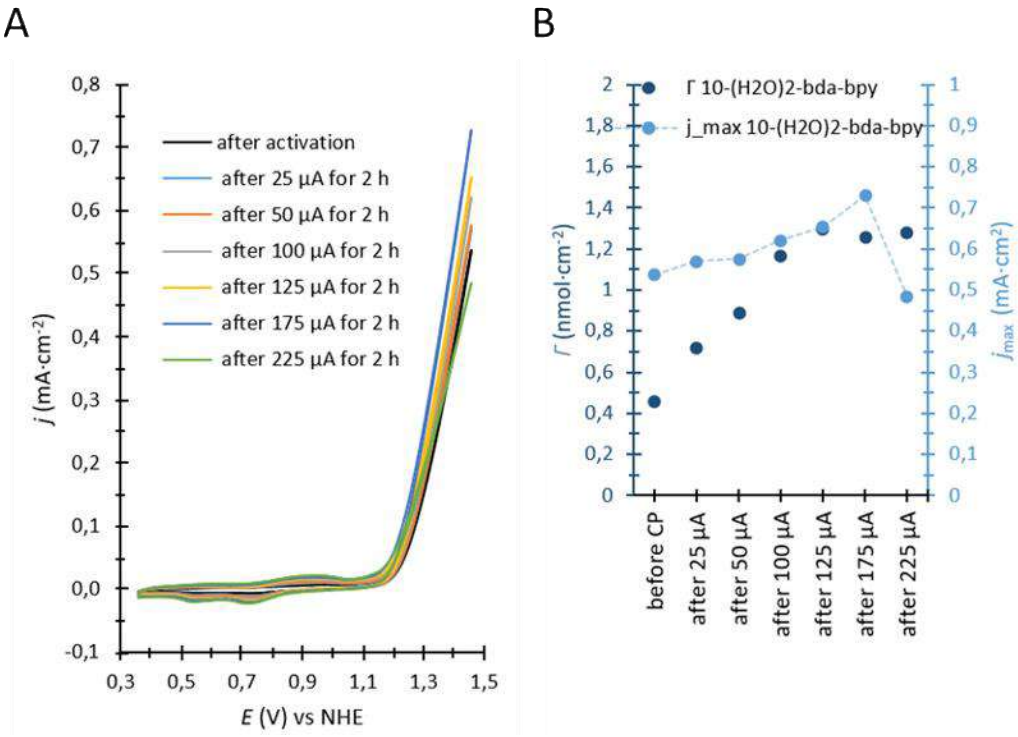

Figure 5. (A) CV evolution of **10-(H_2O)$_2$@CNT@PE** during CP, taken after each CP step, in 1.0 M phbf pH 7 with 10 mV·s^{-1}. **(B)** Γ (dark blue marks) and j_{max} (blue marks with dashed line) of **10-(H_2O)$_2$@CNT@PE**, obtained from the corresponding CV.

3. Conclusions

Herein, we have shown the viability constructing flexible molecular screen-printed electrodes MPEs based on the MBM binder for conductive graphite and adhesive for Nafion membrane, and described their performance, after the immobilization of a catalyst, as a molecular electro-anode for water oxidation catalysis. The catalyst anchoring has been carried out *via* supramolecular CH-π and π-π interactions showing an exceptional stability during turnover. This anchoring achieves a large degree of surface coverage and is preferred to covalent bonding since no additional functionalization is needed in the case of CH-π interaction. In addition, it

does not require the modification of the graphitic surfaces that can lead to a reduce conductivity of the latter.

The overall performance of the electro-anode has been monitored based on electrochemical techniques and display long term stability for 12-20 h reaching TON values of 144.800 in case of **10-$(H_2O)_2$@CNT@PE**. The current densities achieved by the MPE are mainly limited by the overall conductivity of the MPE and not by the surface coverage or the intrinsic activity of the WOC. If higher current densities were needed then more conductive binders or mixing of binders/graphite would be required. Over long catalytic periods of time, the loading of the electrode slowly but progressively decreases due to the de-anchoring of the CNTs from the screen-printed electrode. The possibility of including highly porous graphitic materials where the catalyst could be anchored beforehand will substantially increase its stability.

In conclusion, we have demonstrated the viability of generating robust and efficient MPEs, which still lots of room for improvement but that can already be used for their implementation into printed PECs.

Supporting Information

Additional details on the preparation of printed electrodes and complementary electrochemical experiments.

Acknowledgments

Support from Ministerio de Ciencia, Innovacion y Universidades and FEDER (PID2019-111617RB-I00), AGAUR 2017-SGR-1631, Ministerio de Ciencia e Innovacion for a Severo Ochoa Excellence Accreditation grant 2020-2023 (CEX2019-000925-S, MIC/AEI)" and EU-funded ITN eSCALED (Grant agreement ID: 765376) are gratefully acknowledged.

References:

(1) Lewis, N. S. Research Opportunities to Advance Solar Energy Utilization. *Science*. 2016.

(2) Ventosa, M.; Oliveras, J.; Bastús, N. G.; Gimbert-Suriñach, C.; Puntes, V.; Llobet, A. Nanocrystal-Molecular Hybrids for the Photocatalytic Oxidation of Water. *ACS Appl. Energy Mater.* **2020**.

(3) Nocera, D. G. The Artificial Leaf. *Acc. Chem. Res.* **2012**, *45*, 767–776.

(4) Kärkäs, M. D.; Verho, O.; Johnston, E. V.; Åkermark, B. Artificial Photosynthesis: Molecular Systems for Catalytic Water Oxidation. *Chemical Reviews*. 2014, 11863–12001.

(5) Berardi, S.; Drouet, S.; Francàs, L.; Gimbert-Suriñach, C.; Guttentag, M.; Richmond, C.; Stoll, T.; Llobet, A. Molecular Artificial Photosynthesis. *Chemical Society Reviews*. 2014, 7501–7519.

(6) Sala, X.; Maji, S.; Bofill, R.; García-Antón, J.; Escriche, L.; Llobet, A. Molecular Water Oxidation Mechanisms Followed by Transition Metals: State of the Art. *Acc. Chem. Res.* **2014**, *47*, 504–516.

(7) Garrido-Barros, P.; Gimbert-Suriñach, C.; Matheu, R.; Sala, X.; Llobet, A. How to Make an Efficient and Robust Molecular Catalyst for Water Oxidation. *Chemical Society Reviews*. 2017, pp 6088–6098.

(8) Shaffer, D. W.; Xie, Y.; Concepcion, J. J. O-O Bond Formation in Ruthenium-Catalyzed Water Oxidation: Single-Site Nucleophilic Attack: Vs. O-O Radical Coupling. *Chemical Society Reviews*. 2017, 6170–6193.

(9) Tahir, M.; Pan, L.; Idrees, F.; Zhang, X.; Wang, L.; Zou, J. J.; Wang, Z. L. Electrocatalytic Oxygen Evolution Reaction for Energy Conversion and Storage: A Comprehensive Review. *Nano Energy*. Elsevier July 2017, 136–157.

(10) Schalenbach, M.; Zeradjanin, A. R.; Kasian, O.; Cherevko, S.; Mayrhofer, K. J. J. A Perspective on Low-Temperature Water Electrolysis - Challenges in Alkaline and Acidic Technology. *International Journal of Electrochemical Science*. 2018, 1173–1226.

(11) Matheu, R.; Ertem, M. Z.; Benet-Buchholz, J.; Coronado, E.; Batista, V. S.; Sala, X.; Llobet, A. Intramolecular Proton Transfer Boosts Water Oxidation Catalyzed by a Ru Complex. *J. Am. Chem. Soc.* **2015**, *137*, 10786–10795.

(12) Matheu, R.; Garrido-Barros, P.; Gil-Sepulcre, M.; Ertem, M. Z.; Sala, X.; Gimbert-Suriñach, C.; Llobet, A. The Development of Molecular Water Oxidation Catalysts. *Nature Reviews Chemistry*. 2019, 331–341.

(13) Ye, S.; Ding, C.; Liu, M.; Wang, A.; Huang, Q.; Li, C. Water Oxidation Catalysts for Artificial Photosynthesis. *Adv. Mat.* **2019**, 31, Article number 1902069.

(14) Concepcion, J. J.; Jurss, J. W.; Hoertz, P. G.; Meyer, T. J. Catalytic and Surface-Electrocatalytic Water Oxidation by Redox Mediator-Catalyst Assemblies. *Angew. Chemie - Int. Ed.* **2009**, *48*, pp 9473–9476.

(15) Assembly, C. R.; Norris, M. R.; Concepcion, J. J.; Fang, Z.; Templeton, J. L.; Meyer, T. J. Low-Overpotential Water Oxidation by a Surface-Bound Ruthenium-. *Angew. Chem. Int. Ed. Engl.* **2013**, *52*, 13580–13583.

(16) Hoque, M. A.; Gil-Sepulcre, M.; de Aguirre, A.; Elemans, J. A. A. W.; Moonshiram, D.; Matheu, R.; Shi, Y.; Benet-Buchholz, J.; Sala, X.; Malfois, M.; Solano, E.; Lim, J.; Garzón-Manjón, A.; Scheu, C.; Lanza, M.; Maseras, F.; Gimbert-Suriñach, C.; Llobet, A. Water Oxidation Electrocatalysis Using Ruthenium Coordination Oligomers Adsorbed on Multiwalled Carbon Nanotubes. *Nat. Chem.* **2020**, *12*, 1060–1066.

(17) Creus, J.; Matheu, R.; Peñafiel, I.; Moonshiram, D.; Blondeau, P.; Benet-Buchholz, J.; García-Antón, J.; Sala, X.; Godard, C.; Llobet, A. A Million Turnover Molecular Anode for Catalytic Water Oxidation. *Angew. Chemie Int. Ed.* **2016**, *55*, 15382–15386.

(18) Garrido-Barros, P.; Gimbert-Surinifach, C.; Moonshiram, D.; Picón, A.; Monge, P.; Batista, V. S.; Llobet, A. Electronic I-Delocalization Boosts Catalytic Water Oxidation by Cu(II) Molecular Catalysts Heterogenized on Graphene Sheets. *J. Am. Chem. Soc.* **2017**, *139*, 12907–12910.

(19) Parat, C.; Betelu, S.; Authier, L.; Potin-Gautier, M. Determination of labile trace metals with screen-printed electrode modified by a crown-ether based membrane. *Analytica Chimica Acta* **2006,** *573-574*, 14-19.

(20) Peng, B.; Li, Y.; Zhao, Z.; Chen, Y.; Han, C.C. Facile Surface Modification of PVDF Microfiltration Membrane by Strong Physical Adsorption of Amphiphilic Copolymers. *J. Appl. Polym. Sci.* **2013**, *130*, 3112-3121.

(21) Billon, L.; Gerard, P.; Marcasuzaa, P.; Save, M. Sheets comprising a fluorinated polymer and presenting a variable wettability with respect to a fluid as a function of pH and/or temperature. *WO Patent* 2015170030, **2015.**

(22) Zaouak, O.; Authier, L.; Cugnet, C.; Castetbon, A.; Potin-Gautier, M. Electroanalytical device for cadmium speciation in waters : Development and characterization of a

reliable screen-printed sensor. *Electroanalysis* **2010,** *22*, 1151-1158.

(23) Results, R. paper-U. No Title.

(24) Matheu, R.; Neudeck, S.; Meyer, F.; Sala, X.; Llobet, A. Foot of the Wave Analysis for Mechanistic Elucidation and Benchmarking Applications in Molecular Water Oxidation Catalysis. *ChemSusChem* **2016**, *9*, 3361–3369.

Supplementary information

Robust and Efficient Screen-Printed Molecular Anodes with Anchored Water Oxidation Catalysts

Table of Contents

Method 118

Materials. 118

Instrumentation. 118

Electrochemical Methods 118

Surface Coverage Γ. 119

TOF_{max} Determination by FOWA 120

Synthesis of the Catalysts. 120

Determination of average chain length of oligomer catalysts. 121

^{1}H-NMR Spectroscopy 127

Electrochemical Characterization 129

DPV before and after activation 130

TOF_{max} Calculation by FOWA 131

CPE of 1-tda-pyp@CNT@PE and 15-tda-bpy@CNT@PE 134

CVs for CP 25 – 225 µA 135

CV for CP at 100 µA over 20 hours 138

CVs for CA at 1.45 V over 20 hours 141

Method

Materials. All chemicals utilized in this work were purchased by Sigma Aldrich and used without further purification unless explicitly indicated. $RuCl_3 \cdot xH_2O$ was purchased by Alfa Aesar, Multi-Walled Carbon Nanotubes (MWCNTs) was provided by HeJi, Inc. (Zengcheng city, China) in bulk with >95 % purity, >50 nm OD and ~10 μm length and the MBM triblock copolymer was provided Kuraray Co., Ltd. (LA4285) (Japan). Solvents were dried and purified with a SPS® system and degassed by bubbling with nitrogen before starting the reactions. 4-(pyrene-1-yl)pyridine (pyp), [2,2':6',2''-terpyridine]-6,6''-dicarboxylic acid (H_2tda) and the precursor complexes $[RuCl_2(DMSO)_4]$, [Ru(tda)(DMSO)(X)] and [Ru(bda)(DMSO)(X)], with X being either a second DMSO or chloro ligand, were prepared according to reported procedures.[1] High purity deionized water for the electrochemical experiments was obtained by passing distilled water through a nanopure Mili-Q water purification system. For other spectroscopic and electrochemical studies HPLC-grade solvents were used.

Instrumentation. Bruker Avance 500 MHz was used to carry out ^{1}H-NMR spectroscopic measurements. All measurements were performed at room temperature in the corresponding deuterated solvent, using residual protons as internal reference.
The pH value of the electrolytes was determined with a CRISON Basic 20+ pH meter, which was calibrated before measurements with standard solutions at pH 4.0, 7.0 and 9.2.

Electrochemical Methods. All electrochemical experiments were performed with a CHI-660 potentiostat from IJ-Cambria. Printed electrodes with an area of A = 0.196 cm^2 were used as working electrode (WE), except for the long time chronopotentiometric test at 100 μA of 10-$(H_2O)_2$-bda-bpy. For this test working electrode with an area of $A_{bda,\ 100\ \mu A\ CP}$ = 0.126 cm^2 was used. As counter electrode (CE) a platinum mesh and as reference electrode (RE) a Hg/Hg_2SO_4 (sat. K_2SO_4) was used for all experiments. As electrolyte, a 1.0 M phosphate buffer was used for pH 7. For electrochemical experiments in pH 12 also a 1.0 M phosphate buffer

[1] Creus, J.; Matheu, R.; Peñafiel, I.; Moonshiram, D.; Blondeau, P.; Benet-Buchholz, J.; García-AntÓn, J.; Sala, X.; Godard, C.; Llobet, A., A Million Turnover Molecular Anode for Catalytic Water Oxidation. *Angew. Chem. Int. Ed*. **2016**, 55, 1-6.

was used. All experiments were examined in a two compartment cell (H-shape with frit, V_{total} = 10 mL). All reported potentials are converted to vs NHE by adding 0.65 V.

Preparation of different phosphate buffers, filling up with Mili-Q water:

1) pH 7, I = 1.0 M: NaH_2PO_4 (0.081 mol, 9.75 g) and Na_2HPO_4 (0.141 mol, 19.95 g) in 0.5 L MiliQ H_2O (pH measured 7.14)
2) pH 12, I = 1.0 M: Na_2HPO_4 (0.027 mol, 3.90 g) and Na_3PO4 (0.070 mol, 11.40 g) in 0.5 L MiliQ H_2O (pH measured 11.6)

Cyclic Voltammetry (CV). In a typical CV experiment, the previously described setup was used. The samples were cycled in the 1.0 M phosphate buffer (pH 7) two times between E_i = 0.35 V and E_f = 1.45 V with a scan rate of 10 $mV \cdot s^{-1}$ and 1 kΩ iR compensation. Only the second cycle is reported.

Differential Puls Voltammetry (DPV). The electrochemical cell was the same as for the other experiments. The DPV parameters were ΔE = 4 mV, Amplitude = 50 mV, Pulse width = 0.05 s, Sampling width = 0.0167 s, Pulse period = 0.5 s, E_I = 0.35 V, E_f = 1.45 V. 1 kΩ iR was compensated. The 1.0 M phosphate buffer (pH 7) was used as electrolyte.

Controlled Potential Electrolysis (CPE). The CPE was also done in the two compartment cell in the 1.0 M phosphate buffer (pH 12). The applied potential was 1.32 V for 1000 s. A stirring bar was added in the compartment with the WE.

Chronopotentiometry (CP). Chronopotentiometric measurements were conducted in the previously described electrochemically setup in the 1.0 M phosphate buffer at pH 7. A stirring war was added in the compartment with the WE.

Chronoamperometry (CA). The measurement was done in the usual two compartment cell in pH 7 1.0 M phosphate buffer at 1.45 V. In the compartment with the WE a magnetic stirrer was subjoined.

Surface Coverage Γ. The surface coverage of the electrodes was determined in CV by following equations:

$$\Gamma \ [\mathrm{nmol \cdot cm^2}] = \frac{Q_{\mathrm{Ru}}}{n \cdot A \cdot F} \qquad \text{(SI1)}$$

With Q_{Ru} for the catalysts with bda^{2-} equatorial ligand:

$$Q_{\mathrm{Ru}} = \frac{Q_{\mathrm{Ru^{III}/Ru^{II}}} + Q_{\mathrm{Ru^{IV}/Ru^{III}}} + Q_{\mathrm{Ru^{V}/Ru^{IV}}}}{3} \qquad \text{(SI2)}$$

For catalysts with tda^{2-} equatorial ligand:

$$Q_{Ru} = \frac{Q_{Ru^{III}/Ru^{II}} + Q_{Ru^{IV}/Ru^{III}}}{2} \quad \text{(SI3)}$$

Q_{Ru} is the average charge detected in CV by integrating the area of the reduction peaks (Q). For the catalysts with bda^{2-} ligand there are three one electron transfers (n = 1) for Ru^{III}/Ru^{II}, Ru^{IV}/Ru^{III} and Ru^{V}/Ru^{IV}, respectively. For the catalysts with the tda^{2-} ligand there are only two one electron transfers (n = 1) for Ru^{III}/Ru^{II} and Ru^{IV}/Ru^{III}. The active area of the WE is denoted with A and is either $A = 0.196\ cm^2$ or for the single case describe above for bda^{2-}, 100 µA CP, $A = 0.126\ cm^2$. F is the Faradaic constant (96 485.33 $C \cdot mol^{-1}$). The calculated surface coverages for all electrodes are listed in **Table SI-1**.

TOF_{max} Determination by FOWA. The maximum turnover frequency was calculated by foot of the wave analysis of the CVs according to [REF], following the equation:

$$\frac{i}{Q_{Ru}} = \frac{k_{WNA}}{1 + \exp\left(\frac{F(E^0 - E)}{RT}\right)} \quad \textit{(SI4)}$$

With i as current, Q_{Ru} as average charge detected by the CV as described above, F is the faraday constant, E^0 is the redox potential of the active species (Ru^{V}/Ru^{IV} for 1-H_2O-tda-pyp and 15-H_2O-tda-bpy and Ru^{VI}/Ru^{V} for 10-H_2O-bda-bpy), E is the applied potential, R is the universal gas constant (8.314 $J \cdot mol^{-1} \cdot K^{-1}$) and T the absolute temperature (293.15 K). The pseudo reaction rate constant of the WNA, k_{WNA}, is graphically determined as slope, by plotting $\frac{i}{Q_{Ru}}$ over $\frac{1}{1+\exp\left(\frac{F(E^0-E)}{RT}\right)}$. Since for heterogeneous catalysis TOF_{max} is equal to k_{WNA}, with the determination of the pseudo reaction rate constant, also the maximum turnover frequency is obtained. It is illustrated in Erreur ! Source du renvoi introuvable. to **19**.

Synthesis of the Catalysts.

All catalysts were synthesized under inert atmosphere and according to literature.

[Ru(tda)(pyp)$_2$]. A mixture of [Ru(tda)(DMSO)(X)], with X being DMSO or Cl, and 4-(pyrene-1-yl)pyridine were dispersed in a degassed solution of MeOH:H_2O (3:2) and refluxed for three days. The appeared brown solid precipitate was separated, washed with H_2O, MeOH and Et_2O. After drying under vacuum, an orange-brown powder was obtained. [EF

{[Ru(tda)(bpy)]$_{15}$(bpy)}. In a two neck round bottom flask (100 mL) [Ru(tda)(DMSO)(OH_2)] and bpy was refluxed in degassed TFE for 3 days under argon atmosphere. Afterwards, the TFE solvent was completely evaporated. Dry and degassed MeOH

was added to the solid, resulting in a dark reddish solid in a red solution. The solid was filtered and washed with MeOH, H_2O, aceton, Et_2O and then dried under vacuum.

{[Ru(bda)(bpy)]$_{10}$(bpy)}. In a two neck round bottom flask [Ru(bda)$(DMSO)_2$] (97 mg, mol) was mixed with bpy (31 g, 0.2 mmol) in 10 mL degassed TFE:MeOH (9:1) and refluxed at 80 °C for 3 days. The solvent was evaporated. The solid was washed with a degassed mixture of DCM:MeOH (80:20).

Determination of average chain length of oligomer catalysts. The average chain length of 15-tda-bpy and 10-bda-bpy was detected by ^{1}H-NMR according to [REF]. The protons of 4,4'-bpy show peaks at different chemical shifts, depending on the position of the 4,4'-bpy in the 10-bda-bpy oligomer (
Figure **SI-** ***3***). For a bpy in end position, meaning being ligand to only one ruthenium center, the ^{1}H-NMR shows two distinct doublets for the protons of carbon 3, 3', 5 and 5' at chemical shifts 7.6 ppm – 7.2 ppm. As bridging ligand however, those peaks merge and shift to lower values. Only one doublet at 7.1 ppm – 7.0 ppm is detected for the protons of carbon 3, 3', 5 and 5' of the bridging ligands. By integrating and the following equation the average number of repetitive units is calculated:

$$n_{\mathrm{av,r.u.}} = \frac{2 \cdot \int \mathrm{H}_{\mathrm{bpy\ int.\ 1+2}}}{\int \mathrm{H}_{\mathrm{bpy\ ext.\ 1}} + \int \mathrm{H}_{\mathrm{bpy\ ext.\ 2}}} \qquad \textit{(SI5)}$$

In which $n_{\mathrm{av,r.u.}}$ is the average number of repetitive units of the oligomer $H_{\mathrm{bpy\ int.\ 1+2}}$, $H_{\mathrm{bpy\ ext.\ 1}}$ and $H_{\mathrm{bpy\ ext.\ 2}}$ are the peaks of the bridging ligands (=interior) and the ligands at the end of the chains (=exterior), respectively. The average chain length of the oligomer catalyst indicates the average number of ruthenium units per oligomer and is calculated with

$$n_{\mathrm{av}} = n_{\mathrm{av,r.u.}} + 1 \qquad \textit{(SI6)}$$

In which n_{av} is the average number of ruthenium units, which is equal to the average chain length of the oligomer. The determination of the chain length for **15-tda-bpy** followed the same procedure.

Preparation of MBM electrodes by screen printing method

MBM ink preparation. The hard-soft-hard triblock copolymer of poly(methyl methacrylate)-*b*-poly(*n*-butylacrylate)-*b*-polymethylmethacrylate (PMMA-*b*-PnBuA-*b*-PMMA) (MBM) is provided from Kuraray Co., Ltd. (LA4285). The three homemade conductive inks based on a graphite powder were prepared by thoroughly hand-mixing graphite

powder and MBM in different solvent, mesitylene and O-xylene with varied the percentage ratio of MBM-graphite contents, the concentration of MBM in the mixtures and printing conditions shown in Table1.

Briefly, MBM was add into a glass bottle containing 4 ml of mesitylene or 2 ml of O-xylene under continuous stirring for 6 h for mesitylene and 1.30 h for O-xylene. Then graphite powder for each formula were add and dispersed in the mixture with further stirring for 3 h or until all ingredients completely mixed. Polystyrene (PS) insulator was prepared by dissolved high impact polystyrene (HIPs) 6 g into 13 ml of mesitylene (460 g/L) with continuous stirring for 3-5 h. Electrodes were prepared by manual screen-printing method followed with concept of procedure from Bagel O. et al. and Zaouak O. et al. [2,3] A manual hardwood screen-printer was used to produce an array six couple electrode, the schematic illustration of electrode preparation and each electrode model corresponded to scheme1. MBM conductive ink was printed on a flexible Nafion substrate by forcing the ink pass through a screen mesh stencil. After drying for 2 h at room temperature under air atmosphere, a polystyrene insulator was printed manually over the conductive layer. After a few hours for completely drying under air atmosphere at room temperature the screen-printed electrodes are ready to use with working disk area for conductive reack is 0.126 cm^2 and auxiliary area disk for electrical contact is 0.196 cm^2.

Catalyst deposition for preparing modified electrodes. Hybrid material of multi-walled carbon nanotubes (MWCNT) and [Ru(tda)(L)2] (where tda2- is [2,2':6'2"-terpyridine]-6,6"-dicarboxylato and L is 4-(pyren-1-yl)pyridine) complex was used for modified MBM electrode. In this paper we name CNT-Ru complex for this catalyst. CNT-Ru complex 80 µl was deposited on working area of MBM electrode by drop casting method after electrode completely dry (the schematic illustration of deposition procedure was explained in **Scheme SI**.

[2] Bagel, O.; Limoges, B.; SchÖllhorn, B.; Degrand, C., Subfemtomolar Determination of Alkaline Phosphatase at a Disposable Screen-Printed Electrode Modified with a Perfluorosulfonated Ionomer film. *Anal. Chem*. 1997, 69, 4688-4694.

[3] Zaouak, O.; Authier, L.; Cugnet, C.; Castetbon, A.; Potin-Gautier, M., Electroanalytical Device for Cadmium Speciation in Water. Part1: Development and Characterization of a Reliable Screen-Printed Sensor. *Electroanalysis*. 2010, 22 (11), 1151-1158.

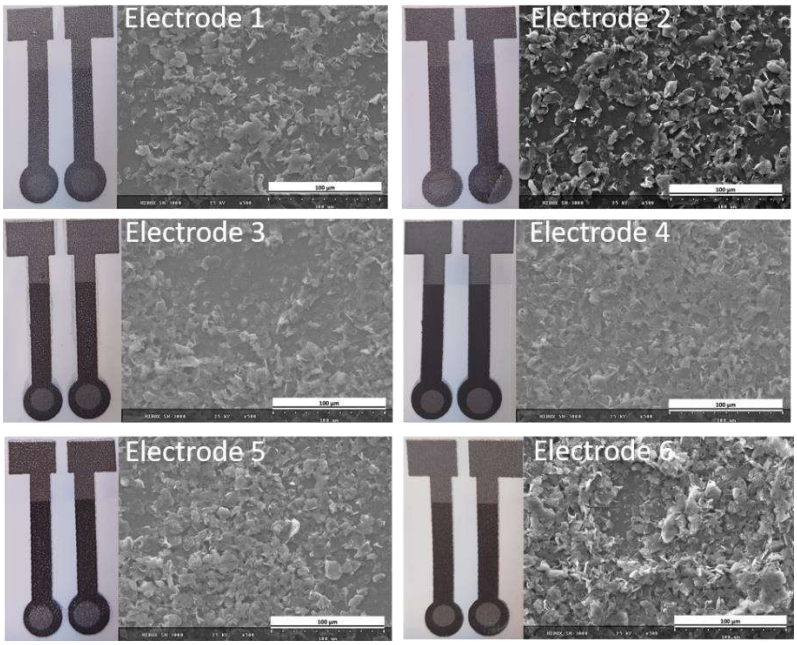

Figure SI. Photography and SEM images of electrodes reported in Table 1.

Anchoring catalyst in CNT and deposition on printed electrode (PE). illustrates the experimental procedure followed for the preparation of the working electrodes. For the anchoring of the catalyst onto the CNT, the catalysts were dissolved in TFE with a mass concentration of 1 mg/mL. The CNT were dispersed in tetrahydofuran (THF) by sonication for 40 minutes in the ultrasonic bath, also with a mass concentration of 1 mg/mL. Then those two solutions, oligomers and CNT, were mixed with a ratio of 1:10 (V:V) resulting in **Cat@CNT**. The dark whisky color of the catalyst in TFE disappeared after anchoring the catalyst onto the CNT. For ink formulation the solvents of the catalyst@CNT were evaporated overnight and the remaining powder dissolved in MeOH with a mass concentration of 1 mg/mL. The ink was sonicated for 4 minutes and then drop casted onto the printed electrodes 10 times with 4 µL each time, leading to a total volume of 40 µL on each printed electrode. Between each drop casting the solvent was completely evaporated (**Scheme SI-1**).

Table SI-1. Surface coverage, resistance and size of active area of all used electrodes.

Cat@CNT@PE	Experiment	iR (kΩ)	A (cm^2)	ρ (Ω·m)	σ S/m S	Surface coverage Γ (nmol·cm^2) Before exposure	After exposure
1-H_2O-tda-pyp	CP 25 µA – 225 µA	3.8	0.196			0.49	-
	CP 100 µA	4.1	0.126			0.05*	-
	CA 1.45 V	1.0	0.126			0.29	0
15-H_2O-tda-bpy	CP 25 µA – 225 µA	3.0	0.196			9.07	5.13
	CP 100 µA	3.8	0.196			6.13	2.25
	CA 1.45 V	1.2	0.196			0.80	0.63
10-$(H_2O)_2$-bda-bpy	CP 25 µA – 225 µA	2.0	0.196			0.46	1.28
	CP 100 µA	1.2	0.126			3.72	3.48
	CA 1.45 V	4.8	0.126			0.95	0.94

*Taken after 2 hours exposure.

	Resistivity, ρ Ω·m	Conductivity, σ = (1/ρ) S/m
Silver	1.59×10^{-8}	6.30×10^{7}

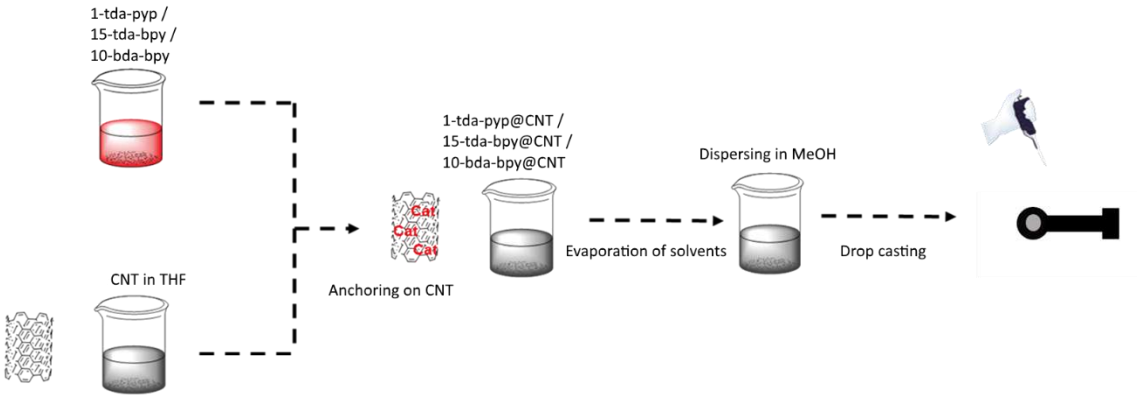

Scheme SI-1. Schematic drawing of the experimental procedure followed for preparing Cat@CNT and Cat@CNT@PE.

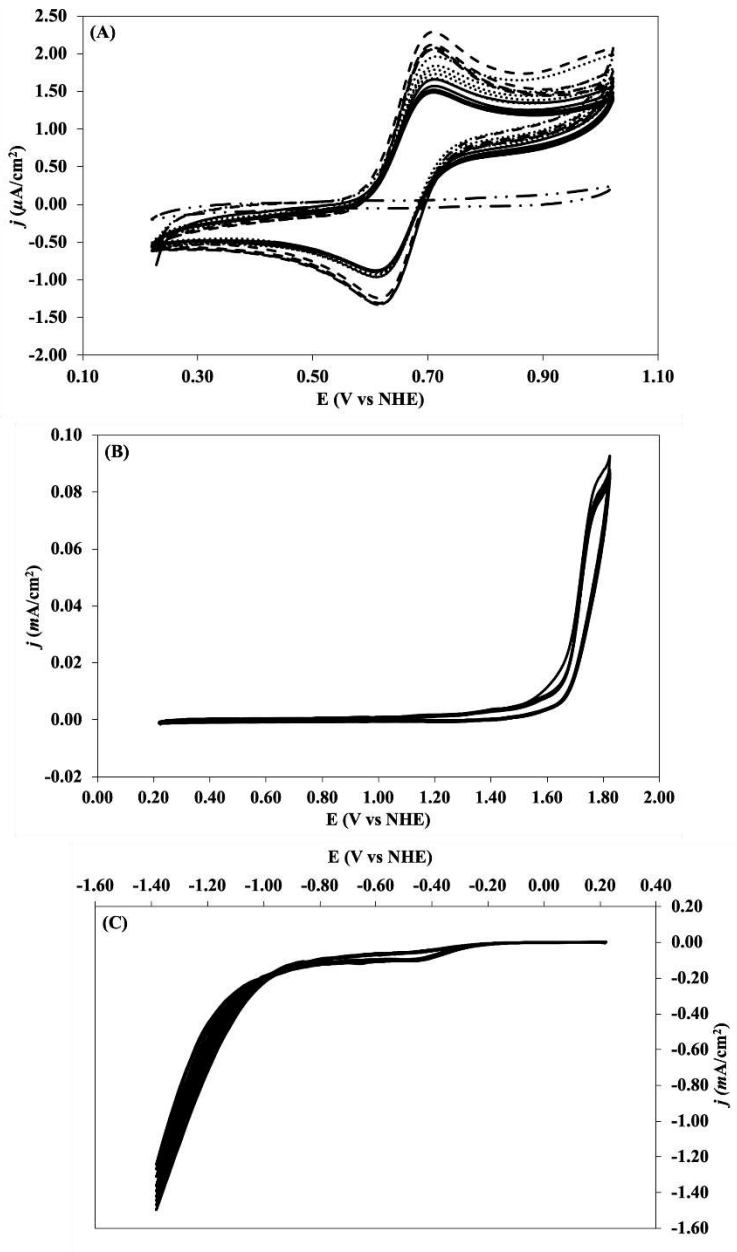

Figure SI-1. Reproducibility experiment (A) cyclic voltammogram (5 cycles) of 3 different electrodes scanning in phosphate buffer pH7 containing ferrocene derivative compound solution at 0.1 V/s; dash, dot and solid line correspond to the different electrodes. The CV of electrode without ferrocene is also shown (dash-dot line). Determination of operating potential window (B) and (C): CV of bare electrode in phosphate buffer pH7 at 0.1 V/s.

^{1}H-NMR Spectroscopy

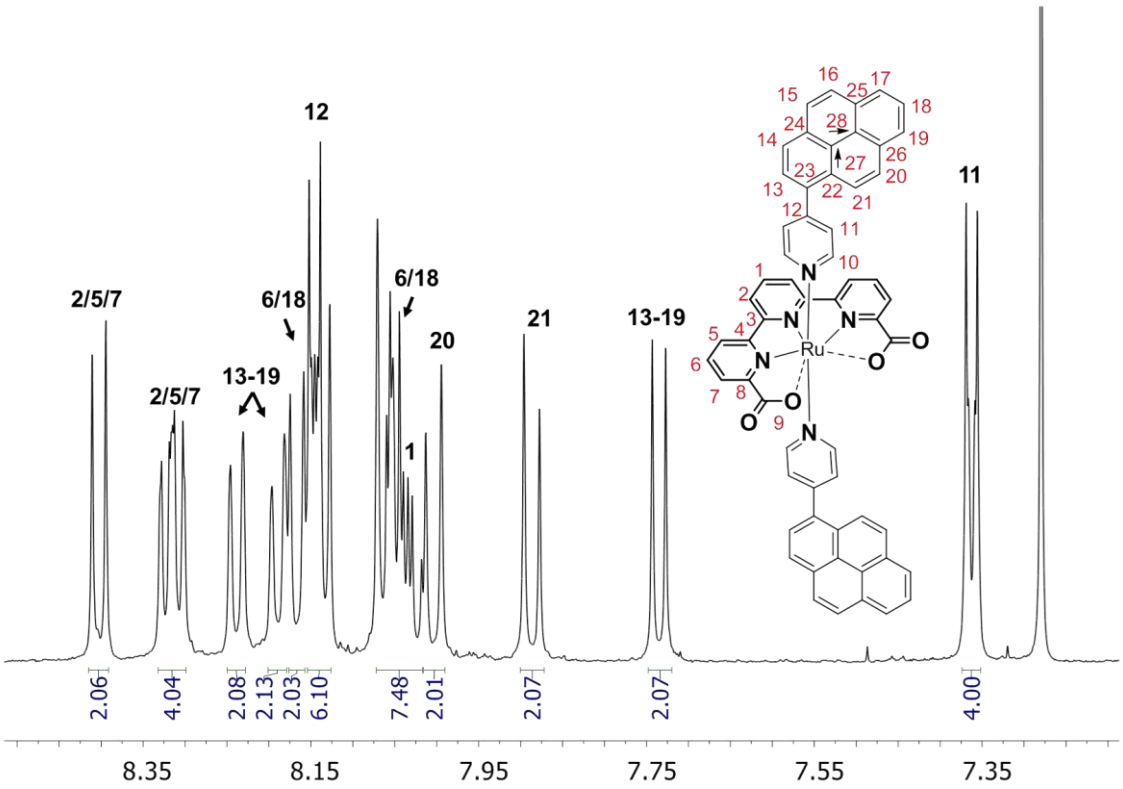

Figure SI-1. ^{1}H-NMR (500 MHz, 298 K, $CDCl_3$-d_3:TFE-d_3 (4:1)) for1-tda-pyp.

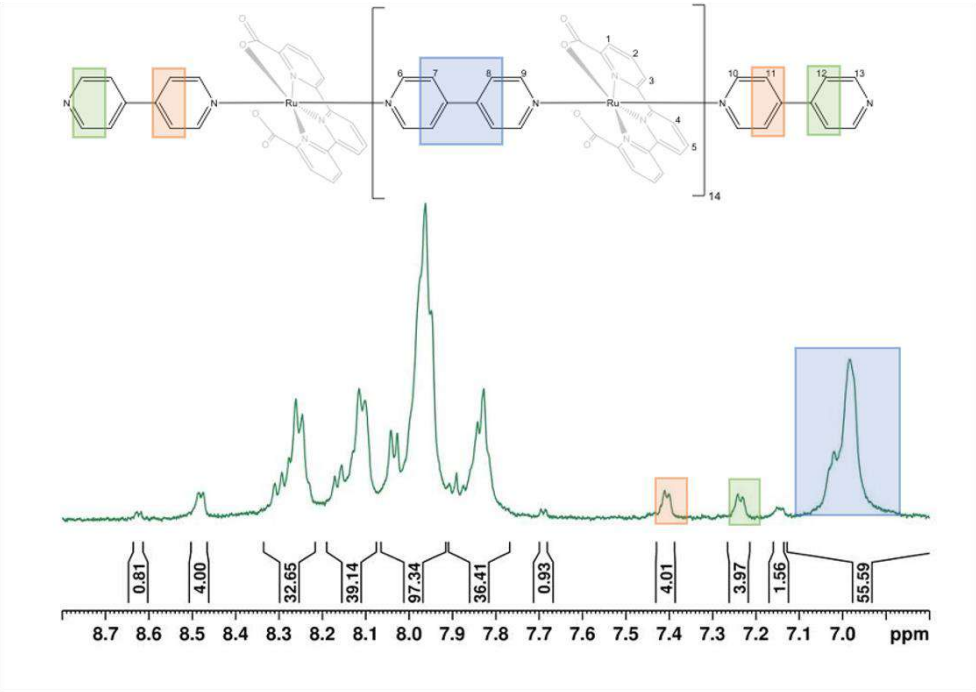

Figure SI-2. *^{1}H-NMR (500 MHz, 298 K, DCM-d_2:TFE-d_3 (4:1)) for 15-tda-bpy.*

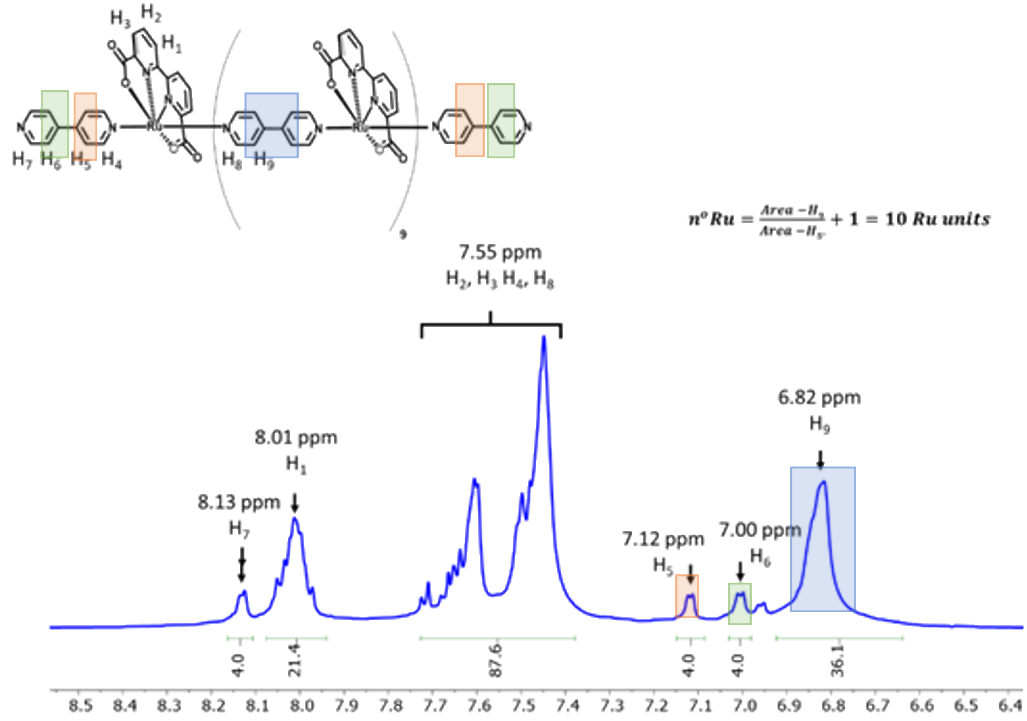

Figure SI- 3. ^{1}H-NMR (500 MHz, 298 K, DCM-d_2:TFE-d_3 (4:1)) of 10-bda-bpy.

Electrochemical Characterization

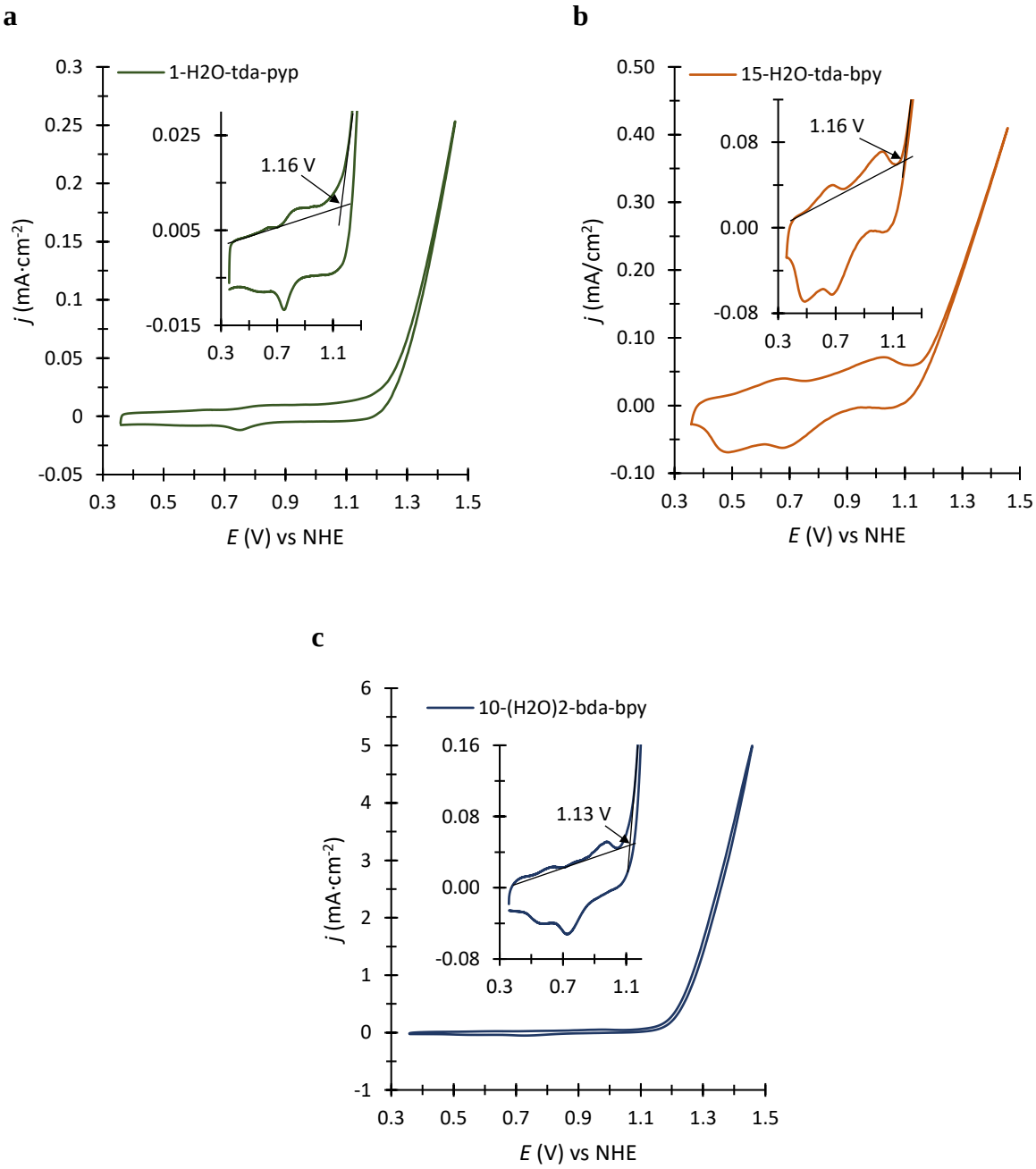

Figure SI-5. CV of the active species for determination of E_{onset}. **a**, for **1-H$_2$O-tda-pyp**. **b**, for **15-H$_2$O-tda-bpy**. **c**, for **10-(H$_2$O)$_2$-bda-bpy**. All catalysts are **@CNT@PE**. *Inset* enlargement of non-catalytic redox waves and E_{onset} region. The value of the onset potential was taken from the intersection of the baseline and the slope of the beginning of catalytic wave.

DPV before and after activation

a	**b**
DPV Ru-pyr on PE before and after activation So far no nice DPV was able to be obtained. For the last tries there was delamination and not Ru redox peaks. A new ink will be prepared and the DPV added ASAP.	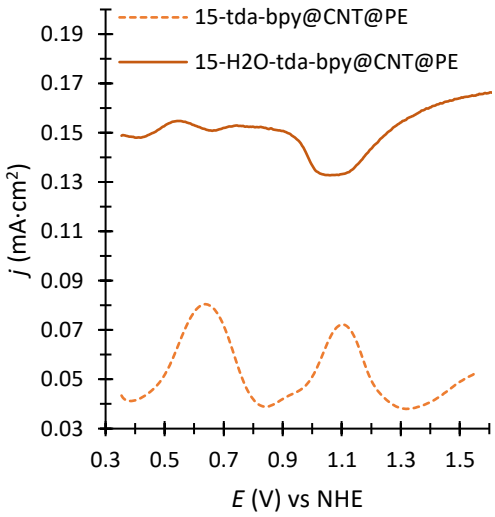
c	
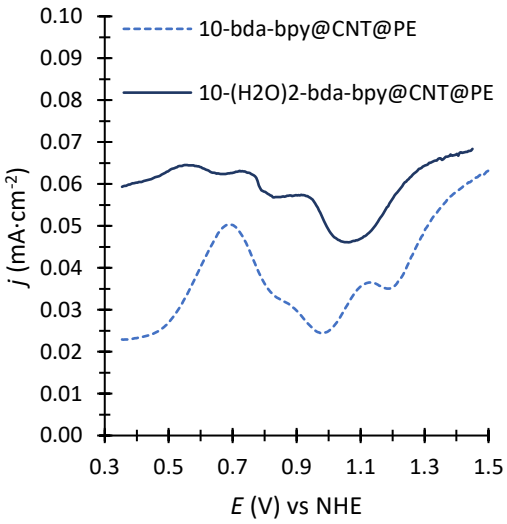	

Figure SI-4: DPV of a, 1-tda-pyp@CNT@PE (green dashed line) and 1-H_2O-tda-pyp@CNT@PE (green solid line), b, 15-tda-bpy@CNT@PE (orange dashed line) and 15-H_2O-tda-bpy@CNT@PE (orange solid line) with the clear shift of the two redox potentials to lower values. c, for 10-bda-bpy@CNT@PE (blue dashed line) and 10-$(H_2O)_2$-bda-bpy@CNT@PE (blue solid line) with the three redox couples, with a shift no lower values for the bisaquo species. All experiments were examined in 1.0 M phosphate buffer at pH 7.

TOF_{max} Calculation by FOWA

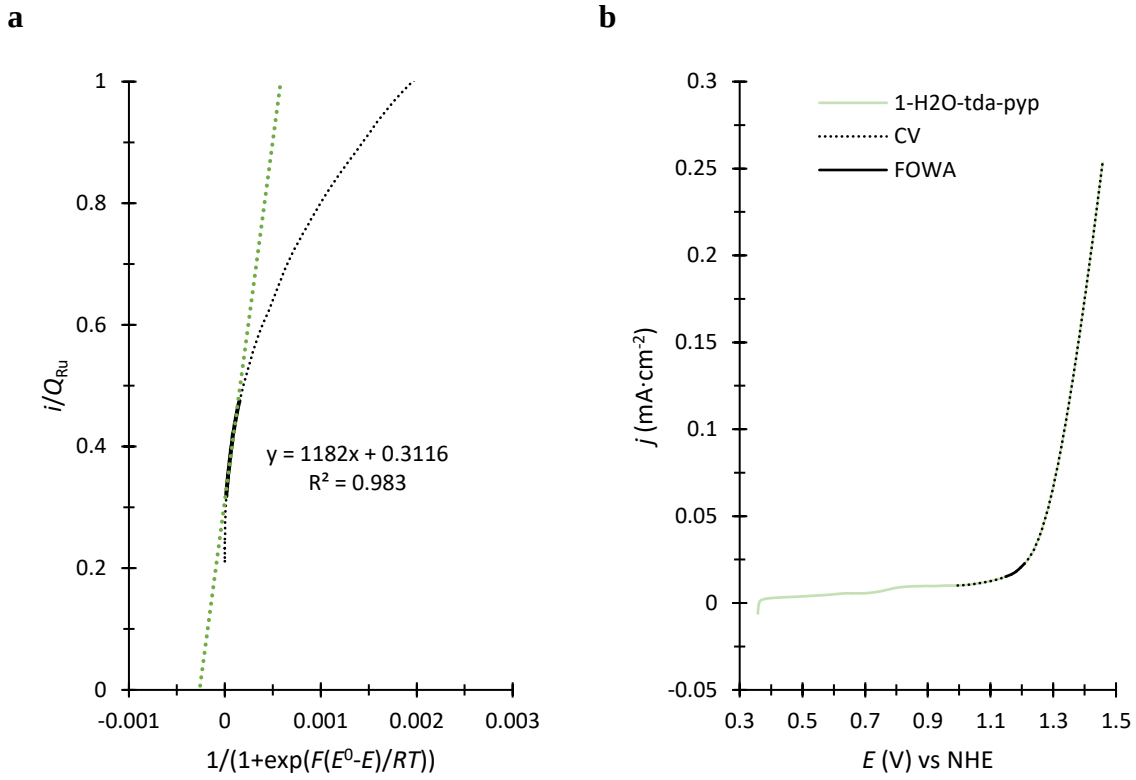

Figure SI-5. (a) TOF_{max} determination based on FOWA for 1-H_2O-tda-pyp@CNT@PE. (b) the corresponding part of the CV of the catalyst @CNT@PE in 1.0 M phosphate buffer (pH 7), taken with 10 $mV \cdot s^{-1}$. The dotted and solid black line shows the part of the CV and foot of the wave used in a.

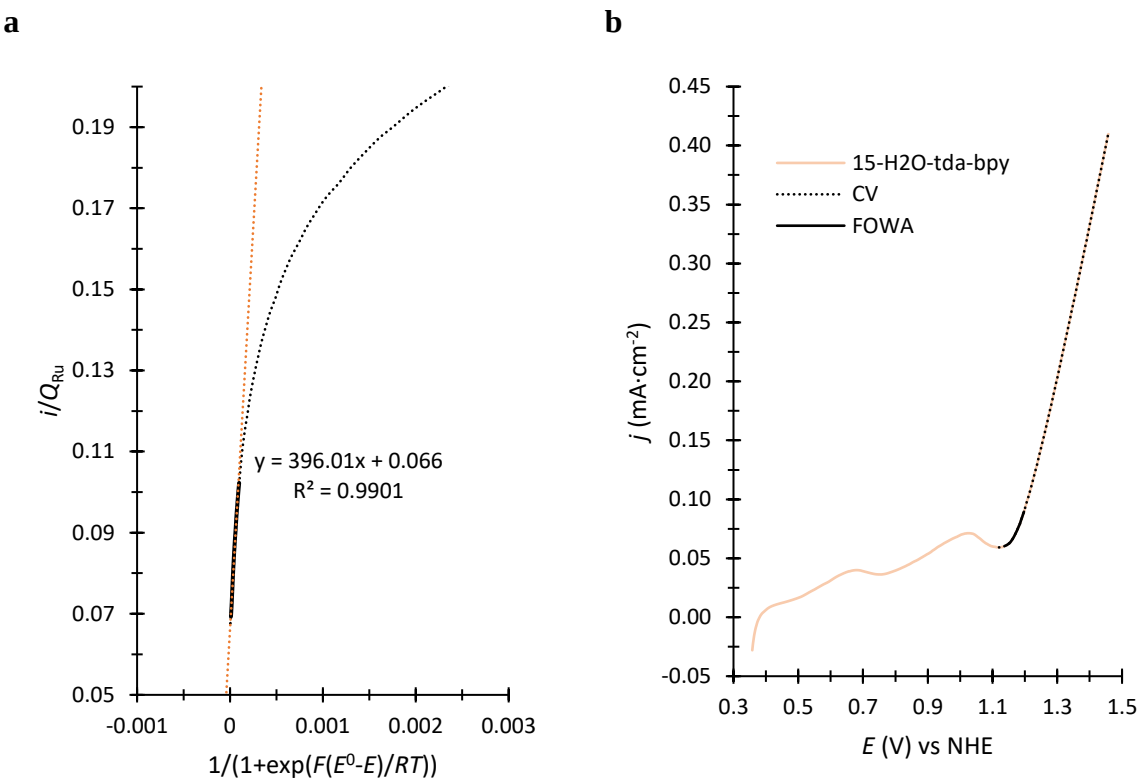

Figure SI-6. (a) TOF_{max} determination based on FOWA for 15-H_2O-tda-bpy@CNT@PE. (b) the corresponding part of the CV of the catalyst @CNT@PE in 1.0 M phosphate buffer (pH 7), taken with 10 $mV \cdot s^{-1}$. The dotted and solid black line shows the part of the CV and foot of the wave used in a.

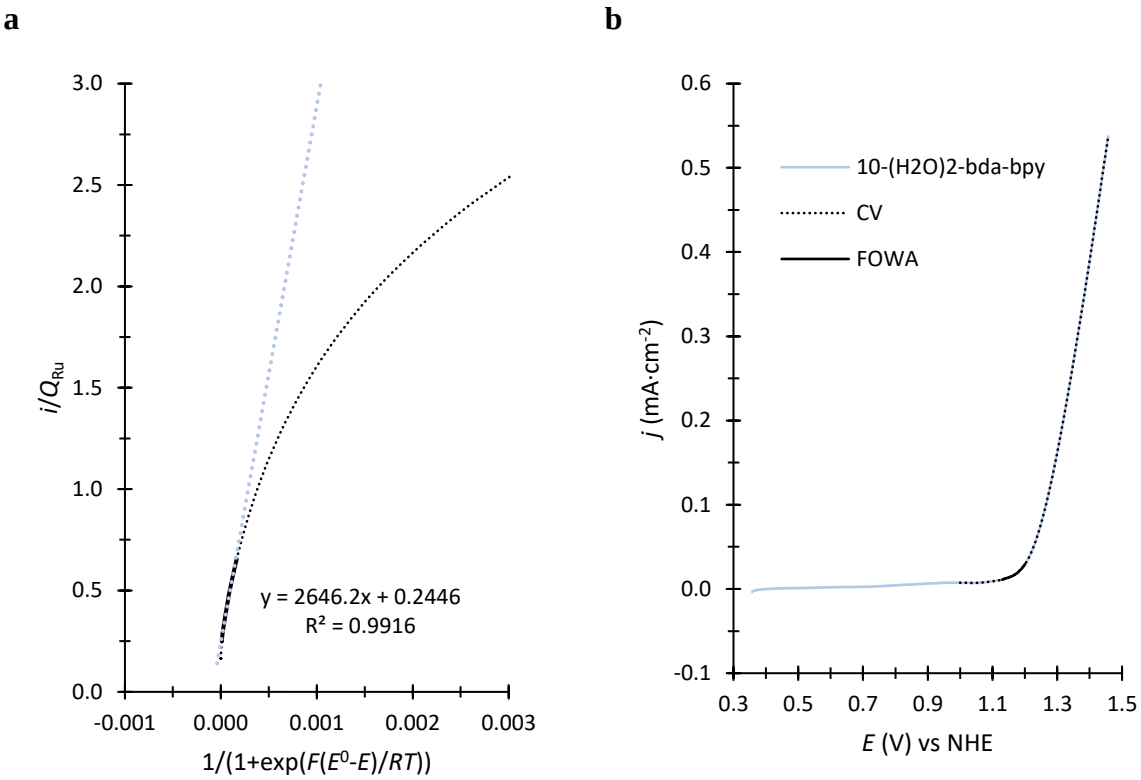

Figure SI-9. (a) TOF_{max} determination based on FOWA for 10-$(H_2O)_2$-bda-bpy@CNT@PE. (b) the corresponding part of the CV of the catalyst @CNT@PE in 1.0 M phosphate buffer (pH 7), taken with 10 $mV \cdot s^{-1}$. The dotted and solid black line shows the part of the CV and foot of the wave used in a.

CPE of 1-tda-pyp@CNT@PE and 15-tda-bpy@CNT@PE

a **b**

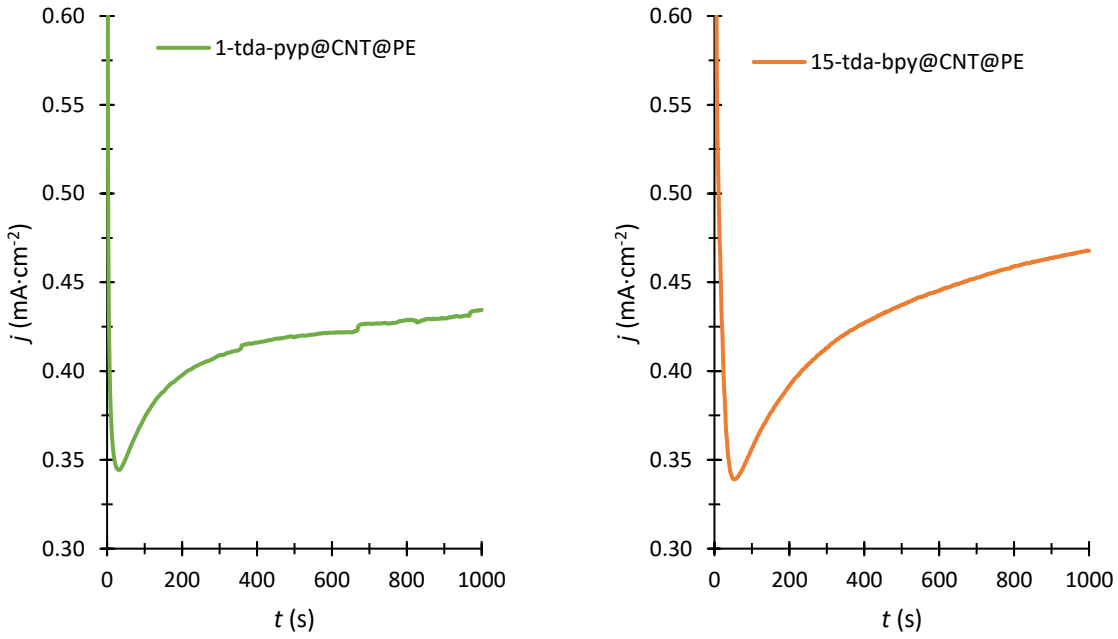

Figure SI-10. CPE of a, 1-tda-pyp@CNT@PE (green solid line) and b, 15-tda-pyp@CNT@PE (orange solid line) in a 1 M pH 12 phosphate buffer solution at 1.32 V for 1000 s. The CPE shows a drop of current density in the first few seconds, due to the oxidation of the precursor. The increase of current density after roughly 100 s is due to water oxidation.

CVs for CP 25 – 225 µA

a **b**

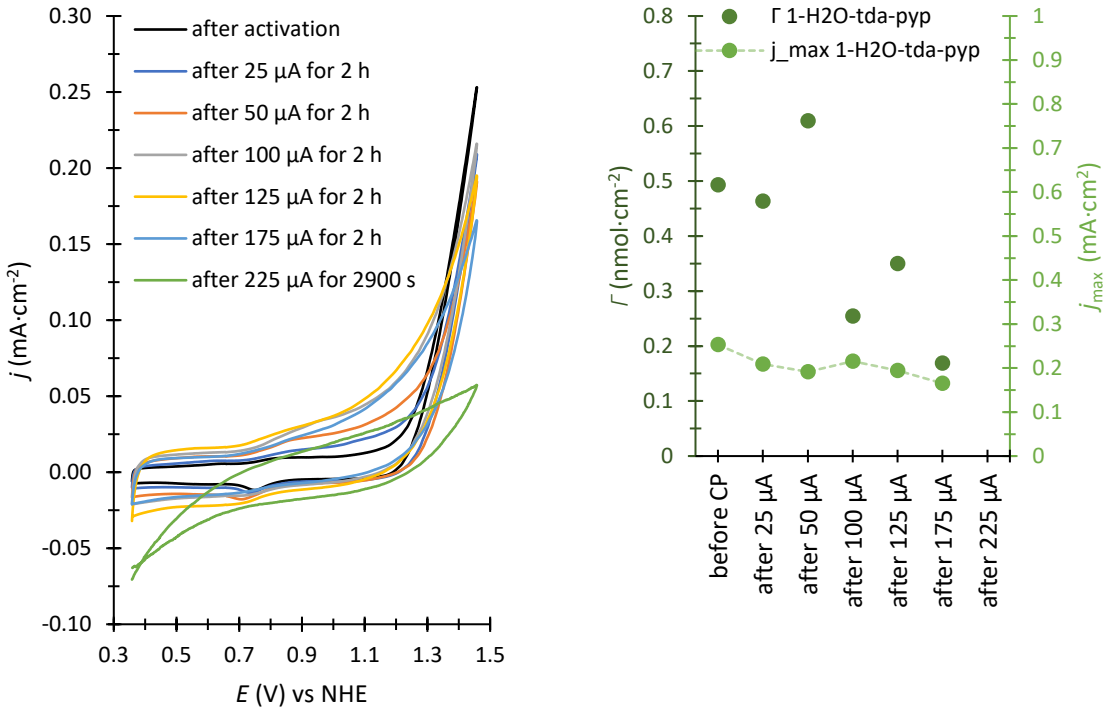

Figure SI-11. (a) CV evolution of 1-H_2O-tda-pyp@CNT@PE during CP, taken after each step, in 1.0 M phosphate buffer pH 7 with 10 $mV \cdot s^{-1}$. (b) Γ (dark green marks) and j_{max} (green marks with dashed line) of 1-H_2O-tda-pyp (@CNT@PE), obtained from the corresponding CV.

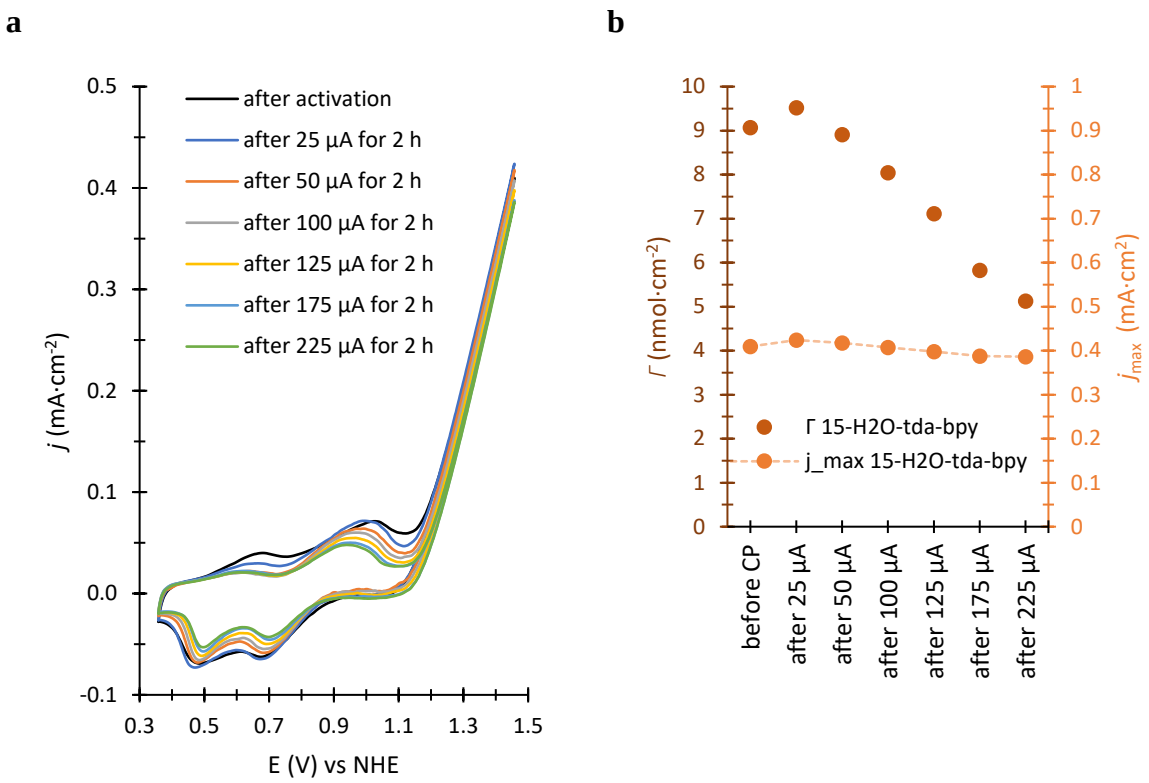

Figure SI-12. (a) CV evolution of 15-H_2O-tda-bpy@CNT@PE during CP, taken after each step, in 1.0 M phosphate buffer pH 7 with 10 $mV \cdot s^{-1}$. (b) Γ (dark red marks) and j_{max} (orange marks with dashed line) of 15-H_2O-tda-bpy (@CNT@PE), obtained from the corresponding CV.

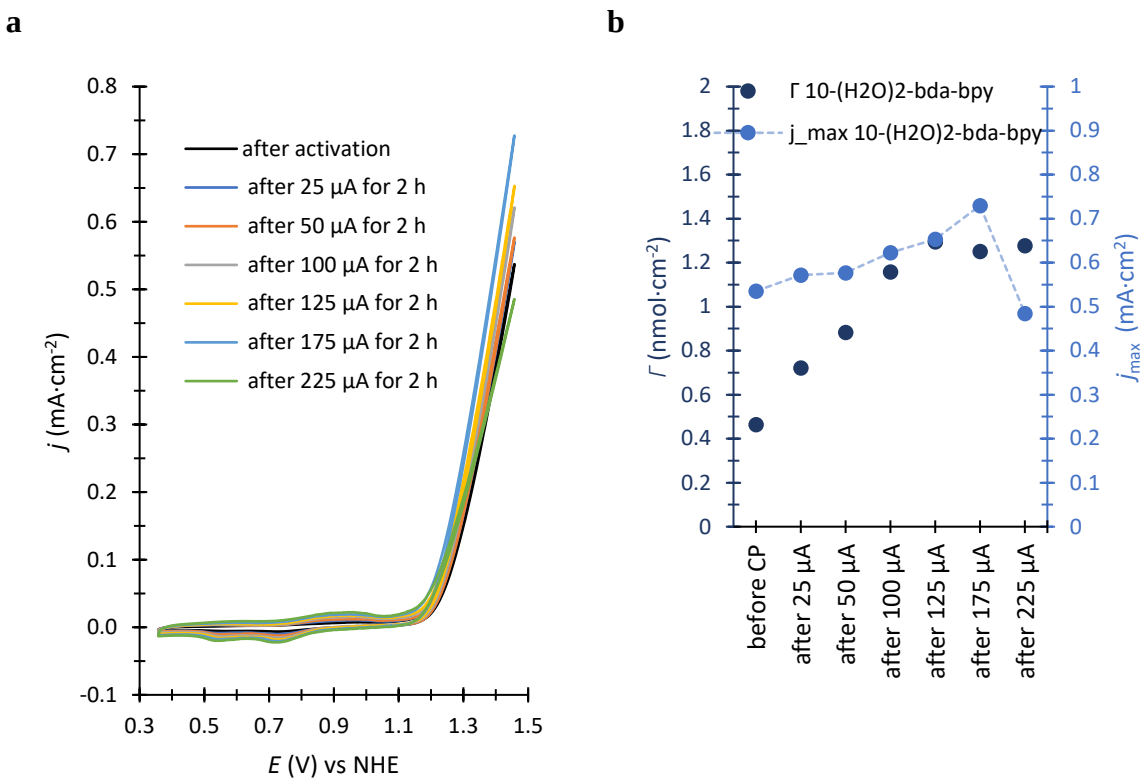

Figure SI-13. (a) CV evolution of 10-$(H_2O)_2$-bda-bpy@CNT@PE during CP, taken after each CP step, in 1.0 M phosphate buffer pH 7 with 10 $mV \cdot s^{-1}$. (b) Γ (dark blue marks) and j_{max} (blue marks with dashed line) of 10-$(H_2O)_2$-bda-bpy (@CNT@PE), obtained from the corresponding CV.

CV for CP at 100 µA over 20 hours

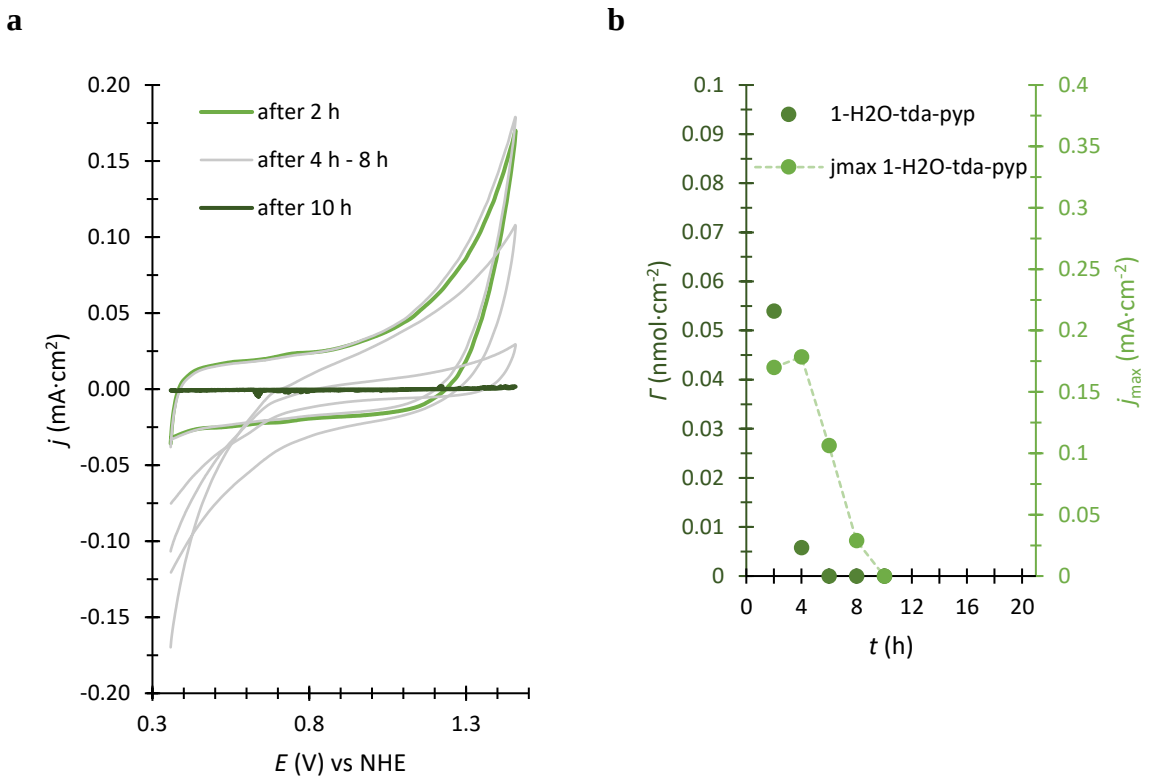

Figure SI-7. (a) CV evolution of 1-H_2O-tda-pyp@CNT@PE during CP at 100 µA, taken after every 2 h in 1.0 M phosphate buffer pH 7 with 10 $mV \cdot s^{-1}$ (after 2 h in green, during the CP in bright grey, after failure in in dark green). (b) Γ (dark green marks) and j_{max} (green marks with dashed line) of 1-H_2O-tda-pyp (@CNT@PE), obtained from the corresponding CV.

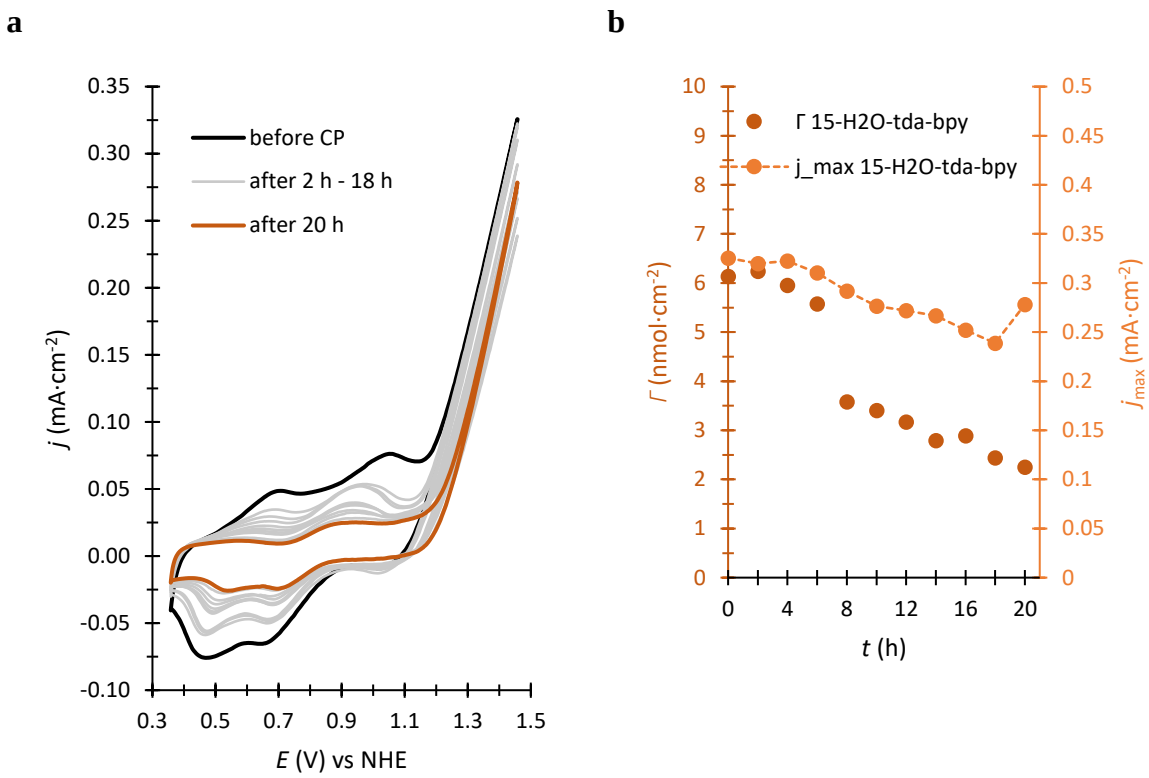

Figure SI-8. (a) CV evolution of 15-H_2O-tda-bpy@CNT@PE during CP at 100 µA, taken after every 2 h in 1.0 M phosphate buffer pH 7 with 10 $mV \cdot s^{-1}$ (before the CP in black, during the CP in bright grey, after the CP in dark red). (b) Γ (dark red marks) and j_{max} (orange marks with dashed line) of 15-H_2O-tda-bpy (@CNT@PE), obtained from the corresponding CV.

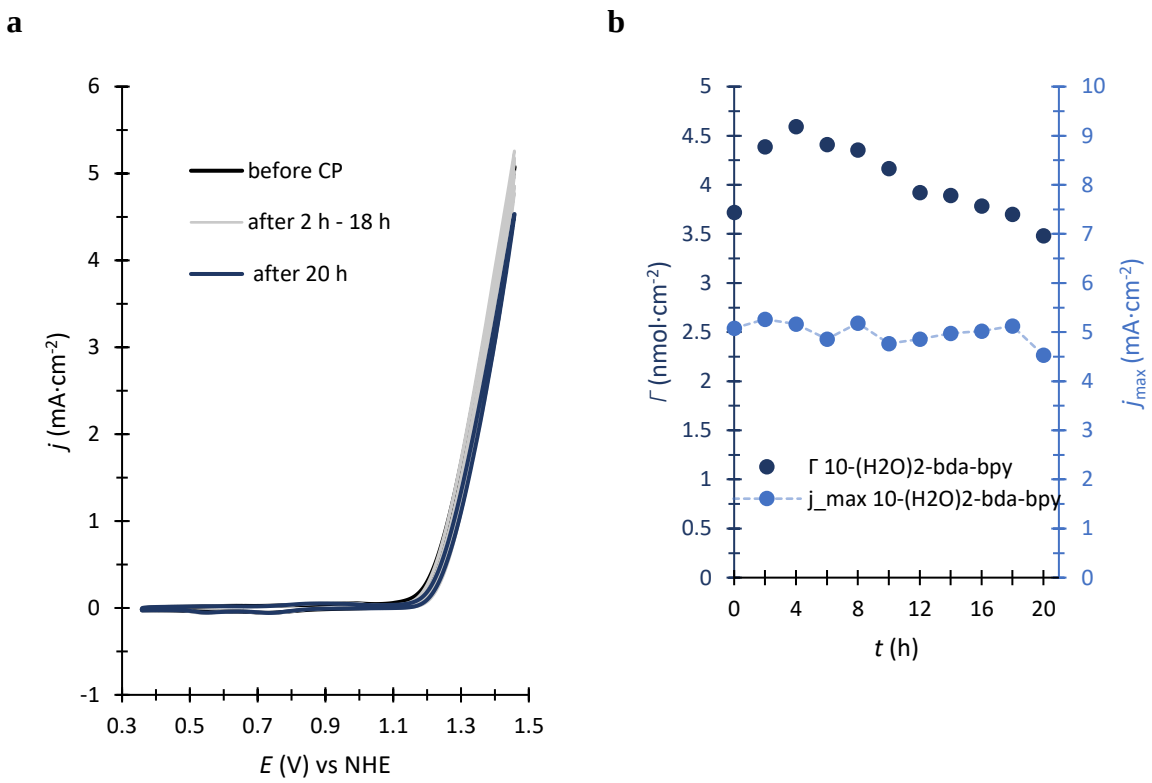

Figure SI-9 (a) CV evolution of 10-$(H_2O)_2$-bda-bpy@CNT@PE during CP at 100 µA, taken after every 2 h in 1.0 M phosphate buffer pH 7 with 10 $mV \cdot s^{-1}$ (before the CP in black, during the CP in bright grey, after the CP in dark blue). (b) Γ (dark blue marks) and j_{max} (blue marks with dashed line) of 10-$(H_2O)_2$-bda-bpy (@CNT@PE), obtained from the corresponding CV.

CVs for CA at 1.45 V over 20 hours

a *b*

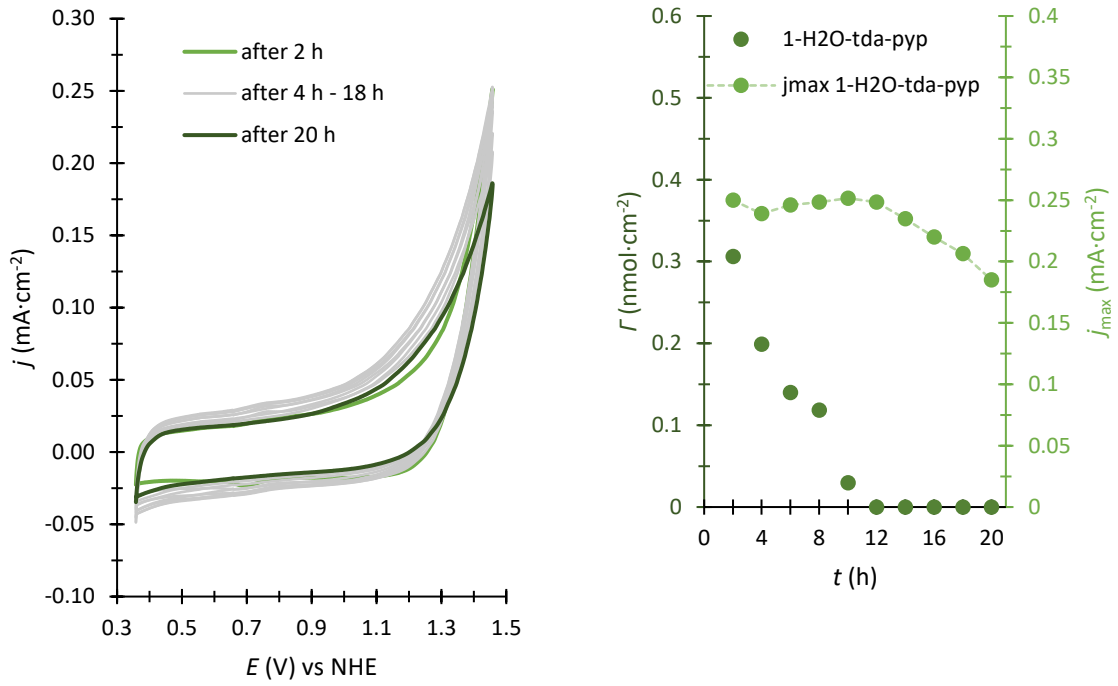

Figure SI-10 (a) CV evolution of **1-H_2O-tda-pyp@CNT@PE** during the CA experiment at 1.45 V, taken after every 2 h in 1.0 M phosphate buffer (pH 7) with 10 mV·s^{-1} (after . **(b)** Γ (dark green marks) and j_{max} (green marks with dashed line) of **1-H_2O-tda-pyp** (**@CNT@PE**), obtained from the corresponding CV.

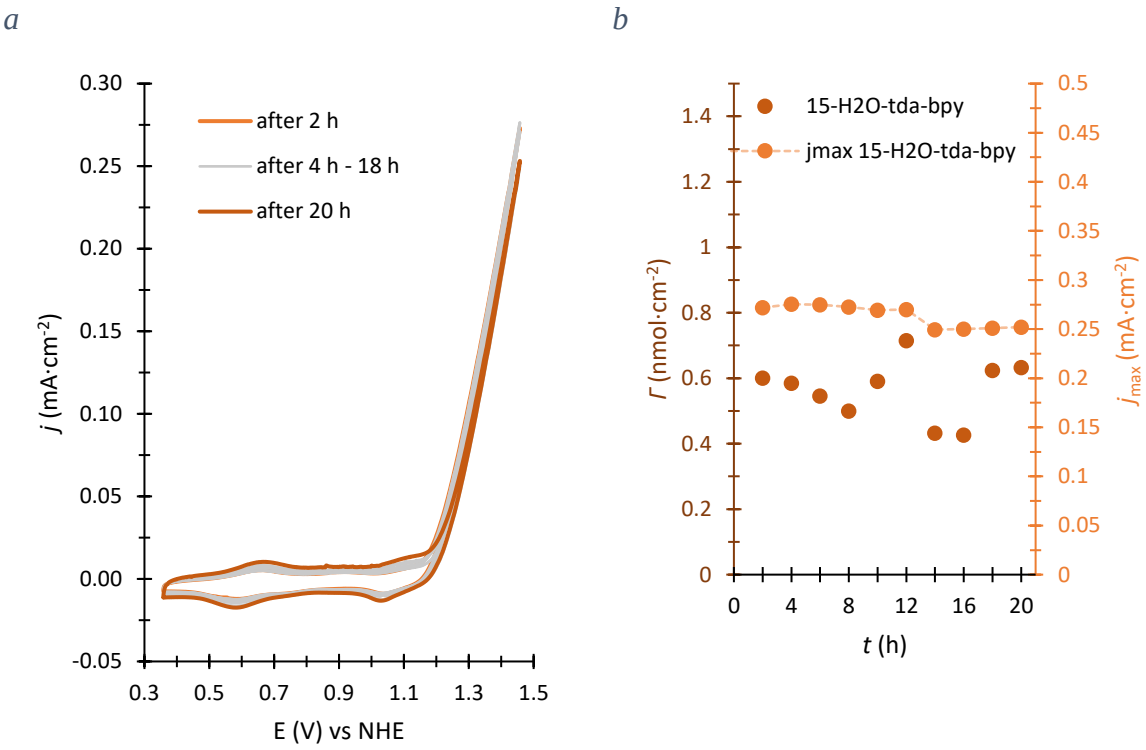

Figure SI-11. (a) CV evolution of **15-H_2O-tda-bpy@CNT@PE** during the CA experiment at 1.45 V, taken after every 2 h in 1.0 M phosphate buffer (pH 7) with 10 $mV \cdot s^{-1}$ (after . **(b)** Γ (dark red marks) and j_{max} (orange marks with dashed line) of **15-H_2O-tda-bpy** (**@CNT@PE**), obtained from the corresponding CV.

a *b*

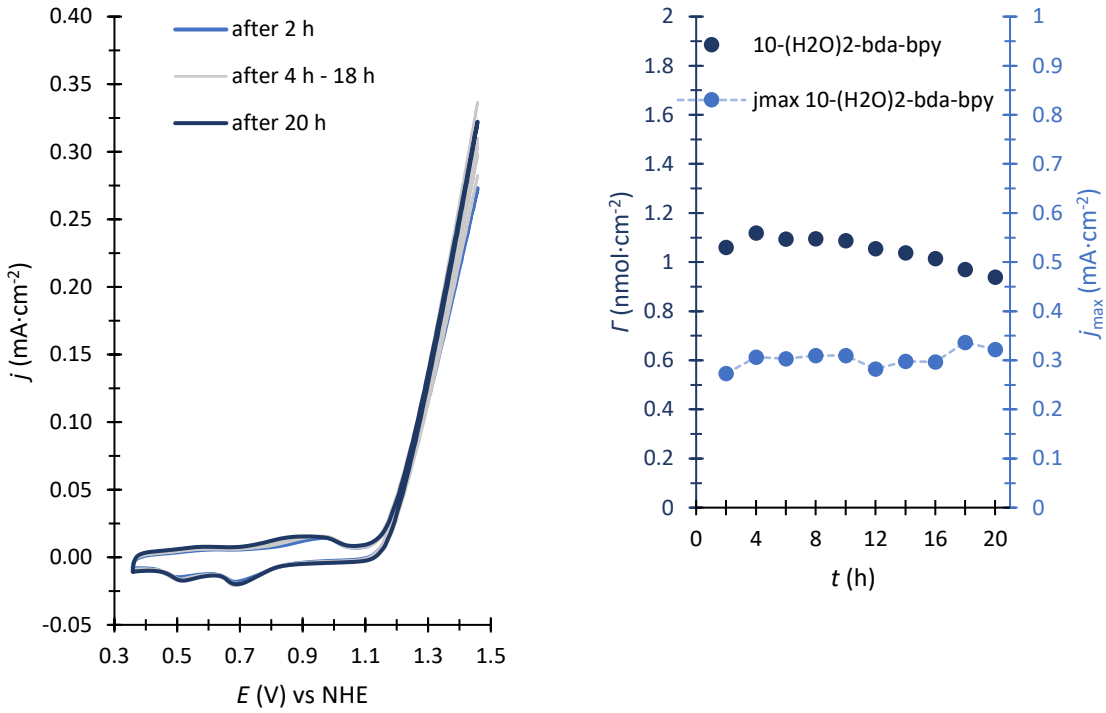

Figure SI-12. (a) CV evolution of **10-(H_2O)$_2$-bda-bpy@CNT@PE** the CA experiment at 1.45 V, taken after every 2 h in 1.0 M phosphate buffer (pH 7) with 10 mV·s^{-1} (after . **(b)** Γ (dark blue marks) and j_{max} (blue marks with dashed line) of **10-(H_2O)$_2$-bda-bpy** (**@CNT@PE**), obtained from the corresponding CV.

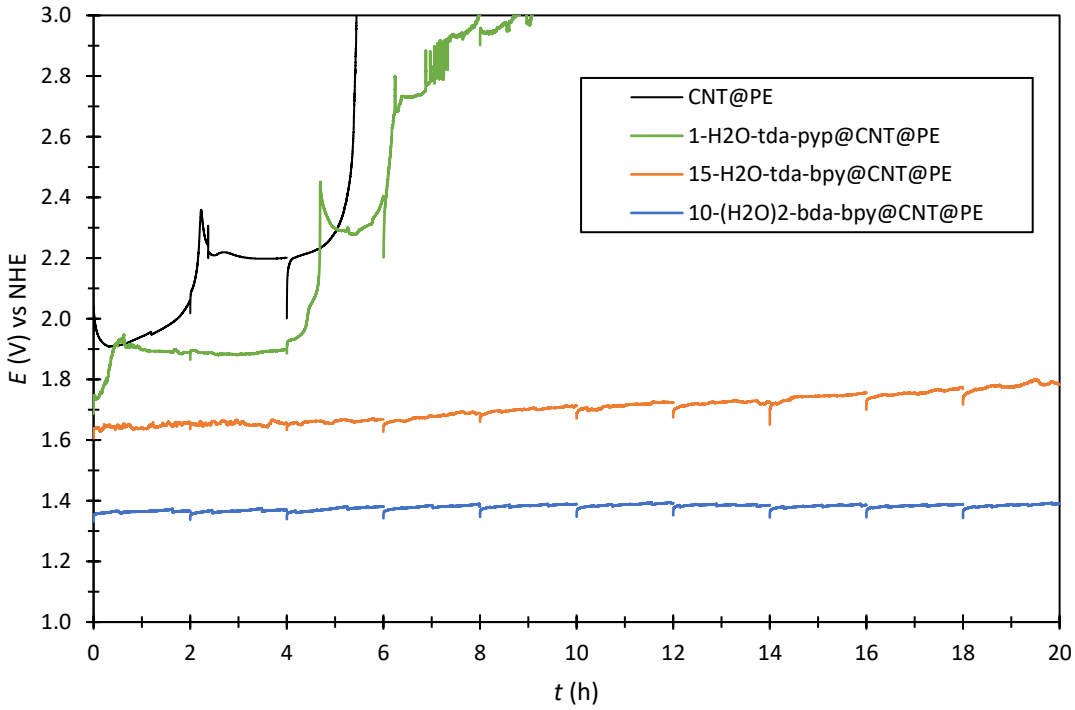

Figure SI-17. CP at 100 µA of the blank CNT@PE (black thin line), **1-H_2O-tda-pyp@CNT@PE** (green line), **15-H_2O-tda-bpy@CNT@PE** (orange line) and **10-$(H_2O)_2$-bda-bpy@CNT@PE** (blue line) at 100 µA for 20 h in pH 7, 1.0 M phosphate buffer.

CHAPTER 4

Fibrils or not fibrils: How to control P3HT-based copolymer thin film morphology?

Context: In this chapter, we describe the synthesis and self-assembly of P3HT-*b*-PMMA diblock copolymer that have been produced with the aim to use them as binder for printed electrode deposited onto NAFION proton conductive mebrane. If, we didn't succeed to go that far nevertheless herein is shown the influence of chemical and physical parameters on the self-assembly of these polymers.

Block copolymers (BCPs) have gained significant attention due to its ability to form nanostructures and offer a low-cost nanolithography technique for generating fine patterns. The power of micro-electronic components lies in their ability to store a huge quantity of information and for that purpose nanolithography using BCP is a very promising technology. Meanwhile, there has been a growing interest in the synthesis of block copolymers containing conjugated polymers since it leads to decrease of the periodic pattern size and therefore an increase of information that can be stored. It offers also a new strategy for the precise and controlled organization of semi-conducting polymers. For example, in organic electronic applications, the domain sizes need to be about 10 nm to match the exciton diffusion length, resulting in enhanced optical and electronic properties. Conjugated polymer are rod macromolecules whose chain rigidity mainly originates from the aromatic monomer unit and their conjugation. They crystallize due to π–π interactions, most of the time to form fibrils. Different strategies to overcome the predominance of π–π interactions on the organization of rod-b-coil copolymer are reported in this chapter. First, we demonstrates changes in the self-assembled morphology of poly(3-hexylthiophene)-*block*-poly(methyl methacrylate) (P3HT-*b*-PMMA) block copolymer BCP, by introducing an ionic group to the linking unit between the two blocks. Second, we use microwave annealing to destroy P3HT fibrils. We observe that after an annealing at 30W for 1 minute, fibrils disappear and high ordered morphologies were successfully created (Figure 0).

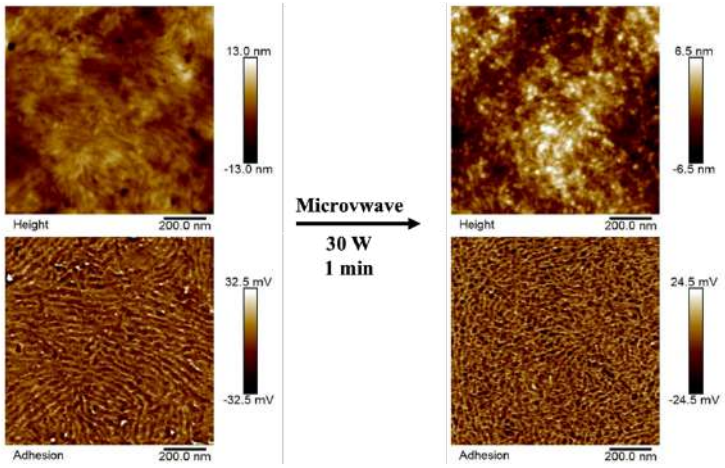

Figure 0. AFM images of P3HT-*b*-PMMA films before and after annealing *via* microwave irradiation.

Table of contents

1. Introduction 148

2. Experimental section 151

2.1. Materials……151

2.2. Instrumentation……...151

2.3. Synthesis of alkyne-terminated P3HT (HC≡C-P3HT) by GRIM……152

2.4. Synthesis of Azide-terminated PMMA (PMMA-N_3) by ATRP…….153

2.5. Synthesis of $P3HT_{5K}$-*b*-$PMMA_{10K}$ by click reaction……..153

2.6. Quaternization of $P3HT_{5K}$-b^+-$PMMA_{10K}.I^-$……153

3. Results and discussion 154

3.1 Synthesis and characterization of $P3HT_{16K}$-*b*-$PMMA_{10K}$ copolymer…..154

3.2. Synthesis and characterization of $P3HT_{16K}$-b^+-$PMMA_{10K}.I^-$ copolymer……..155

3.3. Morphology of block copolymer thin films……158

3.3.1 Solvent/solute interactions.....158

3.3.1.1. Solution temperature 158

3.3.1.2. Effect of concentration.....159

3.3.1.3. Influence of the copolymer composition: Introducing a charge and varying P3HT block length …….....160

3.3.1.4. Influence of the solvent.....162

3.3.2. Physical treatment after the film formation 164

3.3.2.1. Thermal annealing treatment 164

3.3.2.2. Microwave annealing.....165

4. Conclusion.....169

Reference.....171

Supplementary information 178

Fibrils or not fibrils: How to control P3HT-based copolymer thin film morphology?

1. Introduction

Conjugated polymers have received tremendous attention these last 40 years for their abilities to absorb and emit UV/visible/IR light and to be (semi-)conducting materials, which opened their uses in many applications such as photovoltaics, sensors ...[1-6] With research going on, morphology in conjugated polymer films has been revealed as a critical factor significantly affecting intrinsic charge transport characteristics.[2] Therefore, the control of active polymer thin-films morphology became one important challenge for achieving high performance flexible electronic devices. In these polymer films, the morphology is mainly driven by the π–π interaction taking place between aromatic monomer units and leading to an intra or inter-chains stacking. Crystals are formed and many properties such as absorbance and conductivity depend on their size and concentration in the amorphous matrix.[7-9] Specific interest has been placed on polythiophenes, especially on poly(3-hexylthiophene) (P3HT) due to the good solubility in usual organic solvents, the relatively high charge mobility and the high control of its synthesis. Lee *et al.* significantly enhanced poly(3-hexylthiophene) (P3HT) charge mobility by annealing the polymer film at high temperature (~150°C), which resulted in improved polymer crystallinity and contact between the polymer and device electrodes[10]. Fu *et al.* demonstrated enhanced molecular arrangement of P3HT chains *via* exposure of the polymer film to *o*-dichlorobenzene vapor[11]. Achmad *et al.* found that, the side chain length and molar mass of P3HT affected the structure and crystallinity of the film.[12] The substitution of the alkyl side chain has been also used to improve crystallinity property of P3HT. Victor *et al.* showed that the alkyl side chain impacts the π-π packing distance of poly(3-alkylthiophene)(P3AT). Hexyl and branched ethynyl-hexyl side chains polymers were compared and the λ_{max} of UV-vis spectrum of P3EHT presented a blue shift compare to P3HT. The authors showed that branched side chains led to twists in the thiophene backbone and increased the π-π packing distance compared to P3HT[13].

Block copolymer containing a conjugated block are also of high interest in electronic application because they can self-assemble in nano-domain allowing the precise and controlled organization of the semi-conducting part of the chain. For example, in organic electronic

applications, the domain sizes need to be about 10 nm to match the exciton diffusion length, resulting in enhanced optical and electronic properties.[14-15] Following this requirement Botiz and Darling synthesized a poly(3-hexylthiophene)-*block*-poly(L-lactide) copolymer that was then used as a structure directing agent to pattern active material into ordered nanostructures. They removed the polylactide phases by hydrolysis and filled the void with the electron acceptor fullerene. Even though the structuration lacked long-range order, the authors could observe quenching of the P3HT photoluminescence by the fullerene.[16]

Conjugated polymer-based block copolymer (CP based BCP) self-assembly is controlled by competition between the microphase-separation process driven by the Flory−Huggins enthalpic interaction and chain entropy (χN), segregation strength between two different blocks) and the strong crystallization driven by the Maier−Saupe (π−π) interaction parameter (μ) coming from the intermolecular interactions of conjugated segments.[16-19] In the strong rod−rod interaction regime ($\mu > \chi$), the organization is dominated by the rod crystallization and nano-fibrils are obtained as a thermodynamically stable structure. For example, in block copolymer of P3HT and poly(methyl methacrylate) (P3HT-*b*-PMMA) the morphology of BCP is most of the time driven by rod-rod interaction of P3HT and exhibits fibril-like structures.[20-21]

Strategies of chemical modifications have been developed to reduce the predominance of π−π interaction in rod-coil self-assembly. Increasing the coil block length[22-23], varying the chain topology to prepare graft or star copolymers[25-27] or introducing a charge in the junction of the rod and coil blocks,[28-30] all these strategies produced a high interfacial curvature and disturbed crystallization of the semi-conducting block. Previously, our team[31] has already shown that crystallinity of P3HT can be remove by introducing charge at 1,2,3-triazolium-linked unit BCPs of P3HT-*b*-PMMA with iodide counter ion and following anion exchange to replace iodide ion with bis(trifluoromethane) sulfonimide (NTf_2^-). Different copolymers have also been synthesized with a conjugated block in which the crystallinity was intrinsically decreased either by the introduction on thiophene monomer units of long and branched side chains or by lowering the regio-regularity or the rod sequence.[32-34] Victor *et al.* also studied poly(3-(2'-ethyl)-hexylthiophene)-*block*-polylactide (P3EHT-*b*-PLA) self-assembly. The microstructure of BCP presented hexagonally packed cylinder of PLA embedded in P3EHT matrix at high P3EHT content ($0.36 \leq w_{P3EHT} \leq 0.75$) while at low P3EHT content ($0.25 \leq w_{P3EHT} \leq 0.50$) a lamellar structure appeared.[35]

Following all these strategies, based on chemical modifications, the amount of π-π interaction were diminished and lamellar, cylindrical or spherical structure were obtained in place of

fibrils. In another hand, physical methodologies such as thermal, solvent or microwave annealing can be used to tune crystallization and help prepare high ordered BCP nanostructure based on conjugated macromolecules. Since these methodologies have not been really studied on block copolymer, we will present examples of what has been done on P3HT homopolymers. Thermal annealing is the classical physical method that increases the mobility of microdomains in BCPs.[36] In thermal annealing the sample is heated and held at a temperature above the glass transition temperatures (*Tg*) but below decomposition temperatures of the blocks. At the temperature ≥ *Tg*, polymer chains are becoming more mobile allowing the film to approach to the equilibrium morphology.[36,15] Annealing temperature (*Ta*) and annealing time (*ta*) both affect to the dynamics of microdomain stiffness and the orientation of nanostructure in self-assemble of BCPs.[37-39] For rod coil BCPs based on polyalkylthiophene (P3AT), the thermal treatment is set above the glass transition temperature *Tg* of coil block but below crystallization temperature (*Tc*) to induce ordered phase separation.[40-41]

Solvent annealing is also effective for the phase separation of materials. Ligui *et al.* improve the phase segregation of P3HT-PCBM. They found that, the polymer is well-dissolve in *o*-dichlorobenzene (ODCB), the UV-vis spectrum presented only the intra π-π* transition of thiophene ring at 450 nm. On the contrary, after hexane addition, a poor solvent for P3HT, the absorption of P3HT aggregates at 607 nm was observed. Moreover, the AFM images of thin films made from ODCB and chloroform solution did not present fibrils like morphology but it did after hexane addition.[42]

Microwave (MW) annealing is an alternative method, recently developed, to improve the phase separation of BCP. MW annealing is believed to be based on the substrate heating, further melting the coated BCP film. Within very fast irradiation time, in the minute-order, MW annealing has been showed to enhance long range order BCP structurations. BCP such as polystyrene-*block*-poly(methylmethacrylate), polystyrene-*block*-polydimethylsiloxane or polystyrene-*block*-polylactic acid have been self-assembled by MW irradiation in a minute.[43-45] For example, Qiang *et al.* reported the rapid ordering of PS-*b*-PMMA under a maximum MW heating rate of 1.8 °C/s, leading to 97% of surface perpendicular cylinders.[46] Up to now, it is worth noting that nothing has been done with conjugated polymers.

In this chapter, we report chemical and physical strategies to induce or suppress fibrillation of conjugated-based BCP **(Figure1)** and find versatile ways to induce nano-segregation. To be more precise, the effect of solvent is described, either as the liquid solubilizing the copolymer before filmification or as the vapor increasing mobility during microwave annealing. To

investigate the influence of the solvent, different P3HT-*b*-PMMA were synthesized, *i.e.* different sizes of P3HT block and the elaboration of ionomers bearing a charge at the junction of the block.

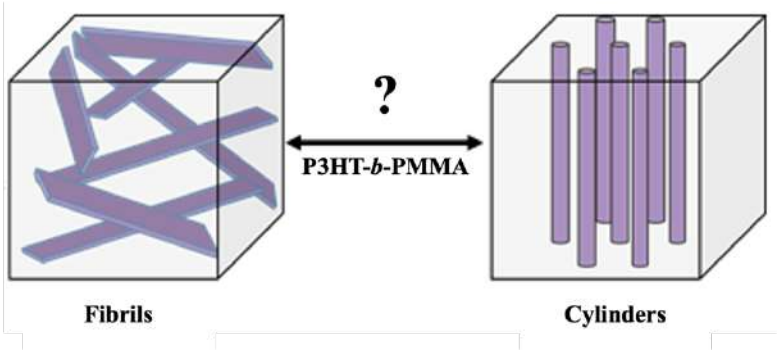

Figure 1. The aim of this study on how to switch from fibril morphology controlled by π–π interaction and cylinder structuration dictated by P3HT-*b*-PMMA segregation.

2. Experimental section

2.1. Materials.

All chemicals were purchased from Sigma-Aldrich and used without further purification except copper bromide, methyl methacrylate (MMA) and THF. CuBr was purified by stirring with acetic acid overnight, washed with acetic acid, absolute ethanol, and diethyl ether and then dried in a vacuum oven. MMA was stirred with inhibitor remover for 30 min and filtered. THF was distilled over calcium hydride.

2.2. Instrumentation.

^{1}H and diffusion order spectroscopy (DOSY) NMR experiments were carried out on a Bruker 400 MHz spectrometer at 25°C.

The molar mass and molar mass distribution of all synthesized polymers were measured using size exclusion chromatography (SEC) and THF as eluent (flow rate 1.0 mL min^{-1}) at 30 °C. SEC is equipped with a Viscotek VE 5200 automatic injector, a precolumn and two columns (Styragels HR 5E and 4E (7.8 ft, 300 mm)) and 4 detectors: UV−visible spectrophotometer (Viscotek VE 3210), a Multiangle Light Scattering detector (Wyatt Heleos II), a viscosimeter (Wyatt Viscostar II) and a refractive index detector (Viscotek VE 3580). Polystyrene standards were used to determine the macromolecular parameters of the polymers. PMMA was also

analysed by SEC with DMF eluent with 1 g L^{-1} of LiCl (flow rate of 0.5 mL min^{-1}) at 50°C. SEC is equipped with a precolumn and two columns. Toluene was used as flow marker. The SEC system was connected to a Refractive index detector ERC 7515-A and a Wyatt Dawn-DSP multi angle light scattering detector. Number-average molar mass (M_n) and dispersity (M_w/M_n, where Mw is the mass-average molar mass) of the polymers were calculated from a conventional calibration derived from PMMA standards. For all SEC, polymer samples were prepared at 5 g L^{-1} and filtered through 0.45 μm PTFE filters.

Atomic force microscopic (AFM) images were obtained using MultiMode 8 Atomic Force Microscope (AFM) from Bruker in a PeakForce QNM (Quantitative NanoMechanics) mode.

Differential scanning calorimetry (DSC) experiments were performed using Q100 DSC from TA Instruments under nitrogen atmosphere with a first cycle at 20°C/min and the second at 10°C/min.

2.3. Synthesis of alkyne-terminated P3HT (HC≡C-P3HT) by GRIM.

In a flamed and dried round-bottom flask, 2,5-dibromo-3-hexylthiophene (0.7 ml, 3.27 mmol, 1 eq) was dissolved in 15 mL of THF. To this solution was added isopropylmagnesium chloride (1.63 ml, 3.27 mmol, 1 eq) to form the Grignard reagent. After 30 min at 0°C, the solution was transferred by cannula and under nitrogen to a THF solution of $Ni(dppp)Cl_2$ (70.8 mg, 0.13 mmol dispersed in THF 10 ml). After 3 h at 0°C, the ice bath was removed. Once at room temperature, 1 mL of ethynylmagnesium bromide (0.52 mmol, 4 eq) was introduced to the reaction flask. After 15 min of reaction, the polymer was precipitated in cold methanol. To avoid possible end-group alteration, no soxhlet extraction was performed. Therefore, the solid obtained was isolated by filtration from the methanol fraction and directly washed with an excess of methanol to remove residual metal salts and unreacted monomers. The yield obtained after purification was 75.7 %. The precipitated polymer was analyzed by ^1H NMR in $CDCl_3$ and by SEC in THF. **Scheme 1** shown the synthesis pathway of alkyne-terminated P3HT.

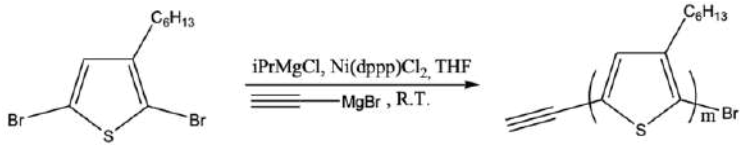

Scheme 1. Synthesis of alkyne-terminated P3HT by GRIM.

2.4. Synthesis of Azide-terminated PMMA (PMMA-N_3) by ATRP.

The PMMA-N_3 was synthesized by ATRP from 2-azidoethyl-2-bromoisobutyrate initiator. In a glovebox, a flamed-dried round bottom flask (of 50 mL) was charged with the CuBr (70.4 mg, 0.3 mmo, 1eq) and the 2,2'-bipyridine (3eq). Then, outside the glovebox, methyl methacrylate (200 eq) was inserted on the reaction flask. The mixture was degassed by nitrogen bubbling for 15 min. Then, 2-azidoethyl 2-bromoisobutyrate (1 eq) was added on the solution. The targeted degree of polymerization (DP) at full conversion was 50. The polymerization was carried out at 90°C. The reaction was stopped after 60 min by cooling the polymer solution to room temperature and air exposure. Monomer conversion was calculated by proton NMR of the crude solution in $CDCl_3$. The mixture was dissolved in THF and passed through a basic alumina column to eliminate copper catalyst and then PMMA was precipitated in methanol before SEC analysis in DMF and THF. The PMMA obtained was also analyzed by ^1H NMR in $CDCl_3$. **Scheme 2** shown the synthesis pathway of azide-terminated PMMA.

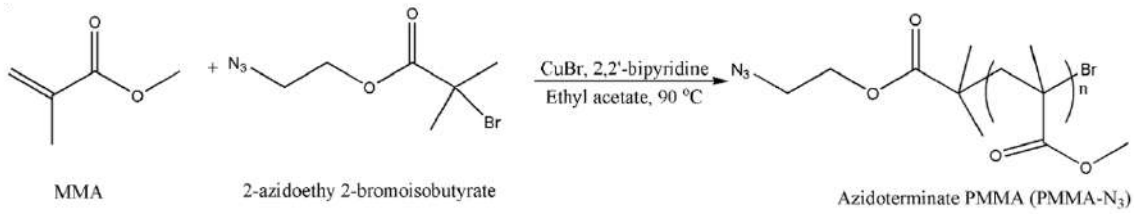

Scheme 2. Synthesis of azide-terminated PMMA by ATRP.

2.5. Synthesis of $P3HT_{5K}$-*b*-$PMMA_{10K}$ by click reaction (see scheme 3).

The conjugated P3HT-*b*-PMMA was prepared by click coupling reaction of P3HT and PMMA. In flame-dried reaction flask, of PMMA (94 mg, 1 eq), P3HT (43 mg, 1eq), CuBr (2.9 mg, 3eq) and of sodium ascorbate (3.5 mg, 3eq) were solubilized in 25 mL of dried THF. Then PMDETA (4.2 μL, 3eq) was added to the mixture. The mixture was deoxygenated by nitrogen bubbling for 15 min, then let to react at 65 °C for 72 h. After 72h, CuBr is removed through an alumina column and the polymer obtained was precipitated on cold methanol. After purification, polymer obtained was analyzed by SEC analysis in THF and 1H NMR and DOSY in $CDCl_3$.

2.6. Quaternization of $P3HT_{5K}$-b^+-$PMMA_{10K}.I^-$ (see scheme 4).

The ionomers were prepared by methylation of P3HT-*b*-PMMA with methyliodide. P3HT-*b*-PMMA (50 mg, 1eq) and CH_3I (100 eq) were added in CH_3Cl. The mixture was deoxygenated by nitrogen bubbling for 15 min and let to react at 80 °C. After 72h of reaction, the polymer

obtained was precipitated in cold methanol and water. The synthesis of $P3HT_{16K}$, $PMMA_{10K}$, $P3HT_{16K}$-*b*-$PMMA_{10K}$ and $P3HT_{16K}$-b^+-$PMMA_{10K}.I^-$ are presented in supplementary data.

3. Results and discussion

3.1. Synthesis and characterization of $P3HT_{16K}$-*b*-$PMMA_{10K}$ copolymer. (Scheme 3)

P3HT was synthesized by the GRIM method[2-6], from the 2,5-dibromo-3-hexylthiophene, the isopropylmagnesium chloride and $Ni(dppp)Cl_2$ as catalyzed. Alkyne end-chain was obtained after addition of ethynylmagnesium bromide which allowed the polymerization termination and the presence of ethynyl end-group. After purification, the ethynyl end-group was confirmed by ^1H NMR spectroscopy in $CDCl_3$ with the appearance of the signal at $\delta = 3.53$ ppm from the alkyne C≡C<u>H</u> proton (**Figure S1**, proton a). The molar mass of P3HT obtained by SEC was 16,600 $g.mol^{-1}$ and dispersity 1.44. The dispersity is a little wider than what can be found in the literature (1.2) because no Soxhlet purification, removing low molar mass chains, was performed. This was done to avoid a probable modification of the end-chain.[1] PMMA was synthetized by ATRP using 2-azidoethyl-2-bromoisobutyrate as initiator allowing the formation of azido-terminated chains. After 25 min, the final conversion was 66.7 % and the final molar mass was 9400 $g.mol^{-1}$ with a dispersity at 1.25. Azido end-group was confirmed by ^1H NMR spectroscopy in $CDCl_3$ with the signal at $\delta = 4.24$ ppm pertaining to the azido group ($C\underline{H}_2$-CH_2-N_3, **Figure S2**, proton b).

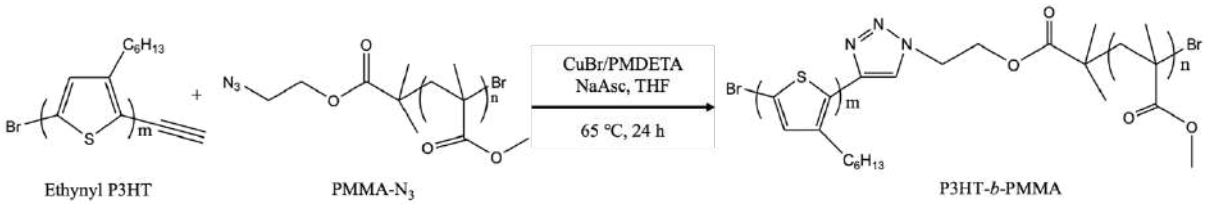

Scheme 3. Synthesis of P3HT-b-PMMA by Huisgen cyclo-addition.

Block copolymers were prepared by the Huisgen cycloaddition (see bibliographic part) between the P3HT ethynyl end-group and the PMMA azido end-group, as shown in **Scheme** . The superposition of the SEC chromatograms of $P3HT_{16K}$-*b*-$PMMA_{10K}$ and the parent homopolymers is presented in **Figure .** The success of the reaction was proven by the

shift toward the high molar mass observed in the SEC analyses. The molar mass of BCP obtained by SEC was 25,000 g.mol^{-1} with dispersity 1.23. The ^{1}H DOSY NMR analysis **(Figure S3)** of the coupling reaction product showed one single diffusion coefficient proving the analysis of one object containing PMMA and P3HT signals, a block copolymer. The formation of the triazole was observed by ^{1}H NMR with the apparition of a signal at δ = 7.7 ppm and it was confirmed by the signals at δ = 4.5 and 4.7 ppm from CH_2-CH_2-N (**Figure S4**, proton 3,4,5). DP obtained by ^{1}H NMR were in accordance with DP obtained by the NMR analysis of the homopolymers parents (DP(P3HT) ≈ 100 and DP(PMMA) ≈ 100).

Following the same synthetic procedure another block copolymer P3HT$_{5K}$-*b*-PMMA$_{10K}$ was produced. The ^{1}H DOSY NMR analysis, ^{1}H NMR spectrum and SEC chromatogram of P3HT$_{5K}$-*b*-PMMA$_{10K}$ is presented in supplementary information **(Figure S5-S7)**.

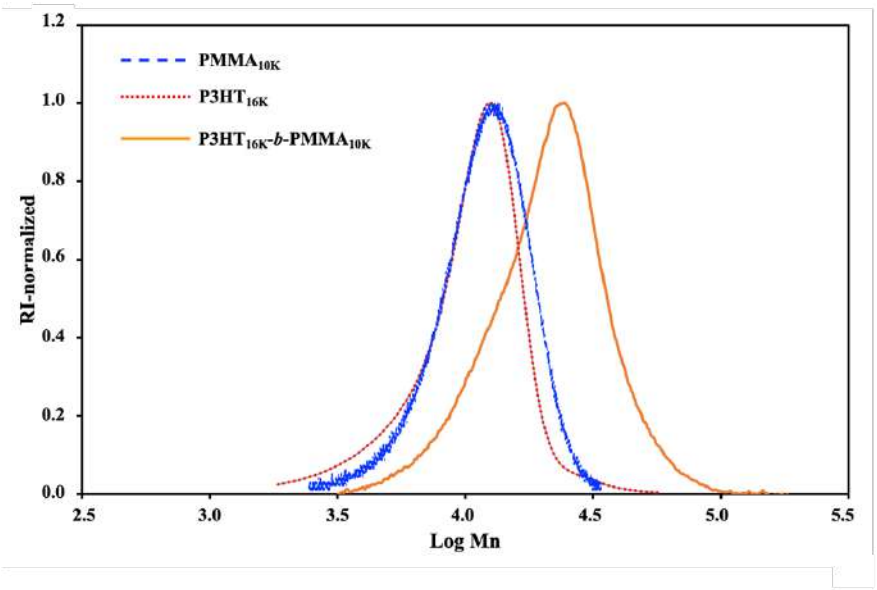

Figure 2. SEC chromatogram of P3HT$_{16K}$-*b*-PMMA$_{10K}$ (orange plain line), PMMA$_{10K}$ (red dot line and P3HT$_{16K}$ ((blue dashed line).

3.2. Synthesis and characterization of P3HT$_{16K}$-*b*$^{+}$-PMMA$_{10K}$.I^{-} copolymer.

In a last step, the block copolymers were charged at the junctions of block by the methylation of the triazole ring, following the experimental procedure of Ji. *et al.*[31] An excess of methyl iodide was added to a chloroform solution of P3HT-*b*-PMMA. The reaction followed the pathway shown in **scheme 4** to produce what we call in the rest of the document P3HT-*b*$^{+}$-PMMA.I^{-}.

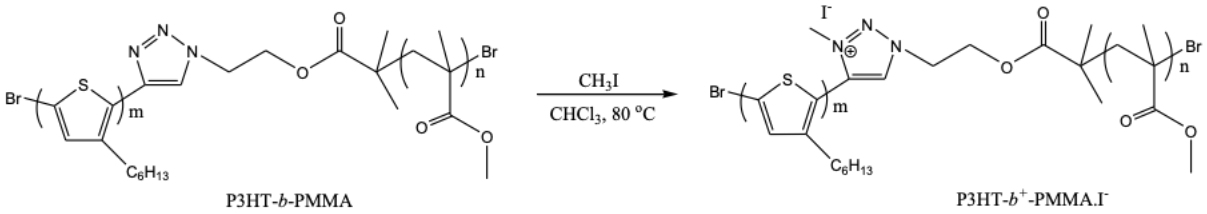

Scheme 4. Charge added of P3HT-*b*-PMMA by methylation reaction.

After the methylation, the ^{1}H NMR spectra of ionized polymer **(Figure S8)** shown the chemical shift of the two methylenes protons adjacent to the triazole ring (N^{1}-CH_2-CH_2 group) from 4.5 and 4.7 ppm to 4.7 and 5.3 ppm before and after modification respectively. Therefore, this demonstrated that the methylation of neutral BCP to produce ionized BCP was a success. ^{1}H NMR spectra of ionized polymer of $P3HT_{5K}$-b^{+}-$PMMA_{10K}.I^{-}$ shown in **Figure S9**.

Table 1: Molecular and thermal characteristics of synthesized block copolymers

Polymer	M_n[a] **BCPs (g.mol^{-1})**	M_n[a] **P3HT (g.mol^{-1})**	M_n[a] **PMMA (g.mol^{-1})**	**DP$_n$[b] P3HT**	**DP$_n$[b] PMMA**	**f$_v$P3HT[c]**	**Đ[a]**	T_g[d] **(°C) PMMA block**	T_m[d] **(°C) P3HT block**
$P3HT_{5k}$-*b*-$PMMA_{10k}$	15 000	4 300	10 000	26	100	0.33	1.4	114	173
$P3HT_{5k}$-b^{+}-$PMMA_{10k}.I^{-}$	15 000	4 300	10 000	26	100	0.33	1.4	114	156
$P3HT_{16k}$-*b*-$PMMA_{10k}$	26 000	16 000	10 000	100	100	0.64	1.2	117	230
$P3HT_{16k}$-b^{+}-$PMMA_{10k}.I^{-}$	26 000	16 000	10 000	100	100	0.64	1.2	117	217

[a] Calculated from GPC with PS standards. [b]Number-average degree of polymerization calculated by using M_n from GPC and molecular weight of each monomer are M_{P3HT} = 166 g.mol^{-1} and M_{PMMA} = 100 g.mol^{-1}. [c]The volume fraction of P3HT were calculated by using M_n from GPC and the density of each polymers: ρ_{P3HT} = 1,11 g.cm^{-3} and ρ_{PMMA} = 1,19 g.cm^{-3}.

Following the same synthesis, several block copolymers were synthesized **(table 1)** to study the influence of the length of the P3HT block because it is well known that the crystallization of chains evolve with the molar mass.[47-49] Secondly a charge has been introduced at the center

of the diblock to affect the P3HT crystallization and the diblock solubility as it has been shown in our group, previously.[42]

All the diblock copolymers were characterized by differential scanning calorimetry (DSC) to determine glass transition and melting temperature, complete thermograms of $P3HT_{5K}$-*b*-$PMMA_{10K}$ compared between neutral and ionized BCP are presented in supporting information **Figure 3** (complete thermograms of neutral and ionized BCP of $P3HT_{16K}$-*b*-$PMMA_{10K}$ are in **Figure S10**).

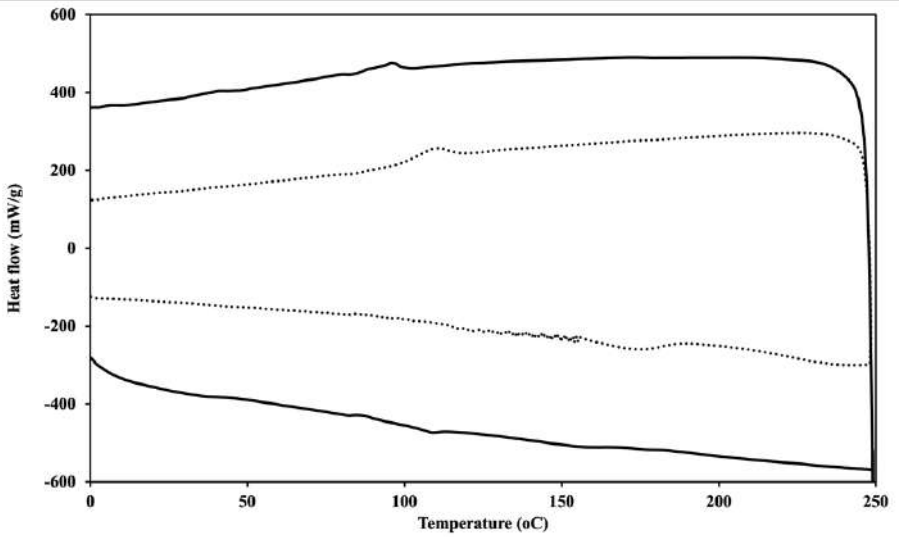

Figure 3. DSC thermograms of the copolymers scan with the heating cycle from -10 to 250 ºC at 10 ºC/min (dot line : $P3HT_{5K}$-*b*-$PMMA_{10K}$; full line : $P3HT_{5K}$-b^+-$PMMA_{10K}$).

The results showed that the melting point of P3HT crystallite increased from 173 to 230°C with the increase of the P3HT molar mass for $P3HT_{5k}$-*b*-$PMMA_{10k}$ and $P3HT_{16k}$-b-$PMMA_{10k,}$ respectively (**Table 1**). This increase came with a raise of the melting enthalpy from 2.2 $J.g^{-1}$ to 16.1 $J.g^{-1}$) meaning that this behavior is due to the P3HT rods increase in the length and edge effects.[50-53] The charged diblock copolymer presented a melting temperature lower than their neutral parents, at 156 and 217 °C for $P3HT_{5k}$-b^+-$PMMA_{10k}I^-$ and $P3HT_{16k}$- b^+-$PMMA_{10k}$ I^-, respectively. This behavior was also observed by Ji *et al.* and explain by a disruption of the crystallization induced by the charge.[31] DSC thermograms of charged copolymer showed the recrystallization peak of $P3HT_{5K}$-b^+-$PMMA_{10K}.I^-$ and $P3HT_{16K}$-b^+-$PMMA_{10K}.I^-$ fully disappeared, confirming the strong decrease of the crystallinity.

3.3. Morphology of block copolymer thin films

Different parameters have been varied to prove their influence on the self-assembly of P3HT-*b*-PMMA. In a first time, they are all linked to the polymer solubility with different solvents. For this, temperature, concentration, nature of the solvent but also nature of the solute has been investigated and presented below. Then, the use of external stimuli such as microwave or thermal annealing in different environment have been applied on thin films.

3.3.1 Solvent/solute interactions

3.3.1.1. Solution temperature:

As described by Oh *et al.*, the solvent and the temperature have a drastic effect on the creation of fibrils in solution and by extension in film produced by solution coating.[54] Temperature of $P3HT_{5K}$-*b*-$PMMA_{10K}$ solutions in chloroform was the first parameter studied on the morphology of diblock. In **Figure 4** are shown the AFM images of film drop-casted from a polymer solution at 5, 15, 20 and 26 °C. Below 20°C, the images illustrate long (l ~ 1 300 nm) fibrils at the surface of the films. Above 20°C, a clear block segregation is observed with yellow dots appearing in the height image in a dark brown matrix. Since the volume fraction of P3HT is 0.33, it represents the minority phase in a PMMA matrix. This minority phase is most probably a cylindrical phase oriented perpendicularly to the surface.

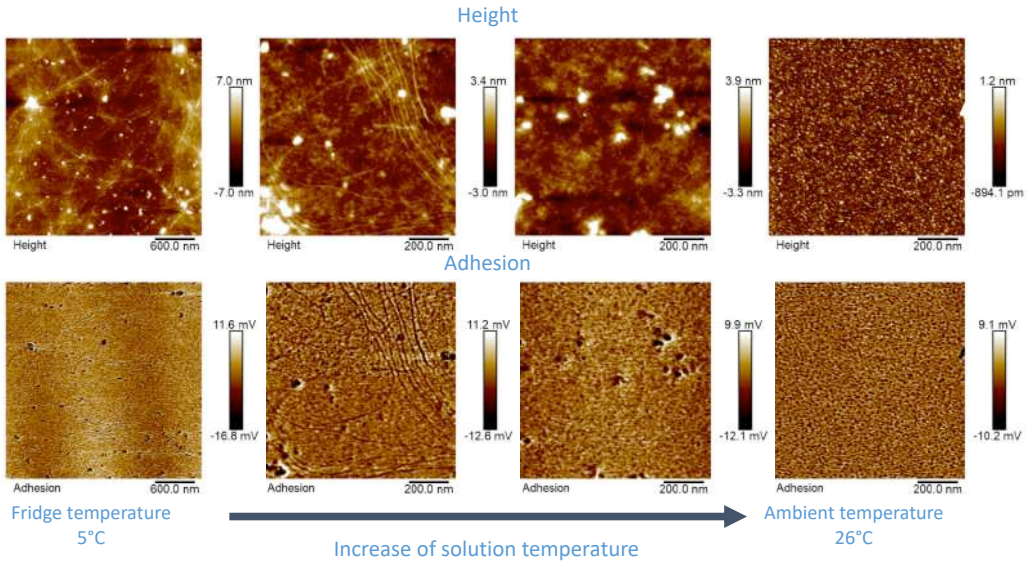

Figure 4 PeakForce QNM-Mode AFM images in height (top) and adhesion (bottom) of films realized from a solution of $P3HT_{5K}$-b-$PMMA_{10K}$ at 3 g mol^{-1} in chloroform. Films were realized at 5, 15, 20 and 26°C (left to right) dip coating method with the withdraw speed was 10 µm/sec at room temperature.

3.3.1.2. Effect of concentration.

In the dip-coating process, the concentration of the solution is highly important for the film formation. First of all, the thickness of the films, measured by ellipsometry, varied from 20, 30 to 100 nm when polymer concentration (in chloroform) of 1, 3 and 5 g.L^{-1} were respectively used at room temperature (22°C). AFM images of the P3HT$_{5K}$-*b*-PMMA$_{10K}$ films obtained showed that *out of plane* cylinders, *i.e.* perpendicular to the surface, were obtained when the solution at 1 g.L^{-1} was used **(Figure 5A)**. Also, clear de-wetting is visible in this image, expressing the fact that not enough matter was deposited on the substrate (large black holes in height image). Charles *et al.* have shown similar effects when the film thickness was thinner than the dimension of the structure, *i.e.* the distance between the cylinder center also called "pitch".[55] Using the solution at 3 g L^{-1} **(Figure 5B)**, *out of plane* P3HT cylinders were obtained at the surface of this thicker film which is in agreement with the above-mentioned study. Finally, fibrils were produced **(Figure 5C)** when a 5 g L^{-1} solution was used. Indeed, Gilroy *et al.*[56] showed that above a certain concentration that depends on the solvent used, P3HT homopolymer self-assembled into fibrils. The same behavior is here observed for P3HT$_{5K}$-*b*-PMMA$_{10K}$.

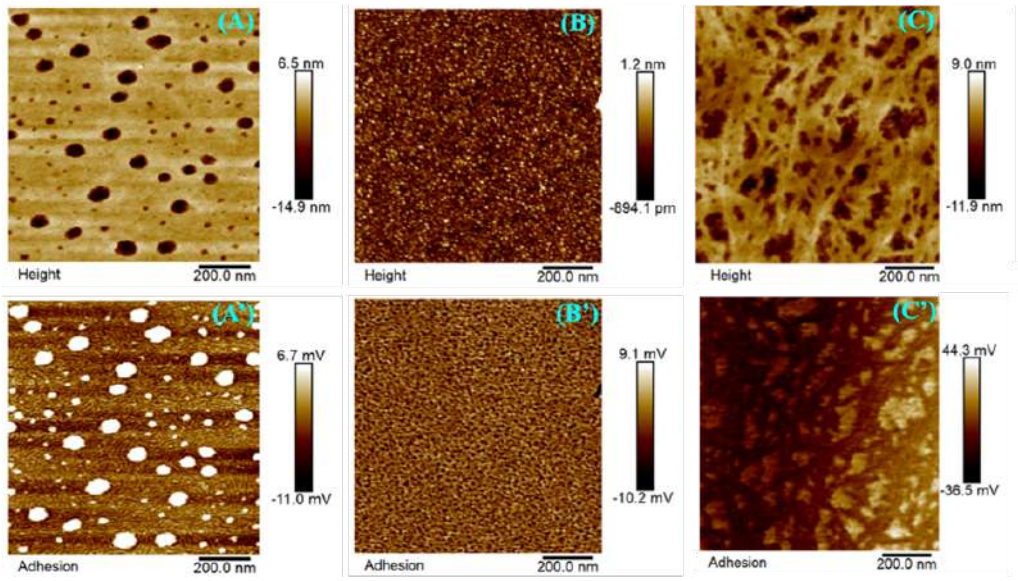

Figure 5. PeakForce QNM-Mode AFM images of diblock copolymers, films were prepared by dip coating method with the withdraw speed was 10 µm/sec at room temperature. Films realized from a solution of P3HT$_{5K}$-b-PMMA$_{10K}$ at (A) 1 g.L^{-1}, (B) 3 g.L^{-1} and (C) 5 g.L^{-1} in chloroform at ambient temperature.

3.3.1.3. Influence of the copolymer composition: Introducing a charge and varying P3HT block length

The effect of the charge was already shown in previous work by our team.[31] Indeed, the crystallization can be controlled by the introduction of a cation on the triazole group. The objective of this work is to verify in which extend the composition of this copolymer influence the fibrillary structuration with and without the charge at the junction of the block, P3HT-*b*-PMMA and P3HT-b^+-PMMA, respectively. In **Figure 6A** and **B**, for a same concentration $P3HT_{5K}$-*b*-$PMMA_{10K}$ solution at 5 $g.L^{-1}$ (chloroform) the AFM images of the neutral copolymer film show a fibrillary structuration whereas the quaternized copolymer formed *out-of-plane* cylinders. It has to be mentioned that temperature and concentration (1, 3 and 5 $g\ L^{-1}$) of the started solution have no effect on the morphology of quaternized copolymer thin films, with only *out of plane* cylinders observed **(Figure S11)**. This means a higher solubility of the quaternized polymer in chloroform than the neutral macromolecule favoring self-assembly over crystallization.

By changing the polymer solute to $P3HT_{16K}$-b-$PMMA_{10K}$, we could observe the influence of the P3HT block length on the morphology of thin films. It has been previously shown in the literature that increasing the P3HT molar mass in homopolymer or copolymer, develop π–π stacking interaction and lead to the formation of crystals.[57-59] The morphology of $P3HT_{16K}$-*b*-$PMMA_{10K}$ neutral and quaternized films, made from solutions at 5 $g.L^{-1}$ using chloroform, can be observed in **Figure 6C** and **D**. The AFM images show organized fibrils of several micrometers long for both copolymers. When solution of lower concentration, 3 and 1 $g.L^{-1}$, were used to prepare the film the same structuration was obtained **(Figure S12)**. The influence of charge affected on the orientation of $P3HT_{16K}$-*b*-$PMMA_{10K}$ only in film made from a low concentration at 0.5 $g.L^{-1}$**(Figure S13)**. These observations showed that the P3HT block was high enough in this copolymer to overcome the effect of the charge added at the junction of the blocks. This agrees with the DSC thermograms and the values of the melting temperatures and enthalpies which are higher in the case of $P3HT_{16K}$-*b*-$PMMA_{10K}$ than for $P3HT_{5K}$-*b*-$PMMA_{10K}$ copolymers.

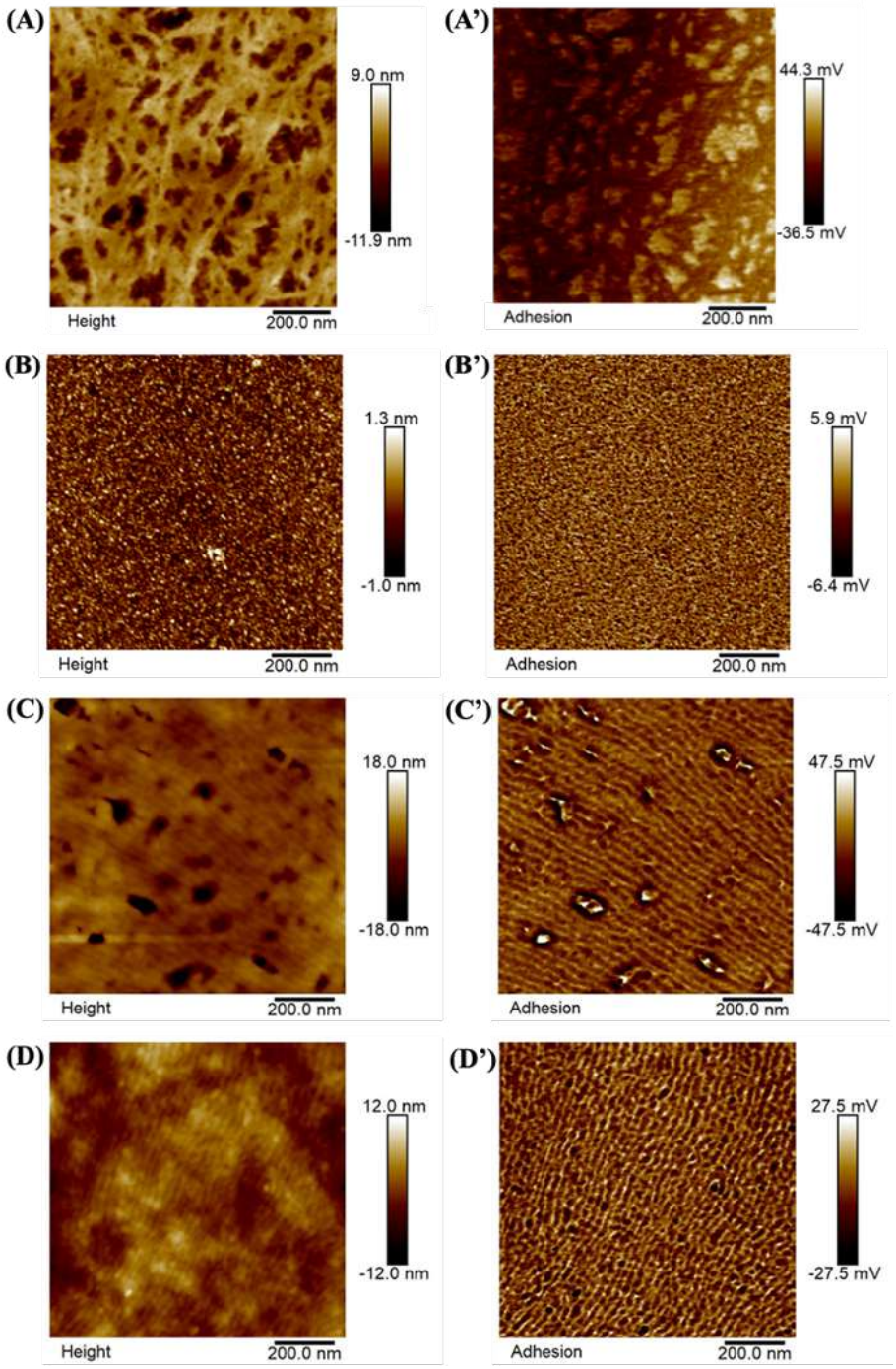

Figure 6. PeakForce QNM-Mode AFM images of diblock copolymers, films were prepared by dip coating method with the withdraw speed was 10 µm/sec at room temperature, (A) Height and adhesion images of $P3HT_{5K}$-b-$PMMA_{10K}$,5 g/L in $CHCl_3$. (B) Height and adhesion images $P3HT_{5K}$-b^+-$PMMA_{10K}$.I^-, 5 g/L in $CHCl_3$. (C) Height and adhesion images of $P3HT_{16K}$-b-$PMMA_{10K}$, 5 g/L in $CHCl_3$. (D) Height and adhesion images $P3HT_{16K}$-b^+-$PMMA_{10K}$.I^-, 5 g/L in $CHCl_3$.

3.3.1.4. Influence of the solvent.

We investigated the influence of the solvent used to prepare the solution by adding in chloroform a non-solvent of P3HT, ethanol (EtOH), which is at the same time a good solvent of PMMA. The polymer solutions were prepared by mixing solvent in a volume percentage of 83%$CHCl_3$-17%EtOH. In **Figure S12** are exposed the AFM images of films made from different solvents and copolymers at an initial concentration of 3 $g.L^{-1}$. We observed that, the solvent additive induced the creation of long fibrils, even when the charged $P3HT_{5K}$-b^+-$PMMA_{10K}$ was used. Indeed, the color of the block copolymer solutions changed from orange in chloroform to purple after the addition of 17% of ethanol. The color change is the result of aggregates due to the crystallization-driven self-assembly of P3HT chains.[60-61] This behavior has been quantified by spectrophotometric method, UV-vis spectra, exhibited two shoulders at 550 nm and 600 nm after adding EtOH **(Figure 7)**. These shoulders appearance is usually linked to the vibronic peaks of intra and intermolecular π–π interaction.[62-65] However, the UV-vis spectrum of $P3HT_{5k}$-*b*-$P3HT_{10K}$ did not present any absorbance features at 550 nm and 600 nm. This is probably due to the low concentration of the polymer solutions used to prepare UV-vis sample, 0.1 $g.L^{-1}$. Indeed, the molar extinction coefficient of P3HT is so high (7,800 $M^{-1}cm^{-1}$ in methylene chloride)[66] that only low concentration can be measured (at least with a 1cm optical cell).

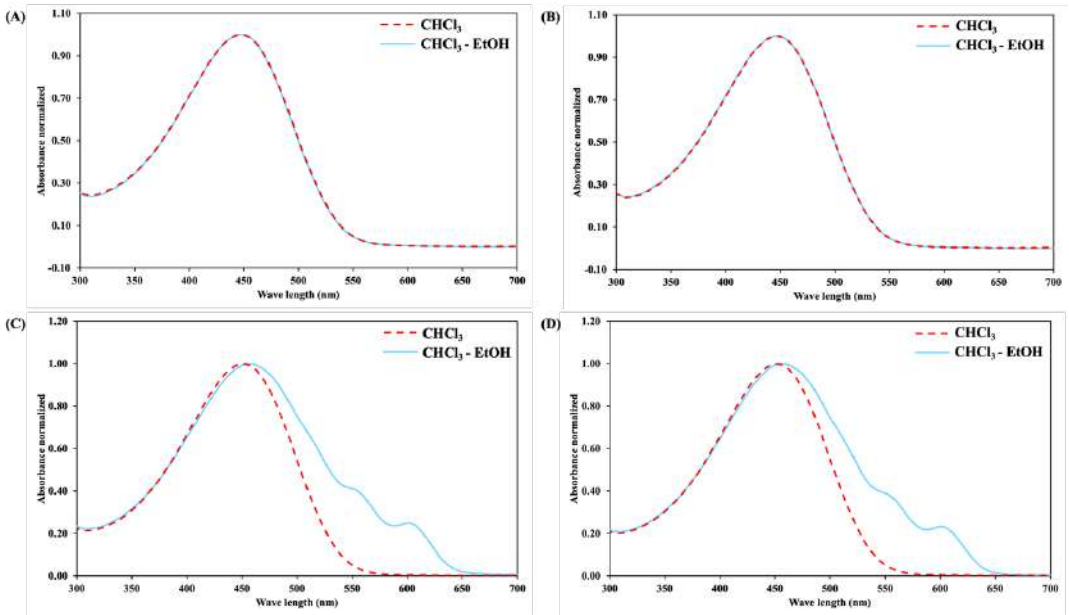

Figure 7. UV-vis spectrum of BCP in $CHCl_3$ compared with in mix-solvent 5:1 of $CHCl_3$-EtOH. (A) $P3HT_{5K}$-b-$PMMA_{10K}$, (B) $P3HT_{5K}$-b^+-$PMMA_{10K}.I^-$, (C) $P3HT_{16K}$-b-$PMMA_{10K}$, (D) $P3HT_{16K}$-b^+-$PMMA_{10K}.I^-$

At higher concentration the P3HT$_{5K}$-*b*-PMMA$_{10K}$ must form crystals in the presence of ethanol and fibrils are observed on the film. **Figure 8** was built to give an idea of the role of the interaction solvent/solute in the formation of structure, first in concentrated solution and then in films. Concerning the solute, the solubility of conjugated copolymers in the solvent used increases from P3HT$_{16K}$-*b*-PMMA$_{10K}$, P3HT$_{16K}$-*b*$^{+}$-PMMA$_{10K}$, P3HT$_{5K}$-*b*-PMMA$_{10K}$ and P3HT$_{5K}$-*b*$^{+}$-PMMA$_{10K}$. This can be seen easily when observing images made from cold (0°C) chloroform solution, where P3HT$_{16K}$ copolymers led to long fibrils whereas P3HT$_{5K}$-*b*-PMMA$_{10K}$ film showed small fibrils and P3HT$_{5K}$-*b*$^{+}$-PMMA$_{10K}$ formed cylinders. In the solvent point of view, the solubility of the copolymers increases in the following order: chloroform ethanol mixture > cold chloroform (0°C) > room temperature chloroform (20°C). This is especially well-seen with the observation of P3HT$_{5K}$-*b*-PMMA$_{10K}$ for which long fibrils are formed when ethanol was added, short fibril from cold chloroform and cylinder in warmer chloroform.

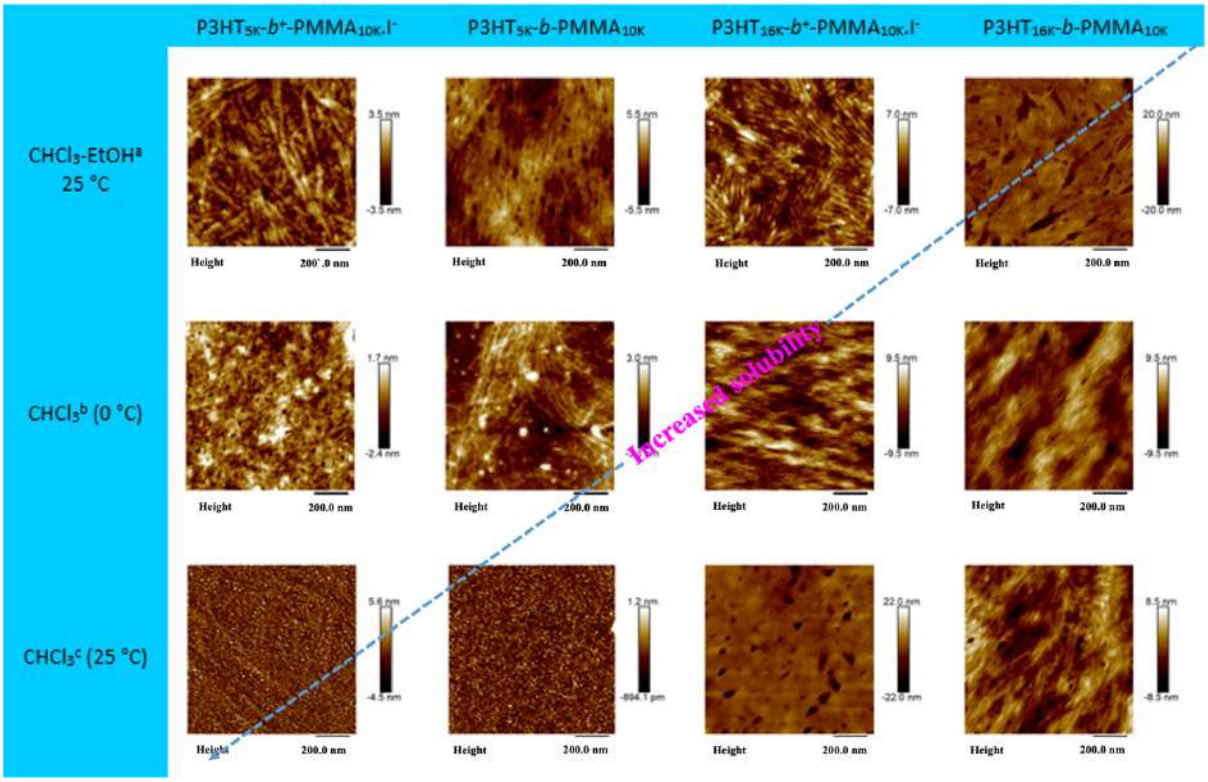

Figure 8. PeakForce QNM-Mode AFM images of diblock copolymers, films were prepared at 3.0 g/L by dip coating method with the withdraw speed was 10 µm/sec. [a] The solution prepared by mixed solvent; 83%$CHCl_3$-17%EtOH. [b] The solution prepared in $CHCl_3$ at 0 °C. [c]The solution prepared in $CHCl_3$ at 25 °C.

In this first part, we studied the formation of fibrils before or during the film manufacturing. By using an appropriate solvent-solute couple, crystallization of P3HT segments can be avoided and block copolymer nano-segregation driven. In the following part, we will look for the conditions in which fibrils appear or disappear after the film formation. For this purpose, thermal, solvent and microwave annealing will be investigated.

3.3.2. Physical treatment after the film formation

In this part, all samples were prepared from two kind of solution; one using $CHCl_3$ and the other using the $CHCl_3$/EtOH mixture as solvent, at room temperature. The concentration of solution at 1.0 $g.L^{-1}$ was used to prepare BCPs films by dip-coating for thermal annealing treatment while the concentration at 3.0 $g.L^{-1}$ were used to prepare BCPs films for microwave annealing treatment.

3.3.2.1. Thermal annealing treatment

For comparison with further discussed processes, the classical thermal annealing was performed on block copolymer films. The heating temperature was set above PMMA T_g but lower than P3HT melting temperature (T_m), at 130 °C for 30 min. **Figure 9A** and **B** show that the fibrillar morphology of $P3HT_{16K}$-*b*-$PMMA_{10K}$ remained after the annealing. Indeed, this temperature was not high enough to give mobility of P3HT chains in the crystal region. Therefore, the annealing temperature was set at 230°C during 10 minutes and ordered nanostructures were observed with disappearance of fibrils (**Figure 9C**) . The temperature was, this time, close enough to *Tm* to allow the relaxation and the diffusion of P3HT chain and led to form ordered nanostructure. The morphology of polymer films present PMMA cylinders due to the fact that the fraction of P3HT is higher than PMMA.[67-68]

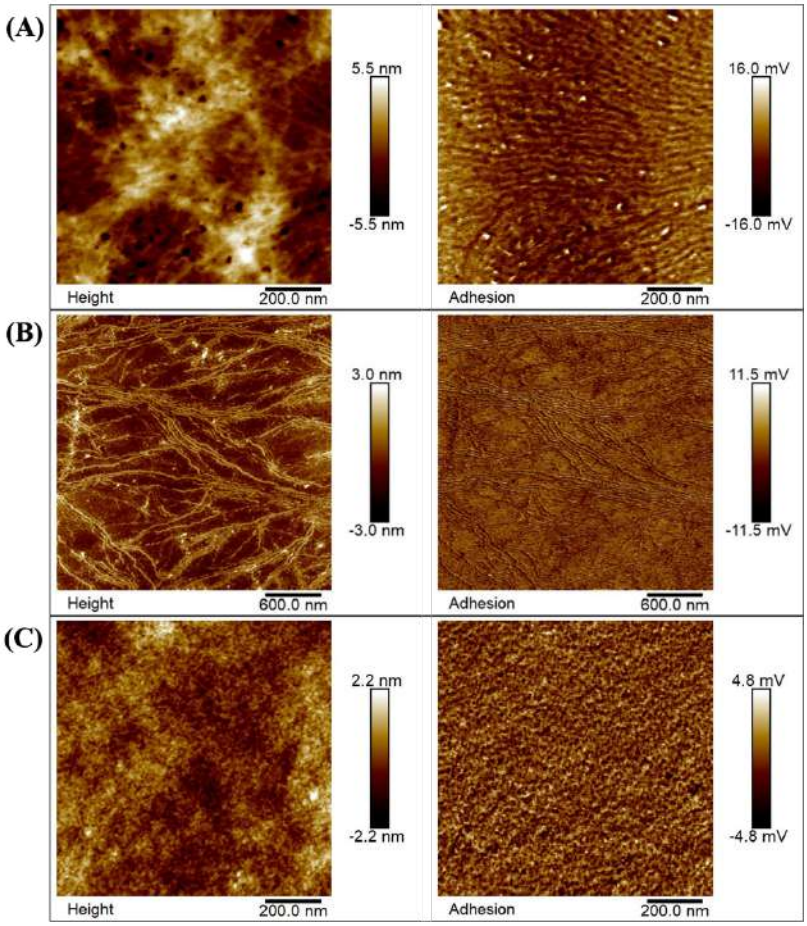

Figure 9. PeakForce QNM-Mode AFM images of diblock copolymers, films were prepared at 1.0 g/L by dip coating method with the withdraw speed was 10 µm/sec. Height and adhesion image of $P3HT_{16K}$-b-$PMMA_{10K}$, film prepared in $CHCl_3$. (A) Before thermal annealing, (B) thermal annealing at 130 °C and (C) annealed at 230 °C for 10 min.

3.3.2.2. Microwave annealing

As explained in the bibliography, the microwaves are absorbed by the substrata which heat the polymer film like a hot pan.[69] With this annealing, long range nano-structurations of block copolymers have been produced in a few seconds.[70-71] In the previous chapter 2, we reported the high ordered nanostructure a triblock copolymer poly(methyl methacrylate)-*block*-poly(n-butylacrylate)-*block*-poly(methyl methacrylate) (PMMA-*b*-PnBuA-*b*-PMMA) obtained *via* microwave-triggered annealing, nano-cylinders were observed. [72] In this part, we will study the microwave (MW) annealing of the P3HT-*b*-PMMA copolymer with the objective to control the nano-structuration in a short time scale.

Several papers have shown that a microwave annealing improves the performances of P3HT based solar cells or transistor.[73-74] MW irradiation was shown to increase the crystallinity of the conjugated polymer by careful AFM and X-ray diffraction analysis. It was also showed that the *p*-conjugated blend, P3HT-PCBM absorbed some of the microwave and heat. In our study, the microwave annealing performed, was made in a chloroform atmosphere. Indeed, 1 mL of chloroform was added at the bottom of the vial before annealing. Therefore, the annealing was dual, a thermal one induced by the microwave absorption of the substrate, and a solvent annealing induced by the evaporation of chloroform in the chamber. This chloroform will help solubilizing P3HT crystals and hopefully damage the fibrils. **Figure 10** shows AFM images of BCP films before and after MW annealing at 30W for 1 min under $CHCl_3$ atmosphere. The $P3HT_{16K}$-*b*-$PMMA_{10K}$ films, dip-coated from chloroform were first analyzed **(Figure 10 A & A')**. A transformation of the surface morphology from fibrils before annealing, to a large majority of cylinders after one minute of microwave irradiation can be observed. Same kind of morphologies were obtained when $P3HT_{16K}$-b^{+}-$PMMA_{10K}$ films (also using a polymer solution in chloroform) were imaged **(Figure 10 B & B')**, with nanofibrils and a mixture of cylinders/fibrils, before and after irradiation respectively. On the contrary, when solution diluted from the chloroform ethanol mixture were used to coat films of neutral and charged polymer, the in-minute microwave annealing was not efficient enough to evolve fibrils into cylinders **(Figure 10 C, C', D & D')**.

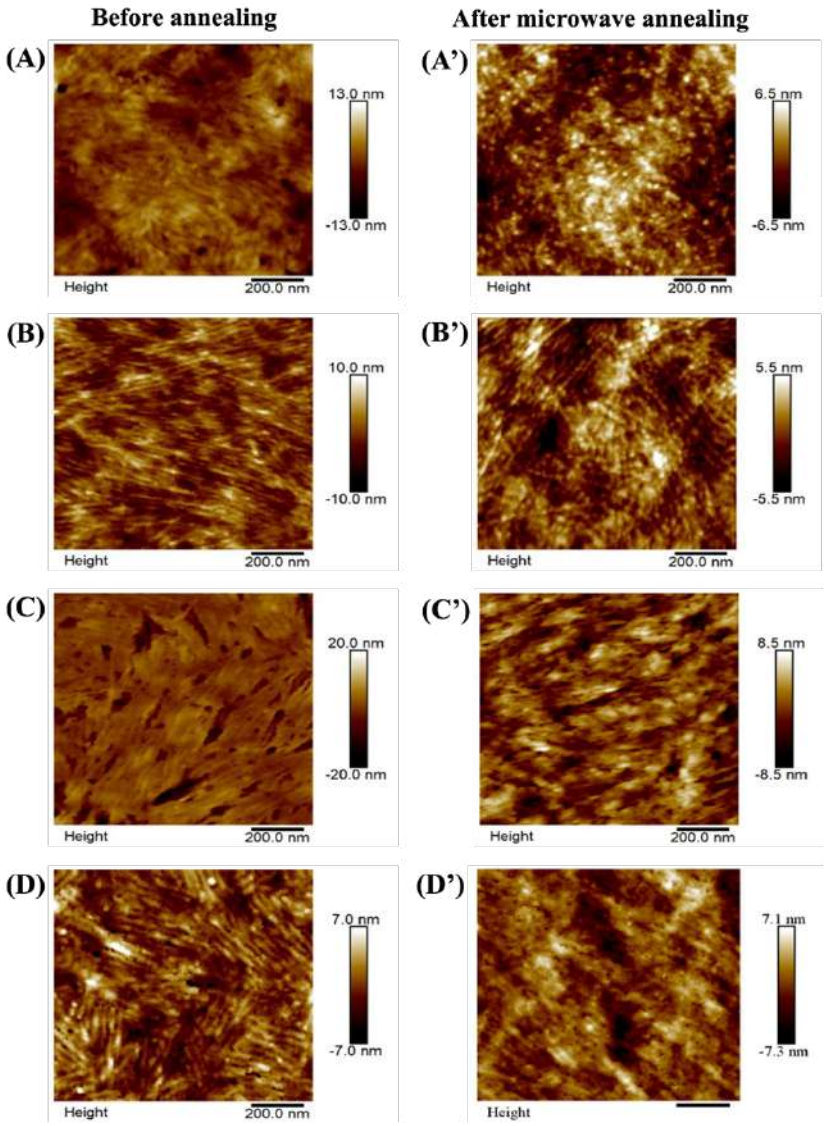

Figure 10. Peakforce QNM-Mode AFM images before and after microwave annealing at 30W for 1 min under $CHCl_3$ atmosphere of diblock copolymers, all films were prepared by dip-coating method with 10 μm/sec and concentration of polymers solution were 3.0 g/L which two difference solvent. (A) $P3HT_{16K}$-*b*-$PMMA_{10K}$ in $CHCl_3$, (B) $P3HT_{16K}$-b^+-$PMMA_{10K}.I^-$ in $CHCl_3$, (C) $P3HT_{16K}$-*b*-$PMMA_{10K}$ in 83%$CHCl_3$-17%EtOH, (D) $P3HT_{16K}$-b^+-$PMMA_{10K}.I^-$ in 83%$CHCl_3$-17%EtOH.

The impact of ionic junction was insignificant for the films morphology evolution as aggregation effect seems to be stronger than the influence of charge on BCPs with high molar mass P3HT blocks (complete height and adhesion AFM images are presented in **Figure S12**). When neutral and ionized $P3HT_{5K}$-*b*-$PMMA_{10K}$ films were used, we also observed a decrease of the surface ratio of fibrils **(Figure 11**).

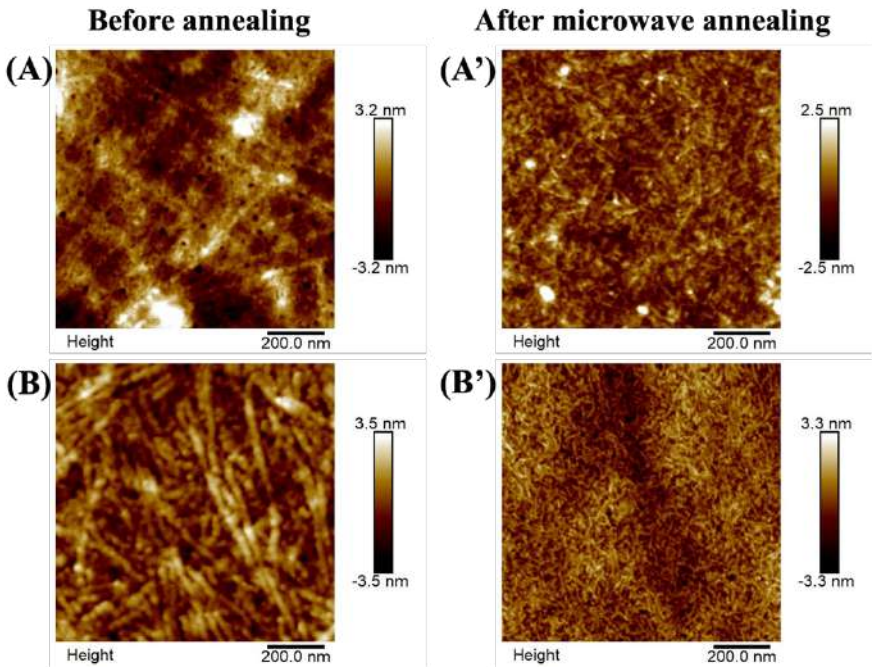

Figure 11. Peakforce QNM-Mode AFM images before and after microwave annealing at 30W for 1 min under $CHCl_3$ atmosphere of diblock copolymers, all films were prepared by dip-coating method with 10 μm/sec and concentration of polymers solution were 3.0 g/L in 83%$CHCl_3$-17%EtOH. (A) $P3HT_{5K}$-*b*-$PMMA_{10K}$, (B) $P3HT_{5K}$-b^+-$PMMA_{10K}.I^-$.

Comparing thermal and microwave/solvent annealing of $P3HT_{16K}$-*b*-$PMMA_{10K}$ films, a thermal annealing of 10 min at T_m of BCP and a MW annealing for 1 min at 30W are equally able to remove fibrils nanostructure from BCP films and obviously, the time gain is interesting. The MW annealing time and power were also checked to know if more ordered nanostructure could be obtained. We compared MW power between 30W and 50 W and annealing time for 1 min to 2 min for $P3HT_{16K}$-*b*-$PMMA_{10K}$ films **(Figure 12)**. AFM images of films after a 30W for 2 min annealing showed that the film roughness increased and some big features appeared. This is consistent with a thermal degradation of the organic film. After an annealing at 50W for 1 min, we clearly observe two phases, probably being film and substrate. Finally, after 2 minutes at 50W, BCP films seemed completely damaged with no features observed on the images **(Figure 12D)**. These results show that a great care should be taken in setting the parameters of the microwave annealing. An excessive time or power irradiation, leads to a raise of temperature so high that it induces a thermal degradation of the organic macromolecules.

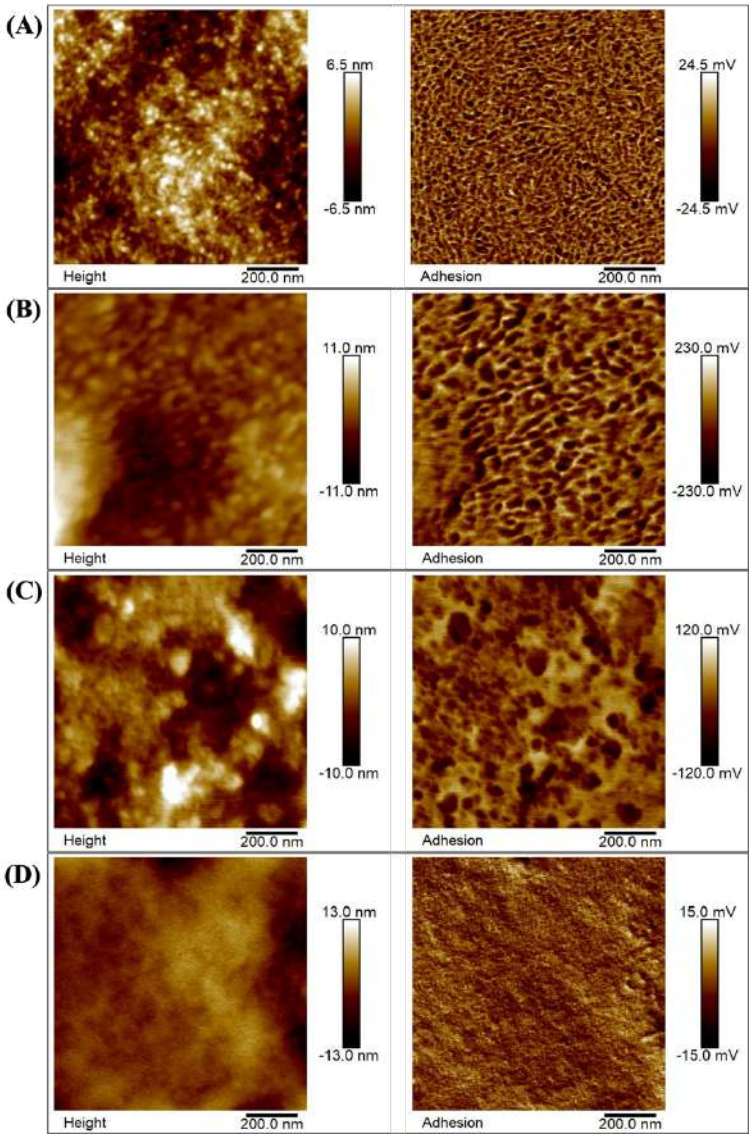

Figure12. High and adhesion peakforce QNM-Mode AFM images of P3HT$_{16K}$-*b*-PMMA$_{10K}$ films after microwave annealing under $CHCl_3$ atmosphere all films were prepared by dip-coating method with 10 μm/sec and concentration of polymers solution were 3.0 g/L in $CHCl_3$ with difference annealing energy and annealing time. (A) annealing at 30W 1 min, (B) annealing at 30W 2 min, (C) annealing at 50W 1 min, (D) annealing at 50W 2 min.

4. Conclusion

In this work, we have synthesized P3HT-*b*-PMMA block copolymers and investigated their self-assembly in thin films. The synthesis was the result of a combination of KCTP, ATRP and Huisgen cycloaddition. With this synthetic strategy, it was possible to easily vary the block chain length and to introduce a charge at the junction of the final BCP by quaternization of the triazole ring. The results of the self-assembly in thin film demonstrated that, interactions

between polymer and solvent in the casting solution drive the morphology obtained after the solution casting on a surface. Solvent, *via* the temperature, the concentration or the amount of non-solvent additive was demonstrated to play a major role in the creation of P3HT fibrils. At high concentration, low temperature and in the presence of a "bad" solvent for P3HT, crystallization is induced and fibrils of a few micrometers long are produced. The solute also is very important, for short P3HT block: the presence of a charge at the junction of the block will increase solubility in chloroform and lower the π–π interaction giving rise to structuration driven by block segregation. All these parameters can be tuned before film casting to obtain desired morphology. After casting, the films are in solid state and chains mobility is low due to the high *Tg* and *Tm* values. To increase this, thermal, solvent or microwave annealing have been studied. At high temperature, above the *Tm* value of the P3HT phase, block segregation is free to happen and the cooling can lead to cylinders structures. This temperature can be reached by either thermal or microwave annealings. A one-minute treatment at 30 W in a chloroform atmosphere was needed to observe the disappearance of P3HT fibrils, phenomena usually occurring by a classical thermal annealing for many minutes at 230°C. We have also showed that the time and power should be finely tuned to avoid degradation of the film.
The next step would be to etch by UV/ozone plasma, the PMMA matrix of well-organized *out of plane* P3HT cylinders, to tailor and pave the way to nano-patterned P3HT conductive surfaces.

Reference:

(1) Z. Li.; R. J. Ono.; Z. Q. Wu.; C. W. Bielawski. Synthesis and self-Assembly of poly(3-hexylthiophene)-block-poly(acrylic Acid). *Chem. Commun*. 2011, 47 (1), 197–199.

(2) R. D. McCullough.; S. T. Nagle.; S. P. Williams.; R. D. Lowe.; M. Jayaraman. Self-orienting head-to-tail poly(3-alkylthiophenes): new insights on structure-property relationships in conducting polymers. *J. Am. Chem. Soc*. 1993, 115, 4910−4911.

(3) R. S. Loewe.; S. M. Khersonsky.; R. D. McCullough. A Simple Method to Prepare Head-to-Tail Coupled, Regioregular Poly(3alkylthiophenes) Using Grignard Metathesis. *Adv. Mater*. 1999, 11, 250−253.

(4) R. S. Loewe.; P. C. Ewbank.; J. Liu.; L. Zhai.; R. D. McCullough. Regioregular, head-to-tail coupled poly(3-alkylthiophenes) made easy by the GRIM method: investigation of the reaction and the origin of regioselectivity. *Macromolecules* 2001, 34, 4324−4333.

(5) A. Yokoyama.; R. Miyakoshi.; T. Yokozawa. Chain-growth polymerization for poly(3-hexylthiophene) with a defined molecular weight and a low polydispersity. *Macromolecules* 2004, 37, 1169− 1171.

(6) R. Miyakoshi.; A. Yokoyama.; T. Yokozawa. Catalyst-transfer polycondensation. Mechanism of Ni-catalyzed chain-growth polymerization leading to well-defined poly(3-hexylthiophene). *J. Am. Chem. Soc*. 2005, 127, 17542−17547.

(7) R. A. Segalman.; B. McCulloch.; S. Kirmayer.; J. J. Urban. Block copolymers for organic optoelectronics. *Macromolecules*. 2009, 42, 9205-9216.

(8) H. Erothu.; J. Kolomanska.; P. Johnston.; S. Schumann.; D. Deribew.; D. T. W. Toolan.; A. Gregori.; C. Dagron-Lartigau.; G. Portale.; W. Bras.; T. Arnold.; A. Distler.; R. C. Hiorns.; P. Mokarian-Tabari.; T. W. Collins.; J. R. Howse.; P. D. Topham. Synthesis, thermal processing, and thin film morphology of poly3-hexylthiophene)-poly(styrenesulfonate) block copolymers. *Macromolecules*. 2015, 48, 2107-2117.

(9) M. G. Alemseghed.; J. Servello.; N. Hundt.; P. Sista.; M. C. Biewer.; M. C. Stefan. Amphiphilic block copolymers containing regioregular poly(3-hexylthiophene) and poly(2-ethyl-2-oxazoline). *Macromol. Chem. Phys*. 2010, 211, 1291-1297.

(10) Y.-H. Lee.; W.-C. Yen.; W.-F. Su.; C.-A. Dai. Self-assembly and phase transformations of π-conjugated block copolymers that bend and twist: from rigid-rod nanowires to highly curvaceous gyroids. Soft matter. 2011, 7, 10429-10442.

(11) Y. Fu.; C. Lin.; F.-Y. Tsai. High field-effect mobility from poly(3-hexylthiophene) thin-film transistors by solvent-vapor-induced reflow. *Organic Electronics*. 2009, 10, 883-888.

(12) A. Zen.; M. Saphiannikova.; D. Neher.; J. Grenzer.; S. Grigorian.; U. Pietsch.; U. Asawapirom.; S. Janietez.; U. Sherf.; I. Lieberwirth.; G. Wegner. Effect of molecular weight on the structure and crystallinity of poly(3-hexylthiophene). *Macromolecules* 2006, 39, 2162-2171.

(13) V. Ho; B. W. Boudouris.; R. A. Segalman. Tuning polythiophene crystallization through systematic side chain functionalization. *Macromolecules* 2010, 43, 7895-7899.

(14) Y.-C. Tseng.; S. B. Darling. Block copolymer nanostructures for technology. *Polymers*, 2010, 2, 470-489.

(15) H.-C. Kim.; S.-M. Park.; W. D. Hinsberg. Block copolymer based nanostructures: materials, processes, and application to electronics. *Chem. Rev*. 2010, 110, 146-177.

(16) I. Botiz.; S. B. Darling. Self-assembly of poly(3-hexylthiophene)-block-polylactide block copolymer and subsequent incorporation of electron acceptor material. *Macromolecules*. 2009, 42, 8211-8217.

(16) C.-L. Liu.; C.-H. Lin.; C.-C. Kuo.; S.-T. Lin.; W.-C. Chen. Conjugated rod-coil block copolymers: synthesis, morphology, photophysical properties, and stimuli-responsive applications. *Progress in polymer science*. 2011, 36, 603-637.

(17) N. Sary.; L. Rubatat.; C. Brochon.; G. Hadziioannou.; j. Roukolainen.; R. Mezzenga. Self-assembly of poly(diethylhexyloxy-p-phenylenevinylene)-b-poly(4-vinylpyridine) rod-coil block copolymer systems. *Macromolecules*. 2007, 40, 6990-6997.

(18) M. He.; F. Qiu.; Z. Lin. Conjugated rod-coil and rod-rod block copolymers for photovoltaic applications. *J. Mater. Chem.* 2011, 21, 17039-17048.

(19) A. F. Hannon.; R. J. Kline.; D. DeLongchamp. Advancing the computational methodology of rigid rod and semiflexible polymer systems: a new solution to the wormlike chain model with rod-coil copolymer calculations. *Jornal of polymer science, part B: polymer physics*. 2019, 57, 29-39.

(20) T. Higashihara.; M. Ueda. Synthesis and characterization of a novel coil-rod-coil triblock copolymers comprised of regioregulqr poly(3-hexylthiophene) and poly(methyl methacrylate) segments. *Reactive & Functional Polymers* 2009, 69, 457-462.

(21) S. Y. Choi.; J. U. Lee. ; J. W. Lee. ; S. Lee. ; Y. J. Song. ; W. H. Jo. ; S. H. Kim. Highly ordered poly(3-hexylthiophene) rod polymers via block copolymer self-assembly. *Macromolecules* 2011, 44, 1771-1774.

(22) B. D. Olsen.; R. A. Segalman. Structure and thermodynamics of weakly segregated rod-coil block copolymers. *Macromolecules*. 2005, 38, 10127-10137.

(23) M. Reenders.; G. ten Brinke. Composition and orientational ordering in rod-coil diblock copolymer melts. *Macromolecules*. 2002, 35, 3266-3280.
(24) C.-C. Ho.; Y.-H. Lee.; C.-A. Dai.; R. A. Segalman.; W.-F. Su. Synthesis and self-assembly of poly(diethylhexyloxy-p-phenylenevinylene)-*b*-poly(methyl methacrylate) rod-coil block copolymers. *Macromolecules*. 2009, 42, 4208-4219.
(25) J. Zhang.; X.-F. Chen.; H.-B. Wei.; X.-H. Wan. Tunable assembly of amphiphilic rod-coil block copolymers insolution. *Chem. Soc. Rev*. 2013, 42, 9127-9154.
(26) Z. Xu.; J. Lin.; Q. Zhang.; L. Wang.; X. Tian. Theoretical simulations of nanostructures self-assembled from copolymer systems. *Polym. Chem*. 2016, 7, 3783-3811.
(27) H. Feng.; X. Lu.; W. Wang.; N.-G. Kang.; J. W. Mays. Block copolymers: synthesis, self-assembly, and applications. *Polymers*. 2017, 9, 494.
(28) V. Schädler.; U. Wiesner. Salt-controlled lamellar spacing in ionically end-capped symmetric diblock copolymers. *Macromolecules*. 1997, 30, 6698-6701.
(29) M. Schöps.; H. Leist.; A. DuChesne.; U. Wiesner. Salt-induced switching of microdomain morphology of ionically functionalized diblock copolymers. *Macromolecules*. 1999, 32, 2806-2809.
(30) Y. Lou.; D. Montarnal.; M. J. Treat.; P. D. Hustad.; M. D. Christianson.; E. J. Kramer.; G. H. Fredrickson.; C. J. Hawker. Enhanced block copolymer phase separation using click chemistry and ionic junctions. *ACS Macro Lett*. 2015, 4, 1332-1336.
(31) E. Ji.; V. Pellerin.; L. Rubatat. ; E. Grelet. ; A. Bousquet. ; L. Billon. Self-assembly of ionizable “Clicked” P3HT-*b*-PMMA copolymers: Ionic bonding group/counterion effects on morphology. *Macromolecules* 2017, 50, 235-243.
(32) K. Yazawa.; Y. Inoue.; T. Shimizu.; M. Tansho.; N. Asakawa. Molecular dynamics of regioregular poly(3-hexylthiophene) investigated by NMR relaxation and an interpretation of temperature dependent optical absorption. *J. Phys. Chem. B*. 2010, 114, 1241-1248.
(33) E. Mena-Osteritz.; A. Meyer.; B. M. W. Langeveld-Voss.; R. A. J. Janssen.; E. W. Meijer.; P. Bäuerle. Two-dimensional crystals of poly(3-alkylthiophene)s: direct visualization of polymer folds in submolecular resolution. *Angew. Chem. Int. Ed*. 2000, 39, 2680-2684.
(34) S.-H. Lin.; S.-J. Wu.; C.-C. Ho.; W.-F. Su. Rational design of versatile self-assembly morphology of rod-coil block copolymer. *Macromolecules*. 2013, 46, 2725-2732.
(35) V. Ho.; B. W. Boudouris.; B. L. McCulloch.; C. G. Shuttle.; M. Burkhard.; M. L. Chabinyc.; R. A. Segalman. Poly(3-alkylthiophebe) diblock copolymers with ordered microstructures and continuous semiconducting pathways. *J. Am. Chem. Soc.* 2011, 133, 9270-9273.

(36) K. E. Smith.; S. Sawicki.; M. A. Hyjek.; S. Downey.; K. Gall. The effect of the glass transition temperature on the toughness of photopolymerizable (meth)acrylate networks under physiological conditions. *Polymer (guildf)*. 2009, 50, 5112-5123.
(37) F. F. Lupi.; T. J. Giammaria.; F. G. Volpe.; F. Lotto.; G. Seguini.; B. Pivac.; M. Laus.; M. Perego. High aspect ratio PS-*b*-PMMA block copolymer masks for lithographic applications. ACS *Appl. Mater. Interfaces*. 2014, 6, 21389-21396.
(38) M. Ceresoli.; F. F. Lupi.; G. Seguini.; K. Sparnacci.; V. Gianotti.; D. Antonioli.; M. Laus.; L. Boarino.; M. Perego. Evolution of lateral ordering in symmetric block copolymer thin films upon rapid thermal processing. *Nanotechnology*. 2014, 25, 275601.
(39) A. M. Welander.; H. Kang.; K. O. Stuen.; H. H. Solak.; M. Müller.; J. J. de Pablo.; P. F. Nealey. Rapid directed assembly of block copolymer films at elevated temperatures. *Macromolecules*. 2008, 41, 2759-2761.
(40) E. C. Davidson.; R. A. Segalman. Thermal control of confined crystallization within P3HT block copolymer microdemains. *Macromolecules* 2017, 50(20), 8097-8105.
(41) H. Erothu.; J. Kolomanska.; P. Johnston.; S. schumann.; D. Deribew.; D. T. W. Toolan.; A. Gregori.; C. D. Lartigau.; G. Portale.; W. Bras.; T. Arnold.; A. Distler.; R. C. Hiorns.; P. M. Tabari.; T. W. Collins.; J. R. Howse.; P. D. Topham. Synthesis, thermal processing, and thin film morphology of poly(3-hexylthiophene)-poly(styrenesulfonate) block copolymers. *Macromolecules.* 2015, 48, 2107-2117.
(42) L. Li.; G. Lu.; X. Yang. Improving performance of ppolymer photovoltaic devices using and annealing-free approach *via* construction of ordered aggregates in solution. *J. Mater. Chem.* 2008, 18, 1984-1990.
(43) D. Borah.; R. Senthamaraikannan.; S. Rasappa.; B. Kosmala.; J. D. Holmes.; M. A. Morris. Swift nanopattern formation of PS-*b*-PMMA and Ps-*b*-PDMS block copolymer films using a microwave assisted technique. *ACS Nano*. 2013, 7(8), 6583-6596.
(44) C. Jin.; J. N. Murphy.; K. D. Harris.; J. M. Buriak. Deconvoluting the mechanism of microwave annealing of block copolymer thin films. *ACS Nano*. 2014, 8(4), 3979-3991.
(45) P. M. Tabari.; C. Cummins.; S. Rasappa. ; C. Simao. ; C. M. S. Torres.; J. D. Holmes.; M. A. Morris. Study of the kinetics ans mechanism of rapid self-assembly in block copolymer thin films during solvo-microwave annealing. *Langmuir* 2014, 30, 10728-10739.
(46) Z. Qiang.; C. Ye.; K. Lin.; M. L. Becker. ; K. A. Cavicchi.; B. D. Vogt. Evolution in surface morphology during rapid microwave annealing of PS-b-PMMA thin films. *Journal of polymer science, part B: polymer physics* 2016, 54, 1499-1506.

(47) S.-H. Lin.; S.-J. Wu.; C.-C. Ho.; W.-F. Su. Rational design of versatile self-assembly morphology of rod-coil block copolymer. *Macromolecules*. 2013, 46, 2725-2732.
(48) J. Gwyther.; J. B. Gilroy.; P. A. Rupar.; D. J. Lunn.; E. Kynaston.; S. K. Patra.; G. R. Whittell.; M. A. Winnik.; I. Manners. Dimensional control of block copolymer nanofibers with a π-conjugated core: crystallization-driven solution self-assembly of amphiphilic poly(3-hexylthiophen)-*b*-poly(2-vinylpyridine). Chem. Eur. J. 2013, 19, 9186-9197.
(49) M. H. M. Cativo.; D. K. Kim.; R. A. Riggleman.; K. G. Yager.; S. S. Nonnemann.; H. Chao.; D. A. Bonnell.; C. t. Black.; C. R. Kagan.; S.-J. Park. Air-liquid interfacial self-assembly of conjugated block copolymers into ordered nanowire arrays. *ACS Nano*. 2014, 8, 12755-12762.
(50) Enthalpy of fusion of poly(3-hexylthiophene) by differential scanning calorimetry. *Journal of polymer science, part B: polymer physics*. 2014, 52, 1469-1475.
(51) S. Joshi.; P. Pingel.; S. Grigorian.; T. Panzner.; U. Pietsch.; D. Neher.; M. Forster.; U. Scherf. Bimodal temperature behavior of structure and mobility in high molecular weight P3HT thin films. *Macromolecules*. 2009, 42, 4651-4660.
(52) C. R. Snyder.; R. C. Nieuwendaal.; D. M. Delongchamp.; C. K. Luscombe.; P. Sista.; S. D. Boyd. Quantifying crystallinity in high molar mass poly(3-hexylthiophene). *Macromolecules*. 2014, 47, 3942-3950.
(53) S. Grigorian.; S. Joshi.; U. Pietsch. Temperature-dependent structural properties of P3HT films. *IOP Conf. Series: materials science and engineering*. 2010, 14, 012007.
(54) J. Y. Ho.; M. Shin.; T. I. Lee.; W. S. Jang.; Y. Min.; J.-M. Myoung.; H. K. Baik.; U. Jeong. Self-seeded growth of poly(3-hexylthiophene)(P3HT) nanofibrils by a cycle of cooling and heating in solutions. *Macromolecules*. 2012, 45, 7504-7513.
(55) C. T. Black.; C. Forrey.; K. G. Yager. Thickness-dependence of block copolymer coarsening kinetics. *Soft Matter*. 2017, 13,3275-3283.
(56) J. B. Gilroy.; D. J. Lunn.; S. K. Patra.; G. R. Whittell.; M. A. Winnik.; I. Manners. Fiber-like micelles via the crystallization-driven solution self-assembly of poly(3-hexylthiophene)-block poly(methyl methacrylate) copolymers. *Macromolecules*. 2012, 2, 5806-5815.
(57) S. Y. Choi.; J. U. Lee.; J. W. Lee.; S. Lee.; Y. J. Song.; W. H. Jo.; S. H. Kim. Highly ordered poly(3-hexylthiophene) rod polymers via block copolymer self-assembly. *Macromolecules*. 2011, 44, 1771-1774.

(58) D. U. Ahn.; E. Sancaktar. Perpendicularly aligned, size-and spacing-controlled nanocylinders by molecular-weight adjustment of homopolymer blended in an asymmetric triblock copolymer. *Adv. Funct. Mater*. 2006, 16, 1950-1958.
(59) U. Jeong.; D. Y. Ryu.; D. H. Kho.; J. K. Kim.; J. T. Goldbach.; D. H. Kim.; T. P. Russell. Enhancement in the orientation of the microdomain in block copolymer thin films upon the addition of homopolymer. *Adv. Mater*. 2004, 16, 533-536.
(60) Y. D. Park.; H. S. Lee.; Y. J. Choi.; D. Kwak.; J. H. Cho.; S. Lee.; K. Cho. Solubility-induced ordered polythiophene precursors for high-performance organic thin-film transistors. Adv. *Funct. Mater*. 2009, 19, 1200-1206.
(61) S. B. Darling. Isolating the effect of torsional defects on mobility and band gap in conjugated polymers. *J. Phys. Chem. B*. 2008, 112, 8891-8895.
(62) J. Y. Oh.; M. Shin.; T. I. Lee.; W. S. Jang.; Y. Min.; J. M. Myoung. H. K. Baik.; U. Jeong. Self-seeded growth of Poly(3-hexylthiophene) (P3HT) nanofibrils by a cycle of cooling and heating in solutions. *Macromolecules* 2012, 45, 7504-7513.
(63) T. Yamamoto.; D. Komarudin.; M. Arai.; B. L. Lee.; H. Suganuma. ; N. Asakawa. ; Y. Inoue. ; K. Kubota. ; S. Sasaki.; T. Fukuda.; H. Matsuda. Extensive studies on π-stacking of poly (3-alkylthiophene-2, 5-diyl) s and poly (4-alkylthiazole-2, 5-diyl) s by optical spectroscopy, NMR analysis, light scattering analysis, and X-ray crystallography. *J. Am. Chem. Soc.* 1998, 120, 2047-2058.
(64) J. Y. Na.; M. Kim.; Y. D. Park. Solution processing with a good solvent additive for highly reliable organic thin-film transistors. *J. Phys. Chem.* C. 2017, 121, 13930-13937.
(65) N. Kiriy.; E. Jähne.; H. J. Adler.; M. Schneider.; A. Kiriy.; G. Gorodyska.; S. Minko.; D. Jehnichen.; Paul S.; A. A. Fokin.; A. Stamm. One-dimensional aggregation of regioregular polyalkylthiophenes. *Nano Lett.* 2003, 3(6), 707-712.
(66) Y. D. Park.; S. G. Lee.; H. S. Lee.; D. Kwak.; D. H. Lee.; K. Cho. Solubility-driven polythiophene nanowires and their electrical characteristics. *J. Mater. Chem*. 2011, 21,2338-2343.
(67) B. D. Olsen.; X. Li.; J. Wang.; R. A. Segalman. Near-surface and internal lamellar structure and orientation in thin films of rod-coil block copolymers. *Soft Matter*. 2009, 5, 182-192.
(68) B. D. Olsen.; R. A. Segalman. Nonlamellar phases in asymmetric rod-coil block copolymers at increased segregation strengths. *Macromolecules*. 2007, 40, 6922-6929.
(69) D. Adam. Out of the kitchen. Microwave chemistry. *Nature* 2003, 421, 571-572.

(70) D. M. P. Mingos.; D. R. Baghurst. Applications of microwave dielectric heating effects to synthetic problems in chemistry. *Chem. Soc. Rev.* 1991, 20, 1-47.
(71) J. H. Ahn.; J. N. Lee.; Y. C. Kim.; B. T. Ahn. Microwave-induced low-temperature crystallization of amorphous Si thin films. *Current Applied Physics* 2002, 2, 135-139.
(72) N. Benoot.; P. Marcasuzaa.; L. Pessoni.; S. Chasvised.; S. Reynaud.; A. Bousquet.; L. Billon. Hierarchically organized honeycomb films through block copolymer directed self-assembly in "breath figure" templating and soft microwave-triggered annealing. *Soft Matter*. 2018, 14, 4874-4880.
(73) C. J. Ko.; Y. K. Lin.; F. C. Chen. Microwave annealing of polymer photovoltaic devices. *Adv. Mater* 2007, 19, 3520-3523.
(74) X. Shang.; H. Yu.; W. Choi.; E. K. Lee.; J. H. Oh. Effects of microwave-assisted annealing on the morphology and electrical performance of semiconduction polymer thin films. *Organic electronics* 2016, 30, 207-212.

Supplementary information

Fibrils or not fibrils: How to control P3HT-based copolymer thin film morphology?

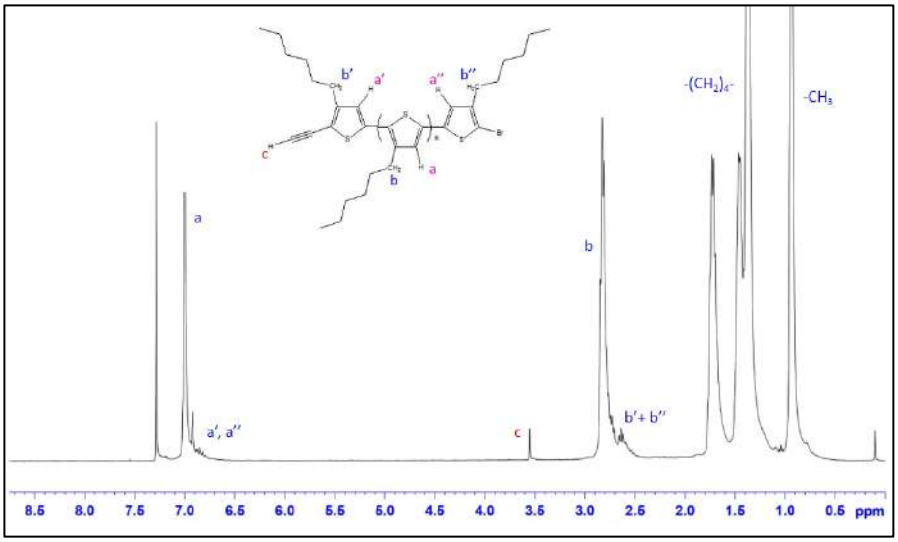

Figure S1. ^{1}H NMR spectrum of P3HT

The ^{1}H NMR spectrum of polymer confirm the ethynyl functionalized was success because the singlet peak of ethynyl group at 3.5 was observed. ^{1}H NMR (400 MHz, $CDCl_3$): δ 0.9 (t, 3H), 1.3(m, 6H), 1.7(t, 2H), 2.8(t, 2H), 3.5(s, 1H), 7.0(s, 1H). For proton at position a, a' and b,b' present at 2.7 and 6.9 respectively.

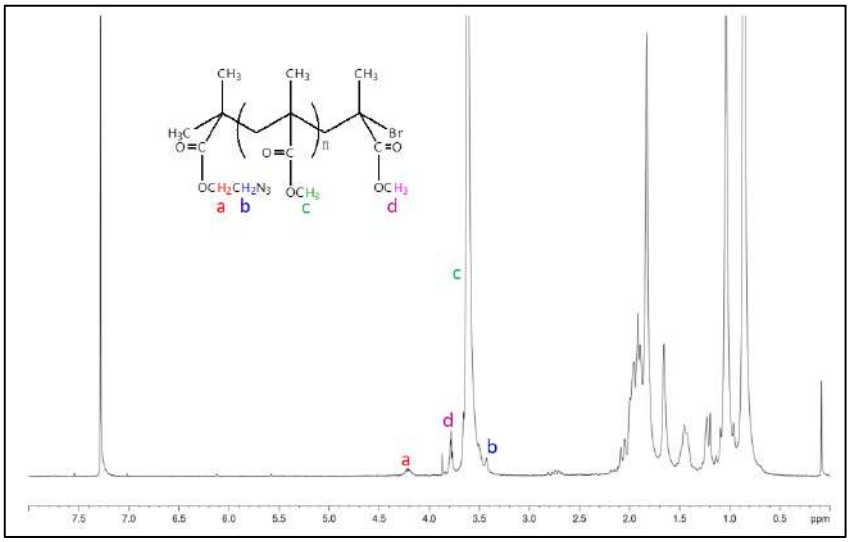

Figure S2. ^{1}H NMR spectrum of PMMA

PMMA was synthesized by ATRP reaction by using 2-azidoethyl 2-bromoisobutyrate as initiator. Result perform by ^{1}H NMR, the methyl ester protons of PMMA-N3 was observed at 3.59 ppm while the methyl ester protons at the bromide-terminate end unit presented at 3.76 ppm, confirming the of polymerization. ^{1}H NMR (400 MHz, CDCl3): δ 0.85 (s, 3H), 1.85 (m, 2H), 3.47 (t, 2H), 3.59 (m, 3H), 3.76(m, 3H), 4.25(m, 2H).

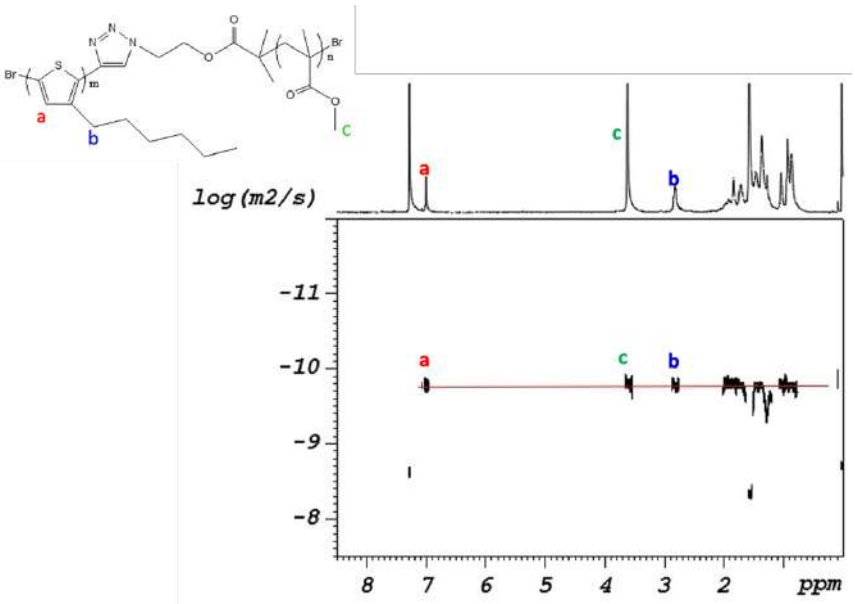

Figure S3. ^{1}H DOSY NMR spectrum of P3HT$_{16KK}$-b-PMMA$_{10K}$.

^{1}H DOSY NMR of P3HT$_{16K}$-*b*-PMMA$_{10K}$ presented single diffusion coefficient that include signal of methyl ester protons of PMMA, methylene protons and single proton of P3HT. We demonstrate that the click coupling reaction was success.

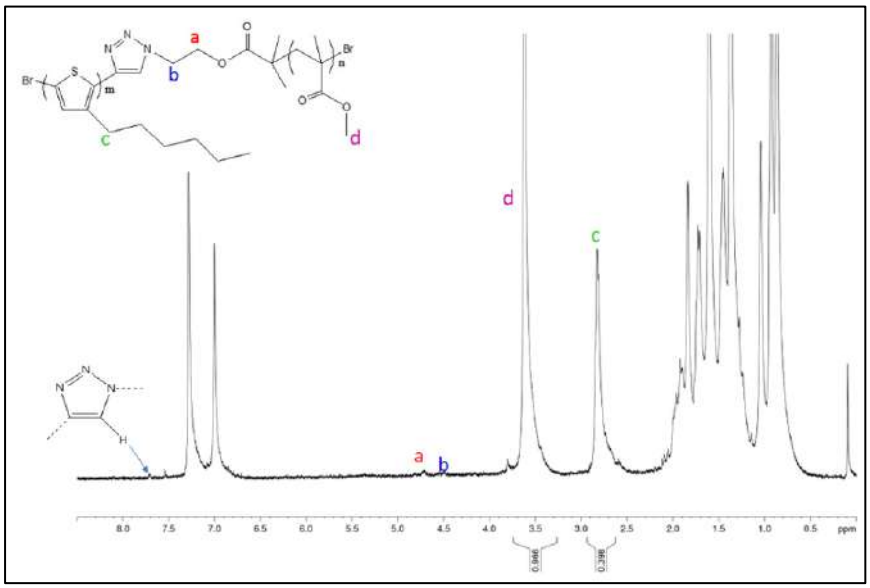

Figure S4. ^{1}H NMR spectrum of P3HT$_{16K}$-b-PMMA$_{10K}$. The chemical shift of triazole ring presented at 7.71 ppm

The succes of click coupling of P3HT and PMMA to P3HT-*b*-PMMA was confirmed by ^{1}H NMR spectrum. The spectrum present methylene protons of P3HT at 2.8 ppm, methyl ester protons of PMMA at 3.6 ppm and the proton of triazole ring at 7.71 ppm. The results were confirming the coupling was success.

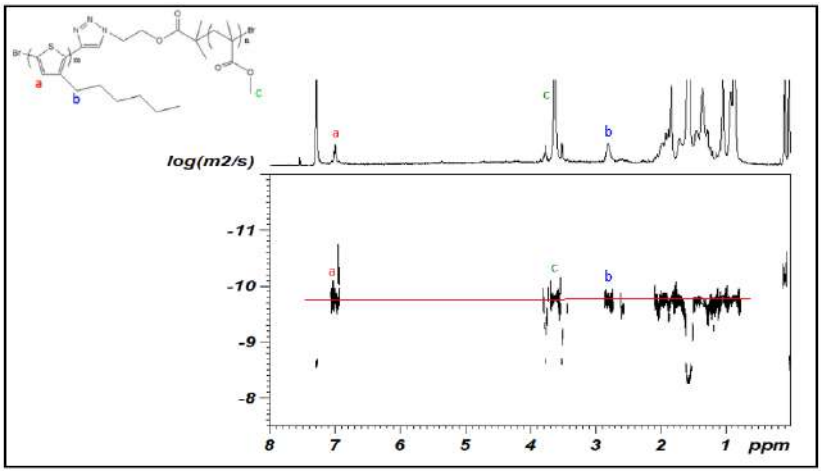

Figure S5. ^{1}H DOSY NMR spectrum of P3HT$_{5K}$-b-PMMA$_{10K}$.

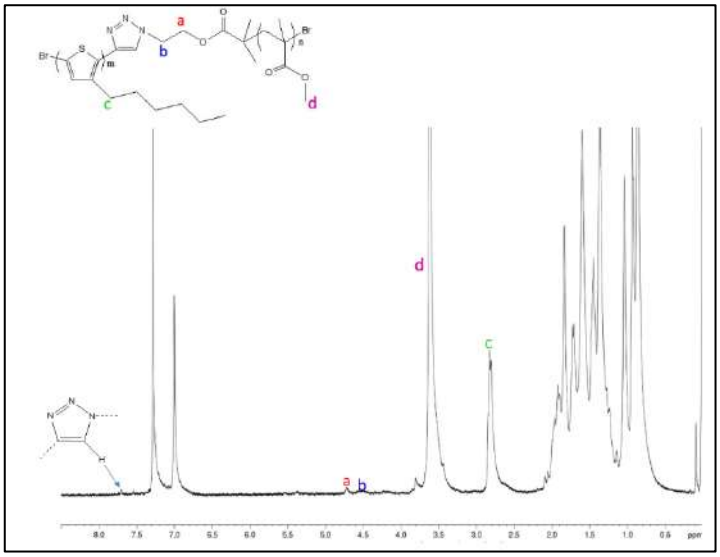

Figure S6. ^{1}H NMR spectrum of P3HT$_{5K}$-b-PMMA$_{10K}$.

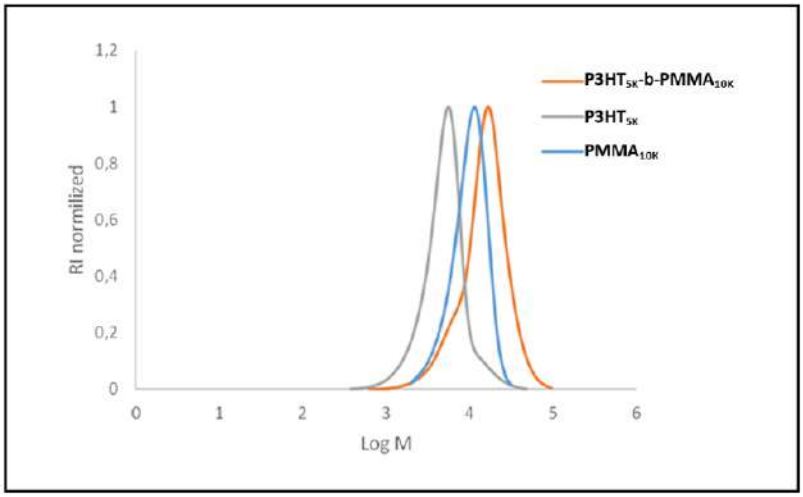

Figure S7. GPC chromatogram of $P3HT_{5K}$-b-$PMMA_{10K}$.

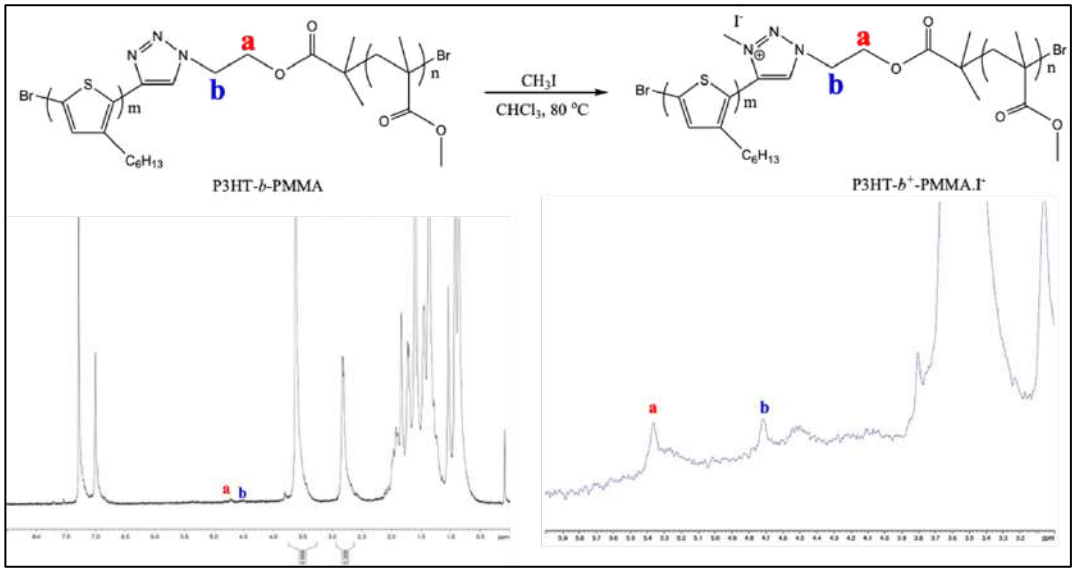

Figure S8. ^{1}H NMR spectrum compared between neutral BCP and ionomer (A) $P3HT_{16K}$-b-$PMMA_{10K}$

A comparison between ^{1}H NMR spectrum of neutral BCP and ionomer as shown in figure S8-S9. The methylene ester protons of neutral BCP at position a and b were shift from 4.7 and 4.5 to 5.39 and 4.71 in quaternized BCP respectively.

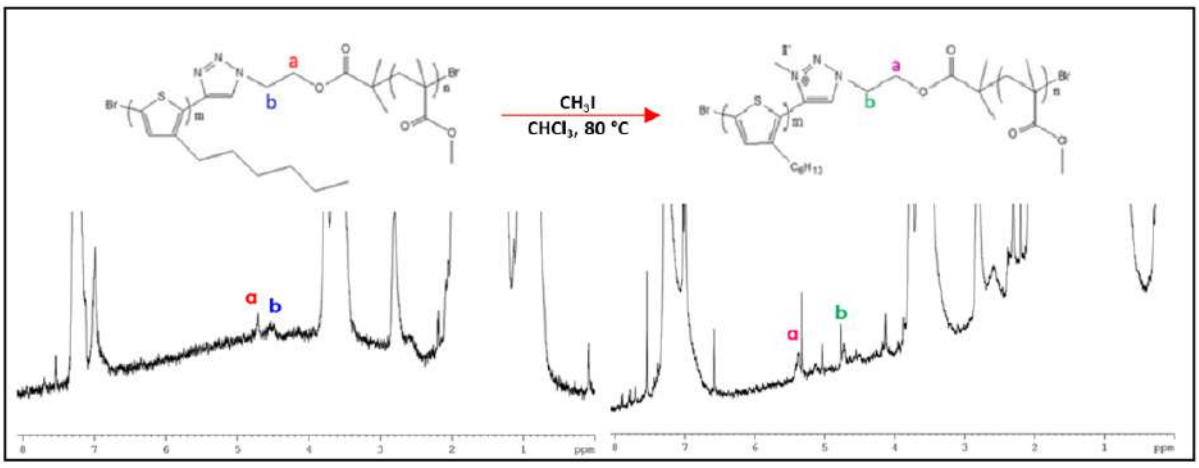

Figure S9. ^{1}H NMR spectrum compared between neutral and ionomer of $P3HT_{5K}$-b-$PMMA_{10K}$

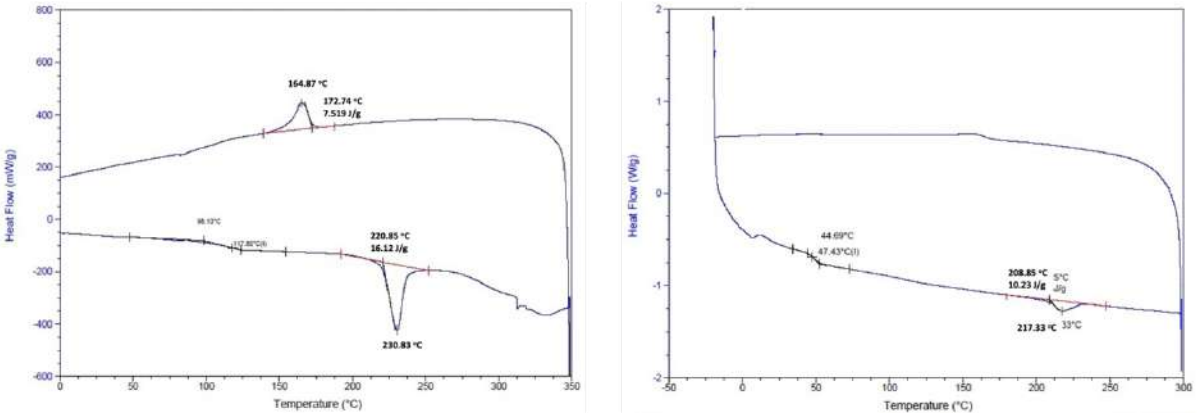

Figure S10. DSC thermogram of the copolymers (A) $P3HT_{16K}$-b-$PMMA_{10K}$. (B) $P3HT_{16K}$-b^{+}-$PMMA_{10K}.I^{-}$

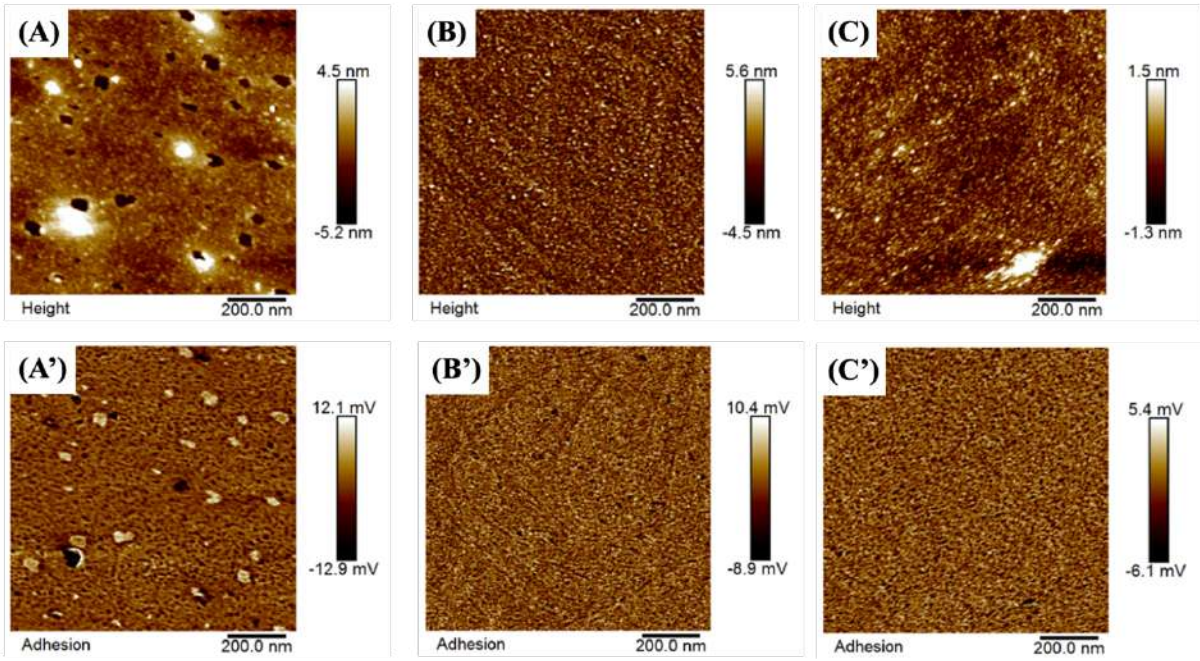

Figure S11. PeakForce QNM-Mode AFM images of diblock copolymers, BCP ($P3HT_{5K}$-b^{+}-$PMMA_{10K}.I^{-}$) dissolved in $CHCl_3$ at room temperature and films were prepared by dip coating method with the withdraw speed was 10 µm/sec. Concentration of solution were 1 $g.L^{-1}$ (A, A'), 3 $g.L^{-1}$ (B, B') and 5 $g.L^{-1}$ (C, C').

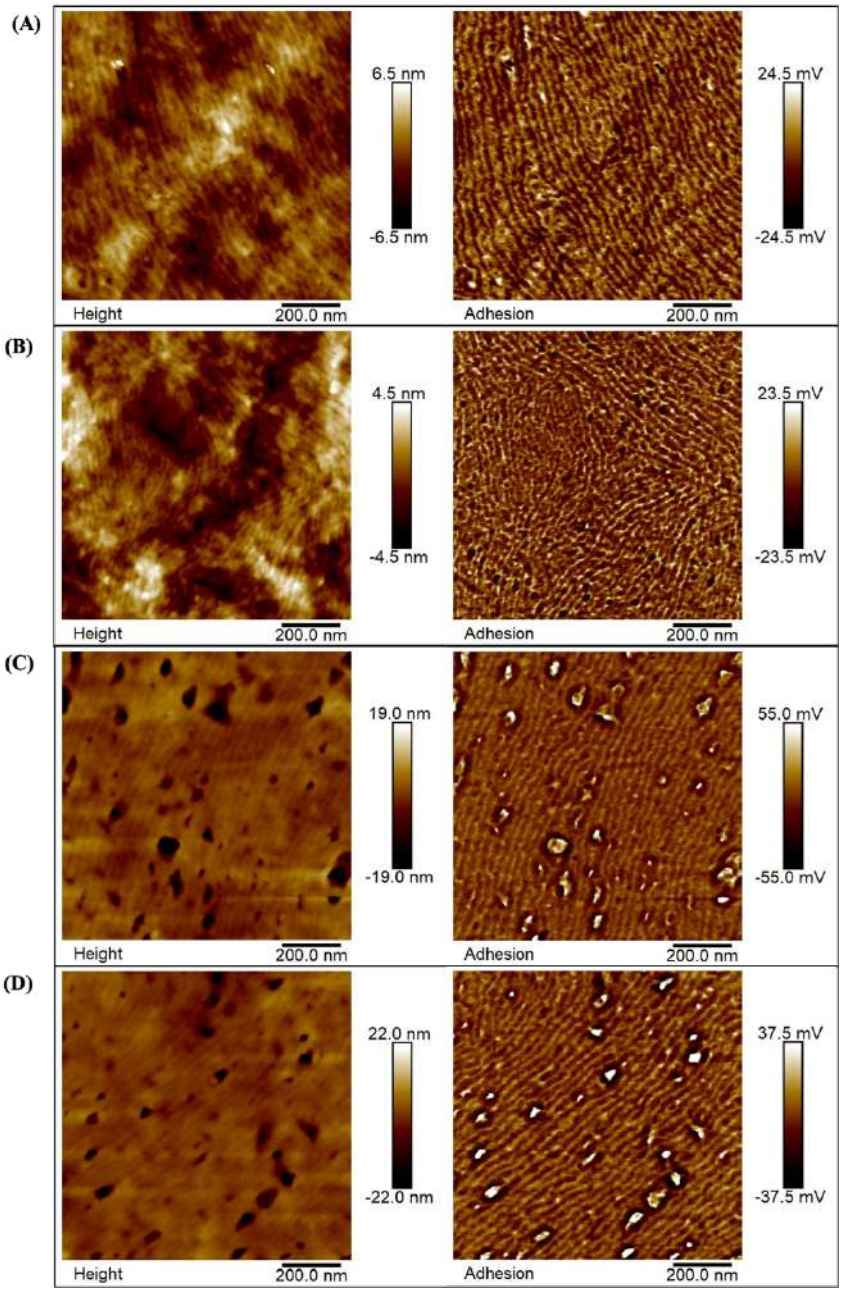

Figure S12. PeakForce QNM-Mode AFM images of diblock copolymers, films were prepared by dip coating method with the withdraw speed was 10 µm/sec AFM at room temperature (A) Height and adhesion images of $P3HT_{16K}$-b-$PMMA_{10K}$, 1.0 g/L in $CHCl_3$. (B) Height and adhesion images $P3HT_{16K}$-b^+-$PMMA_{10K}.I^-$, 1.0 g/L in $CHCl_3$. (C) Height and adhesion images of $P3HT_{16K}$-b-$PMMA_{10K}$, 3.0 g/L in $CHCl_3$. (D) Height and adhesion images $P3HT_{16K}$-b^+-$PMMA_{10K}.I^-$, 3.0 g/L in $CHCl_3$.

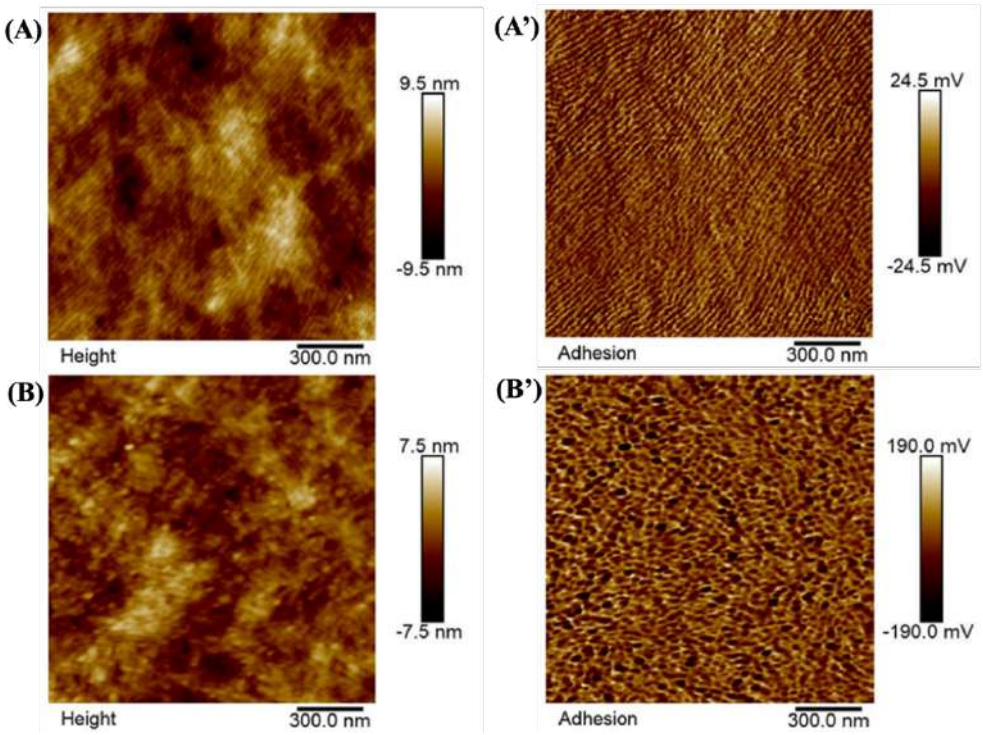

Figure S13. PeakForce QNM-Mode AFM images of diblock copolymers, films were prepared by dip coating method with the withdraw speed was 10 μm/sec AFM at room temperature (A) Height and adhesion images of $P3HT_{16K}$-b-$PMMA_{10K}$, 0.5 g/L in $CHCl_3$. (B) Height and adhesion images $P3HT_{16K}$-b^+-$PMMA_{10K}$.I^-, 0.5 g/L in $CHCl_3$.

CHARPTER 5

Artificial metallo-enzyme based on a diimine-dioxime cobalt complex end-capped conductive poly(3-hexylthiophene)

Context:

Having synthesized the P3HT-*b*-PMMA (Chapter 4), the following study was to use this polymer as binder for tailoring the electrode and adding a macromolecular catalyst able to efficiently bind the electrode material and drive hydrogen production. For this purpose, although precious metals, such as platinum, are often used for H_2-related applications, they are neither cheap nor sustainable resources. There is thus a crucial need to design efficient systems based on earth-abundant first-row transition metals for H_2 evolution from water with high catalytic efficiency. A cobalt catalyst was synthesized in the framework of the eSCALED project by the Artero's group in CEA Grenoble, which contained an azide moiety. We then coupled it with a P3HT sequence to ensure efficient binding with the electrode. Even if we didn't have time to tailor electrodes, a simple and copper free cycloaddition method is presented to couple a cobalt diimine-dioxime complex catalyst and poly(3-hexylthiophene) (P3HT-Co). Then, the electrochemical behavior of the artificial metallo-enzyme is studied by cyclic voltammetry. The P3HT-Co was synthesized from an aniline end-functional poly(3-hexylthiophene) (P3HT-NH_2) precursor which has been prepared by Grignard metathesis polymerization. The molar mass and dispersity of P3HT-NH_2 were determined by size exclusion chromatography (SEC), Mn = 3,500 g/mol and $Đ$ = 1.55. The aniline-end chain functionalization was quantified by MALDI-TOF technique at around 40%. In a second step, P3HT-NH_2 reacted with 2-(cyclooct-2-yn-l-yloxy) acetic acid *via* direct condensation. Finally, the P3HT bearing a cycloalkyne moiety was coupled by copper-free Huisgen cycloaddition with an azido-Cobalt derivative, because usual copper catalyst is a poison of the metal cobalt diimine-dioxime complex. The electrochemical properties of the P3HT-Co catalyst were characterized by cyclic voltammetry, and Co(III/II) and Co (IV/III) transitions were observed proving the successful incorporation of the metal at the polymer chain end for potential hydrogen evolution (Figure 0).

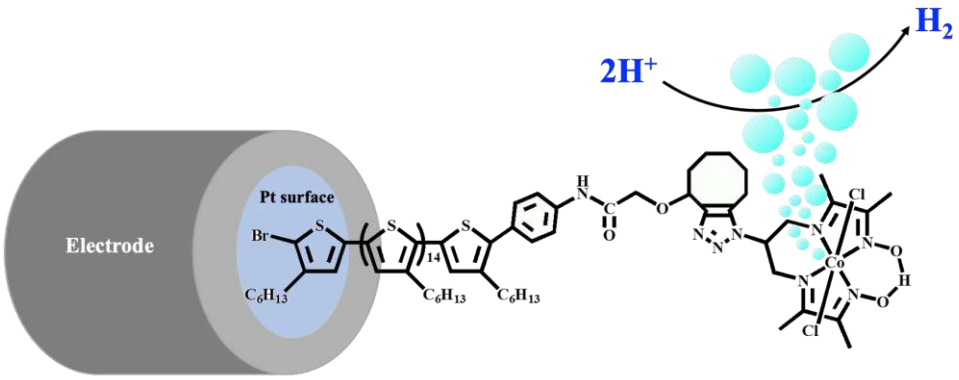

Figure 0. Schematic view of the P3HT-Co material as electrochemical catalyst for Hydrogen evolution.

This work was done in collaboration, thanks to Andrew Bagnall, Murielle Chavarot-Kerlidou and Vincent Artero from CEA.

Table of contents

1. Introduction 193

2. Experimental 195

2.1. Materials……195

2.2. Instrumentation……...195

2.3. Synthesis of cobalt complex-functionalized P3HT (P3HT-Co)…….196

3. Results and discussion 198

3.1. Synthesis and Characterization of the artificial-metallozyme P3HT- cobalt (P3HT-Co)……198

3.2. Electrochemical characterization of P3HT-NH_2 and P3HT-Co complex catalyst……...202

4. Conclusion 204

Reference.....205

Supplementary information 211

Artificial metallo-enzyme based on a diimine-dioxime cobalt complex end-capped conductive poly(3-hexylthiophene)

1. Introduction

Recently, the development of renewable carbon-neutral energy sources such as sunlight is one of the most important challenge mankind has faced.[1] The production of hydrogen from water splitting process, either from electrochemical reaction from sunlight harvesting or photochemical process seems to be a promising and sustainable energy storage in a stable form. Indeed, hydrogen can be easily converted to electricity through fuel cells, that can be used in numerous field such as in the vehicle powering system.[2] Since both hydrogen and water are green energy and reactant for hydrogen production process, respectively, this research field has to be pushed and the present approach is part of the effort.[3] Indeed, such an artificial metallo-enzyme based on semi-conductive polymer was never described, previously. Platinum is often used to catalyze H_2-production due its high efficiency but it is a rare element on earth and as a matter of fact expensive.[4] For an alternative technological production of hydrogen from water, Cobalt-based catalysts (first-row transition metal) have been widely studied due to its efficiency at neutral pH and earth-abundancy.[5-7] The cobaloxime compound based-on (difluoroboryl)dimethyl glyoxime ($dmgBF_2$) ligand has been highlighted because its high catalytic activity to produce hydrogen at low over potential.[8-10] The reaction undergoes the reduction of a Co^{II}-diglyoxime to generate an active species of Co^{I} that can react with a proton source to produce a Co^{III}-hydride. Then two Co^{II}-hydride react through a bimolecular step and eliminate H_2 as a product.

However, practical applications of such molecular catalysts require their incorporation in electrode materials that can be stable and easy to handle. Heterogeneïzation of catalysts have been developed on carbon nanotubes (CNTs) as electrode materials because they are remarkable in terms of conductivity and they provide large surface areas and thus a high catalyst loading.[11-12] Moreover they can be surface functionalized by versatile and straightforward methods, using pyrene linker to create π-stacking with the catalyst[13-16] or using electroreduction of aryldiazonium salts for a covalent anchoring.[17-18] The limitations of carbon nanotubes is that they are not so easy to work with, their dispersion in different solvent can be complicated. In addition, in the absence of a polymer binder/matrix, they can be released from

the surface of the electrode during electrolysis. To make a step forward, the development of a conductive polymeric binder is needed. In this sense, π-conjugated polymers (CPs) could be a solution. Although semi-conducting polymers have been traditionally used in some electronic devices such as photovoltaics or sensors. Recently they have been studied in electro and photocatalysis domains for energy-conversion system.[19] Indeed, on the one end, their high conductiviness at the doped state or their ability to develop π-stacking with conductive graphene materials allow their use as binder in electrocatalysis. On the other hand, their absorption properties and the possibility to tune their HOMO/LUMO levels *via* chemistry make them interesting candidates for photocatalysis. A cobalt complex/conjugated polymer composite was reported by Parnell and co-workers in 2019.[20] They prepared a Co(III) complex and polypyrrole (PPy) composite thin film (CoN_4-PPy) that was electrochemically deposited on the surface of a glassy carbon working electrode. The electro-polymerization of the pyrrole monomer in presence of the cobalt complex led to the formation of hybrid composite films used as supercapacitors. It has to be mentioned that the CoN_4-PPY films coated on glassy carbon electrode displayed excellent electrochemical stability in acidic condition.

P3HT is a widely used conjugated polymer due to the simplicity of its synthesis and easy manipulation.[21] Furthermore, many reports have demonstrated the possibility to end–modify the P3HT chains with functional groups, molecules or macromolecules to increase different properties or develop applications.[22]

In this manuscript, we reported the synthesis of an artificial metallo-enzyme based on diimine-dioxime Cobalt complex functionalized conductive P3HT and its electrochemical properties, for the first time. Aniline P3HT (P3HT-NH_2) was prepared by modifying chain-end P3HT with 4-[bis(trimethylsilyl)amino]-phenylmagnesium bromide during polymerization. Then, a cyclooctyne moiety was introduced by using direct condensation of P3HT-NH_2 with eight-member ring cyclooctyne acetic acid. Finally, the copper free Huisgen cycloaddition was performed between this alkyne polymer and a cobalt complex bearing an azide group. NMR, SEC and IR spectroscopy were used to confirm the success of the different steps and cyclic voltammetry was used to reveal the electrochemical behaviour of the artificial metallo-enzyme.

2. Experimental

2.1. Materials.

All chemicals were purchased from Sigma-Aldrich and used without further purification except for copper bromide (CuBr). CuBr was purified by stirring with acetic acid overnight and washing with acetic acid, absolute ethanol, and diethyl ether and then dried in a vacuum oven.

2.2. Instrumentation.

2.2.1. Proton magnetic nuclear resonance (^{1}H NMR) was carried out on a Bruker 400 MHz spectrometer at 25°C.

2.2.2. Matrix assisted laser desorption ionization time-of-flight mass spectroscopy (MALDI-TOF MS). The end group composition of functionalized polymer was examined by a matrix assisted laser desorption ionization time-of-flight mass spectroscopy and the results are summarized in **table S1**. *MALDI-MS* spectra were performed by the CESAMO (Bordeaux, France) on a Voyager mass spectrometer (Applied Biosystems). The instrument was equipped with a pulsed N_2 laser (337 nm) and a time-delayed extracted ion source. Spectra were recorded in the positive-ion mode using the reflectron and with an accelerating voltage of 20 kV. Samples were dissolved in THF at 10 mg/ml. The DCTB matrix T-2-[3-(4-*t*-butylphenyl)-2-methyl-2-propenylidene]malononitrile solution was prepared at a concentration of 10 mg.mL^{-1} in THF. The solutions were combined in a 10:1 volume ratio of matrix to sample. One to two microliters of the obtained solution were deposited to the sample target and vacuum-dried.

Size exclusion chromatography (SEC). The molar mass and dispersity of the polymers were measured using size exclusion chromatography (SEC) and THF as eluent (flow rate 1.0 mL min^{-1}) at 30 °C. SEC is equipped with a Viscotek VE 5200 automatic injector, a precolumn and two columns (Styragels HR 5E and 4E (7.8 ft, 300 mm)) and 4 detectors: UV−visible spectrophotometer (Viscotek VE 3210), a Multiangle Light Scattering detector (Wyatt Heleos II), a viscosimeter (Wyatt Viscostar II) and a refractive index detector (Viscotek VE 3580). Toluene was used as flow marker. Number-average molar mass (*Mn*) and dispersity (*Đ* = *Mw/Mn*, where *Mw* is the mass-average molar mass) of the polymers were calculated from a conventional calibration derived from polystyrene standards. For all SEC, polymer samples were prepared at 5 g L^{-1} and filtered through 0.45 μm PTFE filters.

2.2.3. Differential scanning calorimetry (DSC) experiments were performed using Q100 DSC from TA Instruments under nitrogen atmosphere with a first cycle at 20°C/min and the second at 10°C/min.

2.2.4. Electrochemical measurements. Cyclic voltammograms were recorded by an Autolab PGSTAT12 potentiostat (Eco Chemie, The Netherlands) controlled by the GPES 4.9 software. A three electrodes cell was used, consisted of a platinum working electrode, a platinum thin sheet embedded in a glass shaft auxiliary electrode and a reference electrode based on a 3 mol.L^{-1} of Ag/AgCl/KCl couple (Ag/AgCl). P3HT-NH_2 or P3HT-Co catalyst (1 mg) and 1 mg of tetrabutylammonium hexafluorophosphate (n-Bu_4NPF_6) were dissolved in THF, then 5 µL of this solution was drop casted onto the working area of the Pt-electrode. All electrodes were transferred into the electrochemical cell in 10 ml of 0.1 M of n-Bu_4NPF_6 in acetonitrile. Cyclic voltammograms of Pt/P3HT-Co were recorded with scan rate at 0.1V/s.

2.3. Synthesis of cobalt complex-functionalized P3HT (P3HT-Co).

P3HT-Co complex was synthesized in 3 steps. First of all, and following the procedure from Higashihara *et. al.*[23], an aniline-terminated regio-regular poly(3-hexylthiophene) (P3HT-NH_2) was synthesized *via* GRIM metathesis polymerization and further addition of 3-[bis(trimethylsilyl)amino]phenylmagnesium chloride at the end of the polymerization. After quenching the reaction with HCL and neutralizing the medium with $NaHCO_3$, and aniline-end chain P3HT could be generated. For this reaction the monomer, 2,5-dibromo-3-hexylthiophene (2 g, 6mmol), was added in a 50 ml Shlenk flask and vacuum for 10 second. To this monomer was added isopropylmagnesium chloride (3.0 ml, 6 mmol) and 20 ml of THF under N_2 atmosphere and stirring to form the Grignard precursor. After 30 min at 0 °C, the solution was transferred *via* a cannula to mix with a suspension of Ni(dppp)Cl_2 dispersed in 30 ml of THF. The polymerization was performed at 0 °C for 3 h, then the ice bath was removed and the reaction was pursued at room temperature. After 30 min, 4-[bis(trimethylsilyl)amino]-phenylmagnesium bromide (3.6 ml, 30 mol % of monomer) was introduced into the reaction flask. The polymer was then precipitated in methanol. The solid polymer obtained was filtered and rinsed with acetone to remove residual metal salts and unreacted monomers. The polymer was dried under vacuum for 12 h. The yield after purification was around 70%. The precipitated product was characterized by ^{1}H NMR in $CDCl_3$, and SEC analysis in THF.

In the second step, cycloalkyne-terminated poly(3-hexylthiophene) (P3HT-cycloalkyne) was prepared by amidification of 2-(cyclooct-2-yn-l-yloxy) acetic acid (cyclooctyne acetic acid)

and P3HT-NH_2 using dicyclohexylcarbodiimide (DCC) as an activating agent in a 3:1:3 ratio. Cyclooctyne acetic acid (I) (92.8 mg, 0.45 mmol), P3HT-NH_2 (404.4 mg, 0.15 mmol), dicyclohexylcarbodiimide (DCC) (81.9 mg, 0.45 mmol) and 60 ml of dichloromethane were added into a 100 ml round-bottom flask. After purging for 10 min the reaction was carried out at room temperature for 24 h. The medium was then quenched by methanol, concentrated by rota-evaporation and finally precipitated in the mixture of methanol-water (70v%-30v%) to remove residual reagent and urea by-product. The cycloalkyne-P3HT was filtered and dried under vacuum for 12 h. The NMR spectra of P3HT-NH_2 and cycloalkyne-P3HT are compared in **Figure2**.

The azido functionalized Cobalt catalyst [Co(DO)(DOH)N_3-pnCl_2] was synthesized following the procedure describded by Andreiadis and co-workers.[10] The azido-functionalized diimine-dioxime ligand N^2,N^2-propanediylbis(2,3-butanedione 2-imine 3-xime $(DOH)_2$pn)) was prepared in five steps from the commercially available of 2-hydroxy-1,3-diaminopropane.[10, 24] The ligand then reacted with Co(II) chloride under air condition to give the [Co(III)(CO)(DOH)N_3-pnCl_2] complex.[10] The cobalt-terminated poly(3-hexylthiophene) (P3HT-Co) was finally prepared by metal-free Huisgen cycloaddition of the azide-functionalized cobalt complex and P3HT-cycloalkyne with a 2:1 molar ratio. Cycloalkyne-P3HT (210 mg, 4.28 x 10^{-5} mol), [Co(DO)(DOH)N_3-pnCl_2] (35 mg, 8.56 x 10^{-5} mol) and 50 ml of dry THF were added into a 100 ml round bottom flask. After purging with nitrogen during 10 min, the reaction was performed at 60 °C for 72 h. The medium was then concentrated by rotary evaporation, precipitated in a cold mixture of methanol-water (70v%-30v%). Finally, the obtained solid was filtrated and dried under vacuum for 12 h. The NMR spectra of cycloalkyne-P3HT and P3HT-Co catalyst are presented in **Figure 4** and **5**.

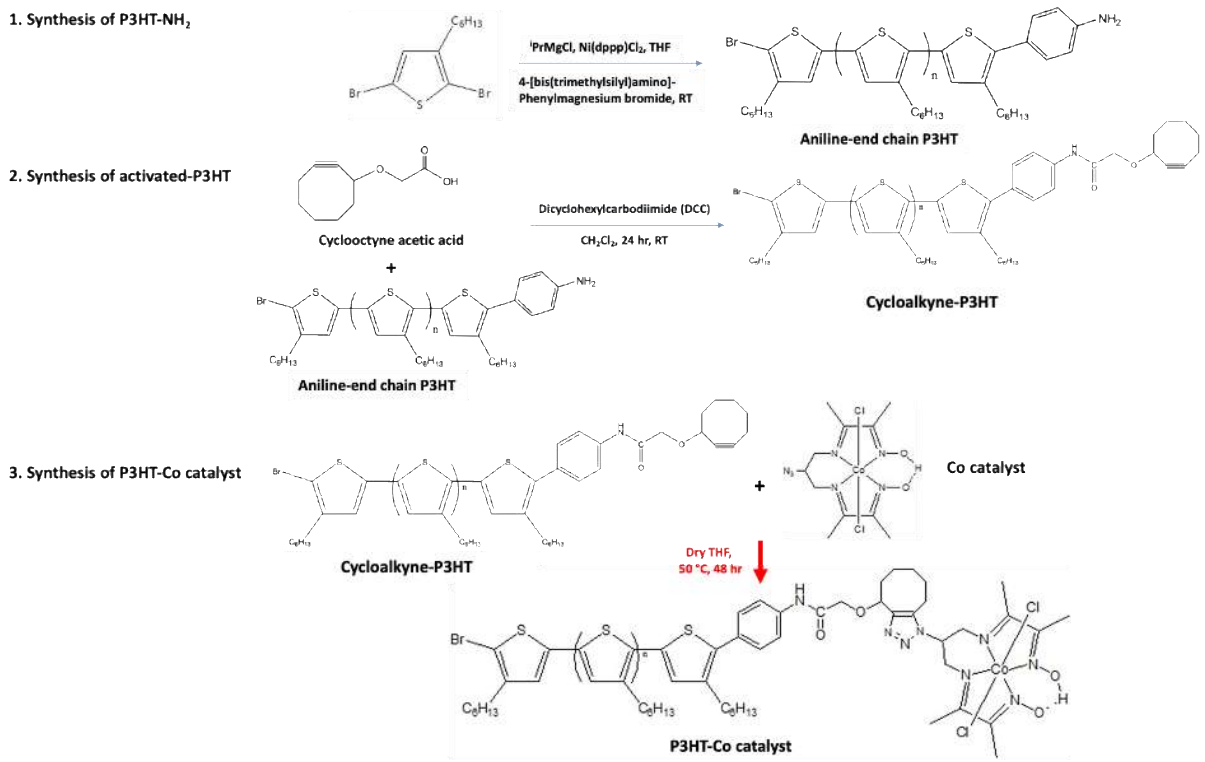

Scheme1. Artificial metallo-enzyme : Synthetic Strategy of poly(3-hexylthiophene) modified by azido functionalized diimine-dioxime Cobalt catalyst.

3. Results and discussion

3.1. Synthesis and Characterization of the artificial-metallozyme P3HT-Cobalt (P3HT-Co).

An amino-terminated P3HT-NH_2 was first synthesized by GRIM metathesis polymerization of 2,5-dibromo-3-hexylthiophene,[23-26] catalysed by Ni(dppp)Cl_2 and subsequently quenched by addition of 4-[bis(trimethylsilyl)amino]-phenylmagnesium bromide as demonstrated previously in the literature by Mc Cullough *et al.*[27] The trimethylsilyl protecting group is very labile and easily hydrolyzed during purification steps and precipitation in methanol, revealing the amine function.[27] The obtained polymer was characterized by SEC, NMR ($CDCl_3$), and MALDI-TOF mass spectroscopy. From the SEC chromatogram shown in Figure 1, the calculated molar mass Mn and dispersity *Đ* of P3HTs polymer were 3,500 g/mol and 1.55 respectively. **Figure 1** shows the SEC diagram of the log molar mass from the RI and UV-vis detectors. The molar mass was determined using conventional calibration with polystyrene standards. The UV-detector absorbance was set at 450 nm to efficiently detect P3HT.

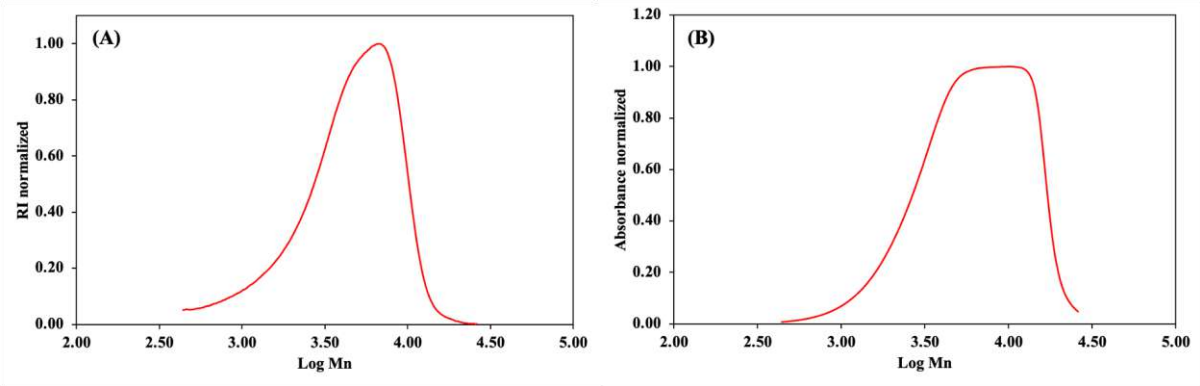

Figure 1. SEC traces of aniline-end functionalized P3HT. (A) and (B) were RI-curve and UV-curve at λ_{max} = 450 nm respectively.

Proton magnetic nuclear resonance proved the chemical structure of the product with the attribution of protons. All the peaks pertaining to the P3HT backbone and hexyl side chain were attributed. The presence of the aniline group was confirmed by ^{1}H NMR spectrum **(Figure 2)**, on which the characteristic resonance of NH_2 protons end group (c) was observed at 3.8 ppm (as previously reported by Higashihara *et al.*).[23] Hydrogen-deuterium exchange (H/D exchange) has been widely used to identify/monitor by ^{1}H NMR the hydrogen lability of some functional groups such as amide, alcohols, phenols or carboxylic acid in protein chain.[28-33] In this study we used this technique to identify the aniline-end chain of P3HT. P3HT was first solubilized in deuterated chloroform and the spectrum was acquired (blue trace in **Figure 2**). Then D_2O was added in the tube and, as a consequence, deuterated amine groups were obtained by the substitution of hydrogen by deuterium (red trace in **Figure 2**). The signal at 3.8 ppm disappeared after H/D exchange hence proving that this peak belonged to NH_2 group. The *Mn* was not calculated from ^{1}H NMR because no end-chain signals could be used since the amine functionalization of the chains may not be quantitative.

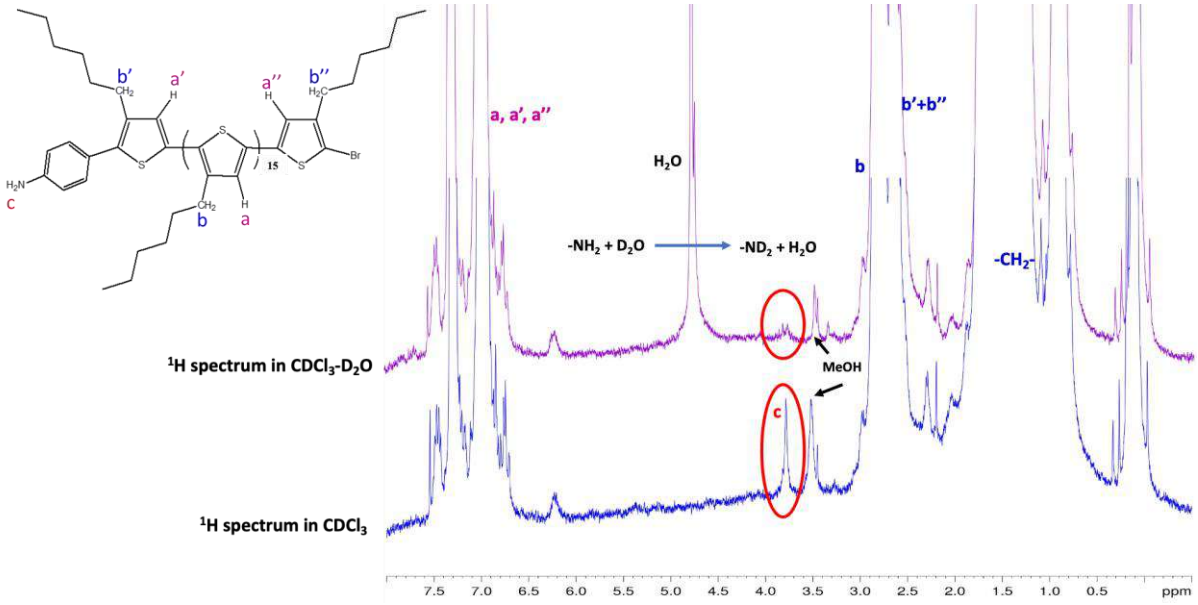

Figure 2. ^{1}H NMR spectrum of P3HT-NH_2 with the comparison of ^{1}H spectrum in $CDCl_3$ and ^{1}H spectrum in $CDCl_3$-D_2O.

The MALDI-TOF MS analysis of P3HT-NH_2 was performed **(Figure S1 and S2)** and different populations of end-capped P3HT were identified (presented in **Table S1**). Detailed analysis revealed that the mass/charge (*m/z)* values can be calculate by 166.1*n* (repeat unit) + M_w of the end chain. For example, **Figure S2** shown a P3HT of 13-mer (13 repetitive units) with Br and aniline end chain corresponds to (166.1 x 13) + 79.9 (A_w of Br) + 92.2 (M_w of aniline end chain, C_6H_6N) (molecular structures of all molecules presented in **Figure S1-S2**). Following this calculation, the M_n of 13-mer, 14-mer and 15-mer with Br/aniline end-groups should afford signals at *m/z* 2,331.4, 2,497.5 and 2,663.6 respectively, these calculated M_n corresponded to *m/z* peaks from MALDI-TOF mass spectrum at 2,333.8, 2,500.9 and 2,667.0 respectively (position A, B, C in **Figure S1**). Therefore, the major population from MALDI-TOF analysis corresponded to Br/aniline end-chain of P3HT, assigning the α- and ω- ends to bromo and aniline groups,[23,34] corresponding to 40 mol%. Two other major conductive P3HT populations were quantified at 20 mol% but could not be identified. Moreover, from the full MALDI-ToF spectrum, a number average molar mass of 2,800 g.mol^{-1} was calculated. This value corresponds to an average degree of polymerization of 17. This value was used for the NMR caculation of the P3HT-NH_2 in which the signal at 2.8 ppm attributed to the CH_2 in *alpha* of the thiophene ring was calibrated at 34. Then, the integration of the amine proton at 3.8 ppm and the terminal phenyl proton at 6.7 ppm **(Figure S3)** were measured at 0.61 and 0.86

respectively, in agreement with a percentage of functionalization between 31 and 43%, consistent with the MALDI-Tof analysis.

The second step of the synthesis involved the amidification of a cyclooctyne functionalized with acetic acid (2-(cyclooct-2-yn-l-yloxy) acetic acid) and P3HT-NH_2. The reaction was carried out in dichloromethane in presence of N,N′-dicyclohexylcarbodiimide (DCC) to increase the electrophilicity of the carboxylate group.[35-36] The reaction was allowed to stir during 24 hours at 25°C and the insoluble urea by-product was directly eliminated by filtration. The cycloalkyne-P3HT was isolated and purified by precipitation in a mixture of methanol and water in a 70%-30% volume ratio. After drying, the product was characterized by ^{1}H NMR ($CDCl_3$). **Figure 3** presents the NMR spectrum of the reaction product, cyclooctyne-P3HT, compared with the reagent P3HT-NH_2. The amine peak at 3.8 ppm (a) disappears due to the connection of P3HT and cyclooctyne acetic acid and the amide proton appears at 8.5 ppm. Then 3 additional protons appear from 4.0 to 4.5 ppm corresponding to *CH* and *CH_2-O* of the octyne moiety, a' and c' in Figure 3. For comparison, the NMR spectrum of the cycloalkyne-P3HT and octyne acid precursor can be found in Figures S4 and S5, respectively.

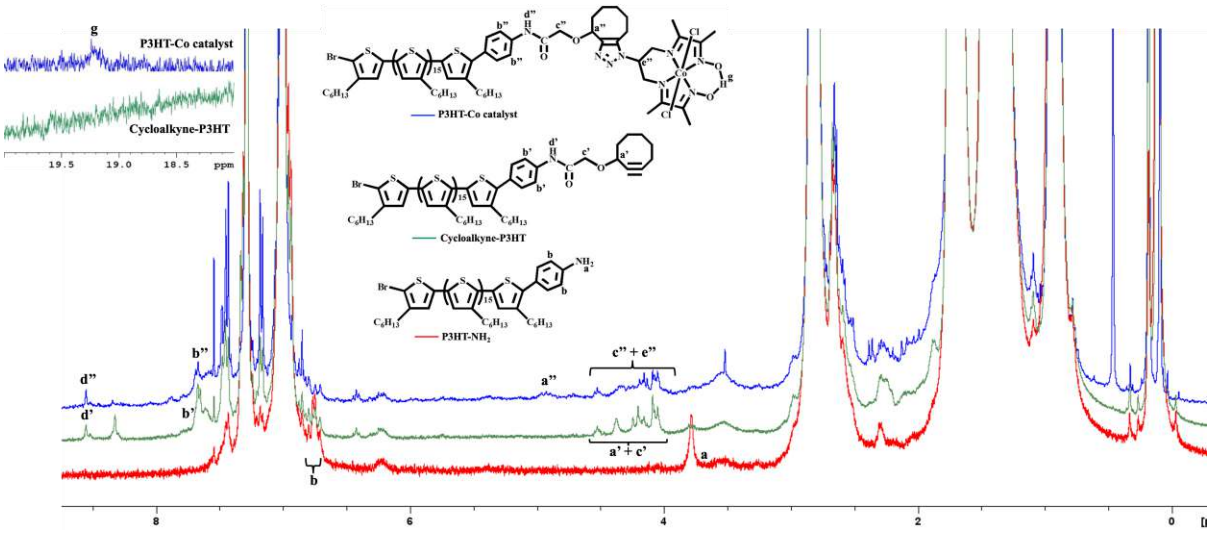

Figure 3. Superposition of ^{1}H NMR spectra of P3HT-NH_2, cycloalkyne-P3HT and P3HT-Co in $CDCl_3$

Finally, the third step in the procedure is the Huisgen cycloaddition of the P3HT-cyclooctyne with the azide functionalized Cobalt complex. The click reaction of azide-alkyne cycloadditon can be activated by copper catalysts, however the metal catalysts can displace the cobalt metal of the catalytic active ligand and induce further undesired electrochemical activity.[10, 37] As a solution, a metal-free Huisgen cycloaddition was developed for coupling these two molecules.

With the use of cyclooctyne, the smallest stable cycloalkyne, a stain-promoted cycloaddition will lead to the expected triazole product. The activated alkyne increased the reactivity by introducing a ring strain and allowed the reaction to proceed without metal-catalysts. This reaction is named in the literature "Strain promoted alkyne azide cycloaddition (SPAAC)".[38-40] In terms of molecular orbitals, the reaction involved the binding of lowest unoccupied molecular orbital (LUMO) of the alkyne and the highest occupied molecular orbital (HOMO) of the azide to form a new C-C bond and produce the triazole ring.[41] The two reagents were mixed in THF and allowed to stir at 60°C during 72 h. Again, the residual macromolecular product or artificial metallo-enzyme, so-called P3HT-Co, presented a noticeable change in solubility and could not be isolated by simple precipitation in methanol/water (70%:30% volume ratio) at room temperature but rather at 0°C. The ^{1}H NMR of the P3HT-Co was recorded and superimposed with the cycloalkyne-P3HT one **(Figure 3)**. Several changes can be observed from the comparison with the cycloalkyne-P3HT precursor. The signal for the *CH* cyclooctyne proton switched from 4.3 to 4.9 ppm and a peak appeared at 19 ppm, attributed to the proton *O-H-O,* position *Hg* in **Figure 3** and **S6**.

To further confirm this result, IR spectra were recorded and **Figure S7** shows the superposition of cycloalkyne-P3HT and P3HT-Co. First the peak related to the stretching mode of the carbonyl group (*C=O*) of the amide of both polymers can be observed at around 1700 cm^{-1}. A weak peak of *C≡C* stretching can be distinguished at 2050 cm^{-1} on the cycloalkyne-P3HT. This peak then disappears in P3HT-Co catalyst spectrum proving the effective click reaction.[42-43]

In addition to NMR and IR spectrophotometry, cyclic voltammetry was used to characterize the presence of the diimine-dioxime cobalt complex and reveal its electrochemical features.

3.2. Electrochemical characterization of P3HT-NH_2 and P3HT-Co complex catalyst.

To confirm the cobalt functionalization of the P3HT chains, the P3HT-NH_2 and P3HT-Co samples were characterized by cyclic voltammetry (CV). For this purpose, polymer solutions were drop-casted onto platinum (Pt) electrodes and introduced in a three electrodes set-up in an electrolyte solution composed of 0.1 M of n-Bu_4NPF_6 in acetonitrile. When scanning to the negative potentials the P3HT-NH_2 sample presented a large reduction peak at -1.75 V (Figure S8). The reduction is reversible and the $E_{1/2}$ was measured at -1.7 V vs NHE commonly attributed in the literature to the reduction of P3HT, and used to calculate it's LUMO level (ranging from 2.7 to 3.1 eV versus vacuum).[44, 45-46]

The P3HT-Co film, coated on Pt electrode, was analysed by CV and the voltammogram is reported in Figure 4. Two reversible waves can be observed , the first one at $E_{1/2}$ = -0.15 V vs NHE (ΔE_p = 17 mV) and the second one at $E_{1/2}$ = +0.67 V vs NHE (ΔE_p = 54 mV) corresponding to the $Co^{III/II}$ and $Co^{IV/III}$ couple respectively.[47-48] For sake of comparison the value of the oxidation/reduction potential of various Cobalt complexes were extracted from the literature (Table S2).[10, 49-53] The redox potential of $Co^{IV/III}$, $Co^{III/II}$ and $Co^{II/I}$ electrochemical processes were reported in the range of +0.5 to 0.9 V, -0.2 to +0.1 V and from -0.35 to -0.5V vs NHE, respectively.[47-55] The wide range of the measured potential is attributed to different parameters from which the most important ones are the electron donating strength of the ligands, the type of working electrode and electrolyte solution. Since this characterization confirms the incorporation of Cobalt catalyst in the P3HT polymer, the following step will be to study the catalysis behaviour and the stability of this new catalyst towards hydrogen evolution.

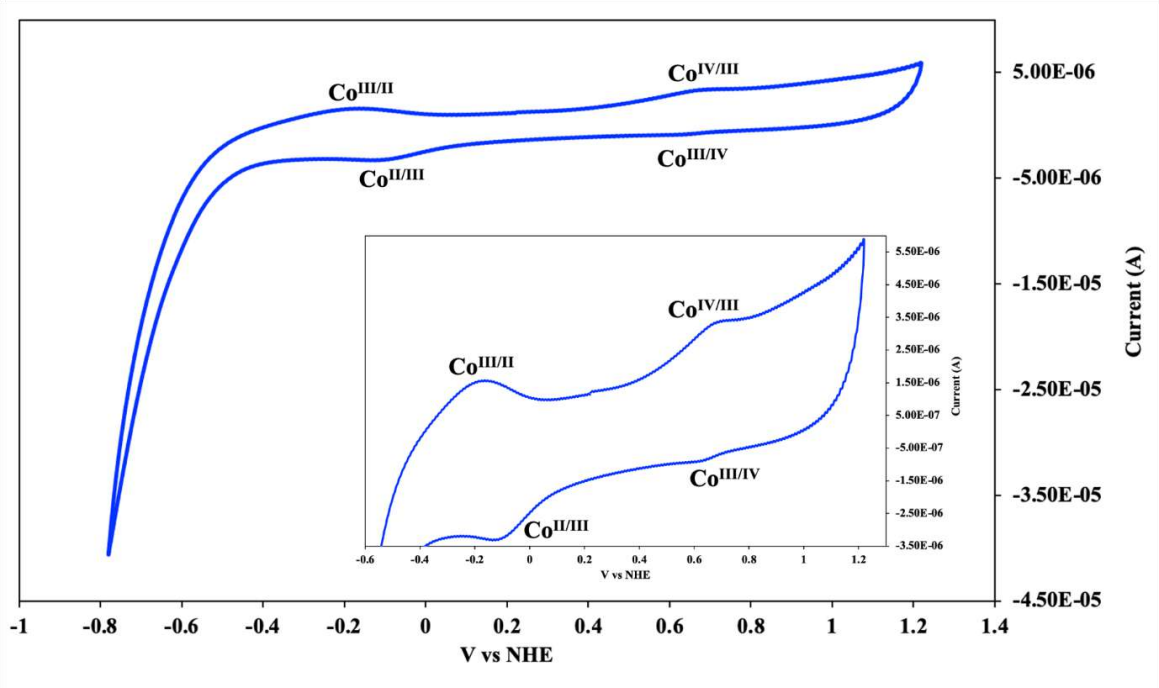

Figure 4. A cyclic voltammogram of P3HT-Co artificial metallo-enzyme film coated on Pt electrode, CV scan rate was 0.1 V/s in 0.1 M 0.1 M of *n*-Bu_4NPF_6 in acetonitrile.

4. Conclusion

This chapter described the preparation of diimine-dioxime cobalt complex end-capped P3HT, as artificial metallo-enzyme, in three steps including 1) the GRIM metathesis to synthesized an amino functionalized P3HT, then 2) direct condensation of P3HT-NH_2 and acid-cyclooctyne derivative, and 3) a final step of copper free click coupling with an azido-functionalized diimine-dioxime cobalt complex. All the steps were confirmed by ^{1}H NMR, MALDI-TOF or IR spectrophotometry. In addition, the electrochemical properties of the artificial, metallo-enzyme have been revealed by cyclic voltammetry. Due to time limitation, this study will further continue, with the artificial metallo-enzyme efficiency upon hydrogen evolution as recently described by Pyun *et al.* in solution[56].

Acknowledgments

Support from Ministerio de Ciencia, Innovacion y Universidades and FEDER (PID2019-111617RB-I00), AGAUR 2017-SGR-1631, Ministerio de Ciencia e Innovacion for a Severo Ochoa Excellence Accreditation grant 2020-2023 (CEX2019-000925-S, MIC/AEI)" and EU-funded ITN eSCALED (Grant agreement ID: 765376) are gratefully acknowledged.

Reference:

(1) N. Armaroli.; V. Balzani. The future of energy supply: challenges and opportuinties. *Angew. Chem. Int. Ed*. **2007**, 46, 52-66.

(2) N. Amaroli.; V. Balzani. The hydrogen issue. *ChemSusChem*. **2011**, 4, 21-36.

(3) G. W. Crabtree.; M.S. Dresselhaus. The hydrogen fuel alternative. *Mater. Res. Soc. Bull*. **2008**, 33, 421-428.

(4) R. V. Gordon.; M. Bertram.; T. E. Graedel. Metal stocks and sustainability. *PNAS*. **2006**, 13, 1209-1214.

(5) R. M. Kellett.; T. G. Spiro. Cobalt(I) phorphyrin catalysis of hydrogen production from water. *Inorg. Chem*. **1985**, 24, 2373-2377.

(6) M. Risch.; v. Khare.; I. ~aharieva.; L. Gerencser.; P. Chernev.; H. Dau. Cobalt-oxo core of a water-oxidizing catalyst film. *J. Am. Chem. Soc*. **2009**, 131, 6936-6937.

(7) N. Queyriaux.; R. T. Jane.; J. Massin.; V. Artero.; M. Chavarot-Kerlidou. Recent developments in hydrogen evolving molecular cobalt(II)-polypyridyl catalysts. *Coord Chem Rev*. **2005**, 304-305, 3-19

(8) X. Hu.; B. S. Brunschwig.; J. C. Peters. Electrocatalytic hydrogen evolution at low overpotentials by cobalt macrocyclic glyoxime and tetraimine complexes. *J. Am. Chem. Soc*. **2007**, 129, 8988-8998.

(9) J. Chen.; P. H.-L. Sit. Density functional theory and Car-Parrinello molecular dynamics study of the hydrogen-producing mechanism of the $Co(dmgBF_2)_2$ and $Co(dmgH)_2$ cobaloxime complexes in acetonitrile-water solvent. *J. Phys. Chem. A*. **2017**, 121, 3515-3525.

(10) E. S. Andreiadis.; P.-A. Jacques.; P. D. Tran.; A. Leyris.; M. Chvarot-Kerlidou.; B. Jousselme.; M. Matheron.; J. Pécaut.; S. Palacin.; M. Fontecave.; V. Artero. Molecular engineering of a cobalt-based electrocatalytic manomaterial for H_2 evolution under fully aqueous conditions. *Nature chemistry*. **2003**, 5, 48-53.

(11) F. Li.; B. Zhang.; X. Li.; Y. Jiang.; L. Chen.; Y. Li.; L. Sun. Highly efficient oxidation of water by a molecular catalyst immobilized on carbon nanotubes. *Angew. Chem. Int. Ed*. **2011**, 50, 12276-12279.

(12) K. E. deKrafft.; C. Wang.; Z. Xie.; X. Su.; B. J. Hinds.; W. Lin. Electrochemical water oxidation with carbon-grafted iridium complexes. *ACS Appl. Mater. Interfaces*. **2012**, 4, 608-613.

(13) K. S. Prasad.; C. Walgama.; S. Krishnan. Enhanced electroactivity and substrate affinity of microperoxidase-11 attached to pyrene-linkers π-π stacked on carbon nanostructure electrodes. *RSC Adv*. **2015**, 5, 11845-11849.

(14) D. Nuevo.; M. Poyatos.; E. Peris. A dinuclear Au(I) complex with a pyrene-di-N-heterocyclic carbene linker: supramolecular and catalytic studies. *Organometallics*. **2018,** 37, 3407-3411.

(15) Z. Li.; A. W. Peters.; V. Bernales.; M. A. Ortuño.; N. M. Schweitzer.; M. R. DeStefano.; L. C. Gallington.; A. E. Platero-Prats.; K. W. Chapman.; C. J. Cramer.; L. Gagliardi.; J. T. Hupp.; O. K. Farha. Metal-organic framework supported cobalt catalysts for the oxidative dehydrogenation of propane at low temperature. *ACS Cent. Sci*. **2017**, 3, 31-38.

(16) B. Reuillard.; K. H. Ly.; T. E. Rosser.; M. F. Kuehnel.; I. Zebger.; E. Reisner. Tuning product selectivity for aqueous Co2 reduction with a Mn(bipyridine)-pyrene catalyst immobilized on a carbon nanotube electrode. *J. Am. Chem. Soc*. **2017**, 139, 14425-14435.

(17) O. A. de Fuentes.; T. Ferri.; M. Frasconi.; V. Paolini.; R. Santucci. Highly-ordered covalent anchoring of carbon nanotubes on electrode surfaces by diazonium salt reaction. *Angew. Chem. Int. Ed*. **2011**, 50, 3457-3461.

(18) L. Pilan. Tailoring the perfamance of electrochemical biosensors based on carbon nanomaterials via aryldiazonium electrografting. *Bioelectrochemistry*. **2021**, 138, 107697.

(19) D. Duraibabu.; Y. Sasikumar. **(2020)** Role of conducting polymer nanostructures in advanced photocatalytic applications. In: M. Naushad.; S. Rajendran.; E. Lichtfouse. (eds) Green photocatalysts. *Environmental chemistry for a sustainable world*. 34, springer, Cham, https://doi.org/10.1007/978-3-030-15608-4_8.

(20) C. M. Parnell.; B. P. Chhetri.; T. B. Mitchell.; F. Watanabe.; G. Kannarpady.; A. B. RanguMagar.; H. Zhou.; K. M. Alghazali.; A. S. Biris.; A. Ghosh. Simultaneous electrochemical deposition of cobalt complex and poly(pyrrole) thin films for supercapacitor electrodes. *Sci. Rep*. **2019**, 9, 5650.

(21) D. Meng.; J. Sun.; S. Jiang.; Y. Zeng.; Y. Li.; S. Yan.; J. Geng.; Y. Huang. Grafting P3HT brushes on GO sheets: distinctive properties of the GO/P3HT composites due to different grafting approaches. *J. Mater. Chem*. **2012**, 22, 21583-21591.

(22) N. V. Handa.; A. V. Serrano.; M. J. Robb.; C. J. Hawker. Exploring the synthesis and impact of end-functional poly(3-hexylthiophene). *Journal of polymer science, part A: polymer chemistry*. **2015**, 53, 831-841.

(23) T. Higashihara.; A. Takahashi.; S. Tajina.; S. Jin.; Y. Rho.; M. Ree.; M. Ueda. Synthesis of block copolymers consisting of poly(3-hexylthiophene) and polystyrene segments through ionic interaction and their self-assembly behavior. *Polymer Journal*. **2010**, 42, 43-50.

(24) K. Ramalingam.; N. Raju.; P. Nanjappan.; D. P. Nowotnik. Synthesis of Nitroimidazole substituted 3,3,9,9-tetramethyl-4,8-diaza-undecane-2,10-dione dioximes (propylene amines, PnAOs) : Ligands for technetium-99m complexes with potential for imaging hypoxic tissue. *Tetrahedron*. **1995**, 51, 2875-2894.

(25) E. Ji.; V. Pellerin.; L. Rubatat.; E. Grelel.; A. Bousquet.; L. Billon. Self-assembly of ionizablo "clicked" P3HT-b-PMMA copolymers: ionic bonding group/counterion effects on morphology. *Macromolecules*. **2017**, 50, 235-243.

(26) R. H. Lohwasser.; M. Thelakkat. Toward perfect control of end groups and polydispersity in poly(3-hexylthiophene) via catalyst transfer polymerization. *Macromolecules*. **2011**, 44, 3388-3397.

(27) M. Jeffries-El.; G. Sauvé.; R. D. McCullough. Facile synthesis of end-functionalized regioregular poly(3-alkylthiophene)s via modified Grignard metathesis reaction. *Macromolecules*. **2005**, 38, 10346-10352.

(28) L. Czerski.; O. Vinogradova.; C. R. Sanders. NMR-based amide hydrogen-deuterium exchange measurements for complex membrane proteins: development and critical evaluation. *Journal of Magnetic Resonance*. **2000**, 142, 111-119.

(29) X. Yao.; U. H. N. Dürr.; X. Gattin.; Y. Laukat.; R. L. Narayanan.; A.-K. Brückner.; C. Meisinger.; A. Lange.; S. Becker.; M. Zweckstetter. NMR-based detection of hydrogen/deuterium exchange in liposome-embedded membrane proteins. *Plos ONE*. **2014**, 9, e112374.

(30) D. Morimoto.; R. Nishizawa.; E. Walinda.; S. Takashima.; K. Sugase.; M. Shirakawa. Hydrogen-deuterium exchange profiles of polyubiquitin fibrils. *Polymers*. **2018**, 10, 240.

(31) A. J. Percy.; M. Rey.; K. M. Burns.; D. C. Schriemer. Probing protein interactions with hydrogen/deuterium exchange and mass spectrometry-A review. *Analytica Chimica Acta*. **2012**, 721, 7-21.

(32) G. Veglia.; A. C. Zeri.; C. Ma.; S. J. Opella. Deuterium/hydrogen exchange factors measured by solution nuclear magnetic resonance spectroscopy as indicators of the structure and topology of membrane proteins. *Biophysical Journal*. **2002**, 82, 2176-2183.

(33) G. R. Fulmer.; A. J. M. Mille.; N. H. Sherden.; H. E. Gottlieb.; A. Nudelman.; B. M. Stoltz.; J. E. Bercaw.; K. I. Goldberg. NMR chemical shifts of trace impurities: common

laboratory solvents, organics, and gases in deuterated solvents relevant to the organometallic chemist. *Organometallics*. **2010**, 29, 2176-2179.

(34) A. Takahashi.; Y. Rho.; T. Higashihara.; B. Ahn.; M. Ree.; M. Ueda. Preparation of nanoporous poly(3-hexylthiophene) films based on a template system of block copolymers via ionic interaction. *Macromolecules*. **2010**, 43, 4843-4852.

(35) G. T. Hermanson. Bioconjugate techniques (third edition), Academic Press. **2003**, pp259-273.

(36) F. A. Carey. Organic chemistry second edition. McGRAW-HILL, INC. **1982**, pp1125-1126.

(37) E. M. Sletten.; C. R. Bertozzi. From mechanism to mouse: a tale of two biorthogonal reactions. *Accounts of chemical research*. **2011**, 44, 666-676.

(38) C. Ornelas.; J. Broichhagen.; M. Weck. Strain-promoted alkyne azide cycloaddition for the functionalization of poly (amide)-based dendrons and dendrimers. *J. Am. Chem. Soc*. **2010**, 132, 3923-2931.

(39) C. R. Becer.; R. Hoogenboom.; U. S. Schubert. Click chemistry beyond metal-catalyzed cycloaddition. *Angew. Chem. Int. Ed*. **2009**, 48, 2-11.

(40) C. G. Gordon.; J. L. Mackey.; J. C. Jewett.; E. M. Sletten.; K. N. Houk.; C. R. Bertozzi. Reactivity of biarylazacyclooctynones in copper-free click chemistry. *J. Am. Chem. Soc*. **2012**, 134, 9199-9208.

(41) J. C. Jewett.; C. R. Bertozzi. Cu-free click cycloaddition reactions in chemical biology. *Chem. Soc. Rev*. **2010**, 39, 1272-1279.

(42) C. Wentrup.; B. Blanch.; H. Briehl.; G. Gross. Benzyne, cyclohexyne, and 3-azacyclohexyne and the problem of cyloalkyne versus cycloalkylideneketene genesis. *J. Am. Chem. Soc*. **1988**, 110, 1874-1880.

(43) P. N. Gunawardene.; J. F. Corrigan.; M. S. Workentin. Golden opportunity: a clickable azide-functionalized $[Au_{25}(SR)_{18}]^-$ nanocluster platform for interfacial surface modifications. *J. Am. Chem. Soc*. **2019**, 141, 11781-11785.

(44) W. T. Choi.; A. J. Bard. Doping of the semiconducting polymer poly(3-hexylthiophene) (P3HT) in organic photoelectrochemical cells. *J. Phys. Chem. C*. **2020**, 124, 3439-3447.

(45) T. F. Harrelson.; Y. Q. Cheng.; J. Li.; I. E. Jacobs.; A. J. Ramirez-Cuesta.; R. Faller.; A. J. Moulé. Identifying atomic scale structure in undoped/doped semicrystalline P3HT using inelastic neutron scattering. *Macromolecules*. **2017**, 50, 2424-2435.

(46) S. Sweetnam.; K. R. Graham.; G. O. N. Ndjawa.; T. Heumüller.; J. A. Bartelt.; T. M. Burke.; W. Li.; W. You.; A. Amassian.; M. D. McGehee. Characterization of the polymer

energy landscape in polymer:fullerene bulk heterojunction with pure and mixed phases. *J. Am. Chem. Soc*. **2014**, 136, 14078-14088.

(47) N. Kaeffer.; M. Chavarot-Kerlidou.; V. Artero. Hydrogen evolution catalyzed by cobalt diamine-dioxime complexes. *Acc. Chem. Res*. **2015**, 48, 1286-1295.

(48) P. Comba.; A.-M. Löhr.; F. Pfaff.; K. Ray. Redox potentials of high-valent Iron-, Cobalt-, and Nickel- oxido complexes: evidence for exchange enhanced reactivity. *Isr. J. Chem*. **2020**, 60, 957-962.

(49) N. Kaeffer.; J. Massin.; C. Lebrun.; O. Renault.; M. Chavarot-Kerlidou.; V. Artero. Covalent design for dye-sensitized H_2-evolving photocathodes based on a cobalt diimine-dioxime catalyst. *J. Am. Chem. Soc*. **2016**, 138, 12308-12311.

(50) P-A. Jacques.; V. Artero.; J. Pécaut.; M. Fontecave. Cobalt and nickel diamine-dioxime complexes as molecular electrocatalysists for hydrogen evolution with low overvoltages. *PNAS*. **2009**, 106, 20627-20632.

(51) J. Willkomm.; N. M. Muresan.; E. Reisner. Enhancing H_2 evolution performance of an immobilized cobalt catalyst by rational ligand design. *Chem. Sci*. **2015**, 6, 2727-2736.

(52) V. V. Pavlishchuk.; A. W. Addison. Conversion constants for redox potentials measured versus different reference electrodes in acetronitrile solution at 25°C. *Inorganica Cimica Acta*. **2000**, 298, 97-102.

(53) S. Niu.; S. Li.; Y. Du.; X. Han.; P. Xu. How to reliably report the overpotential of an electrocatalyst. *ACS Energy Lett*. **2020**, 5, 1083-1087.

(54) P. Huo.; C. Uyeda.; J. D. Goodpaster.; J. C. Peters.; T. F. Meller III. Breaking the correlation between energy costs and kinetic barriers in hydrogen evolution via a cobalt pyridine-diimine-dioxime catalyst. *ACS Catal*. **2016**, 6, 6114-6123.

(55) J. Balapanuru.; PDI-Cobalt complex immobilized on reduced graphene oxide for photoelectrochemical water splitting. *ACS Appl. Mater. Interfaces*. **2015**, 7, 880-886.

(56) M. Karayilan.; K. C. Mccleary-Petersen.; M. O. Hamilton.; L. Fu.; K. Matyjaszewski.; R. S. Glass.; D. L. Lichtenberger.; J. Pyun. Synthesis of metallopolymers via atom transfer radical polymerization from a [2Fe-2S] metalloinitiator: molecular weight effects on electrocatalytic hydrogen production. *Macromol Rapid Commun*. **2020**, 41, e1900424.

Supplementary information

Synthesis and electrochemical behaviour of a cobalt complex covalently attached to poly(3-hexylthiophene)

The Maldi-TOF mass spectrum of the P3HT contains various populations, indicating that each n-mer has several kinds of end-group. Two populations have been identified, Br/aniline and H/Br whereas the other two other populations are still unknown. The summarized m/z value, the percentage of intensity and type of end-group are presented in **Table S1.**

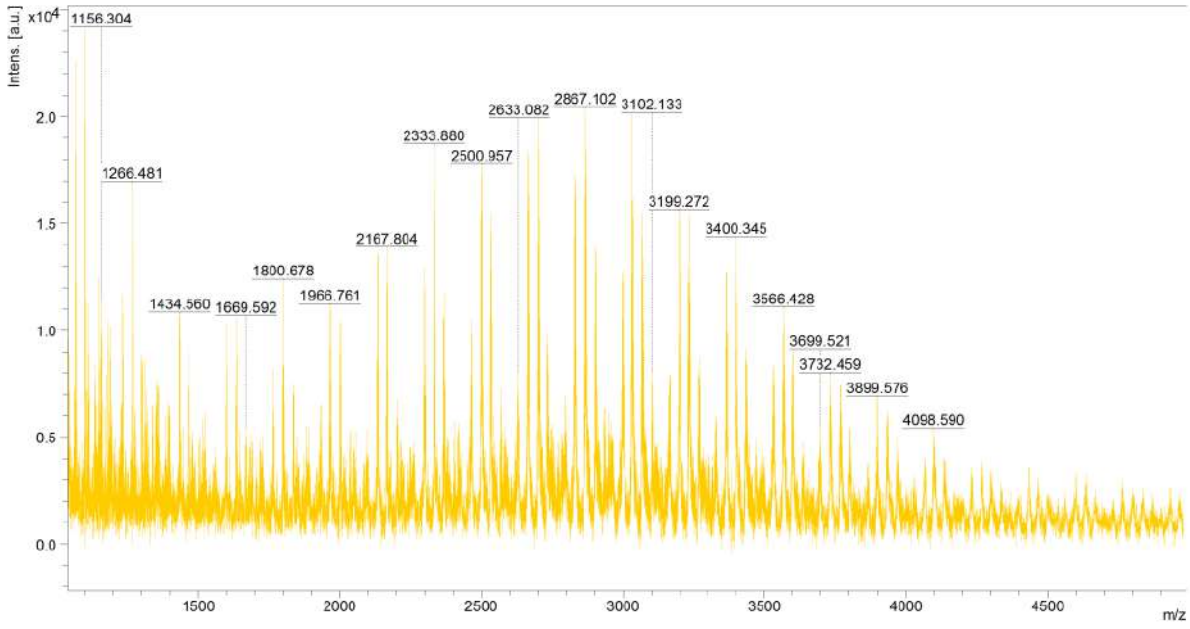

Figure S1. MALDI-TOF mass spectrum of P3HT-NH_2.

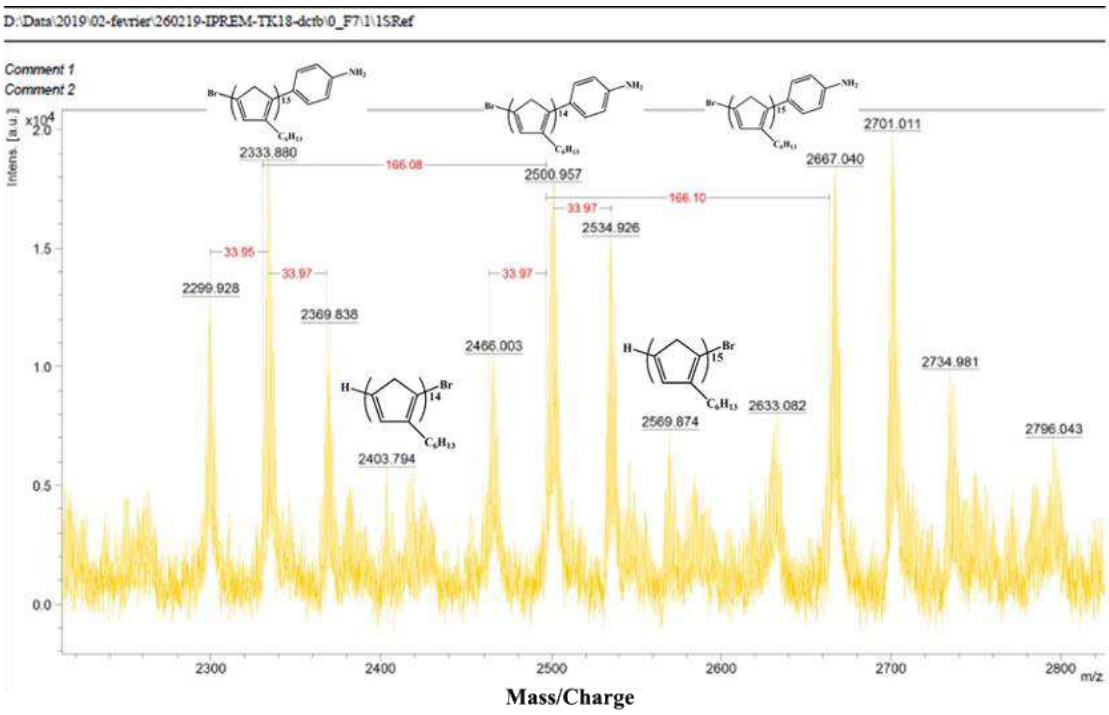

Figure S2. MALDI-TOF mass spectrum of P3HT-NH_2 (Mn = 3,500 g/mol, M_w/M_n = 1.55 determined by GPC), zoom around the 14-mer population.

Table S1. MALDI-TOF detailed analysis of end-group, % intensity and molar mass of polymers compared between Mmeasured and Mcalculate.

$M_{measured}$ (g/mol)	Chain	$M_{calculated}$[a] (g/mol)	% $\frac{Intensity}{\sum Intensity}$ x100	% For DP14
2,333.880	Br-$(C_{10}H_{14}S)_{13}$-C_6H_6N	2,331.4	16.38	-
2,369.836	Could not identify	Could not identify	10.34	-
2,403.794	H-$(C_{10}H_{14}S)_{14}$-Br	2406.3	5.17	11
2,466.003	Could not identify	Could not identify	9.48	21
2,500.957	Br-$(C_{10}H_{14}S)_{14}$-C_6H_6N	2,497.5	15.52	35
2,534.926	Could not identify	Could not identify	13.79	31
2,569.874	H-$(C_{10}H_{14}S)_{15}$-Br	2572.4	6.03	-
2,633.874	Could not identify	Could not identify	6.89	-
2,667.040	Br-$(C_{10}H_{14}S)_{15}$-C_6H_6N	2,663.6	16.38	-

[a](166.1 x 13) + 79.9 (A_w of Br) + 92.2 (M_w of aniline end chain, C_6H_6N) + 1(M_w of H)

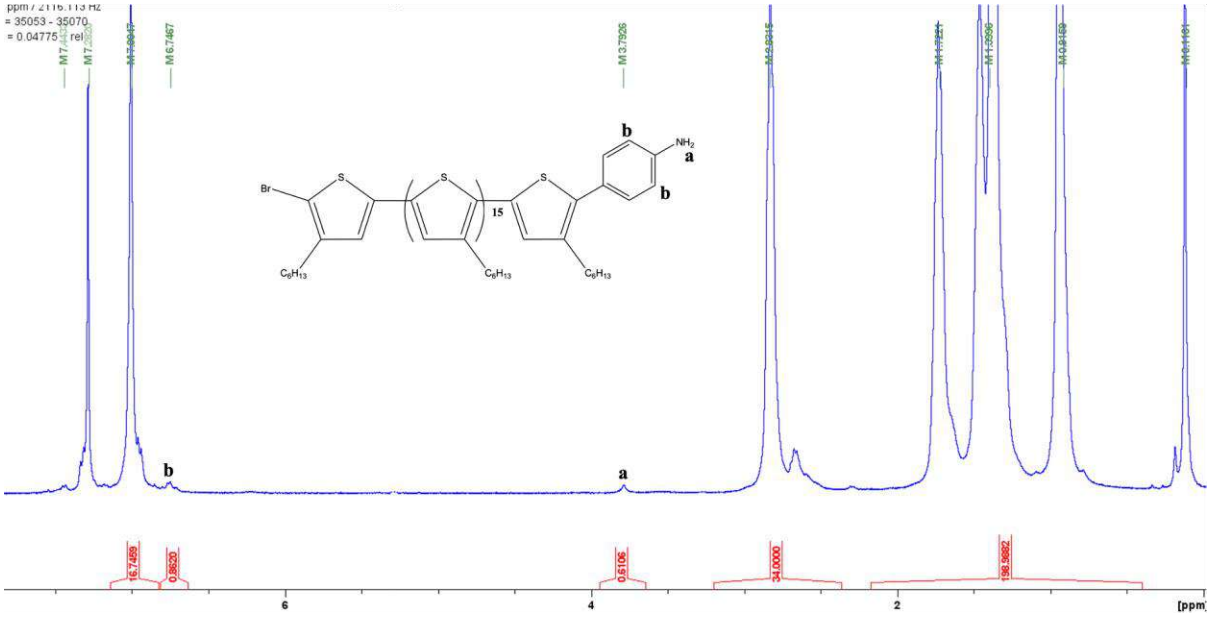

Figure S3. ^{1}H NMR spectrum of P3HT-NH_2 in $CDCl_3$.

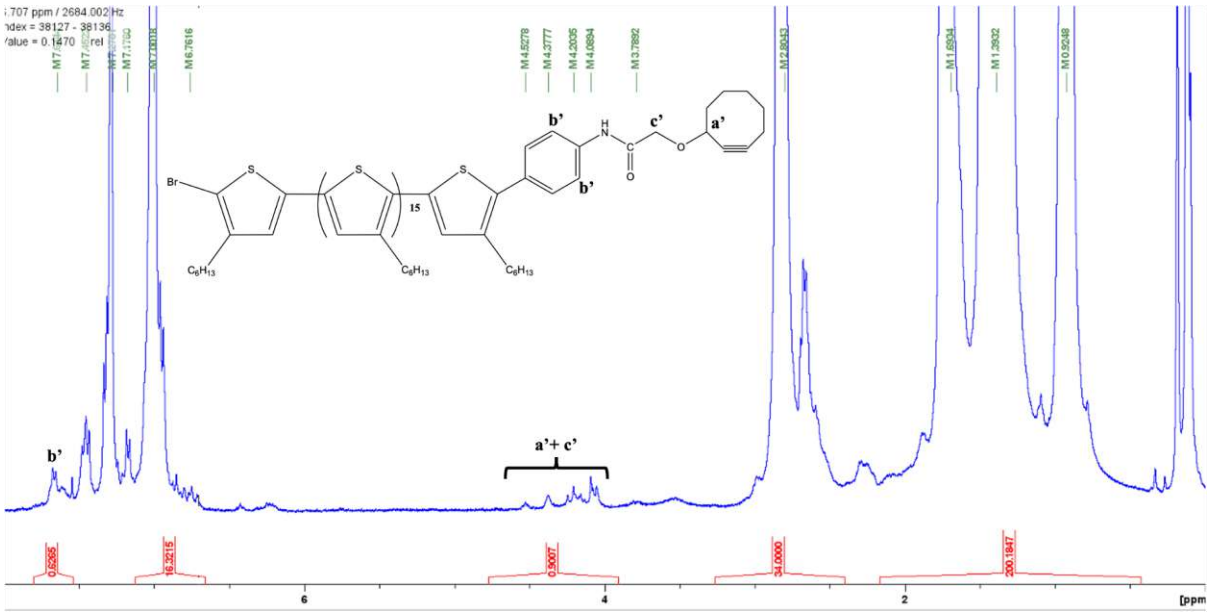

Figure S4. ^{1}H NMR spectrum of cycloalkyne-P3HT in $CDCl_3$.

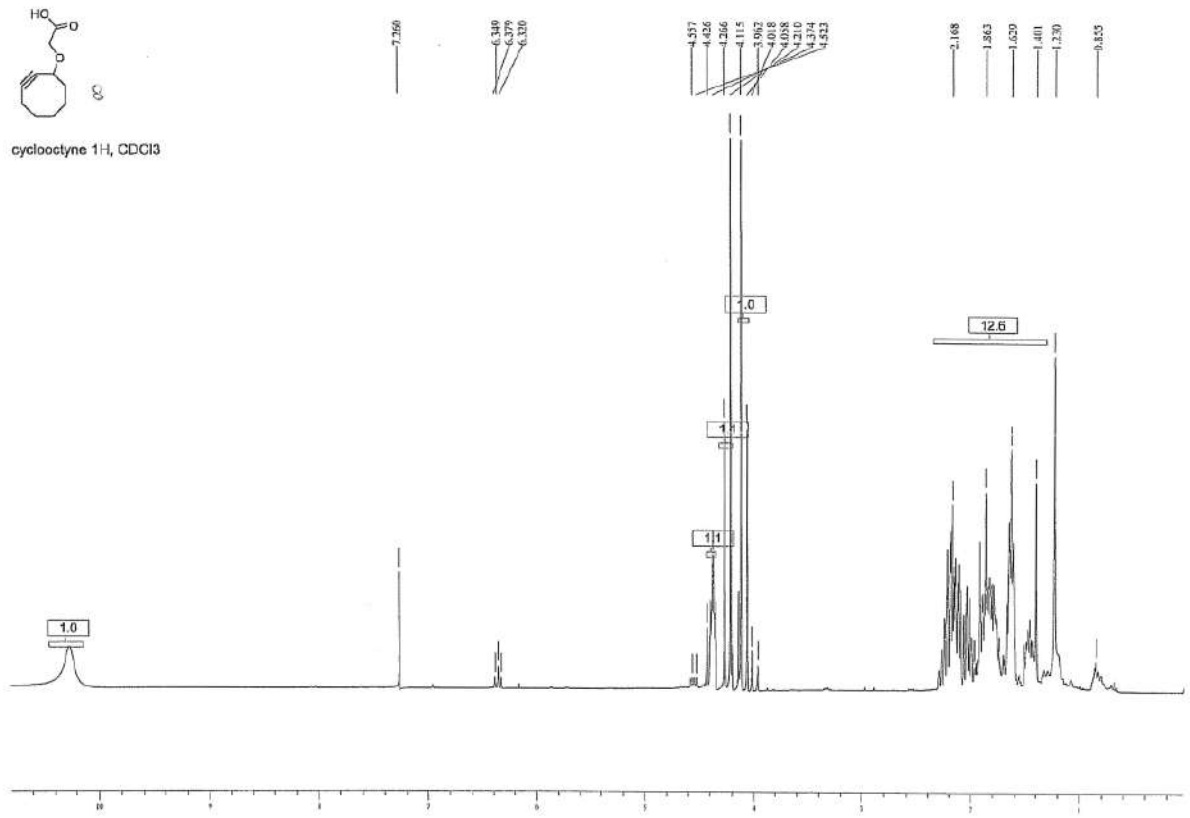

Figure S5. ^{1}H NMR spectrum of cycloalkyne acetic acid in $CDCl_3$ in $CDCl_3$.

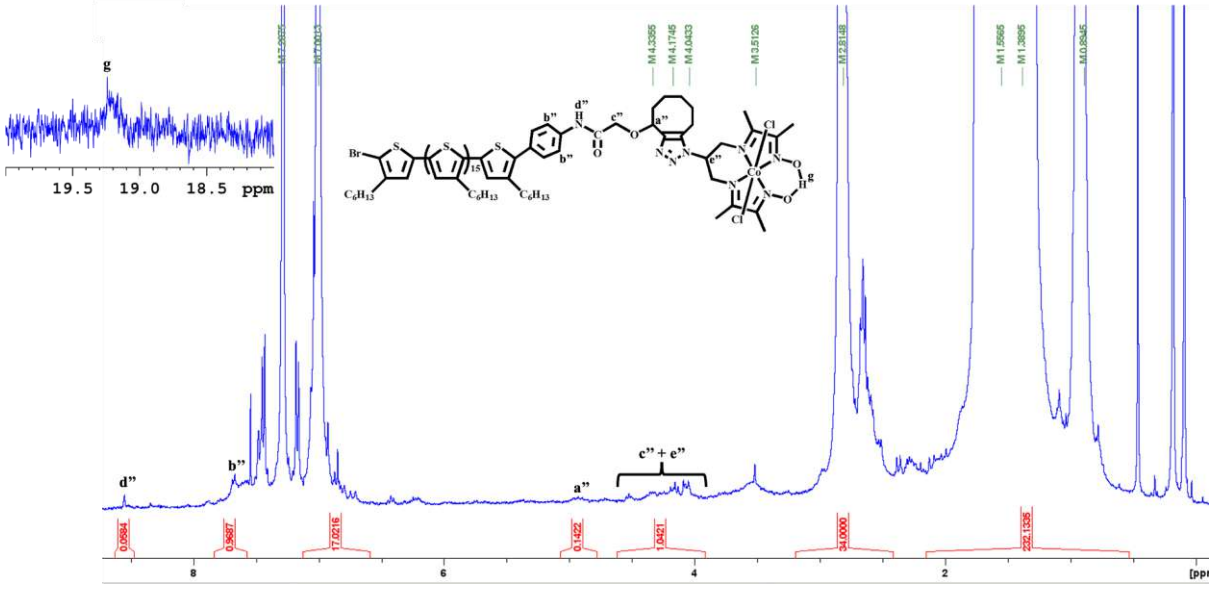

Figure S6. ^{1}H NMR spectrum of P3HT-Co catalyst.

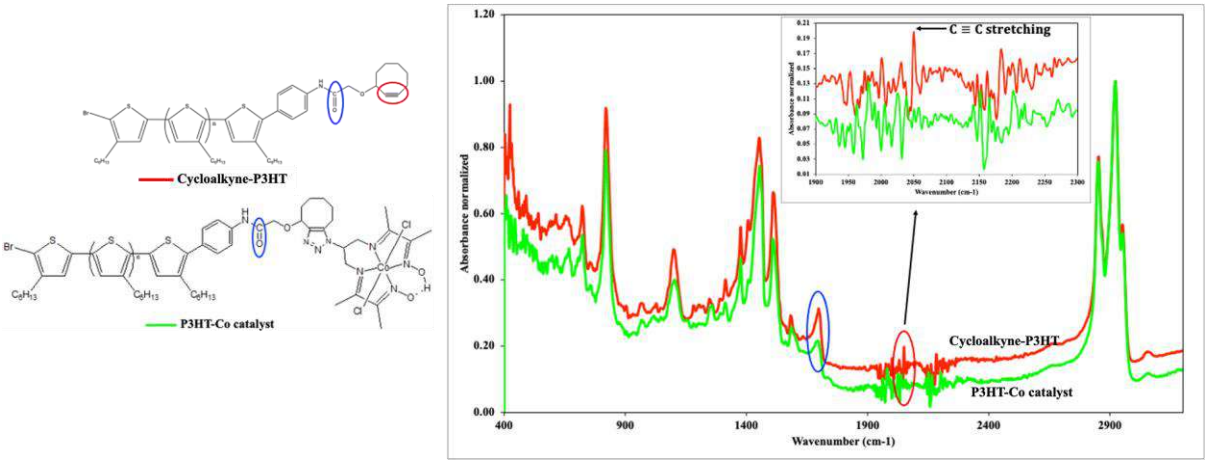

Figure S7. IR spectrums of cycloalkyne-P3HT (red line) and P3HT-Co catalyst (green line).

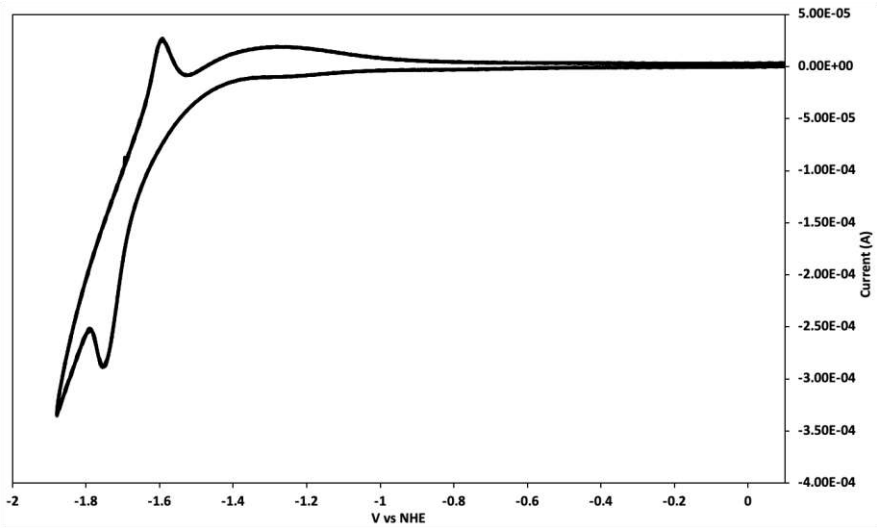

Figure S8. A cyclic voltammogram of P3HT-NH_2 film coated on Pt electrode, CV scan rate was 0.1 V/s in 0.1 M 0.1 M of n-Bu_4NPF_6 in acetronitrile.

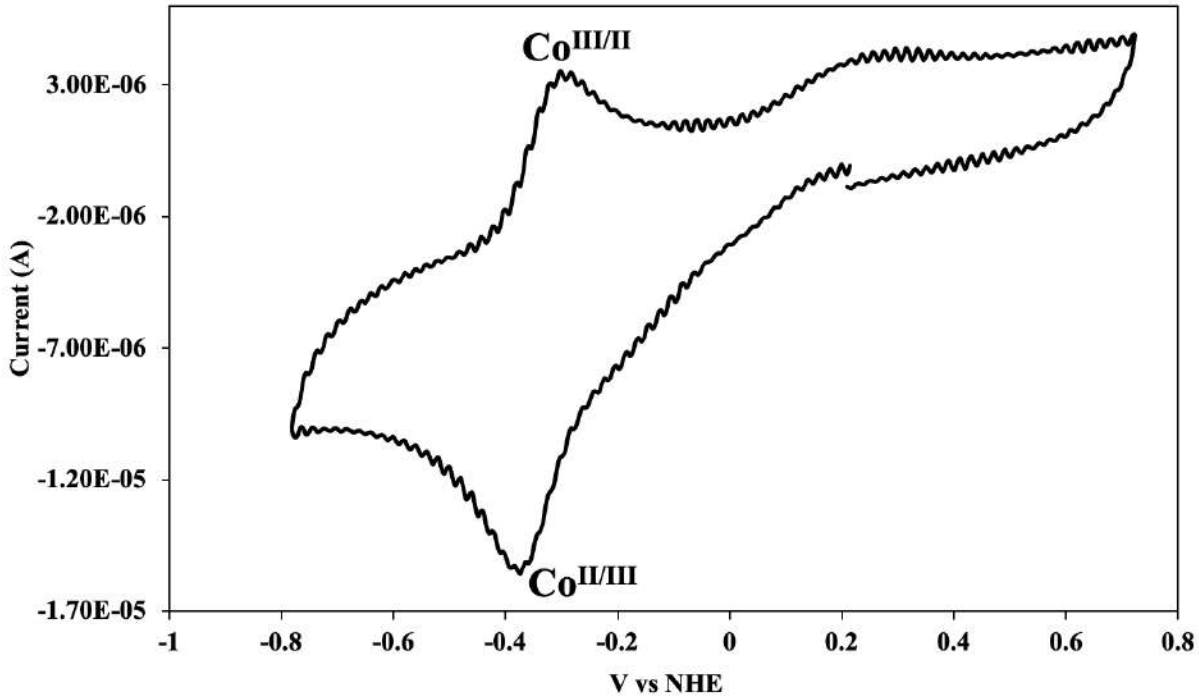

Figure S9. A cyclic voltammogram of Co complex catalyst solution recorded on Pt electrode, CV scan rate was 0.1 V/s in 0.1 M 0.1 M of n-Bu_4NPF_6 in acetronitrile.

Table S2. Cyclic voltammetry parameters for Cobalt complexes (compared oxidation potential wave) (References in this table relate to reference of main manuscript)

Complex	Working electrode	Supporting electrolyte	$Co^{III/II}$ (V vs $_{Fc+/Fc}$)	$Co^{III/II}$ (V vs NHE)	$Co^{II/I}$ (V vs $_{Fc+/Fc}$)	$Co^{II/I}$ (V vs NHE)	ref
P3HT-Co complex catalyst P3HT-[Co(DO)(DOH)-pnCl_2] derivative[a]	Pt	0.1 M *n*Bu_4NPF_6 in acetronytrile	-0.78	-0.15			this work
MWCNT/[Co(DO)(DOH)-pnCl_2] derivative	GDL	0.1 M *n*Bu_4NBF_4 in acetronitrile			-1.08	-0.45	8
MWCNT/[Co(DO)(DOH)-pnCl_2] derivative	GDL	concentrated chloride solution	-0.60	+0.03	~(-1.0)	-0.37	8
Co(DO)(DOH)N_3pnCl_2	MWCNT	0.1 M *n*Bu_4NBF_4 in acetronitrile	-0.56	+0.07	~(-1.0)	-0.37	48
Co(DO)(DOH)N_3pnBr_2 derivative	glassy carbon	0.1 M *n*Bu_4NBF_6 in DMF	-0.55	+0.08	-1.02	-0.39	49
Co(DO)(DOH)pnBr_2	glassy carbon	0.1 M *n*Bu_4NBF_4 in acetronitrile	-0.57	+0.06	-1.11	-0.48	50
Co(MO)(MOH)pnCl_2[b]	glassy carbon	0.1 M *n*Bu_4NBF_4 in acetronitrile	-0.65	-0.02	-0.96	-0.33	50
[CoBr((DO)(DOH)(4-$B_nPO_3H_2$)(2-CH_2py)pn)]Br[c]	glassy carbon	Acetate solution		+0.05		-0.40	51

[a](DO)(DOH)pn = N^2,$N^{2'}$-propanediyl-bis(2,3-butadione-2-imine-3-oxime).

[b]The methyl oxime groups in (DOH)(DOH)ph are replaced by hydrogen

[c]4-$BnPO_3H_2$ group = benzylphosporin acid and 2-CH_2py = methylpyridine.

The conversion constants at 25 °C to convert from Fc^+/Fc to NHE = +0.630 V, from SCE to NHE = +0.250V[53] and Ag/AgCl to NHE = 0.198 V.[54]

General Conclusion

In the context of the global warming and limitless growing energy demand, during my PhD thesis I have investigated the use of polymers in the electrodes for a water splitting device. Two systems were studied as polymer binder with one common PMMA block presenting high affinity with the fluorinated NAFION substrate, used as a proton selective membrane. Both copolymers have been studied for their self-assembly in films before their uses as binder.

In Chapter 2, we report the elaboration of a hierarchically ordered polymer films of PMMA-*b*-PnBA-*b*-PMMA *via* directed self-assembly by using "breath figure" templating and microwave annealing technique. In microwave annealing, the polymer doesn't absorb the microwave but the silicon wafer substrate was used as a heating platform then it can transfer the heat to the coated polymer film. From this study, we found that, the microwave annealing successfully ordered the nano-cylinders microstructure by adjusting the power in a short time, *i.e.* 60 second while the microstructure was not destroy during annealing process.

In Chapter 3, we presented the use of this PMMA-*b*-PnBA-*b*-PMMA as a binder to make a flexible molecular electrode for anchoring ruthenium catalysts. The conducting ink was prepared by MBM blends with graphite powder to provide conductivity. Then the ink was printed on the Nafion substrate by screen-printing technique. We described the performance of the electrodes, after immobilization of a catalyst, as a hybrid material for heterogeneous water oxidation process. The overall performance of the electrode-anode has been monitored by electrochemical technique with long term stability for 12-20 h of reaction. We have demonstrated the preparation of the robust and efficient polymeric electrodes.

In Chapter 4, we have synthesized P3HT-*b*-PMMA block copolymers and investigated their self-assembly behaviors. The synthesis was performed with the combination of KCTP for P3HT, ATRP for PMMA and finally Huisgen cycloaddition. We varied the P3HT block chain length and introduce a charge at the triazole linkage unit by quaternization. The temperature, the concentration and the amount of non-solvent additive were varied to tune the P3HT fibrils morphology. The fibril like morphology is increasing at high concentration, low temperature and a presence of non-solvent of P3HT. The introducing charge at the linkage unit of the block can increase the solubility of BCPs in chloroform, giving a lower π-π interaction between P3HT blocks, and driving towards block segregation. Thermal annealing above the melting temperature *Tm* of P3HT and microwave annealing were used to improve phase separation of polymer films. Results demonstrated that, microwave annealing of 60 seconds at

30W can decrease the fibrils of P3HT while this can also be done by thermal annealing at 230 ºC for 10 minutes.

In Chapter 5, we described the preparation of an artificial metallo-enzyme, diimine-dioxime cobalt complex end-caped P3HT. Synthesis process undergoes three steps: 1) the KCTP to prepare aniline end-chain of P3HT, then 2) direct condensation of P3HT-NH_2 and cyclooctyne-acid derivative to obtain highly reactive P3HT chains bearing a terminal cyclooctyne moiety, and 3) finally the copper free click reaction to couple cyclo octyne-P3HT and azido-functionalized cobalt complex. All steps were monitored by 1H NMR, MALDI-TOF or IR spectroscopy. Furthermore, the electrochemical properties of P3HT-Co complex have been performed by cyclic voltammetry. Due to lack of time, the frustrating point of this PhD is that we didn't study the catalysis behavior for hydrogen evolution and the elaboration of screen-printed electrode from P3HT-*b*-PMMA.

We demonstrated that polymer should be considered as fundamental materials to develop cheap energy device through multiple implications. Indeed, polymers are already used in organic photovoltaic devices produced *via* roll-to-roll processes and proton conducting membrane are also produced at the industrial scale with the well-known NAFION. This PhD work paved the way towards the use of polymeric materials to tailor the electrodes for hydrogen evolution and water oxidation.